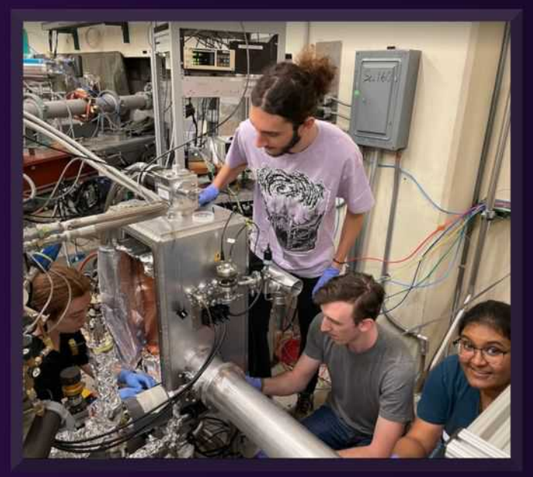

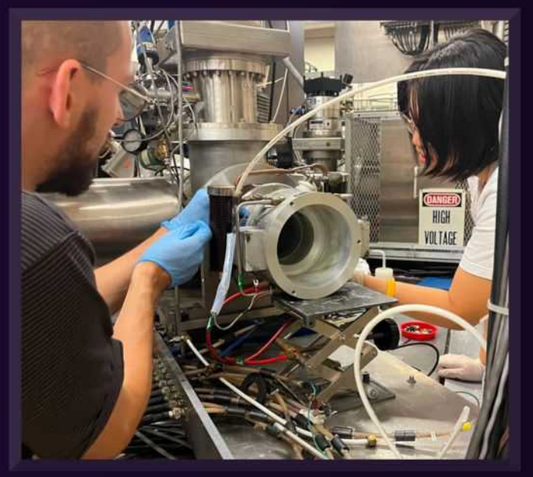

Annual Report 2024 CENTER FOR EXPERIMENTAL NUCLEAR PHYSICS AND ASTROPHYSICS University of Washington

CENPA

Center for Experimental Nuclear Physics and Astrophysics

Annual Report 2024

University of Washington

CENPA ANNUAL REPORT 2024

Center for Experimental Nuclear Physics and Astrophysics
University of Washington
February 1, 2025

Sponsored in part by the United States Department of Energy
under Grant #DE-FG02-97ER41020.

Cover photos: *(front:)* Undergraduate Research Assistant Arif Chu cleans dust particles from the inside of the Van de Graaff accelerator (VdG), as a final maintenance step before closing the tank and running the accelerator. The accelerator marks 60 years at the lab this year, and while the cleaning procedure is simpler than in the days where the VdG was belt-driven, absolute attention to cleanliness allows the machine to be run after six decades at the lab. Photo by Clint Wiseman. *(back, top left:)* Graduate students working on the He6-CRES apparatus. From left to right: Heather Harrington (UW), Luciano Malavasi (UW), RJ Taylor (NCState), Sumeera Gopal (UW). *(back, top right:)* Graduate students Sam Borden and Grace Song reinstall parts of the Sputter Ion Source on the Van de Graaff's ion source Injector Deck, as part of their work on R&D for the LEGEND experiment. The SpIS will enable onsite research with heavy-ion beams for the first time in over 10 years. Photo by Clint Wiseman. *(back, bottom left:)* Research Engineer Brittney Dodson shows off the inner workings of the Van de Graaff accelerator to postdoc Louis Variano of LEGEND. Photo by Clint Wiseman. *(back, bottom right:)* Postdoc Heng Lin prepares the first DAMIC-M CCD wafer for transfer from storage in NPL to the CCD packaging lab in PAB. Photo by Kush Aggarwal.

FOREWORD

We are delighted to be preparing this Annual Report at a time when CENPA is thriving. We are particularly delighted to mention that Elise Novitski accepted an Assistant Professor position last year and Quentin Buat accepted one this year. Elise leads the important Project 8 program that seeks to measure the neutrino mass. Quentin splits his time between analysis of ATLAS data from the LHC and, at CENPA, developing the rare pion decay experiment PIONEER. This Annual Report will feature a snapshot of the latest findings and as well as detailed projects reports that individuals and groups are engaged in at the moment. Please enjoy.

-- David Hertzog, Director of CENPA –

CENPA Group Photo 2024

Front Row: Gary Holman, Derek Storm, Ryan Roehnelt, Elise Novitski, David Hertzog, Hamish Robertson, Jason Detwiler, Erik Swanson, Clint Wiseman, Heather Harrington, Paul Kolbeck.
Second Row Seated: Gray Rybka, Nicholas Buzinsky, Matthew Kallander, Leo Weimer, Louis Varriano, Yuan-Ru Lin, Dan Zhang.
Standing Back: Megan Harrison, Adam Yusopov, Patrick Schwendimann, Armina Moghadasi, Forest Tschirhart, Heng Lin, Emily Miller, Quentin Buat, Shoshana Apple, Alex Gorman, Conner Gettings, Sam Borden, Nicolas Oaxaca, Joshua LaBounty, Luciano Malavasi, Brynn MacCoy, David Peterson, Nate Miedema, Bradley Taylor, Charles Hanretty, Kieran Enzian, Pater Park, Tim Van Wechel, Marcos Marroquin, James Sinnis, CJ Nave, Peter Kammel, Grace Song, Marcel Conde, Michaela Guzzetti, Alejandro Garcia.
Photo Credit: Conner Gettings

INTRODUCTION

The Nuclear Physics Lab at the University of Washington was established 1948. In 1998, it evolved into CENPA, the Center for Experimental Nuclear Physics and Astrophysics. CENPA is the institutional home for a broad program of research in nuclear physics and related fields. Research activities — with an emphasis on fundamental symmetries and neutrinos — are conducted locally and at remote sites. In neutrino physics, we concentrate on the pursuit of the direct measurement of the neutrino mass. CENPA has been a lead US institution in the KATRIN since its inception and is currently driving the local Project 8 experiment. Both study the tritium beta decay spectrum, whose end-point shape is sensitive to the neutrino mass. We also study neutrinoless double beta decay as a collaborating institution in the ^{76}Ge based LEGEND experiment, which derives from our extensive experience in the recently completed MAJORANA effort. Looking beyond the ton scale, we continue to explore a next-generation R&D effort with the SELENA experiment. The Muon Physics group has been a major player in the high-precision measurement of the muon's anomalous magnetic moment at Fermilab. At the time of this report, the 6-year data collection campaign is complete and the last results will soon be published. This group's attention been strongly focused on the new PIONEER experiment that will measure lepton flavor universality to unprecedented levels in its first phase of rare pion decay studies. Our local fundamental symmetries program also includes an experiment using our Tandem Van de Graaff accelerator to measure the Fierz interference in ^{6}He decay, using the CRES technique developed by Project 8. This year, we proudly celebrate the 60th year of operation of the Van de Graaff. It is going strong and has been providing a variety of beams to PIONEER, LEGEND, and Project 8 for calibrations and other tests.

In addition to the research directly supported by DOE's Office of Nuclear Physics through the CENPA core grant, other important programs are located at CENPA, forming a broader intellectual center with valuable synergies. The "Gravity" group carries out, with both DOE and NSF support, studies of the weak and strong Equivalence Principles, fundamental precepts of General Relativity, as well as searches for non-Newtonian forces such as those predicted by theories with extra dimensions. In addition, they participate in LIGO with unique instrumentation that aids the functioning and stabilization of the interferometers. The DOE Office of High Energy Physics supports the unique ADMX axion search experiment. The NSF supports the DAMIC experiment that looks for light dark matter.

CENPA is home to a large number of faculty, research faculty, postdoctoral scholars, graduate students, and undergraduate students. The core professional engineering and technical staff provide diverse capabilities and skills such as state-of-the-art detector development, fabrication of custom electronics, large-scale computing, and design engineering. New advancements, capabilities, and ideas are regularly shared at seminars by CENPA members and visitors alike.

Personnel updates

Faculty: Elise Novitski joined the faculty as a tenure-track Assistant Professor. She is leading the Project 8 effort and has recently been selected for a DOE Early Career award. Alvaro

Chavarria was promoted to Associate Professor with tenure. Jason Detwiler and Gray Rybka were both promoted to the rank of Professor. Research Professor Peter Doe retired and is a still-active Emeritus Professor, concentrating on the Project 8 Atomic Source development. In 2025, Research Professor Peter Kammel will transition to Emeritus Professor status, concentrating on many efforts he has been leading for the PIONEER experiment. New Research Assistant Professor Claudio Savarese will initially focus on support of the LEGEND experiment. Quentin Buat joined UW as an Acting Assistant Professor in 2021 and began involvement in PIONEER in 2022. He is presently a tenure-track Assistant Professor working on ATLAS and on PIONEER.

Staff: Research Scientist Duncan Prindle and Machine Shop Manager Tom Burritt each retired in 2023. Senior Accelerator Engineer Eric Smith accepted a new position at Sandia Laboratory to operate their Van de Graaff (VdG) end stations. Junior Research Engineer Brittney Dodson was promoted to lead the accelerator operations and has assembled an expert team. Over the past 12 months, they have delivered on a variety of very challenging beam requests for several CENPA groups. Machinist Nate Miedema is now running the CENPA professional shop and overseeing the student shop. Clint Wiseman is a new Research Scientist replacing Prindle. He works on Van de Graaff system upgrades, the CENPA computing cluster, and supports the He-6 CRES experiment. Junior electronics engineer Mason Newman was recently hired to assist with the VdG and other electronics support. We welcome Angela Lawson as our new front office administrator.

Postdocs: Zach Hodge (Muon g-2), Alexander Marsteller (KATRIN/Project 8), and Christine Claessens (Project 8/Muon g-2) have left the group. Postdoctoral scholars at present (Oct. 2024) include Svende Braun (Muon g-2 / PIONEER), Nick Buzinsky (He-6), Heng Lin (DAMIC/Selena), Patrick Schwendimann (PIONEER), Michelangelo Traina (DAMIC/Selena), Louis Varriano (LEGEND), Brynn MacCoy (Muon g-2), Josh LaBounty (g-2/Pioneer), and Yu-Hao Sun (KATRIN/Project 8).

Graduate Students: Ph.D.'s awarded to date recently include Alex Hostiuc (MAJORANA), Josh LaBounty (Muon g-2), Brynn MacCoy (Muon g-2), Ethan Muldoon (MuSun), Alex Piers (DAMIC/Selena), and Nick Ruof (MAJORANA / LEGEND.)

Recognitions: Elise Novitski won the APS DNP Stuart Jay Freedman Award in 2023. Jason Detwiler was once again recipient of the UW Faculty Excellence in Teaching award. Leslie Rosenberg won the 2024 APS Panosfsky Prize for his work on the CENPA-housed ADMX experiment. Eric G. Adelberger is the recipient of the APS 2025 Einstein Prize for his work in experimental gravity here at CENPA. Several of our graduate students have been recognized for their accomplishments. Harry Ni won the 2024 UW Dehmelt Prize for his work on Selena. Brynn MacCoy and Josh LaBounty both won awards in 2024 for their theses on the Muon $g-2$ experiment: MacCoy earned the Fermilab URA PhD Thesis Award and LaBounty the UW Henderson Prize.

Recent Accomplishments

- KATRIN accumulated over 70% of the total anticipated data and has produced its third neutrino mass measurement, setting a limit of m_ν at 0.45 eV (90% CL), a factor

of two improvements over the previous result.

- Project 8 measured the conversion-electron spectra of the 32-keV ^{83m}Kr transition with 1.66-eV FWHM resolution, demonstrating the very high-resolution of Cyclotron Radiation Emission Spectroscopy (CRES). The first CRES-based measurement of the tritium spectrum was published from 82 days of data, where no background events above the endpoint were observed.
- The MAJORANA DEMONSTRATOR project was largely completed during this reporting period, with the publication of several milestone papers, including results on the decay of ^{180m} Ta, searches for several models of "exotic" dark matter, and tests of quantum mechanics via charge non-conservation and Pauli exclusion principle violation. The UW group led by Detwiler (spokesperson) and Wiseman (postdoc, now staff) led the analysis effort for the dark matter and quantum mechanics tests, resulting in publications in Nature Physics and Physical Review Letters.
- The LEGEND-200 detector made its first physics run, and with 50 kg yr of exposure reported a preliminary combined ^{76}Ge $0\nu\beta\beta$ half life limit of $T_{1/2} > 1.9 \times 10^{26}$ yr at 90% CL. A cleaning and assay campaign is currently underway, then the detectors will be redeployed for new physics run that represents humanity's next significant chance to discover this ultrarare physics.
- The LEGEND-1000 project has progressed to readiness for a DOE CD-1 review, and a portion of the scope including the UW contribution was proposed to the NSF.
- COHERENT reported first results on coherent elastic ν-nucleus scattering on Ge, along with updated results on CsI. We also reported a measurement of CC neutrino scattering on ^{127}I and neutrino-induced neutron production on Pb, with relevance to $0\nu\beta\beta$ decay nuclear matrix element calculations and supernova neutrino detection. Following these achievements, we closed off our participation in this project.
- KamLAND-Zen 800 reported a new, world-leading ^{136}Xe $0\nu\beta\beta$ half life limit of $T_{1/2} > 3.8 \times 10^{26}$ yr at 90% CL. Japanese funding has been secured for KamLAND2 and data taking has been halted for detector refurbishment.
- The Muon $g-2$ Run-2/3 results, published in 2023, are completely consistent with the Run-1 findings and the combined precision is now 200 ppb. Systematic uncertainties are smaller than proposal projections. Analysis of data from Runs-4/5/6 are mature with an expected release in early 2025.
- The PIONEER Experiment design has evolved considerably, with leadership by UW in many areas of hardware and simulation/physics software. The CENPA Van de Graaff was used on numerous occasions to evaluate LGAD sensor strips and LYSO calorimeter crystals, both leading to publications.
- The He6-CRES experiment has demonstrated detection of betas from ^{6}He and ^{19}Ne using cyclotron radiation emission spectroscopy (CRES) for precise beta spectroscopy over the few-keV to few-MeV range of energies. This opens the path for searching for tensor and scalar currents with high sensitivity.
- The Selena R&D program brought complementary metal–oxide–semiconductor (CMOS) sensor design in-house. We have procured and characterized the first generation of sen-

sors optimized for charge collection in amorphous selenium, achieving several design specifications for the Selena Neutrino Experiment.

- The DAMIC-M detector design was completed and validated. Detector construction is ongoing, with the production of the final skipper-CCD modules taking place at UW. Twenty-six CCD modules (a 0.35 kg silicon target) will be deployed at Modane underground lab by the CENPA group in the first half of 2025. DAMIC-M is expected to improve by three orders of magnitude the sensitivity to dark matter particles with MeV masses.
- ADMX has been operating in its "Run1D" configuration scanning the 1.2 to 1.3 GHz range for axions since the beginning of 2024. This has been the longest continuous science operations period for ADMX to date and we anticipate it to lead to wider coverage of promising axion parameter space in the future.
- The Gravity group is operating its rotating torsion balance apparatus with a fused quartz torsion fiber. The differential acceleration sensitivity towards the Sun or galactic dark matter is improved by a factor of five. The group has designed, built and installed inertial rotation sensors for LIGO to sense ground rotations. A new version of these sensors measures the Newtonian noise, which would limit future gravitational wave detectors at their coveted low frequency end.
- The Van de Graaff delivered beams for the He6-CRES program (for production of ^{6}He and ^{19}Ne via ^{7}Li(d,^{3}He) and ^{19}F(p,n)), for the PIONEER program for characterizing LGADs (using Rutherford proton back-scattering) and LYSO calorimeter detectors (using the high-energy photons from ^{7}Li(p,γ)), for the LEGEND program (producing ^{56}Co sources needed for calibrations via ^{56}Fe(p,n)), for the DAMIC program (using the high-energy photon cascade from ^{24}Na that was produced via ^{27}Al(n,α)) and for a class on basic nuclear physics taught for the evening Master students that includes experiments with the accelerator, on Rutherford backscattering, nuclear resonances and basic elements of nuclear spectroscopy.

As always, we encourage outside applications for the use of our facilities. As a reference for potential users, the table on the following page lists the capabilities of our accelerator. For further information, please contact Gary Holman, Associate Director (holman@uw.edu) or Brittney Dodson, Research Engineer (wynn8@uw.edu) CENPA, Box 354290, University of Washington, Seattle, WA 98195; (206) 543 4080. Further information is also available on our web page: `http://www.npl.washington.edu`. We close this introduction with a reminder that the articles in this report describe work in progress and are not to be regarded as publications nor to be quoted without permission of the authors. In each article the names of the investigators are listed alphabetically, with the primary author underlined in the case of multiple authors, to whom inquiries should be addressed.

David Hertzog, Director
Gary Holman, Associate Director
Clint Wiseman and Jason Detwiler, Editors

TANDEM VAN DE GRAAFF ACCELERATOR

Our tandem accelerator facility is centered around a High Voltage Engineering Corporation Model FN purchased in 1966 with NSF funds, with operation funded primarily by the U.S. Department of Energy. See W. G. Weitkamp and F. H. Schmidt, "The University of Washington Three Stage Van de Graaff Accelerator," *Nucl. Instrum. Methods* **122**, 65 (1974). The tandem runs the majority of its time using the Direct Extraction Ion Source (DEIS) to produce up to 9 MeV proton and 18 MeV deuterium beams for the He6-CRES experiment. The Model 860 Sputter Ion Source is available for heavier ion beams.

Some Available Energy Analyzed Beams

Ion	Max. Current (particle μA)	Max. Energy (MeV)	Ion Source
^{1}H or ^{2}H	50	18	DEIS or 860
^{3}He or ^{4}He	2	27	Double Charge-Exchange Source
^{3}He or ^{4}He	30	7.5	Tandem Terminal Source
^{6}Li or ^{7}Li	1	36	860
^{11}B	5	54	860
^{12}C or ^{13}C	10	63	860
^{*14}N	1	63	DEIS or 860
^{16}O or ^{18}O	10	72	DEIS or 860
F	10	72	DEIS or 860
* Ca	0.5	99	860
Ni	0.2	99	860
I	0.001	108	860

*Negative ion is the hydride, dihydride, or trihydride.

Several additional ion species are available including the following: Mg, Al, Si, P, S, Cl, Fe, Cu, Ge, Se, Br and Ag. Less common isotopes may be generated from enriched material. We have recently produced rare-isotope calibration sources such as ^{56}Co and ^{79}Kr, and provide proton beams at variable energies as low as 1 MeV. We maintain capabilities to create pulsed ("chopped") ion beams for experimental background rejection, including a separated beam of 15-MeV ^{8}B at 6 particles/second. We maintain hardware for a terminal ion source with its non-inclined beam tube, which enable high intensity beams of hydrogen and helium isotopes from 100 keV to 7.5 MeV. We are capable of production of positive ion beams of the noble gases He, Ne, Ar, and Kr at ion source energies from 10 keV to 100 keV for implantation, in particular the rare isotopes ^{21}Ne and ^{36}Ar.

Contents

1 Neutrino Research

LEGEND

1.1 Commissioning and status of the LEGEND search for $0\nu\beta\beta$ in Ge-76

S. Borden, J. Detwiler, Y.-R. Lin, E. Miller, C. J. Nave, D. A. Peterson, R. Roehnelt, G. R. Song, L. Varriano, T. D. Van Wechel, and C. Wiseman

LEGEND is a next-generation neutrinoless double-beta ($0\nu\beta\beta$) decay search in ^{76}Ge. By combining the technological expertise and experience from the MAJORANA DEMONSTRATOR and GERDA experiments, LEGEND is expected to reach a design sensitivity two orders of magnitude greater than its predecessors.

The phased program advances from the intermediate-scale LEGEND-200 experiment to the future LEGEND-1000 experiment. LEGEND-200 is currently collecting physics data with ∼140 kg of enriched HPGe detectors deployed at the Laboratori Nazionali del Gran Sasso (LNGS) in Italy. The first physics results from LEGEND-200 have been presented in Neutrino 2024 and will be published in early 2025.

LEGEND-1000 is a leading candidate for a future US-led tonne-scale $0\nu\beta\beta$ experiment. It uses advances from the ^{76}Ge program, through LEGEND-200, to retire risks by demonstrating scalability of the array and the achievement of background goals. It will yield an additional order of magnitude sensitivity to the $0\nu\beta\beta$ half-life, covering the neutrino mass parameter space allowed by the inverted ordering of neutrino masses.

Members of the LEGEND group at CENPA play a leading role in the development of the analysis framework for the project, which is actively tested on the data collected with our local test stands. Professor Detwiler is a member of the LEGEND Steering Committee, an Analysis Co-Coordinator, and the lead of the Analysis Framework task group. Locally, we are pursuing R&D jefforts to understand the surface response of HPGe detectors and the light detection of SiPM detectors. These efforts are described in the subsequent sections.

1.2 First results from LEGEND-200 on the search for $0\nu\beta\beta$ decay

S. Borden, J. Detwiler, Y.-R. Lin, E. Miller, C. J. Nave, G. R. Song, and L. Varriano

The LEGEND experiment searches for neutrinoless double beta decay in ^{76}Ge-enriched high-purity germanium detectors operating in liquid argon, whose scintillation acts as an active veto against external background events. Using specialized detector geometries, pulse shape discrimination is performed to further veto background events. LEGEND-200 has completed about one year of stable physics data-taking at Laboratori Nazionali del Gran Sasso (LNGS) in Italy, with the first data recently unblinded. With only 7 events located in the fit window around $Q_{\beta\beta}$ and an exposure of 48 kg·yr, LEGEND-200 did not find evidence for $0\nu\beta\beta$ decay. The events found were consistent with background and gave a background index of $5.3 \pm 2.2 \times$

10^{-4} cts/(keV·kg·yr), obtained by profiling over background and signal rates. By combining this result with the results of the preceding MAJORANA and GERDA experiments, a new limit on the ^{76}Ge $0\nu\beta\beta$ half-life is placed at $T_{1/2} > 1.9 \times 10^{26}$ years at 90% CL.

At CENPA, we have contributed to the experiment and analysis in several ways. S. Borden, C.J. Nave, and G.R. Song performed detector calibration and pulse shape discrimination cross-checks for the analysis, as well as contributing to the analysis chain of the experiment. L. Varriano, S. Borden, and G.R. Song, with contributions from Y.-R. Lin and C.J. Nave, led a frequentist statistical analysis that confirmed and improved upon the primary frequentist analysis further experiment. Due to the higher than desired background found in LEGEND-200, L. Varriano participated in the disassembly of the experiment for a screening campaign to identify possible sources of higher background.

With a planned ultimate exposure of 1 ton· years and a target background index of 2×10^{-4} cts/(keV·kg·yr) at $Q_{\beta\beta} = 2039$ keV, LEGEND-200 is expected to reach a discovery sensitivity of 3 σ years of 10^{27} years half-life. The next generation experiment, LEGEND-1000, will operate 1000 kg of detectors and reach an expected discovery sensitivity of 10^{28} years half-life, covering the inverted neutrino mass hierarchy.

This work is supported by the US DOE and the NSF, the LANL, ORNL, and LBNL LDRD programs; the European ERC and Horizon programs; the German DFG, BMBF, and MPG; the Italian INFN; the Polish NCN and MNiSW; the Czech MEYS; the Slovak RDA; the Swiss SNF; the UK STFC; the Russian RFBR; the Canadian NSERC and CFI; the LNGS and SURF facilities.

1.3 LEGEND L-1000 Lock System

J. Detwiler, E. Miller, R. Roehnelt, and L. Varriano

The experience of the GERDA, MAJORANA and LEGEND-200 experiments has guided the design and development of the lock system. Previously, in LEGEND-200, the entire detector array was able to be raised and lowered within a single lock. However, since LEGEND-1000 is a much larger and heavier stage, this is not possible. LEGEND-1000 will deploy individual strings of eight detectors that will be suspended from their own flange and sealed on their own port on the cryostat lid, then submerged in a bath of underground liquid argon UGAr. The underground liquid argon shall maintain purity levels of less than 0.1 ppm nitrogen and 1 ppm oxygen and shall not be mixed with the outer bath of atmospheric argon. The LEGEND-1000 lock system enables long strings of germanium detectors to be installed and removed from the cryostat containing UGAr. This design avoids coiling and uncoiling of cables and other mechanical supports but requires a large headspace above the main cryostat to fit the tubes that allows for string deployment. The lock system also minimizes the lock deployment cycle time, reducing the deployment time to be no more than a 24- or 48-hour period.

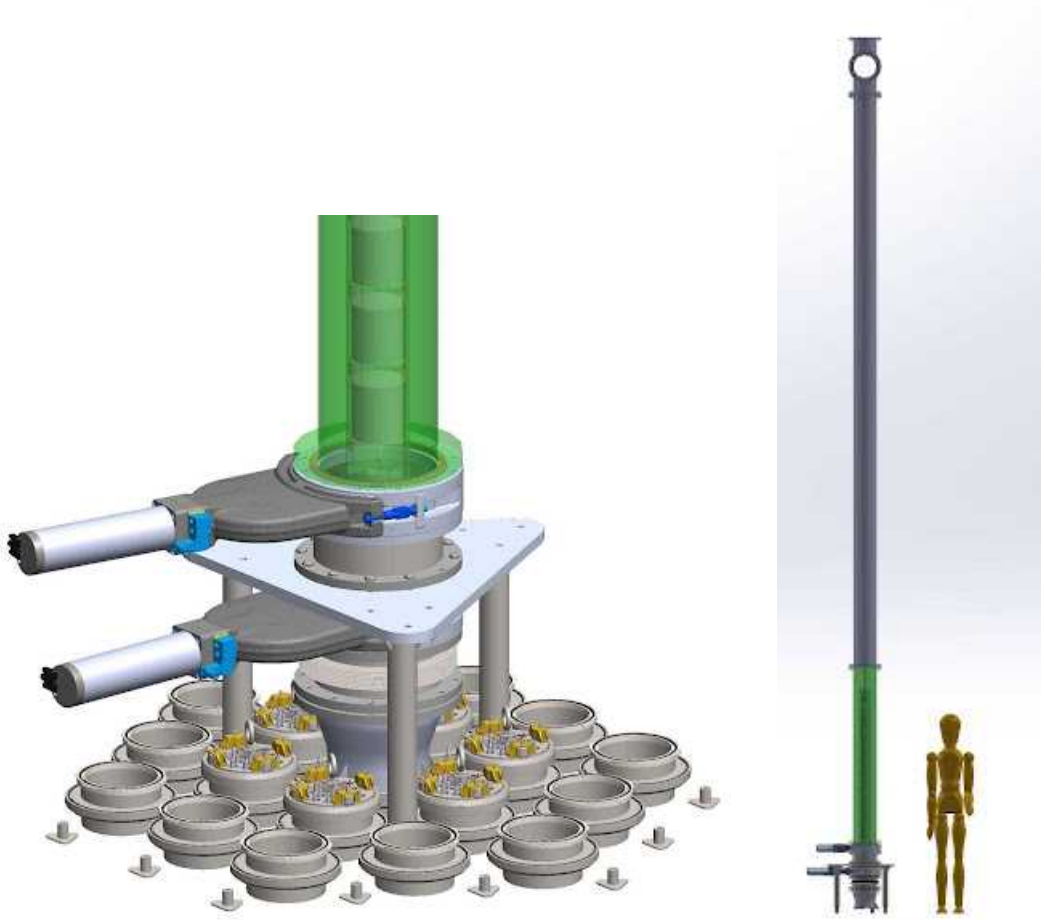

Figure 1.3-1. *(left:)* Close up view of the lock table with gate valve with the lock tube loaded with detector string, ready for deployment. *(right:)*: View of the tube and lock system with full length of the lock tube loaded with detector string.

One of the tasks the LEGEND team at UW has taken on is the design and prototyping of the Lock apparatus for LEGEND-1000. The primary components of the system include vacuum pumps and UGAr gas handling systems, controls and interlock systems to monitor operation, sealing actuator, lock tube, internal crane system, and a system to move and align the flange and the cable. The design allows the strings to be assembled in the LEGEND-1000 glovebox, attached to a flange, and secured inside an 8m long tube, then purged and pressurized with argon before being moved to the cryostat port for installation. The sealing actuators, gate valves, and interlock systems will then allow the string and flange to be installed on the cryostat lid without contaminating the UGAr.

Figure 1.3-2. *(left:)* Assembly of stage one prototype in the high bay of CENPA. *(right:)* CAD model of stage one prototype in the high bay, with linear-plus-rotary feedthroughs, DPRF, and vacuum chamber with port and mock string flange (inside chamber).

At UW, we have several stages of prototyping underway. The first stage has been constructed in the high bay of CENPA, where we have begun prototyping the sealing actuator, which consists of the linear plus rotary feedthroughs, chamber, string-flange port, and pumps. The second stage is being constructed in Cave 1 of CENPA, where we will prototype the overhead crane movement, lock interface with crysotat, raising and lowering of mock strings, insertion and removal of cryogen, and gasket exchange in the glovebox.

1.4 Characterizing low-energy surface backgrounds with KrSTC

J. A. Detwiler, N. Fuad, L. Gehring, J. Kaler, N. Miedema, E. Miller, C. J. Nave, D. A. Peterson, W. Pettus, T. D. Van Wechel, L. Varriano, and C. Wiseman

Understanding the energy spectrum produced by high-purity germanium (HPGe) detectors used in the LEGEND experiment is a critical check against our understanding of the components making up the background for the experiment. This is of particular importance near the $Q_{\beta\beta}$ value of 2039 keV in ^{76}Ge, the energy at which we expect neutrinoless double beta decay ($0\nu\beta\beta$) to occur. Due to the extremely slow (if existing) decay rate of $0\nu\beta\beta$, the region near $Q_{\beta\beta}$ must be practically background-free to claim a discovery. There are a number of

backgrounds that can contribute to the measured LEGEND energy spectrum. One background of interest for the UW LEGEND group arises from surface events. Ionizing radiation that does not penetrate far (< 1 mm) into an HPGe detector can produce signals that do not fully contain the total energy deposited by said radiation, degrading the reconstructed energy. CAGE studies this effect with surface alphas which is relevant for $0\nu\beta\beta$ analysis, and the Krypton String Test Cryostat (KrSTC) uses low-energy electrons, gammas, and x-rays to study this phenomenon at low energy. These energies are well below $Q_{\beta\beta}$, but this energy region is worth studying due to LEGEND's sensitivity to potential beyond the Standard Model (BSM) physics.

A picture of the experimental setup of KrSTC is shown in Fig. 1.4-1. Inside the cryostat, we install a p+ point contact (PPC) ^{76}Ge detector connected to the electronics inside and outside the cryostat. All of these electronics are made by engineers in CENPA and are optimized for our detector and data-taking needs. The detector is also connected to a high voltage supply, which allows us to bias the detector up to its maximum operating voltage of 2700 V. During operation, the cryostat is pumped in by a two-stage vacuum pump where we can achieve pressures below 10^{-6} mbar when warm. There is also a copper cold finger that connects the detector assembly and a liquid nitrogen dewar to cool the detector to ~ 90 K. These cold surfaces provide us with cryopumping, allowing our cryostat to achieve pressures below 10^{-7} mbar.

Figure 1.4-1. The KrSTC hardware setup. The main cryostat body contains a PPC ^{76}Ge detector and is connected to a vacuum pump and our ^{83m}Kr source. Above the cryostat are the electronics used to extract signals which are then sent to a digitizer for data collection.

The cryostat is also connected to a ^{83}Rb source that produces radioactive ^{83m}Kr gas. This krypton gas emits monoenergetic photons and electrons below 33 keV. The fact that these photons and electrons are monoenergetic makes it in theory easier to determine the nature of the energy degradation of the krypton decay products.

Data were taken across about a year (February 2023 - April 2024), typically starting with

background runs before introducing krypton gas into the cryostat. The most basic analysis is making a background-subtracted krypton spectrum. Three examples of these spectra are shown in Fig. 1.4-2. The most interesting part of this analysis is that depending on data-taking conditions–most heavily correlated with the cryostat pressure at which we began cooling with liquid nitrogen–the krypton spectrum would drastically change. One theory is that, when cooling at higher temperatures, more water vapor and other residual gases can condense on cold surfaces, changing the surface charge configuration on the insulating passivated surface of the germanium detector.

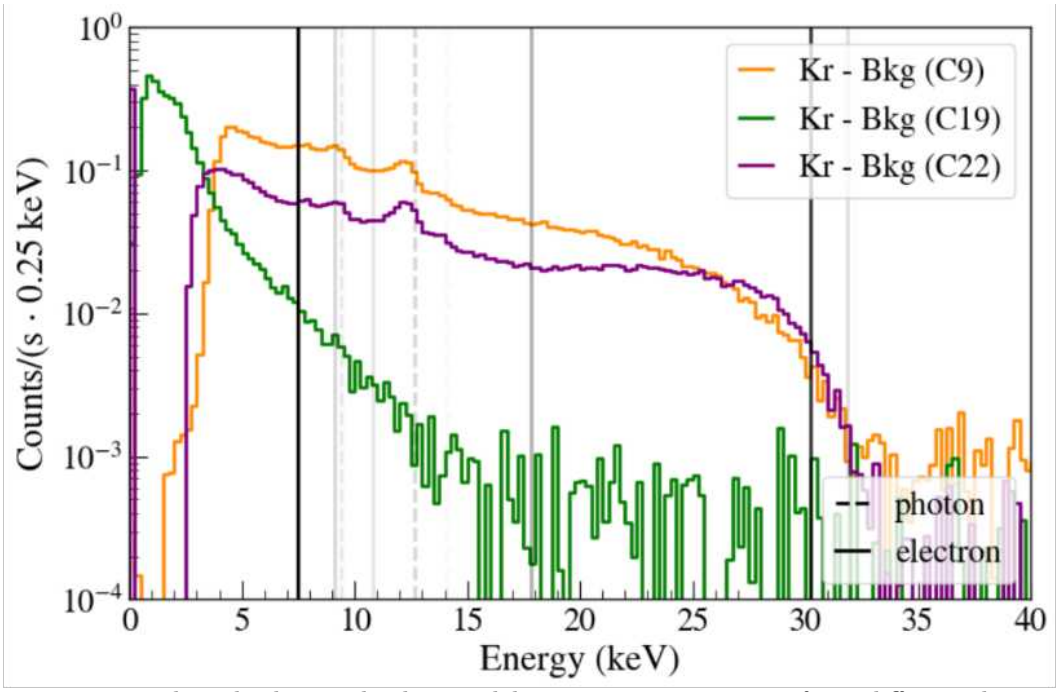

Figure 1.4-2. Three background-subtracted krypton energy spectra from different data-taking campaigns are shown above. The spectra labeled "C9" and "C22" were taken from campaigns with higher pressure-at-cooldown values, with the "C19" spectrum showing a spectrum with a lower pressure-at-cooldown. There are distinct differences in each energy spectrum suggesting a strong dependence on this pressure-at-cooldown value. Expected krypton decay products are depicted as vertical lines with opacity scaling as expected intensity.

If free charges are collected on the passivated surface (made of amorphous germanium), those charges can influence the drift of charge carriers within the Ge crystal. In particular, a negative surface charge can pull holes towards the passivated surface and cause incomplete charge collection (the holes are "stuck" on the passivated surface and released on time scales longer than our waveform collection time). Since our signals are hole-dominated, this would generate a large region of the detector near the passivated surface that is not fully active. An activeness map for a surface charge of $\sigma = -3 \times 10^8$ e/cm^2 is shown in Fig. 1.4-3.

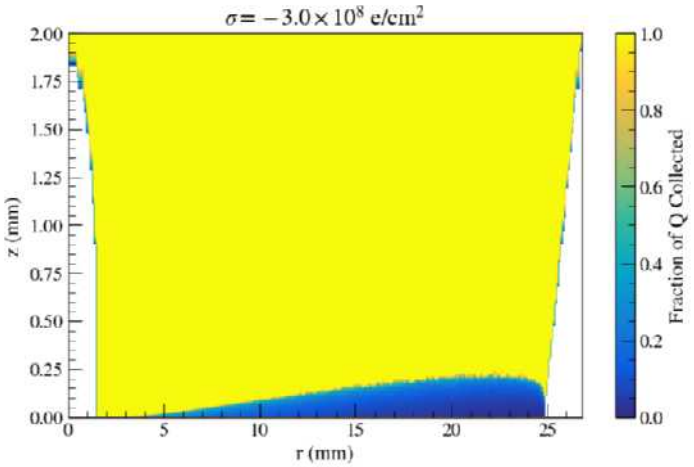

Figure 1.4-3. Depiction of "elephant ear" dead layer near the passivated surface of the OPPI detector. Surface charge density of $\sigma = -3 \times 10^8$ e/cm^2 applied to passivated surface ($z = 0$). Based on simulations from the `siggen` package. Deadness along p+ point contact surface at small r and n+ bevel at large r is due to interpolation along physical boundaries.

Applying this "elephant ear" activeness map to a GEANT4 simulation of ^{83m}Kr decays results in a simulated energy spectrum, shown in Fig. 1.4-4. Although the simulated spectrum does not match the data spectra completely, there are components of the data that are recreated in simulation. We see a clear increase in both starting at ~ 32 keV due to degradation of the higher-energy electron lines. No electron peaks are visible but some photon peaks are. The continua above and below the expected 12.6 keV x-ray peak do not agree perfectly, but this is overall a promising explanation of what we see in the KrSTC data.

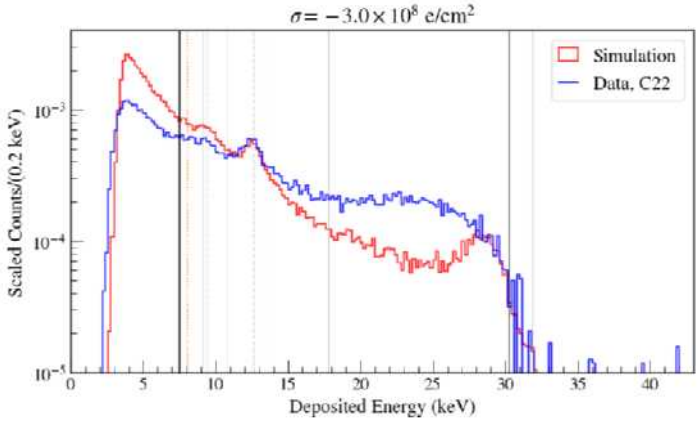

Figure 1.4-4. Comparison between background-subtracted krypton energy spectrum from data and the resultant simulated spectrum. The two spectra are scaled to match at the high-energy rise at ~ 31 keV and the expected 12.6 keV x-ray peak. There is disagreement in the continua above this 12.6 keV peak as well as below it and studies are ongoing to rectify these differences.

Another way to further study this surface charge-induced energy degradation is to solely

use photons of different energies incident on the passivated surface. An x-ray fluorescence source[1] has been developed and the hardware required to deploy it is in development. Additionally, we have plans to install an electrode above the passivated surface and will attempt to "tune" the surface charge and observe any difference in the low energy spectrum. There is also interesting analysis work to be done on the KrSTC data set. We see a clear difference in the risetimes of krypton waveforms compared to background events, and a proper pulse shape study could help tag these surface events in KrSTC and in LEGEND data.

1.5 The UW SiPM test Stand

S. Borden, J. A. Detwiler, D. A. Peterson, W. Pettus*, N. W. Ruof†, I. Wang, T. D. Van Wechel, and L. Varriano

Silicon photomultipliers (SiPMs) are solid-state semiconductor devices operated in Geiger mode that are capable of single photon detection. Many experiments, such as LEGEND-200, operate these SiPMs directly in cryogenic liquid noble gas detectors to measure scintillation light. Maximizing the light collection of these experiments optimizes their sensitivity for new physics, and this requires maximizing the photon detection efficiency (PDE) of the SiPMs used in an experiment. An estimate of the PDE of these devices is available from the manufacturer; however, this estimate is only reported at room temperature, and not at the cryogenic temperatures at which these experiments operate. We have built a test stand here at CENPA to measure the PDE at liquid nitrogen temperatures.

We have finished the analysis of our first results using the test stand at CENPA. Two SiPMs were characterized at cryogenic temperatures using 560 nm light, and both displayed a 20 % reduction in the PDE at cryogenic temperature as compared to room temperature. These measurements verify Ruof's previous results [2] with an alternative methodology based on Poisson statistics of baseline events. Numerous systematic studies were performed to ensure that no optical properties of the test stand were changing as a function of temperature. These studies allowed us to place a systematic uncertainty of 2 % on our measurements and are summarized in Borden *et al*[3].

Updates have been made to the test stand to reduce downtime between data-taking periods: a liquid nitrogen fill line and level meter have been added, as well as a gaseous nitrogen purge line to prevent the formation of condensation on core electronics. This improved configuration and procedure circumvents the need for a warm-up period between liquid nitrogen and room temperature measurements by reversing the order in which they are done; room temperature data is taken first, and the fill line facilitates the cool-down process without disassembly of the apparatus.

*Indiana University, Bloomington, IN.
†Lawrence Livermore National Laboratory, Livermore, CA.

[1] S. R. Elliott, B. Dodson, C. Wiseman, *et al*, arXiv:2211.05691 [physics.ins-det] (2022).
[2] CENPA Annual Report, University of Washington (2023) p. 34.
[3] S. Borden, J. Detwiler, N. Ruof, W. Pettus, arXiv:2405.01529, (2024).

The SiPM test stand has also been upgraded to be capable of PDE measurements at multiple wavelengths: our most recent datasets have included PDE measurements using 385 nm, 470 nm, and 740 nm wavelength LEDs for both Broadcom and Hamamatsu SiPMs at room temperature and liquid nitrogen temperature. Analysis of this data indicates that PDE is consistently decreased at cryogenic operation of the SiPMs, regardless of detected photon wavelength. The results of the Hamamatsu data are shown in Fig. 1.5-1.

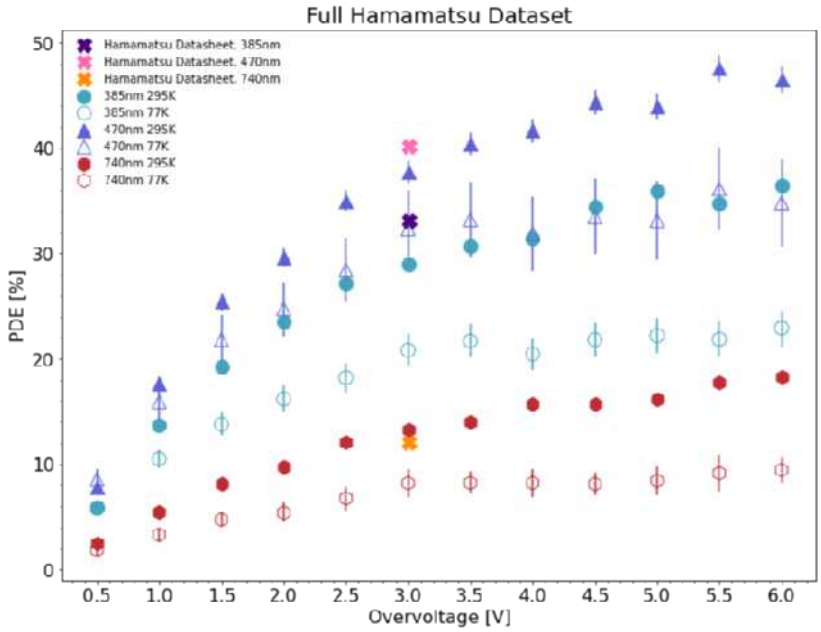

Figure 1.5-1. Cryogenic PDEs for the Hamamatsu S13360-3050CS SiPM at three different wavelengths. All three wavelengths show a decrease in the PDE at cryogenic temperature.

We are currently investigating the physical phenomena that contribute to the observed PDE quenching by performing a nonlinear regression of our data to a proposed set of functions from Gallina *et al*[1] that model PDE as a function of geometric parameters and wavelength dependent optical variables. Fit results indicate that a majority of the temperature dependence of the PDE originates from changes in quantum efficiency, which is voltage independent, while a smaller contribution comes from variation in the SiPMs' Geiger discharge probability, which is voltage dependent. This is visually striking when data are acquired at equal relative overvoltages, as shown in Fig. 1.5-2. These curves have roughly the same shape that is set by the Geiger discharge mechanism, but a different asymptotic value that is set by the quantum efficiency.

[1]G. Gallina, F. Retière, P. Giampa, J. Kroeger, P. Margetak, S. Mamahi, IEEE TED **66**, 10 (2019).

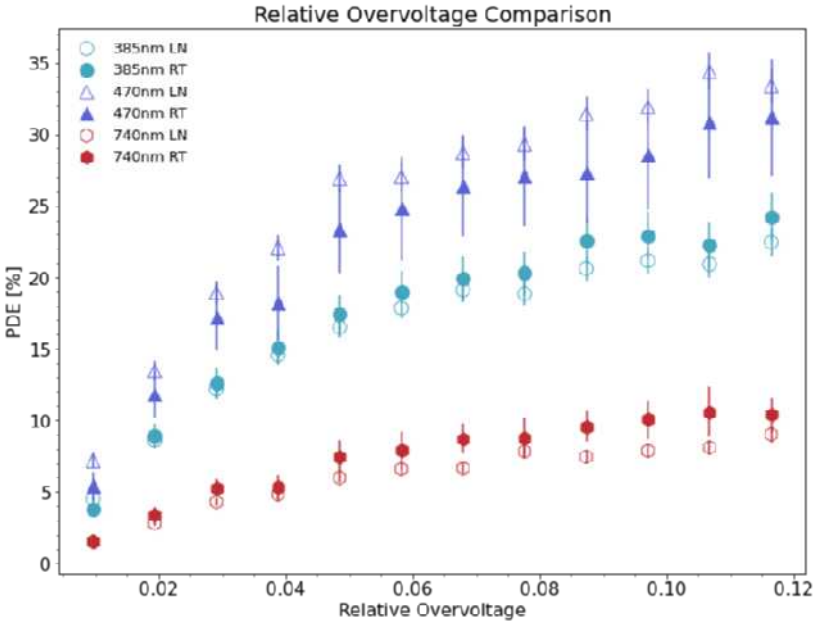

Figure 1.5-2. Comparison of the PDEs for the Hamamatsu SiPM as a function of relative overvoltage. The difference in PDE at large relative overvoltages indicates the the quantum efficiency of this device drops at cryogenic temperature.

1.6 Alpha event characterization with the CAGE Scanner

J.A. Detwiler, N. Miedema, D. A. Peterson, G. Song, T. D. Van Wechel, and C. Wiseman

The CAGE Scanner is designed to study the response of the HPGe detector to potential background sources that penetrate the passivated surface. Radiation that enters the active volume through the passivated surface can become energy degraded, causing normally high-energy radiation to be reconstructed into our region of interest. In particular, alpha radiation from the ^{238}U and ^{232}Th decay chains is emitted in the 4-5 MeV range, but can be reconstructed with energies near the 2039 keV $0\nu\beta\beta$Q value. CAGE uses an Am-241 source to direct a collimated beam of 5 MeV alpha particles onto the passivated surface at specific radii, rotary angles, and incidence angles. This year we completed the hardware upgrades necessary to study the influence of the HV contact on pulse shapes and began development of a new pulse shape discrimination (PSD) parameter targeted at alpha discrimination.

Our hardware changes allow us to attach our HV supply to the aluminum pad bonded to the N+ surface of the detector, as opposed to the copper HV ring on which the detector sits. Resistance measurements from the front end electronics to the aluminum pad showed a better connection than to the HV ring. We wanted to investigate whether this better connection would lead to more stable pulse shape parameters over time. Our preliminary results suggest that it does not make a noticeable difference, but need to be verified with more measurements.

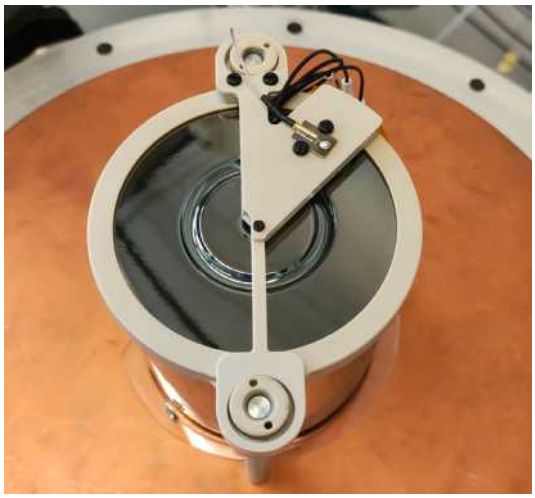

Figure 1.6-1. New HV contact pin that connects to the aluminum pad for a lower resistance HV connection.

We also began the process of developing a new PSD parameter, the early charge (EQ) parameter. The idea was born from an observation that bulk and alpha superpulses differ greatly in the early stages of the rising edge. We decided to calculate EQ by adding the 500 ns window before each waveform reaches 20% of its maximum and normalizing it by the uncalibrated energy. This method was compared with other fixed time windows, windows set by different amplitude thresholds, and an entirely different method that calculated the second derivative of the waveform and was found to maximize the separation of alpha events from the bulk. Future work includes comparing the performance of EQ with the existing parameters in LEGEND. We will do this both by computing the LEGEND parameters in the CAGE data and by computing the EQ for the LEGEND-200 data.

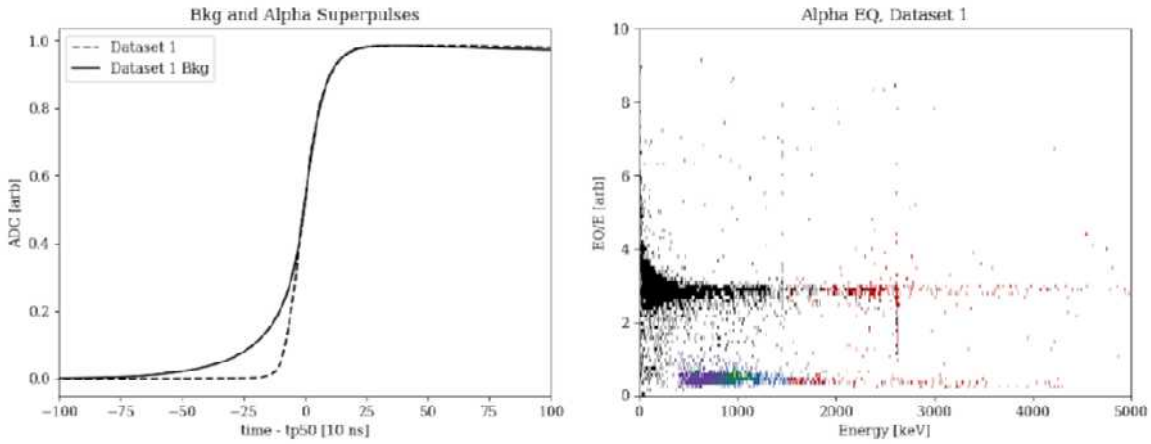

Figure 1.6-2. *(left)* Superpulses of waveforms taken in CAGE. The solid line is a superpulse of background data, taken with the source directed away from the detector, and the dashed line is a superpulse of alpha events, identified through PSD cuts. *(right)* EQ/E vs. calibrated energy. Different colors represent alphas identified at different positions on the detector.

1.7 Silicon detector α, β pulse shape discrimination

S. Borden, J. A. Detwiler, A. Garcia, P. Kammel, E. Miller, C. J. Nave, G. R. Song, F. Tschirhart, and L. Varriano

Motivated by recent measurements of the ^{8}B neutrino spectrum[1] and ^{8}B and ^{8}Li angular correlation measurements to search for a tensor contribution to the weak interaction [2] , we are interested in applying some of the pulse shape discrimination techniques developed by LEGEND to silicon detectors. In these recent measurements, ^{8}B or ^{8}Li ions are trapped between four 1 mm thick silicon detectors which detect the < 16 MeV α and β decay products. These decay products are differentiated by their deposited energy alone, which makes distinguishing < 1 MeV α nearly impossible from the minimimum-ionizing β. However, due to the different topology of the electron-hole pair ionization tracks in the detector from α and β, it may be possible to discriminate between the α and β by their pulse shape.

To investigate LEGEND-style pulse shape discrimination techniques, F. Tschirhart and P. Kammel developed an experimental setup to quickly switch between α and β sources, allowing for rapid testing of legacy silicon detectors to determine which were still operable. F. Tschirhart also developed and ran simulations to predict the expected pulse shape difference and identify appropriate β sources to use. For this work, a ^{207}Bi source was used to provide minimum-ionizing β and a ^{244}Cm source was used to provide 5.8 MeV α. These α were then degraded by an aluminum foil to around 1 MeV. Having identified a usable partially depleted silicon detector, mitigating many sources of noise, and optimizing data acquisition, F. Tschirhart was able to produce a preliminary analysis demonstrating the feasibility of pulse shape particle identification for a silicon detector, as shown in Fig. 1.7-1. Based on the β energy, a region of only minimal ionizing particles was selected for analysis. The superpulse of the selected events indicates that the pulse shape classifier may be able to distinguish between α and β with good efficiency, which will be studied further.

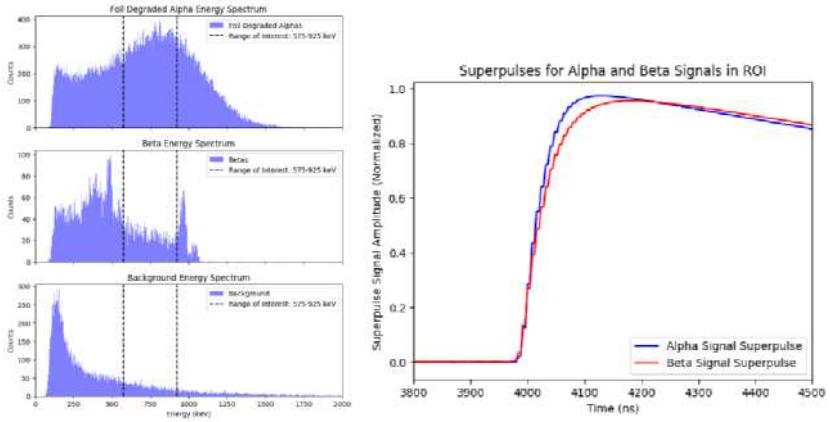

Figure 1.7-1. *(left top)* degraded α energy spectrum, *(left middle)* β energy spectrum, and *(left bottom)* background energy spectrum. *(right)* Superpulse of waveforms in the indicated energy region, showing the difference between the α and β signals.

[1] B. Longfellow et al., Phys. Rev. C 107, L032801 (2023).
[2] B. Longfellow et al., Phys. Rev. Lett. 132, 142502 (2024).

Project 8

1.8 Project 8: overview

E. Novitski and R. G. H. Robertson

In the CRES technique[1] pioneered by the Project 8 collaboration[2,3,4,5], radioactive gas is confined within a uniform magnetic field. When a charged particle is emitted in decay, it is trapped axially in a weak magnetic bottle trap, undergoes cyclotron motion, and emits electromagnetic radiation with a frequency f_{cyc}, given by

$$f_{\mathrm{cyc}} = \frac{1}{2\pi}\frac{|e|B}{m + E_{\mathrm{kin}}/c^2}, \tag{1}$$

where B is the magnetic field, m is the mass of the particle, c is the speed of light, and E_{kin} is the kinetic energy of the particle. With the charged particle in a magnetic bottle to increase the observation time, the ∼aW to ∼fW of cyclotron radiation (depending on the magnitude of B) can be directly detected with an RF receiver, amplified, and digitized, generating data as shown in Fig. 1.8-1.

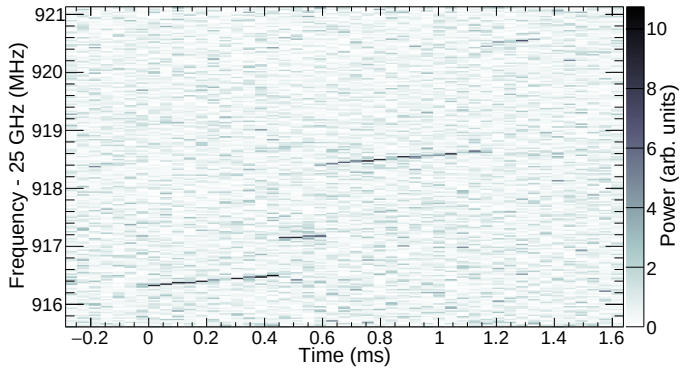

Figure 1.8-1. Spectrogram of the first CRES event detected from a tritium beta decay electron.

The energy of the charged particle at the time of its creation can be determined from f_{cyc} at the beginning of the signal. CRES has several advantages for tritium β^- spectroscopy over previous methods. Electron energies are determined via frequency, which can be measured with extremely high precision. As a differential spectroscopy technique, it continuously builds the entire endpoint spectrum, which increases statistical efficiency and protects against time-dependent systematic effects. The inability to extract electrons from the source makes the CRES technique scalable by volume and compatible with the use of an atomic tritium source,

[1] Monreal, B. & Formaggio, J. A. Phys. Rev. D 80, 051301 (2009).
[2] Asner, D. M. et al. Phys. Rev. Lett. 114, 162501 (2015).
[3] Esfahani, A. A. et al. Phys. Rev. C 99, 055501 (2019).
[4] Ashtari Esfahani, A. et al. Phys. Rev. Lett. 131, 102502 (2023).
[5] Ashtari Esfahani, A. et al. Phys. Rev. C 109, 035503 (2024).

which must be magnetically isolated from the walls to prevent recombination. Finally, CRES is an extremely low-background technique. For example, electrons from radioactive decay on the walls collide again with the wall after a single cyclotron period and do not produce a detectable signal. Electrons that are outside the energy range of interest or that are not trapped within the magnetic bottle also do not contribute to CRES spectrum. The dominant background, thermal RF noise, can be precisely characterized and excluded given sufficient SNR.

With these advantages, an experiment using CRES is potentially sensitive to neutrino masses significantly smaller than KATRIN's anticipated 0.3 eV/c^2 limit. The neutrino mass sensitivity for Project 8 has been estimated both analytically [1] and in a Bayesian framework [2], with agreement in their conclusions (Fig. 1.13-2). The statistical sensitivity for an observation interval ϵ below the Q-value is: $\sigma^{\rm stat}_{m^2_\nu} = \frac{2}{3rt}\sqrt{rt\epsilon + \frac{bt}{\epsilon}}$, where r is the rate into the last 1 eV of the $m_\nu = 0$ spectrum, t the observation time, and b the background rate per eV.[3] Fig. 1.8-2 shows the dependence of neutrino mass sensitivity on energy resolution, and on the precision to which the width of the energy resolution (detector response function) is known, for the planned cavity-based CRES experiments using an atomic tritium source. For a molecular tritium source the final state spectrum of the daughter He^3T^+ ion (Fig. 1.8-2) would set the ultimate limit at around 100 meV. For an atomic source at 1 mK the sensitivity can be further improved, approaching 40 meV in a very large instrument.

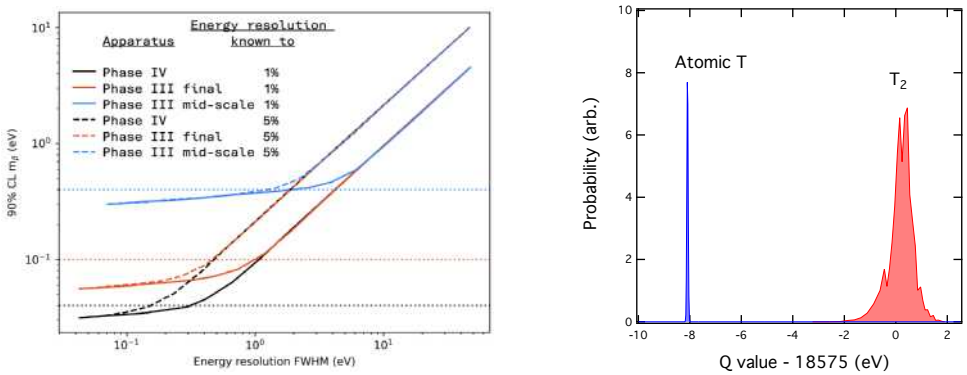

Figure 1.8-2. Left: Predicted neutrino mass sensitivity vs. FWHM energy resolution for the LFA (here listed as "mid-scale Phase III") and Pilot-scale (here listed as "final Phase III") experiments and the Phase IV experiment. The solid lines represent the energy resolution needed if the uncertainty on the resolution width is characterized to 1% and the dashed lines if it is characterized to 5%. The dotted lines represent the target neutrino mass sensitivities for each of these experiments. Right: Line widths for T and T_2 decay to electronic ground states.

[1] Doe, P. J. et al. arXiv:1309.7093 (2013).

[2] Ashtari Esfahani, A. et al., Phys. Rev. C 103, 065501 (2021).

[3] Contributions from molecular daughter ion final states, magnetic field non-uniformity, and thermal Doppler and collisional broadening (*i.e.*, finite mean free lifetime) are also considered (not shown). For concreteness, an assumption is made that the systematic contributions are each known to 1% unless otherwise stated.

Phases of Project 8

A neutrino mass measurement sensitive to m_β of 40 meV/c^2 would either detect neutrino mass or disfavor the entire parameter space of the inverted ordering. Project 8 is proceeding toward this full sensitivity in four phases (Fig. 1.8-3) by systematically addressing each of the factors that contribute to improved sensitivity.

Phase I was the first demonstration of CRES. Phase II recently set the first CRES-based neutrino mass limit. Phase III is a multi-pronged program that will demonstrate the technologies needed to reach full scale, combine them to do a mid-scale experiment with m_β sensitivity comparable to KATRIN, and culminate in a "Pilot-scale" experiment with world-leading 0.1 eV/c^2 sensitivity. With the CRES-enabled ultra-low background, it will set limits on sterile neutrino mass without assumptions about active neutrino masses. Phase IV will be the full-scale experiment that reaches 40 meV/c^2 sensitivity.

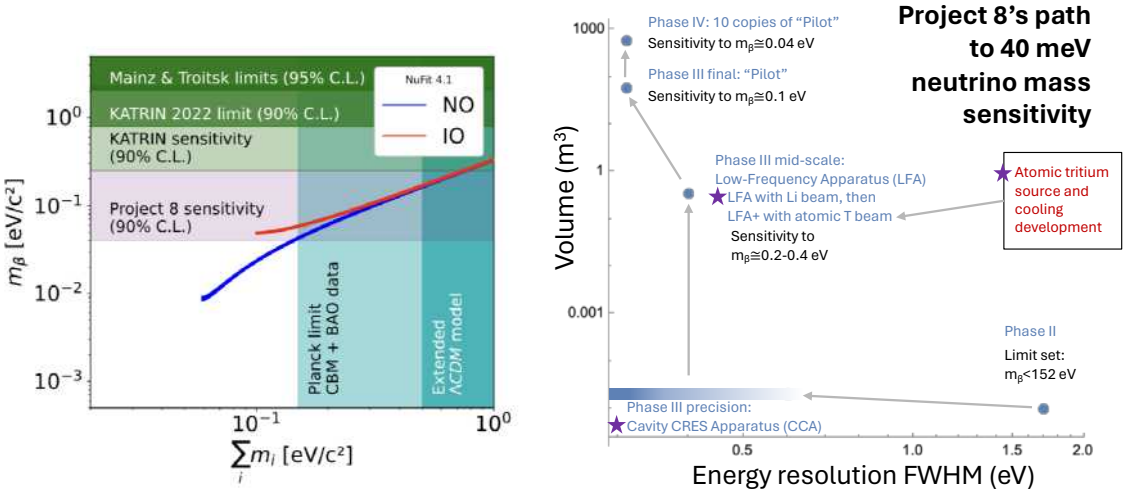

Figure 1.8-3. Left: Neutrino mass parameter space excluded by or accessible to direct kinematic measurements, and excluded by cosmological observations under two sets of model assumptions. Right: Volumes and resolutions of Project 8's major CRES apparatuses. Purple stars mark the topics of the three hardware-focused work packages of this proposal.

1.9 Project 8: plasma source of atomic hydrogen

R. G. H. Robertson

We are starting to design a microwave plasma source of atomic H/D/T. Our experience so far with thermal crackers has been that they do produce a dissociated beam, but have some drawbacks:

- At higher flow rates the dissociation efficiency is low,

- Tungsten absorbs some hydrogen, which represents an inventory sink when running tritium,
- At operating temperatures, tungsten evaporates and forms a film on nearby surfaces such as an accommodator,
- The beam is very hot,
- Coupling to the accommodator is not without loss because a gap is needed to avoid melting the accommodator.
- The lifetime of a thermal cracker in continuous use is not known, but is inevitably shortened by tungsten evaporation. Frequent replacement is undesirable in a tritium system as well as being a source of livetime inefficiency.
- The deposition of tungsten on the accommodator changes its surface from aluminum (with low recombination rates) to tungsten (presumably with higher recombination rates).

Plasma sources also have drawbacks, and those were initially considered serious enough to deflect our attention to thermal crackers. DC and RF plasma sources were used in the original 3 experiments that produced beams of atomic tritium to determine its hyperfine structure[1,2,3]. All 3 experiments reported terminal inventory loss after only a few hours. This is now understood (at least partially) to be a result of the attack of the plasma discharge on the walls of the dissociator, which was made of glass or silica. The discharges are chemically aggressive, with UV light, radicals, and fast electrons. The tritium evidently combines with the oxygen to make water, which is then lost to cold traps, or the tritium is implanted into the walls of the discharge tube. Experiments we carried out at Los Alamos in the 1980s with a 50-MHz RF dissociator for H_2 and D_2 showed significant damage to the Pyrex discharge tube after some time (a day) and significant water loads on vacuum system cold traps at the end of a run, loads much higher than when the discharge was not running.

We therefore revisit the plasma source with plans to choose a resonant cavity with a well-defined mode structure (TE011) that accelerates electrons and ions only in the central region. This mode structure also means that a layer of unexcited gas separates the discharge region from the wall. These measures are expected to better protect the wall from damage. The wall itself is not a dielectric but aluminum. The cavity and the accommodator are an integrated object, without a gap for coupling. A temperature gradient can, moreover, be established from the discharge region to the exit to reduce the beam temperature further, down to about 40 K or possibly below, with a thin-wall accommodator section. The good performance of aluminum is generally attributed to a native oxide layer that forms on the surface, and the survival of this layer is important. It can be regenerated by oxygen exposure, but that step would involve downtime and complexity, and one goal of the R&D is to measure and maximize the uptime between regenerations.

[1] B. S. Mathur, S. B. Crampton, D. Kleppner, and N. F. Ramsey. Phys. Rev., 158:14–17 (1967).
[2] A. G. Prodell and P. Kusch. Phys. Rev., 106:87–89 (1957).
[3] E. B. Nelson and J. E. Nafe. Phys. Rev., 75:1194–1198, (1949).

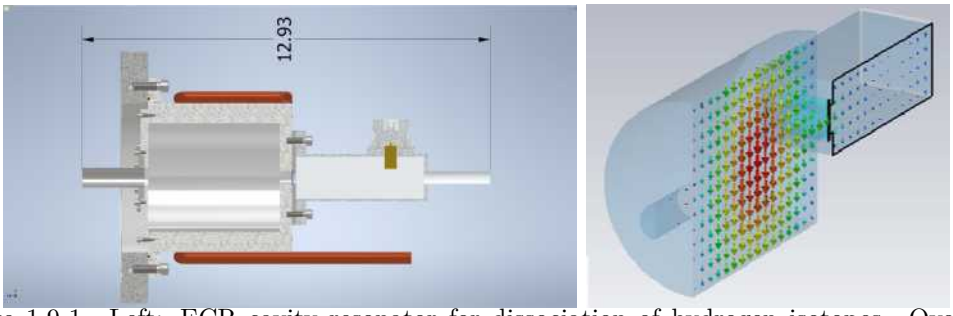

Figure 1.9-1. Left: ECR cavity resonator for dissociation of hydrogen isotopes. Overall length shown is in inches. Right: Electric field in TE111 mode.

The design is shown in Fig. 1.9-1. The cavity resonates at 2.45 GHz in the TE111 mode. Power is supplied from a 1-kW solid-state microwave generator via a cable to a WR-284 transition stub coupled to the cavity through a sapphire window. The cavity is water-cooled and inside a coil (not shown) that provides a magnetic field of 0.0875 T, the condition for cyclotron resonance.

The RF modeling in CST was carried out by Tianhuan Luo at LBNL. The design and modeling of dissociation have advanced to the point that construction can begin at Indiana University in the Project 8 collaborative environment.

1.10 Project 8: the Cavity CRES Apparatus (CCA)

M. Huehn, M. Kallander, E. Novitski, R. G. H. Robertson, M. Wynne, and P. Kolbeck

The Cavity CRES Apparatus (CCA), currently under construction at UW and pictured in Fig. 1.10-1, is being built as a platform for developing sub-eV-precision CRES techniques. It will be the first demonstration of CRES in a cavity, a detector geometry that scales to the larger volumes and lower frequencies that will eventually be necessary for improved neutrino mass sensitivity. It will also enable key improvements over Phase II in energy resolution (expected $\sim$ 0.3 eV FWHM) and effective volume. It will also be a testbed for calibration tools, including an electron gun.

The CCA cavity design has now been completed. UW has led the design and fabrication of the CCA, with Novitski and Huehn leading the cryogenic apparatus and Robertson and Kallander the electron gun. There have also been significant collaborative contributions from MIT, JGU Mainz, and Yale. Fabrication has begun; assembly and commissioning are expected to finish in 2024 and scientific operations to begin in early 2025. By the end of the current grant period, we expect to achieve the goal of the previous proposal: using the CCA with an electron gun source to demonstrate first sub-eV precision with CRES.

The CRES frequency in the CCA is the same as in Phase II, allowing for reuse of the receiver and digital DAQ from Phase II. Software interfacing with the DAQ has been updated to recent versions and moved to python3 to be compatible with the Project 8 Dripline framework (more details on Dripline in (Sec. 1.12)). Improved signal/noise simulations were run on

the Yale high-performance computing cluster using the Phase III cavity and trap properties, and are used to optimize event triggering parameters. A repurposed medical MRI magnet provides a 0.04 m^3 volume with 1-ppm magnetic field homogeneity. A new gas-handling system is capable of controlling and analyzing conditions more precisely than in Phase II. The cavity design was led by MIT in close collaboration with UW. The electron trap coils were also carefully designed to maximize desirable signal properties in a collaboration between JGU Mainz in Germany, Yale, and UW.

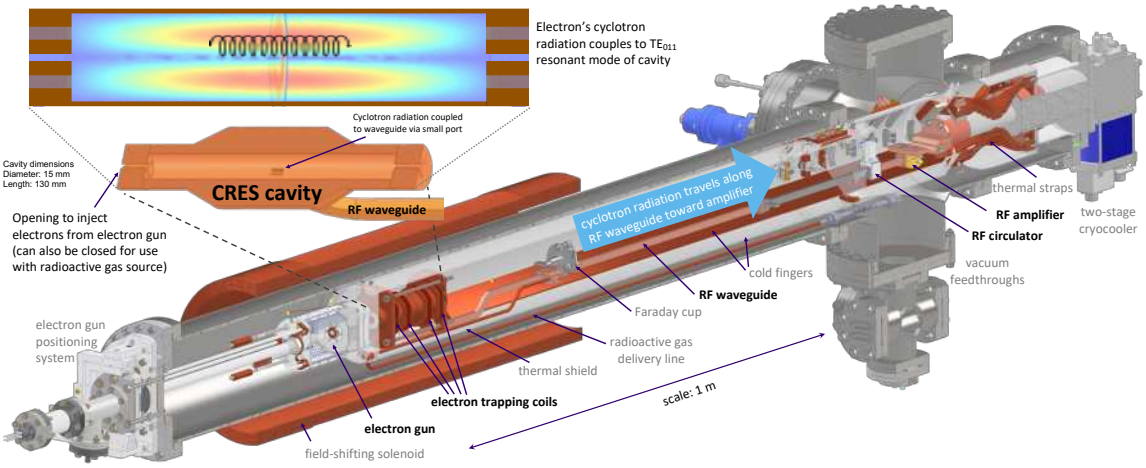

Figure 1.10-1. A schematic view of the Cavity CRES Apparatus (CCA). The TE_{011} cavity is maintained at 85 K to keep ^{83m}Kr in the gas phase; in an alternative running mode, removable endcaps allow the electron beam a path into the cavity. Electron trap coils around the cavity create small distortions in the magnetic field to confine electrons axially. Cyclotron radiation travels to the right in the RF waveguide toward the amplifier, held near 4 K. Not pictured is the medical MRI magnet in which this sits, which provides the high-homogeneity 1-T background field.

We have designed the CCA with improvements to make sub-eV resolution with CRES possible for the first time. A repurposed medical MRI magnet provides a 0.04 m^3 volume with 1-ppm magnetic field homogeneity. A new UW-made gas-handling system is capable of controlling and analyzing conditions more precisely than in Phase II. The baseline design includes a cavity with one readout channel corresponding to the TE_{011} resonant mode, a design conceived at UW. This detector architecture takes advantage of cyclotron radiation enhancement on resonance due to coupling with the cavity[1,2].

It is also far less susceptible to the Doppler effect than Phase II was, increasing useful signal power by preventing excessive shunting of the RF main-carrier power into RF sidebands[3]. Sideband data, which was not available in Phase II, will be present in the CCA and will permit axial-amplitude-dependent field-shift corrections to improve resolution. The electron trap coils were carefully designed to provide a magnetic trap shape where magnetic field

[1]Purcell, E. M. Phys. Rev. 69, 681. (11-12 1946).
[2]Brown, L. S., Gabrielse, G., Helmerson, K. and Tan, J. Phys. Rev. A 32, 3204–3218 (1985).
[3]Ashtari Esfahani, A. et al. Phys. Rev. C 109, 035503 (2024).

information is optimally imprinted in these sidebands. While the physical detector volume is not much larger than in Phase II, the better use of the volume by a cavity as compared to a waveguide yields a hundred-fold larger effective volume than in Phase II. The cavity has removable vacuum endcaps, allowing for operation either with an ^{83m}Kr source or with an electron gun. UW has built an electron gun that will inject known-energy electrons via Mott scattering with helium gas. With its expected 0.3-eV linewidth, it will allow for a precise characterization of detector response. Data-taking with both types of electron source, and a detailed response characterization, is planned with the baseline CCA hardware.

Figure 1.10-2. CCA electronics, thermal shield, and cryogenic feedthoughs, under construction.

1.11 Project 8: electron gun for CRES calibration

M. Kallander and R. G. H. Robertson

A calibration and diagnostic technique for use in Project 8 is based on an electron gun (egun). A beam of electrons injected along a magnetic field line passing through the CRES

cell creates some trapped electrons via Mott scattering from an added gas, such as He, in the cell. With a gas pressure around 10^{-6} mbar and a beam of 1 μA, a trapped electron rate of order 1 per second can be obtained. The scattering process is basically elastic with only recoil energy being lost, and the energy resolution is dominated by the energy spread in the incident beam. The cathode of Y_2O_3 yields a spread of about 0.25 eV FWHM, with additional small contributions from thermal Doppler broadening of gas atoms and recoil energy variation with scattering angle.

The egun uses a Pierce gun design, which can produce a tightly collimated beam with a single supply voltage. The cathode is heated by direct current drawn from a solar panel array illuminated by high-intensity red LEDs at ground potential. Voltages up to 30 kV are provided by a Spellman TOF-3000 mass-spectrometry power supply with total noise and ripple less than 70 mV p-p. Some images of the system are shown in Fig. 1.11-1.

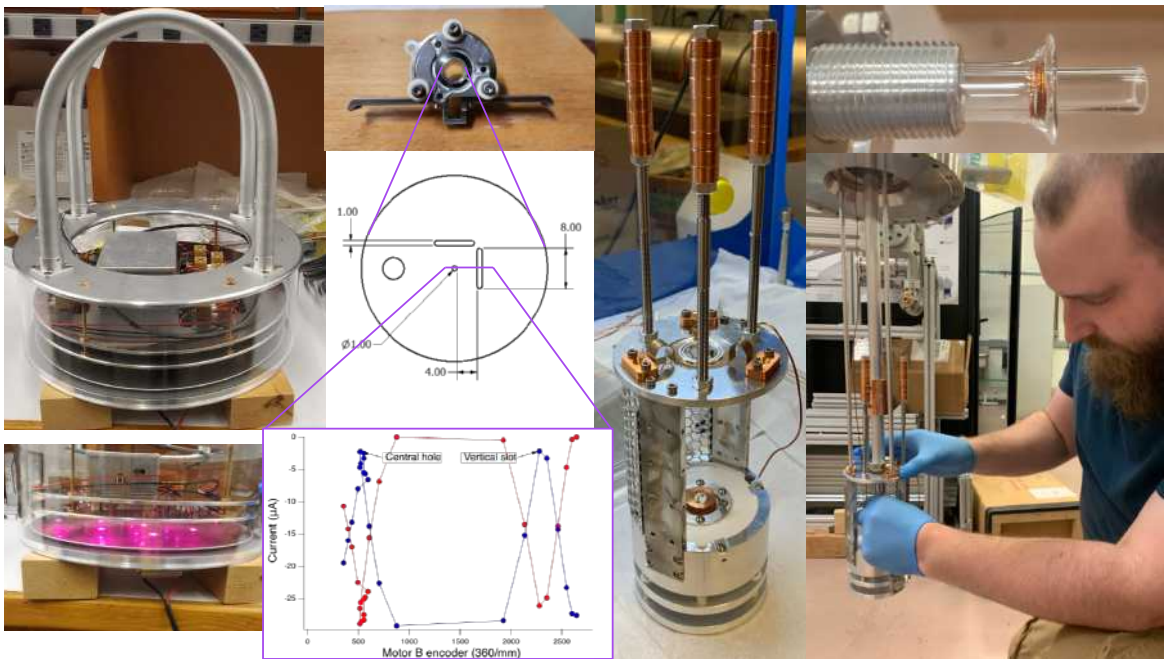

Figure 1.11-1. (Clockwise from top left.) High voltage stack with hoops to reduce field strength around egun vacuum feedthrough (not present); Faraday cup with test plate and slots for measuring beam positioning and spot width; egun with counterweights; Fused silica insulator tubes carrying filament power and egun bias through the grounded positioning 'joystick' to the egun; M. Kallander assembling egun; HV stack with LED array on.

The egun is positioned with two piezoelectric motors driving a gimbal mechanism with a balanced vacuum bellows linkage. The egun itself is kept parallel to the magnetic field via a pantagraph mechanism. The egun is mounted in the 1-T MRI magnet shown in Fig. 1.11-2.

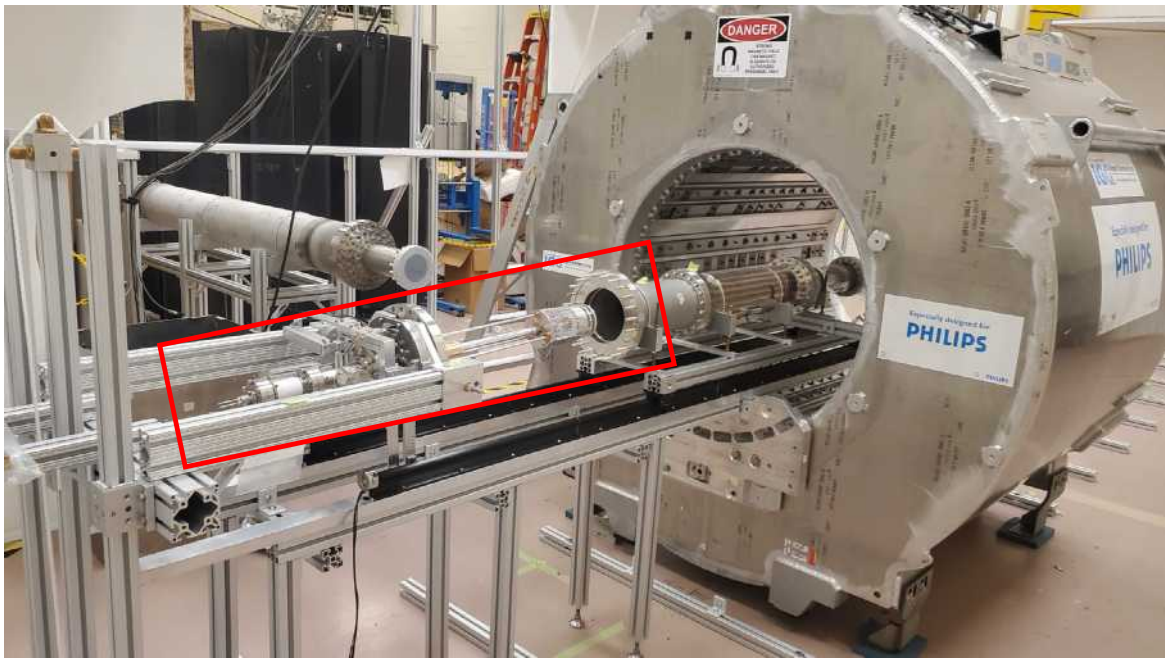

Figure 1.11-2. MRI magnet with egun mount and vacuum system. The egun is supported here by its transporter, which is subsequently removed and replaced by the HV stack with the hoops surrounding the ceramic feedthrough visible at the near end.

Development and testing are nearing completion. Satisfactory beam currents of tens of microamperes have been obtained with beam spot sizes consistent with the 0.85-mm diameter cathode. The main challenge has been voltage-holding capability, but steady progress and improvements have extended the range to 21 kV, with further improvements under way.

1.12 Slow-Controls

S. Enomoto

The slow-control system for Project-8 Phase-III consists of two layers. The first layer is Dripline, which was developed by the collaboration for Phase-II and provides readout from simple Ethernet devices, data and message exchange between multiple processes using RabbitMQ, and data storage to PostgreSQL. This was successfully used for Phase II, and improvements are being made for Phase-III. The second layer, SlowDash, is being developed at CENPA to provide an interactive data browser and graphical control of the instrument.

The goal of SlowDash is:

- Grafana-like data browser, for time-series data and ROOT-like data objects (histograms, graphs with error bars, etc.)
- LabVIEW-like visual control (graphical control panel and control logic attached behind the panel)

- Jupyter-like Python scripting for control and analysis

As of August 2024, the visualization part is mostly completed (Fig. 1.12-1), the basic parts of controls are working, and some experimental implementations of analysis scripting have been made.

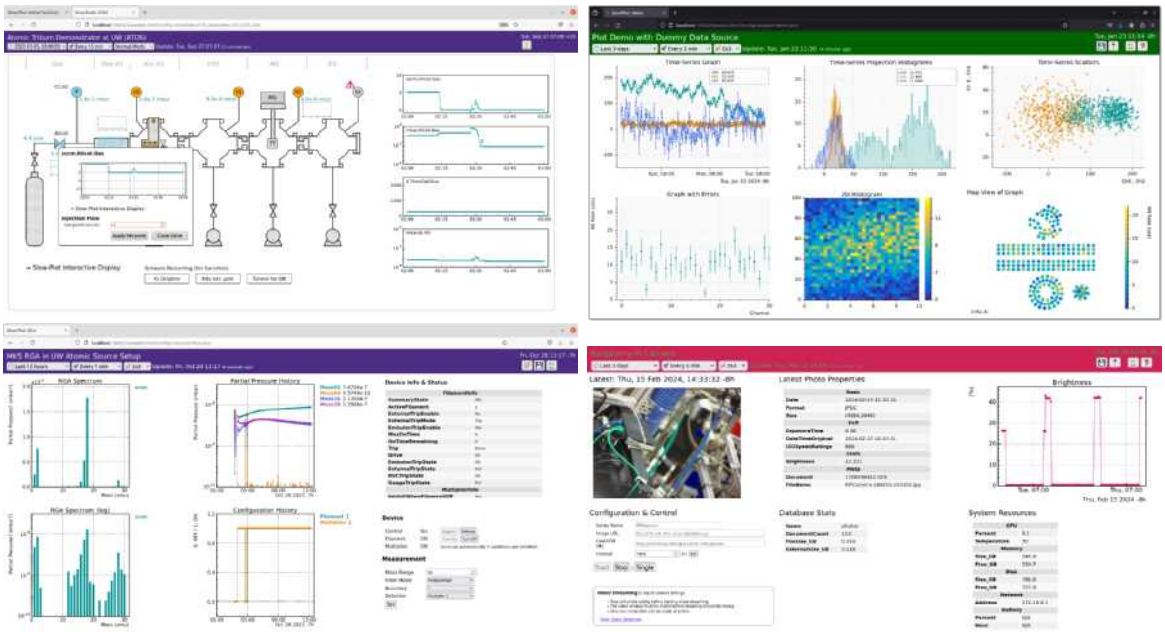

Figure 1.12-1. Screenshots of SlowDash. From top left: graphical control panel, data browser demonstrating various plot types, RGA application including controls, and Raspberry-Pi camera application including image handling.

SlowDash integrates GUI panels on Web browsers and user Python scripts on the control system. User Python functions can be attached to buttons on the GUI, with function arguments bound to GUI input elements. Variables in user Python scripts can be mapped to GUI display elements for real-time updating. Scripts can be edited on a Web browser and dynamically loaded and started. There are no specific requirements for user Python scripts (other than being Python 3), and users do not have to write any JavaScript.

SlowDash includes a Python library, SlowPy, for use in user Python scripts. With the library, readout from a simple Ethernet device can be written in a few lines, and storing the data in a database is another few lines (Fig. 1.12-2). The library has a plug-in structure, enabling users to add devices and use any external libraries. Dripline is connected through this plugin mechanism and accessed just like the examples above.

Example to read data from a Ethernet voltmeter

```
from slowpy.control import ControlSystem
voltmeter = ControlSystem.ethernet("10.0.0.43",17674).scpi()
ch0 = voltmeter.command("MEASURE:V0")      # binding to a device command

while True:                    # readout loop
    ch0_value = ch0.get()      # issue the command and receive a reply
    ...
```

Example to write data to PostgreSQL database

```
from slowpy.store import DataStore_PostgreSQL
datastore = DataStore_PostgreSQL("localhost:5432/SlowData", "DataTable")

while True:                    # readout loop
    ch0_value = ...
    datastore.append(ch0_value, tag="ch0")
```

Figure 1.12-2. Examples of SlowPy user scripts

Making use of the flexible scripting feature, SlowDash is used for Phase-III to handle non-simple devices that would have been very difficult to integrate otherwise. Examples include the chopper motor control, which requires a vendor-provided USB library, an RGA device that streams spectrum data in a way Dripline cannot handle, and a Raspberry-Pi camera with image data analysis using popular Python libraries. By combining Dripline and SlowDash, the slow-control system covers all the devices currently used in Project-8 at the UW lab.

Although SlowDash was initially developed for Project-8, it does not have anything specific to Project-8, and its plug-in architecture allows it to integrate with any devices, database systems, messaging systems, and data analysis libraries. SlowDash will be used for the slow-control systems of the LEGEND 1000 and KamLAND2 experiments and is under consideration for the upgraded CENPA Van de Graaff control system. SlowDash is publicly available on GitHub at `https://github.com/slowproj/slowdash`.

1.13 Project 8: sensitivity studies for future experiments

C. Claessens

In 2023 and 2024, we have performed detailed analyses of sensitivity for the future Project 8 demonstrators and Phase IV. For these analyses we use an analytical model of sensitivity[1]

[1]Formaggio, J. A., de Gouvêa, A. L. C., Robertson, R. G. H. Phys. Rept. 914 (2021).

$$\sigma_{m_\beta^2} = 4\sqrt{\frac{1}{\left(6\,C_{\mathrm{T}}\,V_{\mathrm{eff}}\,n\,t\right)^2}\left[C_{\mathrm{T}}\,V_{\mathrm{eff}}\,n\,t\,\Delta E + \frac{bt}{\Delta E}\right] + \sum_i \sigma^2_{\mathrm{syst},i}(n)\cdot\delta\sigma^2_{\mathrm{syst},i}}, \tag{1}$$

$$\text{Upper limit}(m_\beta)\ [90\%\ \text{C.L.}]\ = \sqrt{1.28\sigma_{m_\beta^2}}. \tag{2}$$

Here, V_{eff} is the effective volume (source volume $\times$ total efficiency), n is the source gas density, t is the livetime, b is the background rate, and C_T is a constant given by the fraction of events in the last electronvolt of the spectrum divided by the tritium lifetime. Some contributions to energy broadening depend on the density n. The conversion from $\sigma_{m_\beta^2}$ to an upper limit on m_β assumes that the neutrino mass is close to zero.

The first term in the square root of Equation 2 yields the statistical uncertainty for an experimental effective volume V_{eff} and a run time t. It follows from the number of events observed in the window $0 < \epsilon < \Delta E$, where $\epsilon \equiv E_0 - E$. The optimum energy interval is

$$\Delta E = \sqrt{\frac{b}{r_0} + 2.35^2\ \Sigma_i \sigma^2_{\mathrm{syst},i}}, \tag{3}$$

where r_0 is the rate into the last 1 eV of the spectrum with $m_\beta = 0$, $\sigma_{\mathrm{syst},i}$ is the contribution of the ith systematic, and the factor 2.35 converts standard deviations to full-widths-at-half-maximum.

The second term in the square root of Equation 2 adds the systematic uncertainty, which depends on the products of two variables: the standard deviations $\sigma_{\mathrm{syst},i}$ of contributions to energy broadening of the beta spectrum (i.e., to the detector response function), and the uncertainties $\delta\sigma_{\mathrm{syst},i}$ on estimates of these broadening contributions, during analysis.

Equation (2) has been validated with a Bayesian analysis of Monte Carlo data, accounting for instrumental broadening of the beta-decay spectrum[1]. In addition, as displayed in Fig. 1.13-1 (top), the neutrino mass result measured in Phase II aligns with the analytic sensitivity model.

[1] Ashtari Esfahani, A. et al., Phys. Rev. C 103, 065501 (2021).

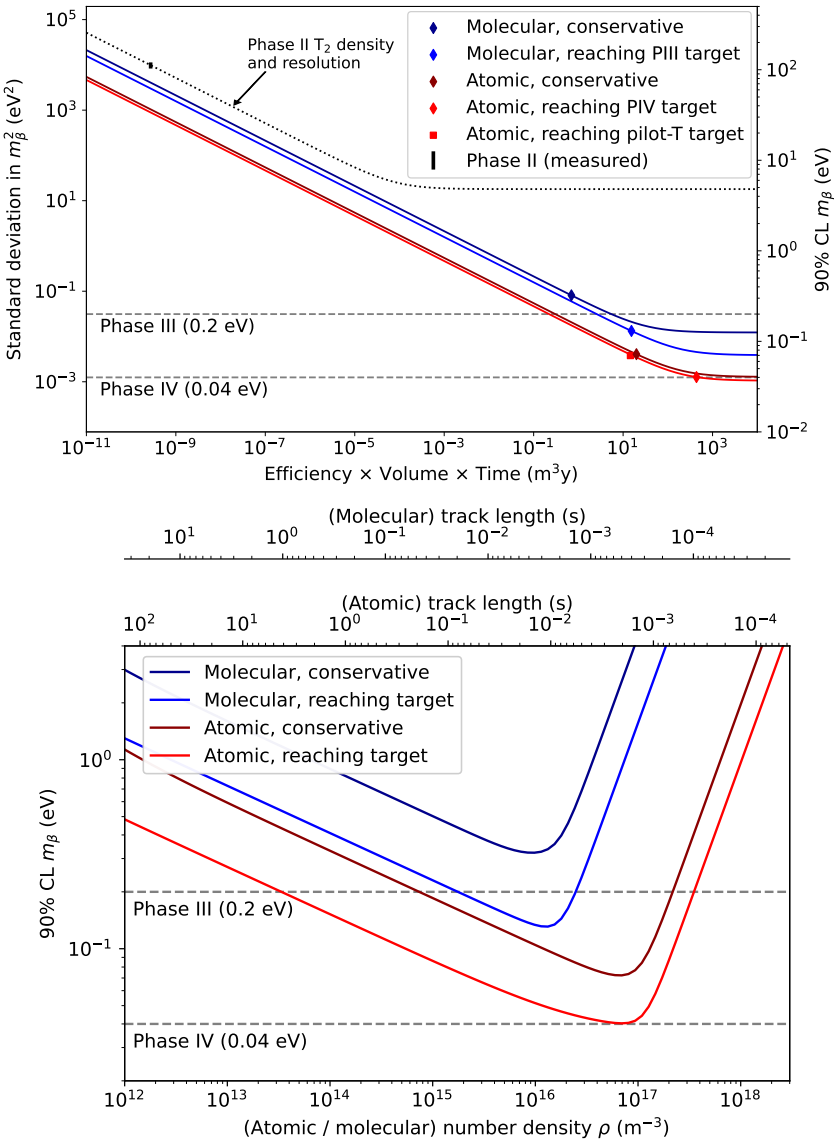

Figure 1.13-1. Top: Dependence of mass sensitivity (90% C.L. upper limits) on efficiency × volume × livetime. Markers denote sensitivity measured in Phase II and targeted for future experiments. The height of the Phase II marker represents the uncertainty in $\sigma_{m_\beta^2}$. Each solid curve corresponds to a gas density, optimized for the design parameters at the marker. Bottom: Optimization of sensitivity over tritium density, for each scenario in the top plot. For markers in the top plot, and curves in the bottom plot, molecular-tritium experiments run for one year with one cavity, while full-scale atomic experiments run for three years with ten cavities. The pilot-T marker on the top plot assumes one year of runtime with one cavity. "Conservative" curves reflect current knowledge of experimental design and event reconstruction capabilities. "Reaching target" curves assume state-of-the-art noise figures and a factor of 22 increase in efficiency × volume × time, relative to presently-conceived designs. If systematics are improved and contribute sub-dominantly, a factor of 2-7 increase would instead be needed to reach targets.

Sensitivity Dependencies in Cavity CRES experiments

The top panel in Fig. 1.13-1 shows how neutrino mass sensitivity varies with total efficiency to trap and detect electrons, volume, and observation time. Each curve corresponds to a gas density of molecular or atomic tritium. Solid curves are generated for 325 MHz cavities, which each have a volume of $11\,\mathrm{m}^3$. Thus, the volume in Fig. 1.13-1 (top) is altered only by changing the number of cavities. The total efficiency is the product of the electron trapping efficiency, event detection efficiency, and a factor accounting for the range of usable radii. Large radii are not useful because electrons hit the wall during their cyclotron motion. In an atomic experiment, the Halbach magnet also limits usable radii by producing field non-uniformity near the walls, making electron energies difficult to reconstruct in this region. The effective volume V_{eff} is calculated by multiplying these three efficiency factors by the total volume.

At high exposures, the curves in Fig. 1.13-1 (top) converge to the systematic sensitivity limitation, corresponding to the second term in Equation (2). This total systematic uncertainty is specific to the experimental design parameters and the chosen source gas density. The following contributions to energy broadening are included: uncertainty on the initial cyclotron frequency, broadening from the axial trap after correcting for electron pitch angles, radial and azimuthal field non-uniformity, thermal Doppler broadening, and (for T_2) the molecular final state distribution.

The bottom panel in Fig. 1.13-1 displays how, for a given experimental design, there exists an optimum gas density that minimizes the neutrino mass uncertainty. Phase III curves have one-year runtimes with one cavity, while Phase IV curves have three-year runtimes with ten cavities. At lower densities, the sensitivity is limited by the reduced event rate. At higher densities, by contrast, the sensitivity is dominated by systematic uncertainty in the reconstruction of the decay energy, since high densities produce short CRES tracks, increasing uncertainty on the cyclotron frequency. We calculate the achievable cyclotron and sideband frequency precision using the Cramér-Rao Lower Bound (CRLB), which is a function of the SNR, the relative power content in each band, and the track duration. SNR is determined using the radiated cyclotron power coupled to the TE_{011} mode and the noise power within the mode width. Both noise and signal power are therefore functions of the mode's quality factor Q. We require that the mode width contains the main carrier and one sideband, which is crucial for determining the pitch angle to correct the electron energy for the trapping field that it experiences. We also require that the mode width contain the range of carrier frequencies among all trapped electrons. The uncertainties on the main carrier and sideband frequencies obtained with the CRLB propagate to an uncertainty on the correction of the reconstructed electron energy. All uncertainties are added in quadrature to compute the total systematic energy broadening. The minimum of a curve in the bottom plot sets the density of the corresponding curve in the top plot, as well as the sensitivity at the marker.

1.14 Project 8: magnetic field design for the Low Frequency Apparatus

R. G. H. Robertson

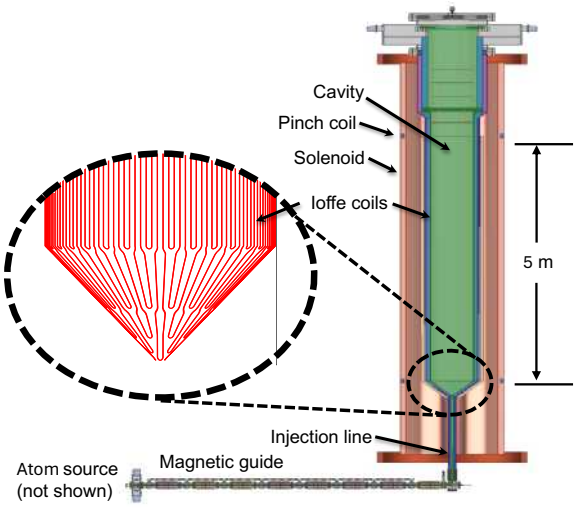

Figure 1.14-1. The Low-Frequency Apparatus (LFA) concept.

The goal of the Low-Frequency Apparatus (LFA) Fig. 1.14-1 is to demonstrate the feasibility of CRES in a large-volume resonant cavity and the compatibility of CRES with atom trapping. By lowering the CRES frequency while increasing the volume, we continue to couple to the TE_{011} readout mode while increasing the volume and therefore the event rate, improving neutrino mass sensitivity. The LFA will have a 1.5-m^3, 560-MHz cavity, a 20-mT magnetic field, and an integrated Ioffe trap for confining atomic lithium and (ultimately) tritium. The magnetic design consists of 4 interlocking magnetic elements, a superconducting Ioffe coil to trap atomic tritium, a large room-temperature uniform-field solenoid, trap coils for trapping electrons, and a magnetic compensation system for the earth's field and other environmental fields. This integrated system must meet the specifications necessary for a high-resolution experiment in a large volume. The research program toward the LFA consists of two stages:

- LFA stage 1: The cavity, magnetic elements, cryogenic system, and detection system will be constructed. CRES will be performed using electron-gun and ^{83m}Kr electron sources, testing its efficiency and energy resolution. The atom-trapping capability will be tested with lithium. Project 8 is currently writing a pre-CDR for this, which will be followed by the full CDR process to fund the construction and operation of this phase of the LFA.
- LFA stage 2: The LFA apparatus will be upgraded to accept a cold atomic tritium beamline, enabling a neutrino mass measurement with sensitivity comparable to KATRIN's ($m_\beta \approx$ 0.2-0.4 eV).

The main magnetic field in which CRES spectroscopy is performed is a vertical homogeneous background field of 20 mT, corresponding to the chosen frequency of 560 MHz.

Additional magnetic fields provide electron and atomic trapping. The resolution requirements dictate that the azimuthal uniformity is $< 10^{-7}$ because azimuth is not a derivable parameter in TE011 cavity readout. A field standard deviation of 10^{-7} corresponds to an energy standard deviation of 53 meV. Temporal stability at this level is also required. The radial location of an electron can be determined at the 10% level or better from the coupled power, and the radial uniformity specification is therefore $< 10^{-6}$. Axial uniformity is less stringent still since the CRES configuration is in any case an axially non-uniform trap for electrons. Notwithstanding that, the uniformity in the orthogonal components determines also the axial uniformity, from Maxwell's equations. The addition of the electron trap introduces an inherent radial non-uniformity. The mean CRES field for electrons undergoing axial oscillations in a trap can be precisely determined from the axial frequency as revealed in the sideband splitting. A prior calibration with the electron gun is required to relate the mean CRES field to the axial frequency. These specifications are demanding, well beyond what is readily achievable, but we have reached a design that we consider can meet them.

Operational Principles

A short solenoid is not uniform but can be made so if the current density is allowed to vary along its length. This can be achieved in several ways; we elect to divide the solenoid into a stack of equally-spaced identical coils each carrying an appropriate, slightly different current to achieve uniformity. This choice has practical advantages in both manufacture and versatility of use. If in a solenoid the magnetic field is perfectly uniform along the axis, then it is also perfectly uniform off the axis until one reaches current-carrying conductors. This follows from the divergenceless character of the magnetic field.

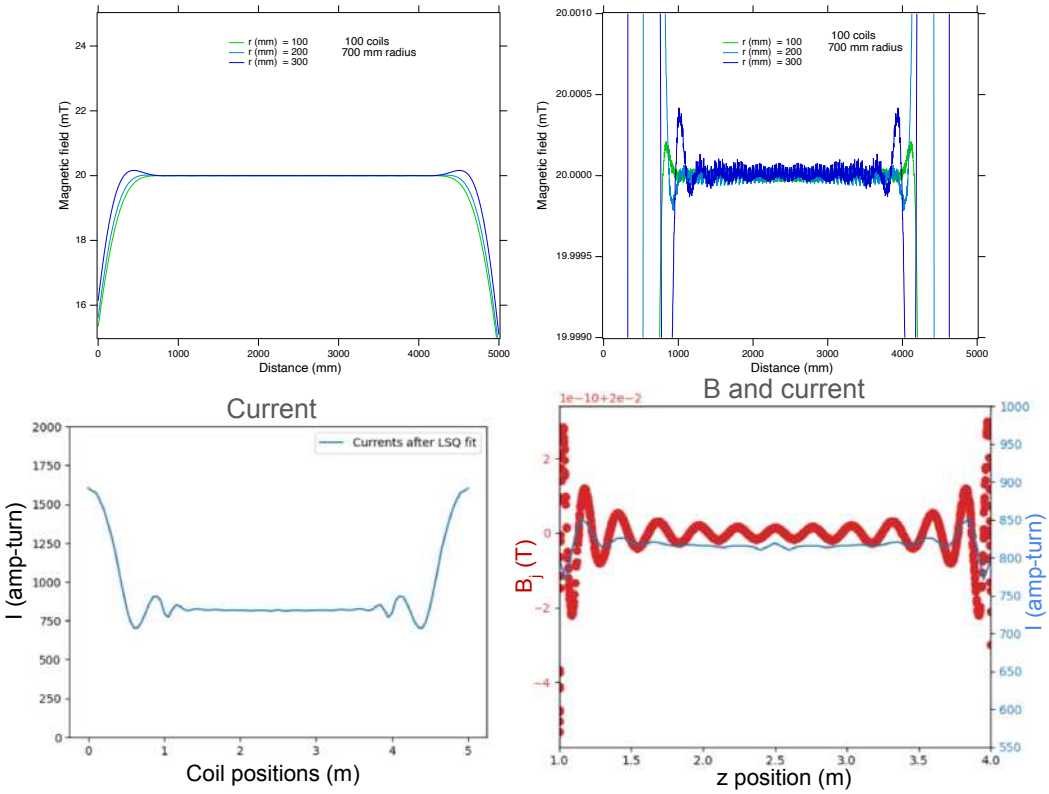

Figure 1.14-2. (Top left) Magnitude of the magnetic field for 3 radial displacements from the axis, 100, 200, and 300 mm. (Top right) Expanded view. (Bottom left) Coil ampere-turns. (Bottom right) Residuals from 20 mT on axis at 200 randomly distributed points, with the scale 2×10^{-10} T per division. The coil currents are superimposed (solid blue line), showing that the periodicities of the coil currents and residuals are not quite the same.

In Fig. 1.14-2 are shown the results from a fit for a magnet with 101 coils 1400 mm in diameter and equally spaced by 50 mm. Radial uniformity is confirmed at roughly the 1 ppm level, although the limits of numerical precision in this calculation are being approached. The structure of such a magnet is indicated in Fig. 1.14-3.

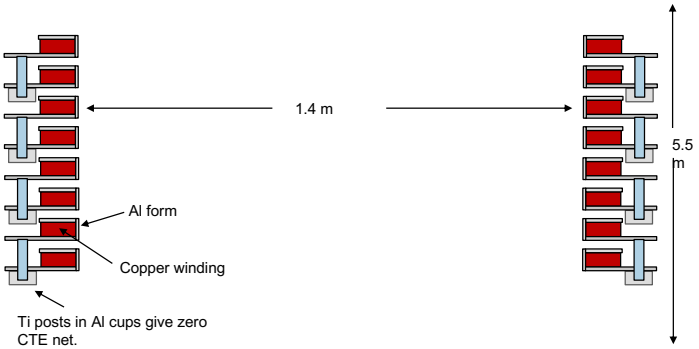

Figure 1.14-3. Part of a coil stack comprising the 20-mT background field solenoid (water cooling not shown).

The magnet coils are connected in series and energized by 102 independent power supplies. The primary current supply is to be stabilized by NMR or ESR free-induction decay probes positioned between the magnet and the cryostat to achieve the necessary 10^{-7} stability. Each individual coil is set to its exact current with a current-source supply. Powering the coils in this way is convenient and flexible, and leads to the simplest possible (and therefore lowest cost) coil. If the coils have a single winding, the number of turns determines the voltage for a specified number of ampere-turns, which cannot exceed the tolerance of the topmost supply for ground isolation. (An alternative is to include separate secondary windings on each coil to be powered close to ground potential.) The stability of the low-current trim supplies is less stringent, about the 10^{-5} level that is commercially available.

Atomic trap for the LFA

Free atomic tritium is the source that Project 8 plans to use for measuring neutrino mass because it has a simple structure that offers an intrinsically narrow instrumental line width and freedom from theoretical uncertainties. Another advantage is that the electron scattering cross section per atom is about one-half that for the molecule. An atomic source then has about twice the activity of a molecular one for the same track length. These advantages are summarized in Table 1.14-1. The zero-point energy of the vibrational states of the tritium

Parameter	T_2	T	Unit
FSD σ	433	0	meV
Doppler σ	162	1	meV
Cavity temperature	85	4	K
e^- cross section per atom	1.8	0.9	10^{-22} m^2

Table 1.14-1. Comparison of some key parameters for atomic and molecular tritium. FSD is the Final-State Distribution of the molecule.

molecule sets a practical limit to neutrino mass measurements with the molecule. The total broadening is about 436 meV rms[1]. If an atomic source can be made and operated at very low temperature, this spread can be essentially eliminated. The rms energy broadening is

$$\sigma(E)_{\mathrm{Doppler}} \quad = \quad 2E_0\sqrt{\frac{k_BT}{mc^2\beta^2}}. \tag{1}$$

Because atomic tritium (T) is reactive and tends to recombine with other tritium atoms, it must be magnetically confined and kept away from surfaces. Even superfluid He, which is usable as a container wall surface for atomic H, is not usable for T because the adsorption energy on He is too large[2]. In the gaseous state two-body recombination is not allowed and only three-body recombination can occur. Fortunately, this process is negligible at the densities of interest. The optimum density depends somewhat on experimental considerations, but is about 5×10^{16} m^{-3}. A continuous supply of atoms is necessary to replenish the source against other losses.

[1]L. I. Bodine, D. S. Parno, and R. G. H. Robertson. Phys. Rev. C 91, 035505 (2015).
[2]Silvera, I. F. and Walraven, J. T. M. Prog. Low Temp. Phys. X pp.139–370 (1986).

Electrons are also magnetically trapped in a CRES experiment, but quantitatively the magnetic trap depth suitable for electrons is much smaller than that for atoms, unless impractically low atomic temperatures are reached. The two constraints can be decoupled by using a magnetogravitational trap in which the magnetic boundary at the top is the right strength for electron trapping while the trap's height is sufficient to prevent atoms from escaping. Pioneering work on magnetogravitational traps has been carried out for measuring the lifetime of the neutron.[1] The temperature scales for gravitational and magnetic trapping are, respectively,

$$k_B T = mgh \quad (2)$$

$$k_B T = \mu \cdot \mathbf{B}. \quad (3)$$

Numerically (for T), these correspond to 3.54 mK/m and 671 mK/T. The magnetic field equivalent to 1 m height is 5.27 mT.

Two technologies are known for pure static magnetic trapping, the permanent-magnet Halbach array and the Ioffe-Pritchard trap, an array of conductors carrying currents in alternating directions so as to create a strong field near the array. Both can produce a field that falls off steeply toward the interior where the CRES spectroscopy takes place. Atoms are adiabatically reflected at the magnetic 'wall' while the uniform CRES field ideally remains undisturbed. The Ioffe method is selected for trapping T in the LFA for the most accurate control of the field configuration.

A low physical temperature of surfaces is required for other reasons. As may be seen in Fig. 1.14-2, the endpoint energy of the T spectrum is about 10 eV less than that of the T_2 spectrum[2]. Any molecules remaining in the trap represent a background at the T endpoint, and must be kept to less than $\sim 10^{-4}$ abundance. The saturated vapor pressure of T_2 and HT over the solid is given by Souers *et al.*[3] as an empirical equation,

$$\ln Q = A + \frac{B}{T} + B' \ln T. \quad (4)$$

This calls for a cavity with physical walls at a temperature $\sim 3.5 - 4.0$ K to assure negligible molecular contamination. The molecule, having no appreciable magnetic moment, is not trapped, strikes a wall, and is frozen out there with negligible vapor pressure. Desorption of tritium induced by beta decay in the deposited layer [4] is a separate source of contamination that limits the amount deposited on the wall before the wall must be warmed to pump away and recycle the tritium accumulated there. The low cavity temperature also is valuable in reducing noise and improving the SNR.

The LFA is the first large-scale tritium experiment to be usable with atomic tritium. It is large enough to test all the principles of the final Phase IV experiment and to be capable of delivering a measurement of neutrino mass at the frontier established by KATRIN.

[1] P. L. Walstrom, J. D. Bowman, S. I. Penttila, C. Morris, A. Saunders. Nucl. Instr. Meth. A 599, 1 (2009).

[2] L. I. Bodine, D. S. Parno, and R. G. H. Robertson. Phys. Rev. C 91, 035505 (2015).

[3] Souers, P. C., Briggs, C. K., Pyper, J. W. and Tsugawa, R. T., Report UCRL-52226, LLNL (1977).

[4] J. Vac. Sci. Technol. A 26, 68–77 (2008).

The magnetic design of the atomic trap must have a magnetic 'wall' height at the physical wall of the cavity that is large enough to reflect low-field-seeking atoms with high efficiency back into the central volume of the cavity without allowing them to reach the cavity wall. The magnetic wall must nevertheless have negligible effect on the uniform central field where CRES spectroscopy takes place. A steep spatial decline from the wall is therefore required. The magnetic wall must be free of low spots where atoms could escape and it must not create magnetic zeroes where Majorana spin-flips could occur, requirements that are similar but not the same. The height of the magnetic wall is tied to the overall physical height of the cavity – losses of hotter atoms at the top sets a temperature limit for the trapped atoms, and the magnetic wall should contain those same atoms without contributing significant additional losses. The design must meet external constraints including injection of the continuous supply of cold atoms, compatibility with operation below 4 K and the periodic recycling of cryosorbed T_2, and long-term stability and reproducibility.

A superconducting (SC) Ioffe trap has been designed in collaboration with Vikas Teotia of the Magnet Division of Brookhaven National Lab. The dimensions needed by Project 8 for the LFA are a match to a direct-winding machine, the largest in the world, built at BNL for EIC magnets. The Ioffe conductor locus calculated by us is shown in Fig. 1.14-4.

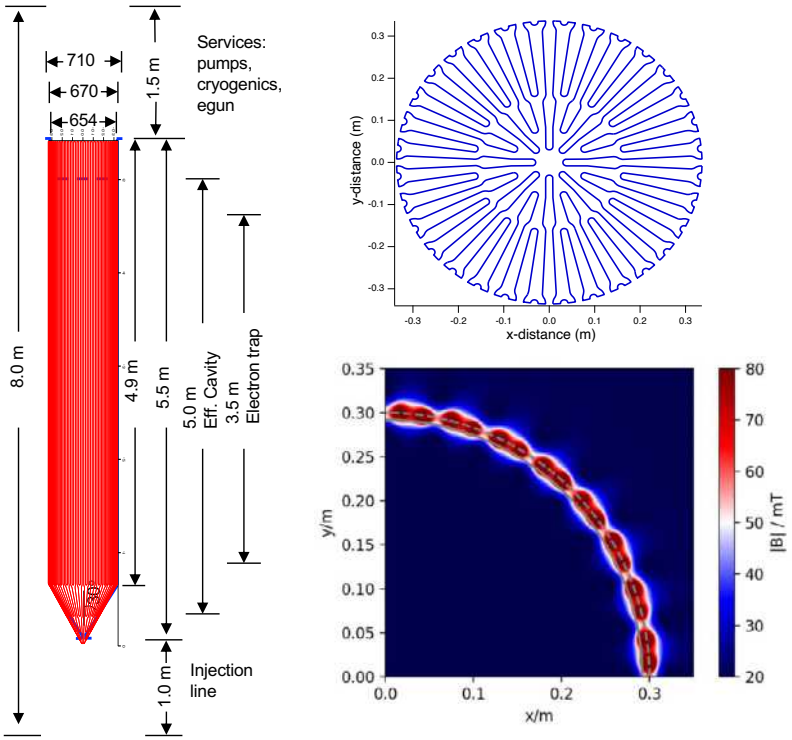

Figure 1.14-4. Design for superconducting Ioffe trap for the LFA. The left panel shows the 64-pole magnet wound on the exterior surface of the cavity. The magnetic closure at the bottom is conical to avoid field zeroes. Dimensions are only indicative. The top right panel is an end-on view of the locus on the cone. The lower right panel shows the calculated field magnitude part way down the cone. The dotted line is the Ioffe conductor position and the solid line is the cavity wall.

It is a 64-pole multipole (128 parallel conductors on the surface of the cylinder). Multipolarities m that are powers of 2 have no residual transverse field components. The field declines radially inward as $(r/r_{\text{cavity}})^{m/2-1}$. A 32-pole magnet produces a field that falls off too slowly, limiting the usable volume of the cavity. With a 128-pole magnet the turning radii at the ends of the loops on a 560-MHz cavity are too tight for standard SC cable and the field declines so quickly it becomes too small for practical cavity wall thicknesses. The cavity is aluminum. The default superconductor choice is NbTi strands 40% by volume in a 1.45-mm diameter copper matrix epoxied into precision-milled slots. The number of conductors required to reach the desired 50-mT field is not yet determined. To withstand collapse against atmospheric pressure (not a normal condition in operation) the wall thickness must be at least 6.24 mm from cavity wall to the slot nadir.

We conclude that we have identified a practical and cost-effective design for a large Ioffe trap, one that meets the needs of Project 8 in conducting a future atomic tritium experiment with the LFA. The trap in the LFA will first be used with Li atoms for diagnostic evaluation.

KATRIN

1.15 KATRIN Overview

P. Doe, R G H. Robertson, S. Enomoto, A. Marsteller*, and Q. Li

KATRIN motivation Contrary to the standard model of particle physics, we know from neutrino oscillation experiments that the neutrino has mass, although unexpectedly small. KATRIN is currently the most sensitive experiment making a direct, largely model independent probe of the mass of the neutrino, requiring only the kinematic parameters of the decay and the conservation of energy to extract a value or limit on the neutrino mass. The consequences of a massive neutrino, the second most prolific particle in the universe are profound, offering guidance into extensions of the standard models of particle physics and of cosmology. Some questions arising from neutrino mass are:

- What is the absolute mass scale? How does this affect the structure of the universe?
- Of the three known flavors of neutrino, what is the hierarchy, normal or inverted.
- As suggested by other experiments, do sterile neutrinos exist?
- Neutrino astronomy is a recognized component of the multi-messenger signature of cosmic events. What can neutrino's reveal of these event mechanisms?
- Other experiments are addressing the nature of the neutrino, is it its own anti particle? A Majorana or a Dirac particle? Is it responsible for the baryon asymmetry of our universe, where matter dominates antimatter?
- By looking for neutrino capture on tritium, is it possible to detect the relic neutrino background from the big bang, penetrating deeper in time than the cosmic microwave background?

The neutrino remains the most enigmatic of particles, a constant source of surprise and illumination.

KATRIN overview KATRIN, with a design sensitivity of 0.2eV, is the culmination of a long line of neutrino mass experiments utilizing tritium beta decay, a detailed description of the KATRIN apparatus can be found in this paper[1]. In the beta decay, essentially all the energy of the decay goes to the electron antineutrino resulting in the smooth beta decay spectrum. If the neutrino possesses mass this will rob the beta spectrum of the equivalent

*Presently at Karlsruhe Institute of Technology, Karlsruhe, Germany.

[1] "The Design, Construction, and Commissioning of the KATRIN Experiment", M. Aker *et al.* (KATRIN Collaboration), JINST 16 T08015, August 2021.

amount of energy, resulting in a distortion of the spectrum that is most visible at the end point as shown in Fig. 1.15-1.

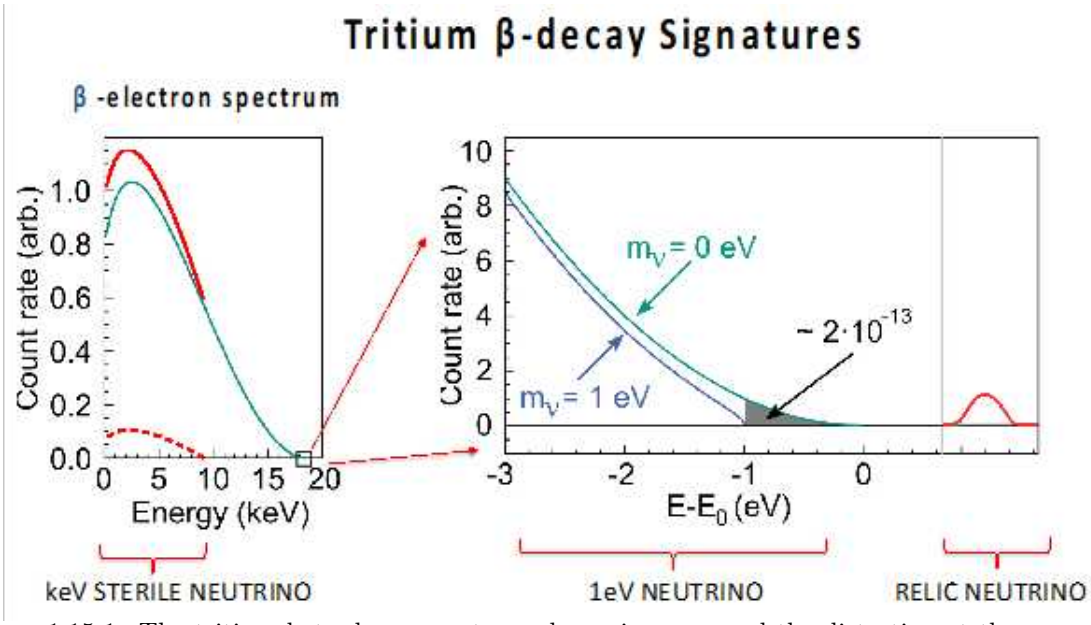

Figure 1.15-1. The tritium beta decay spectrum shown in green and the distortion at the endpoint of the spectra resulting from a 1eV neutrino mass. Also shown at the spectral distortions expected from a keV steril neutrino (LHS) and relic neutrino capture on tritium (RHS)

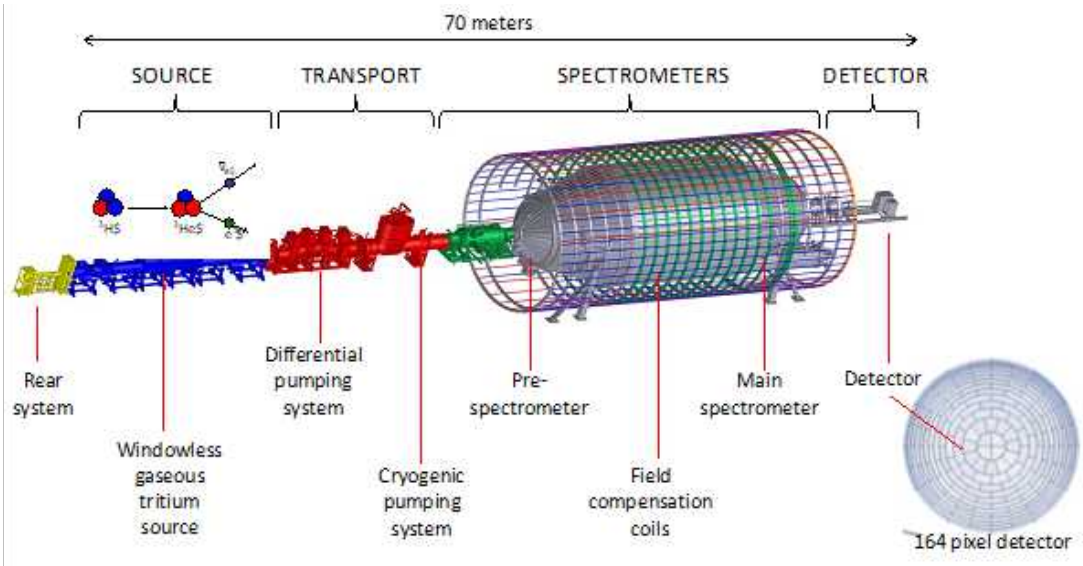

Figure 1.15-2. Principal elements of the KATRIN apparatus. The 10cm diameter, 164 pixel detector is shown on the lower right.

This distortion amounts to a few parts in 10^{-13}. Tritium is an ideal candidate for study

since its low decay energy of 18.6 keV enhances the end point effect and the short half-life of 12.3 years enables an intense source that the low-end point count rate statistically demands. Fig. 1.15-2 shows schematically the elements of the KATRIN apparatus.

Tritium beta decays occur in the windowless gaseous tritium source (WGTS), pioneered by the LANL neutrino mass experiment. Beta particles resulting from tritium decays are adiabatically transported to a pair of electrostatically retarding spectrometers. Differential and cryogenic pumping reduces the flux of tritium escaping the WGTS by a factor of 10^{14}, ensuring that only beta particles enter the second high-energy resolution ($\sim$ 1 eV) spectrometer, which makes a very precise measurement of the beta energy. When operating in the integral mode, only those beta particles with enough energy to surmount the retarding potential of the spectrometer escape to be counted in the beta detector. The background in the detector is $<<$ 1 count per second. This custom focal plane detector (FPD) supplied by CENPA and seen in Fig. 1.15-2 is a 10-cm-diameter monolithic array of 164 silicon diode pixels arranged in a dart board fashion, optimal for imaging the beta particles exiting the spectrometer. To lift the beta signal above sources of natural and other backgrounds, up to 20 keV of post-acceleration can be applied to the beta particles. The detector is calibrated by introduction of radioactive sources and variable energy photoelectrons and an electron gun. In a complex apparatus such as KATRIN there are many sources of systematic error. The FPD has been central in both commissioning the KATRIN hardware beginning in 2012 and identifying and understanding the many sources of systematic error, including those associated with the FPD itself. Maintenance of the FPD system, ensuring data quality, and understanding the FPD performance remain the focus of the CENPA responsibilities.

KATRIN Operations Once commissioned, the 'first light' with electrons in KATRIN was achieved in October 2016. Regular tritium data taking operation commenced in June 2018 and consists of "campaigns", typically 70 days long, interspaced with a maintenance period during which the cryogenic pump is regenerated and systematic studies carried out over a period of typically 20 days. Currently KATRIN is on the KATRIN Neutrino Mass campaign #15 (KNM15). Analysis of data from KNM1 to KNM5 is complete and provides the current best mass limit of $m_\nu < 0.45$ eV (90% CL)[1]. The plan is to continue the tritium campaigns into December 2025, accruing a total of $\sim$1000 days of tritium operation and an anticipated limit of $m_\nu < 0.3$ eV. All data is first preprocessed at CENPA to ensure data quality before distributing to other institutes for analysis. It is expected that CENPA will continue to ensure data quality and detector systematic studies beyond the cessation of tritium operations in 2025. In 2025 the CENPA supplied FPD will be replaced by the TRISTAN detector, explicitly designed to search for evidence of sterile neutrinos by looking for distortions deeper within the tritium beta spectra. TRISTAN will run until 2027. For KATRIN to probe the neutrino mass below 0.1 eV will require operation with atomic rather than molecular tritium. The development of such a high flux atomic source is a goal it shares with the Project 8 experiment.

[1]Direct neutrino-mass measurement based on 259 days of KATRIN data. arXiv:2406.13516.

1.16 In-situ electron backscattering measurements of the focal plane detector

S. Enomoto, and A. Marsteller*, and C. Rodenbeck†

The detector model of the KATRIN focal plane detector can simulate the energy spectrum of recorded electrons and is capable of replicating the measured energy spectrum [1]. A variety of measurements aiming to validate the output of the detector model have been performed in the past, all of them achieving good agreement between prediction and measurement outcome, enabling the detector model to be used to determine systematic effects, such as changes in region of interest coverage during a scan, from first principles and external measurements rather than having to estimate them from the data.

One systematic effect difficult to access experimentally is the backscattering of electrons off the FPD with little energy loss and subsequent escape across the MAC-E type spectrometer. This effect can induce a very subtle slope depending on the spectrometer potential for the measurement, which would affect the neutrino mass measurement of KATRIN. However, a direct measurement is difficult, as the effect is a tiny $O(10^{-5})$ loss in rate. For KATRIN's neutrino mass measurement, only backscattered electrons with less than O(100 eV) are relevant. To experimentally access this loss in rate, an electron source with high rate and energy stability is needed. Due to this, only measurements with the spectrometer potential at several keV below the incident electron energy were used for validation. Of particular interest are plasmon excitations in silicon, imprinting a periodic structure with 17 eV periodicity close to the incident energy into the spectrum of backscattered electrons. However, some of the simulation tools have already described the plasmon excitations, until now without experimental validation.

In order to make a measurement of the backscattered electrons close to the incident energy, we have developed a measurement procedure which allows a direct measurement of these electrons rather measuring a decrease in rate. For this, we make use of the pulsed electron gun and both MAC-E type spectrometers (the pre- and main-spectrometer) available in the KATRIN setup. The electron gun produces electrons with a narrow temporal, angular, and energy distribution. For our measurements, we are interested in electrons with a pitch angle of close to 0°to the magnetic field and an energy slightly above the endpoint of tritium. These electrons are guided towards the spectrometer section, where the prespectrometer is set such that the electrons from the electron gun can barely pass it, and any electrons with lower energy or higher angle are reflected. After passing the main spectrometer, which is set at a lower potential than the pre-spectrometer, the electrons reach the focal plane detector and can backscatter. A fraction of backscattered electrons pass the main spectrometer and reach the prespectrometer, where they are reflected as a result of the small change in energy or angle due to backscattering. After reflection, the electrons pass the main spectrometer for the third time before hitting the detector, where they are detected.

*Presently at Karlsruhe Institute of Technology, Karlsruhe, 76344, Germany.
†Karlsruhe Institute of Technology, Karlsruhe, Germany.

[1] CENPA Annual Report, University of Washington (2023f) p. 7.

The advantage of this complex setup is that electrons with energies close to the potential of a spectrometer are slowed down and spend a significant time (of up to several tens of μs) transiting the main spectrometer. The electron gun produces electrons in 20 kHz pulses of nanosecond time spread, which allows reconstruction of the electron flight time. The backscattered electrons escaping over the main spectrometer can be separated by their longer flight time from the not-backscattered electrons or the electrons reflected close to the focal plane detector. In addition, the time-of-flight is a measure of the energy of the backscattered electrons, which makes it possible to obtain their energy spectrum.

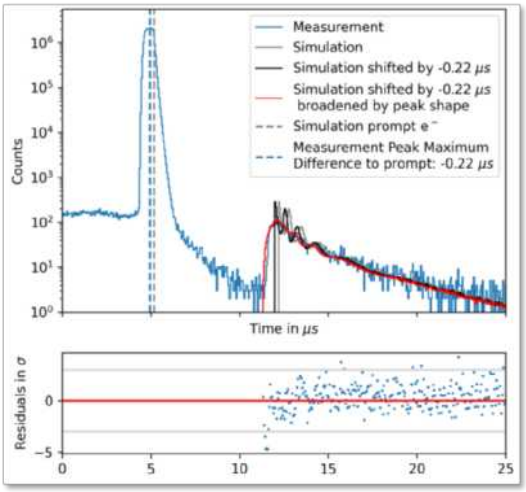

Figure 1.16-1. Time-of-Flight spectrum of electrons backscattered off the KATRIN FPD.

A first proof-of-principle measurement was performed and the result is shown in Fig. 1.16-1. To interpret and analyze the measurement results, we have combined the detector model with time-of-flight simulations through both MAC-E spectrometers, deriving the expected time-of-flight spectrum. We find a good agreement between our model and the measurement. On the basis of this initial success, we have performed further measurements at optimized spectrometer potential settings, which are sensitive to different regions of the backscattered energy spectrum and will be analyzed in the near future.

The in situ measurements allow us to validate the systematic effect of backscattered electrons escaping over the main spectrometer potential, which so far only been measured indirectly. The good agreement between our detector model and the recorded data further improves confidence in the capability of the model to accurately describe all electron detection-related effects in the KATRIN experiment.

1.17 FPD Drift Characterization

Q. Li, S. Enomoto, and A. Marsteller*

Unexpected jumps in focal plane detector signal gain (FPD) were observed in 2020 and a thermal model was constructed to explain it[1]. This model takes the temperature sensor readouts of the detector wafer mounting plate in the vacuum ("Carousel Temperature") and of the detector platform in the KATRIN building ("Detector Platform Temperature") as independent variables, and the FPD gain (ADC or energy output per incident charge deposit) as dependent variable. The previous report focused on the average gain of all the FPD pixels. This time, we applied the model to individual pixels for two KATRIN data-taking campaigns, KNM4 and KNM5. We found that some pixels behave oppositely in the gain drift structure compared to the other majority of the FPD pixels.

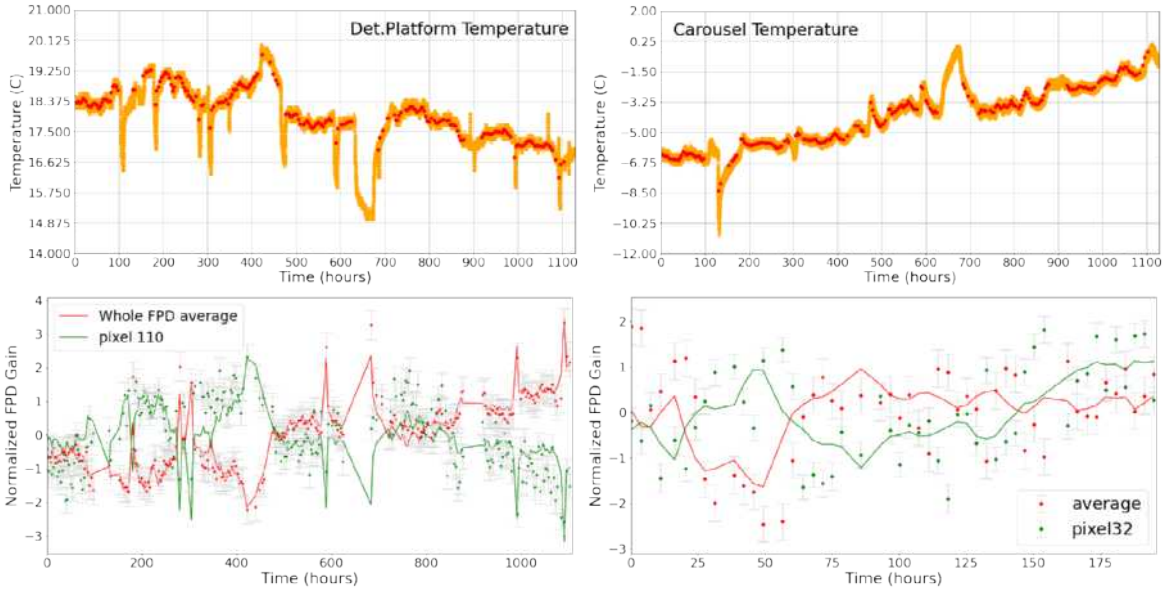

Figure 1.17-1. Top-left: Raw Detector Platform Temperature. Top-right: Raw Carousel Temperature. Bottom-left: Example of strange pixel in KNM4. The red points are the normalized average gain of the whole detector, and the red curve is the fitted model for the points. The green points are the normalized gain of pixel 110 in KNM4, and the green curve is the fitted model. Bottom-right: Example of strange pixel in KNM5. The red points and curve are the FPD-average gain and fitted model to the points. The green ones are for pixel 32.

Fig. 1.17-1 shows the temperature readings and normalized FPD gains. Our gain drift model is constructed by a linear combination of temperature drifts:

$$G = \alpha_{\text{car}} \times T_{\text{car}} + \alpha_{\text{det}} \times T_{\text{det}} \tag{1}$$

*Presently at Karlsruhe Institute of Technology, Karlsruhe, Germany.

[1]CENPA Annual Report, University of Washington (2021) p. 7.

where the variable G stands for the normalized gain of the whole FPD average or individual pixels. The variables T_{car} and T_{det} represent the temperature data of the carousel and the detector platform, respectively. And variables α_{car} and α_{det} are their respective dependence variables. Here, we applied the normalization to a set of data points by subtracting the mean value and then dividing it by the standard deviation.

As represented in the bottom plots in Fig. 1.17-1, pixel 110 and pixel 32 showed clear opposite gain structures from the whole FPD average in KNM4 and KNM5, respectively. Among the parameters that include α_{car}, α_{det}, errors and reduced chi, we found that α_{det}, the dependent variable of the detector platform temperature, has a distribution structure similar to the strange pixels on the detector. This is shown by the left and middle pixels in Fig. 1.17-2.

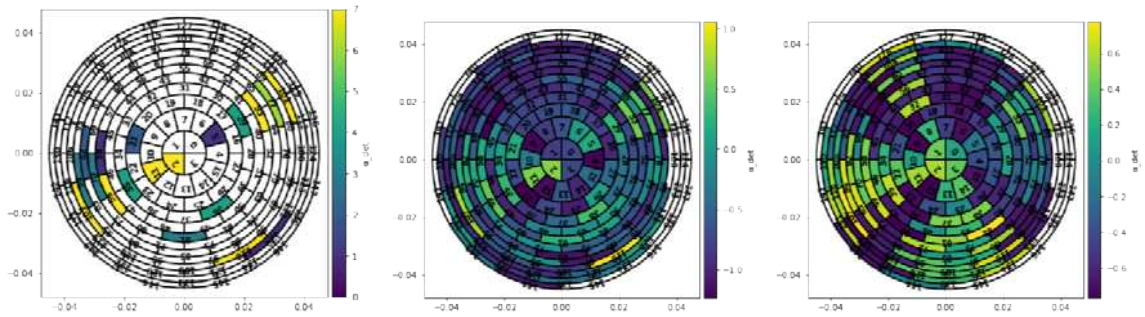

Figure 1.17-2. Left: Distribution of strange pixels in KNM4. Pixels in white are the ones that showed no noticeable opposite gain structure. Other pixels showed the opposite structure, and their colors represent the degree of opposition to the average. Pixels in yellow has similar gain structures as pixel 110 and 32 in Fig. 1.17-1. Pixels in darker colors have less obvious opposite gain structure. Middle: α_{det} for single pixels in KNM4. Color represents the value of α_{det} of that pixel. Right: α_{det} for single pixels in KNM5.

The radial alternate pixel structure visible in Fig. 1.17-2 corresponds to the preamplifier structure: One preamplifier card connects to six or seven pixels aligned in this way. As in Fig. 1.17-2, the middle and right plots, KNM4 and KNM5 do not share exactly the same strange pixels. These observations indicate that the preamplifiers are responsible for the strange gain drift behavior and are likely not due to hardware breakdowns but to some sporadic metastable states of the electronics.

The behavior of the preamplifiers will be further analyzed using datasets taken during quick temperature changes.

Selena

1.18 Package for aSe/CMOS Devices

A. E. Chavarria, M. Conde, and X. Ni

The deposition of amorphous selenium (aSe) on a prototype CMOS imager is a critically important step in Selena R&D. We had previously described our attempts to flip-chip bond the Topmetal-II$^-$ active pixel sensor (APS) to a sapphire interposer[1]. This was unsuccessful because of the device's weak bond pads, which led to shorts between metal layers under the forces necessary to flip-chip bond. The good performance of the prototype TopmetalSe (Sec. 1.19) motivated us to proceed onto preparing the TopmetalSe for aSe deposition instead. We are currently preparing for aSe deposition both flip-chip and wire bonded packages.

The wire bonded packages consist of the TopmetalSe bare die glued onto a printed circuit board (PCB) and then wire bonded to the respective pads. As with Topmetal-II$^-$, the bonding force caused power lines inside the chip to short during aluminum wedge bonding. We learned from the open-source community Slack that this is a common problem for other projects on the same Multi Project Wafer (MPW) run. Following suggestions from the community, we proceeded to gold-ball wire bond at the Washington Nanofabrication Facility (WNF) onto PCB pads with an Electroless Nickel Electroless Palladium Immersion Gold (ENEPIG) finish, which yielded good and reliable results. A wire bonded package is shown in Fig. 1.18-1. For deposition, we plan for a large fraction of the package to be coated in aSe, wire bonds included. So long as the wires do not get too hot to crystallize the selenium, the wire bonds should remain electrically isolated. However, there is some uncertainty on whether the voltage present on the wires might affect the electric field lines in the aSe.

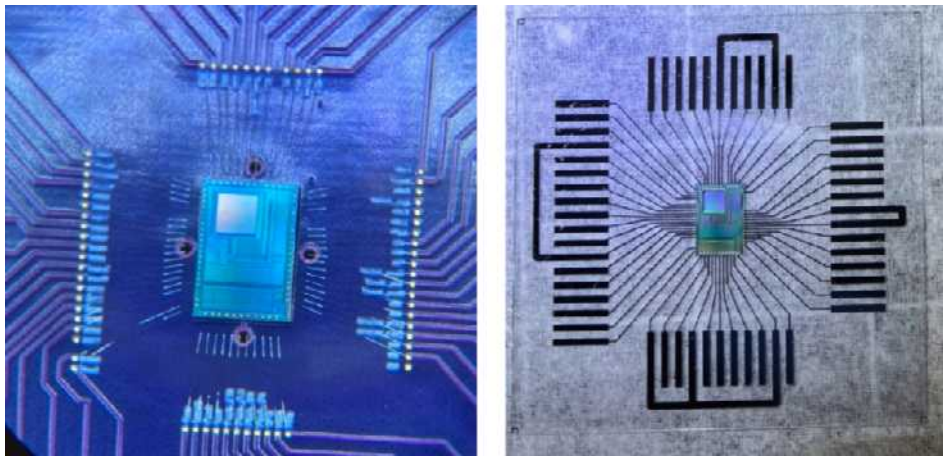

Figure 1.18-1. Left: wire bonded package. Right: flip-chip bonded package.

We are also preparing a flip-chip package for TopmetalSe, which should provide better electric field uniformity in the aSe. We use a sapphire interposer with a window cut over

[1]CENPA Annual Report, University of Washington (2023) p. 37.

our pixel array, where aSe coats the topside and the TopmetalSe is flip-chip bonded to the bottom side. The idea is the same as described in a previous annual report[1], but the electrical connections and window are adapted for TopmetalSe. Because the bond-pad pitch of TopmetalSe (200 μm) is much larger than Topmetal-II$^-$, we were able to attempt more flip-chip techniques. In the past year, we tried *i)* ultrasonic flip-chip attachment, *ii)* stencil-printed solder paste reflowed onto gold bumps, *iii)* stencil-printed silver epoxy cured on gold bumps, and *iv)* hand-applied silver epoxy cured on gold bumps. We found option *iv* to produce the best results. We first apply gold stud bumps onto the TopmetalSe bond pads. We use M. Conde's steady hand to then apply small amounts of EP3HTSDA-2 low-outgassing conductive epoxy onto the interposer pads. For additional mechanical support, we also place a dab of a nonconductive underfill epoxy in an unused area of the chip. Using a Finetech pico flip-chip bonder at WNF, we then align, bond and cure the two parts together. A flip-chip package is shown in Fig. 1.18-1.

We are preparing to send the packages to our partners at Hologic for deposition of a 500 μm-thick layer of aSe and a 10 nm-thick chromium electrode. A sketch of the flip-chip device with aSe deposited is shown in Fig. 1.18-2. R. Roehnelt designed a deposition jig to be machined by the CENPA shop, shown in Fig. 1.18-3, which will hold our devices and provides the shadow masks for aSe and electrode depositions. The exact number of wire bond and flip-chip packages will depend on the final number of successful flip-chip packages. The parts will be sent out in November 2024.

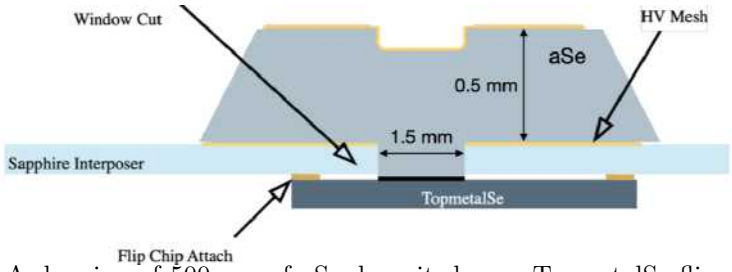

Figure 1.18-2. A drawing of 500 μm of aSe deposited on a TopmetalSe flip-chip package. The drawing is not uniformly scaled.

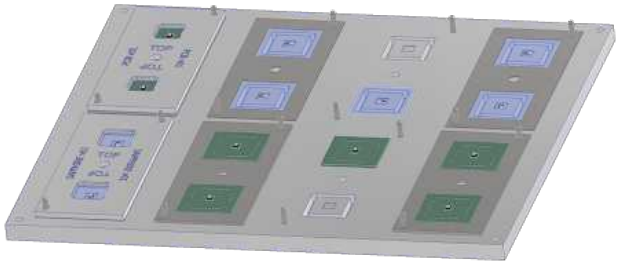

Figure 1.18-3. Drawing of the deposition jig. Both flip-chip and wire bonded packages are placed in the bottom plate in pairs. The leftmost column has the shadow mask over the packages.

[1] CENPA Annual Report, University of Washington (2023) p. 37.

1.19 Characterization of TopmetalSe

A. E. Chavarria, H. Lin, Y. Mei*, and X. Ni

TopmetalSe is a low-noise, charge sensing complementary metal-oxide-semiconductor (CMOS) pixel array that we designed at CENPA and was fabricated in the Skywater 130nm Open-Source process. The sensor consists of an array of 100×100 pixels of size $15 \times 15\,\mu\text{m}^2$ with an exposed topmost metal layer, which allows for direct coupling to amorphous selenium (aSe), and a low-power charge-sensitive amplifier (CSA). The topmost metal layer features $8.2 \times 8.2\,\mu\text{m}^2$ collection electrodes surrounded by $0.8\,\mu$m-wide guard rings, which can be biased to improve charge collection. We received the sensors in June 2023, and we have since made significant progress in demonstrating their capabilities as prototypes for the Selena Neutrino Experiment.

The test setup involves a test printed circuit board (PCB), which was designed and populated by the CENPA Electronics Shop, a BASYS 3 field-programmable gate array (FPGA) board, and carrier boards to which the TopmetalSe bare die is wire bonded. The test PCB includes circuitry to properly bias the pixel amplifiers and to amplify the analog output of the pixel array. The FPGA was used to handle the digital signals to control the pixel switching.

The first test was to characterize the in-pixel amplifiers by injecting a test pulse through the pixel guard ring, which has a parasitic capacitance to the pixel input. The injected charge can be calculated from the voltage-amplitude of the pulse and the parasitic capacitance provided by the integrated circuit (IC) design software. We used the FPGA to select the output signal of a single pixel in the array, digitized the pixel output for many injected pulses, and then applied a trapezoidal filter in software. We recorded the pulse heights after filtering and estimated the charge-conversion gain and the Equivalent Noise Charge (ENC) from the mean and r.m.s. of the pulse-height distribution, respectively. Fig. 1.19-1 shows the results for a representative pixel, where we achieved a gain of $50\,e-/\text{mV}$ and an ENC of $10\,e^-$.

*University of Texas, Arlington.

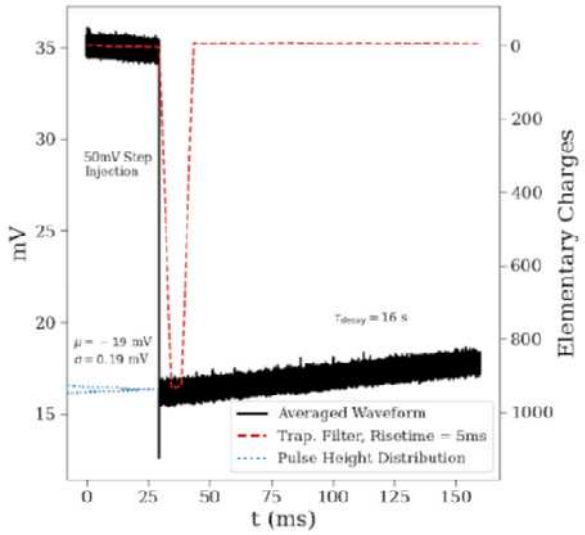

Figure 1.19-1. An injected pulse into a single pixel's amplifier from the guard ring. A 50 mV pulse corresponds to 965 elementary charges ($C_{gring} = 3.1$ fF). The black line shows the pixel output waveform averaged over $\approx$ 1000 pulses. The red line shows the pulse after implementing a trapezoidal filter in software. The distribution of pulse heights after filtering is shown in blue on the y-axis.

We then demonstrated charge collection by the sensor by imaging ion clouds generated by alpha particles in air. We used a high-voltage electrode to apply an electric field toward the pixel array across the air volume above the sensor, and placed a ^{241}Am source roughly 5 cm above the sensor. The emitted alphas ionize molecules in air that are drifted toward, and collected by, the electrodes of the pixel array. From the pixel signals, we were able to reconstruct images of the ion clouds.

The final step in our characterization of the TopmetalSe sensors prior to aSe deposition is a measurement of the collection efficiency. We rely on the photoelectric effect to emit a calibrated amount of charge onto the pixel array. The photoelectron source consists of a gold photocathode on which light from a 235 nm LED is focused using a series of fused silica lenses. The 10 nm-thick gold photocathode is illuminated from the back through the 200 μm thick sapphire wafer on which it is evaporated. A wire is epoxied to the photocathode to apply a high voltage ($\approx$100 V). The surface of the chip, located a few mm below the photocathode, is at ground. To calibrate the emitted charge from the photocathode, we replace our chip with a metal electrode in the exact same location, which is then connected to a picoammeter for an absolute measurement of the photocurrent.

Fig. 1.19-2 shows initial results from a measurement in air demonstrating our ability to generate and image external charge with the photoelectron beam. The charge measured per frame agrees with our expectation from our photocurrent measurement with the picoammeter. Unfortunately, the precision of the measurement is currently limited by large fluctuations in the photocurrent caused by charge losses in air. We are currently moving the calibration system into vacuum for a percent-level measurement of the charge collection efficiency.

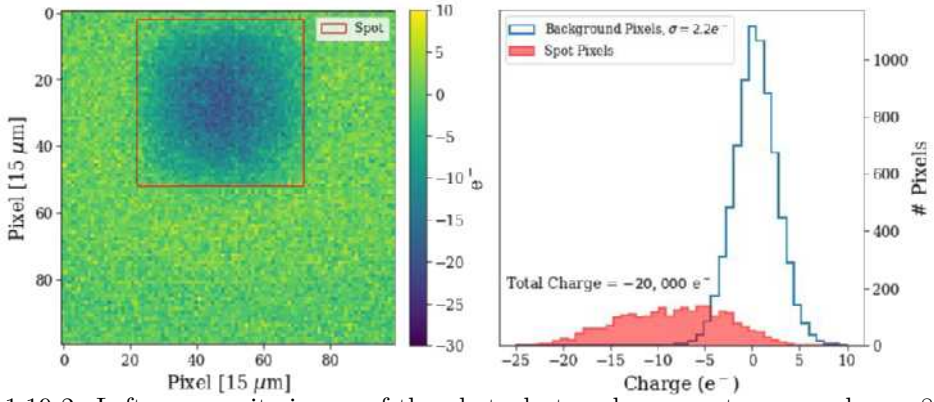

Figure 1.19-2. Left: composite image of the photoelectron beam spot, averaged over 8000 LED pulses. Right: histogram of pixel values in the composite image, separated into background pixels and pixels within the beam spot.

1.20 Further CMOS Sensor Development

Y. Mei* and X. Ni

The positive results from the TopmetalSe CMOS imager (Sec. 1.19) motivate us to further develop and design new prototypes. We have designed two more sensors: one for testing the "digital pixel sensor" (DPS) structure[1], as well as a larger 2.85 × 2.85 mm^2 pixel array with the same functionality as TopmetalSe.

TopmetalSe-DPS was originally submitted for fabrication in September 2022 and was already described in the 2023 annual report[2]. We received the sensors from the foundry in Winter 2024 and we are preparing to test them.

In June 2024, we submitted the larger pixel array for tape-out in the EFabless ChipIgnite Multi Project Wafer (MPW) run with the Skywater 130nm process. The design was included, together with another project, in a submission by our colleague Yuan Mei. The pixel structure remains largely the same as in TopmetalSe, with small modifications to improve the frame readout speed. The size of the pixel array was set by the available project area and consists of four sub-arrays, each 95×95 pixels in size, totaling 190×190 pixels. The larger active area will increase the sensitive volume of aSe to better contain β tracks, and the larger lateral size relative to the aSe thickness will minimize edge effects.

*University of Texas Arlington.

[1] S. Kleinfelder, S. Lim, X. Liu, A. Gammal, IEEE Journal of Solid-State Circuits, **36**, 2049-2058 (2001).
[2] CENPA Annual Report, University of Washington (2023) p. 40.

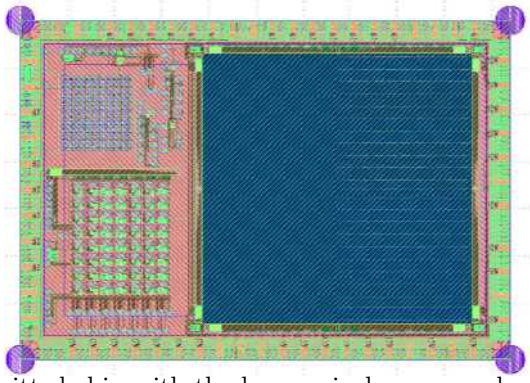

Figure 1.20-1. The submitted chip with the larger pixel array rendered in the layout software, KLayout. The blue square on the right is the array of 190 × 190 pixels.

The design was first submitted in June 2024 but had to be modified because of metal-density rule changes by EFabless/Skywater. The design was resubmitted in September 2024 and we expect the chips to be delivered in Winter 2025. An image of the full chip in the design software is shown in Fig. 1.20-1.

1.21 Selena module in PIONEER beam

A. E. Chavarria, X. Ni, and M. Traina.

The main goal of the PIONEER experiment is to measure the branching ratio:

$$R_{e/\mu} = \frac{\Gamma(\pi^+ \to e^+\nu(\gamma))}{\Gamma(\pi^+ \to \mu + \nu(\gamma))},$$

in order to test lepton-flavor universality (Sec. 2.5). Theory predicts $R_{e/\mu}$ with a precision of 1 part in 10^4, with $\pi^+ \to \mu^+(\to e^+)$ being about 10^4 times more likely than $\pi^+ \to e^+$. By distinguishing the two processes, PIONEER aims to experimentally determine $R_{e/\mu}$ with an uncertainty comparable to the theoretical uncertainty. The salient features of the PIONEER experiment (from the beam axis outwards) are:

- A 300 kHz, 55 MeV/c π^+ beam;
- A highly segmented active target (ATAR) to detect pions (muons) and their decay location;
- A tracker to link particle tracks in the target to showers in the calorimeter;
- An electromagnetic calorimeter with 3π sr solid angle and 25 radiation lengths to measure the energy of the outgoing e^+ with high efficiency.

The ATAR, based on silicon low-gain avalanche diodes (LGADs), is currently under development. In this exercise, we begin exploring the possibility of a Selena aSe/CMOS module

as a future upgrade to the ATAR. The final module for Selena will offer exquisite three-dimensional (3D) particle tracking capabilities with improved energy resolution[1]. The lateral size of the CMOS pixel array and the several-mm thickness of the amorphous selenium (aSe) target are large enough to fully contain the stopping pions from the beam and their muon daughters, without any losses in detector dead layers. This is demonstrated in Fig. 1.21-1, which shows a $\hat{xz}$ cross section of an event simulated with GEANT4. A positive pion impinges on the aSe target and subsequently decays into a positive muon (and a muon neutrino), which in turn decays into a positron and an electron neutrino.

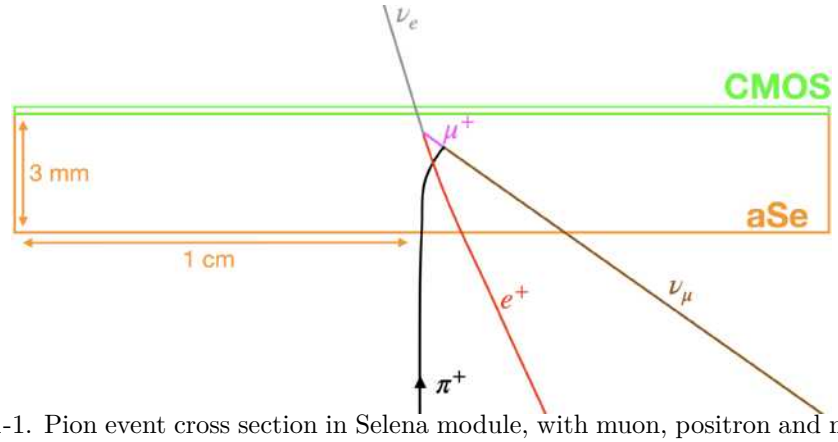

Figure 1.21-1. Pion event cross section in Selena module, with muon, positron and neutrino decay products labeled.

In order to distinguish $\pi^+ \to e^+$ from $\pi^+ \to \mu^+$, space, time and energy information can be used. Pions and their muon daughters are fully contained in the aSe and the topology of their tracks can be used for particle identification and event discrimination. Positrons tracks can also be identified from their energy-deposition profiles but they ultimately escape the aSe and their total energy must be measured with the calorimeter.

Our simulations show that an average of 470 pixels are populated per event, which corresponds to an average time of 12.5 ms between same-pixel hits, assuming a 15 μm $\times$ 15 μm CMOS pixel pitch. This period is much longer than the few μs required for charge to drift across the aSe into the pixel array, and provides sufficient time to measure, digitize and read out the pixel values with $\mathcal{O}(10\,e^- = 0.1\,\text{keV})$ and $\mathcal{O}(10\,\text{ns})$ resolutions in the amplitude and time-of-arrival of the charge signals. A typical $\pi^+ \to \mu^+ \to e^+$ event is shown in Fig. 1.21-2 in xyz space (left) and, as imaged by a Selena module (charge diffusion not included), in the xyt (right) space. As can be seen on the right-hand side, clear $\mu^+ - e^+$ separation in time can be achieved due to the relatively long 2197 ns lifetime of the muon. Separation between $\pi^+ - \mu^+$ (or $\pi^+ - e^+$ of the subdominant decay mode) cannot be performed by timing alone because of the much shorter 26 ns lifetime of the pion. This is a significant limitation of the Selena module compared to the LGAD ATAR, but it could perhaps be addressed by relying on the energy-deposition profile of the stopping/starting particles and kinks along the tracks.

[1] A.E. Chavarria *et al.*, arXiv:2203.08779 (2022).

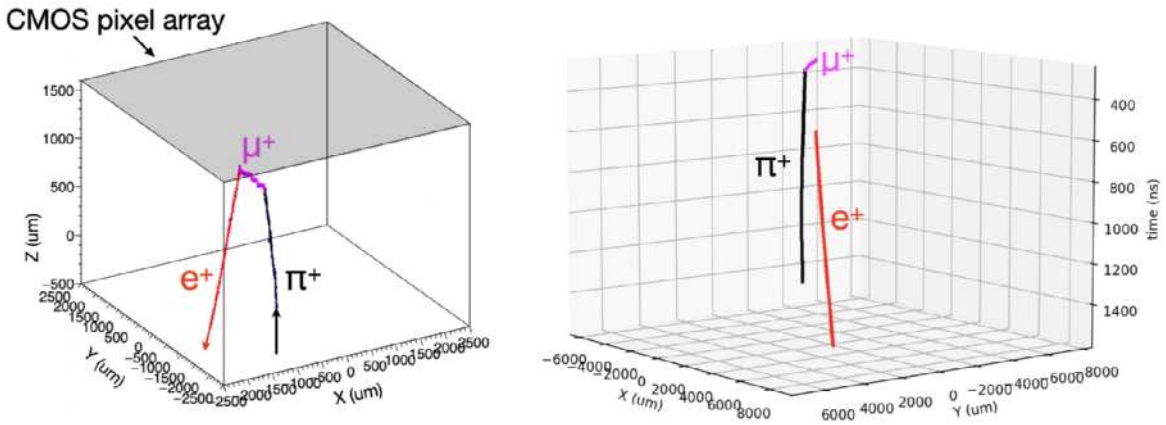

Figure 1.21-2. Typical $\pi^+ \to \mu^+ \to e^+$ event in the xyz space (left) and, as imaged by a Selena module, in the xyt space (right, charge diffusion not included).

Lateral charge diffusion during drift in the aSe must be taken into account to ensure that it does not affect topological discrimination. This was simulated using a charge-transport model and accounting for the electric-field profile in the aSe, and found to have a negligible effect. A projection of an event on the pixel array including charge diffusion is shown in Fig. 1.21-3.

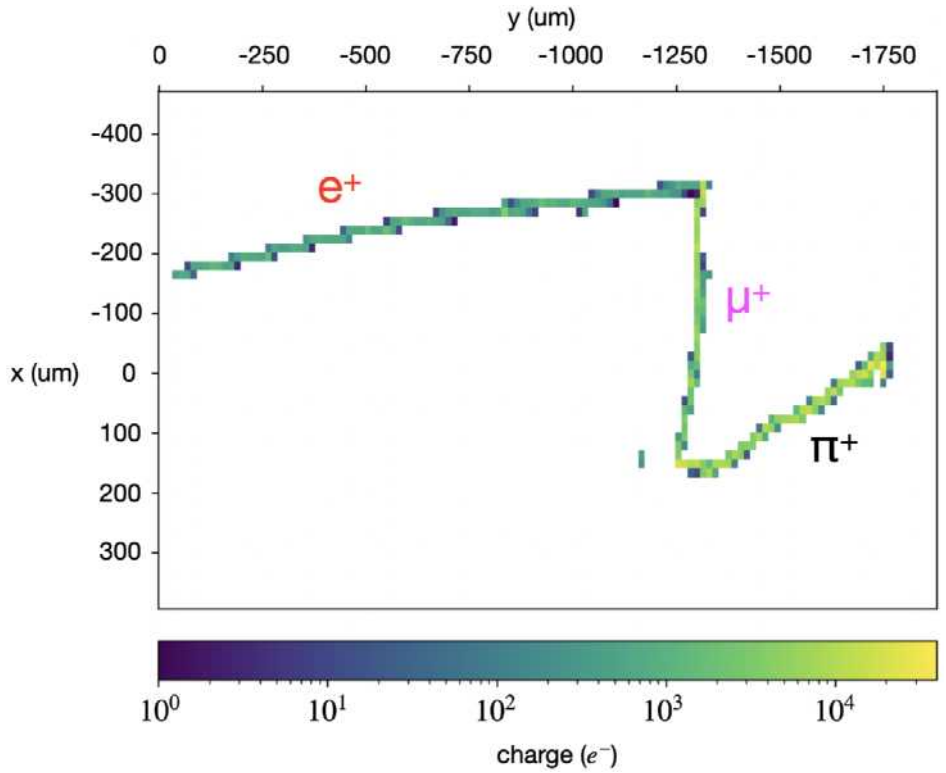

Figure 1.21-3. Image for a typical $\pi^+ \to \mu^+ \to e^+$ event. The small width of the tracks are a result of charge diffusion. Pixel noise is not included.

The electric field also affects charge recombination and trapping in the aSe, which were also modeled in our simulation. We thus have the information to explore how well the measured energy-deposition profiles of pions, muons and positrons could be used for discrimination purposes.

A significant challenge is the large data throughput of the module in the pion beam. The pixel hit rate of $\mathcal{O}(10^8\,\mathrm{s}^{-1})$ corresponds to several Gbit/s of data that must be downloaded from the in-pixel dynamic random access memory (DRAM) cells where pixel values are stored. This may be possible by optimizing the pixel switching and readout strategy, and instrumenting the pixel array with 16 output channels and reading out via optical fiber.

Lastly, we found a mean radiation dose in the CMOS pixel array of $0.01\,\mu$rad per event. Amorphous targets have high radiation tolerance and CMOS monolithic active pixel sensors (MAPS) have demonstrated good performance up to 1 Mrad. Therefore, several years of operation under constant pion illumination would be possible with this detector.

This study serves as a starting point to explore the detector response and resolution capabilities (time, space, energy) of a Selena module in the PIONEER beam, for a possible future upgrade of the ATAR. More in-depth studies are needed to determine the feasibility of this approach.

2 Precision Muon Physics

2.1 Overview

D. W. Hertzog

The Precision Muon Physics Group designs and conducts experiments that determine fundamental Standard-Model parameters, low-energy effective-field-theory constants, or provide sensitive tests for new physics. Our Muon $g-2$ experiment efforts have dominated the group's work for the last 15 years, resulting in the training of 7 Ph.D. students and 10 UW postdocs. In anticipation of the completion of $g-2$, we have devoted considerable resources to the design of PIONEER, a next-generation rare pion decay experiment. We present overviews and individual articles that represent just some of the technical work we have been doing on Muon $g-2$ and PIONEER. It is, as always, but a small sample of the actual work accomplished recently, but provides a flavor for the variety of UW work. In this Intro, I summarize some highlights.

The 2009 Muon $g-2$ experimental proposal had the goal of measuring the muon's anomalous magnetic moment to a precision of 140 ppb, requiring 21 times the data set obtained at Brookhaven National Lab in the early 2000's, and a significant reduction in systematic uncertainties. Our Fermilab E989 experiment has completed six data-taking campaigns, harvesting the required statistics. We also devoted running time to numerous systematic tests to establish uncertainties. The Run-2/3 results are published in a 2023 PRL[1] and a detailed PRD[2] (both Editor's Suggestions). The result is completely consistent with the Run-1 findings and the combined precision is 200 ppb; the systematic uncertainties are smaller than our proposal projections.

The UW analyses impacting the Run-2/3 results were driven by Ph.D. students Binney (2022), MacCoy (2023)[3], and LaBounty (2024)[4], and postdoctoral scholar Braun. An intense effort is ongoing at the time of this Annual Report to complete the analysis of the Run-4/5/6 data sets and unblind and publish in 2025. Our final hardware contribution to the experiment was a system of innovative, in-vacuum beam-imaging detectors built by Claessens, MacCoy, and Kammel. They used these detectors extensively during Run-6 to directly measure the stored muon profiles and dynamics. All members of the UW group contributed to the operations, analyses, and authorship of papers across many speciality areas within the $g-2$.

Our longer term future vision is guided, as always, by the identification of a compelling measuring campaign with impact to the current and future discovery landscape. A few years ago, we proposed that a Rare Pion Decay Spectrometer developed using the very latest detector and electronics technologies and coupled to the world's brightest low-energy pion beam, could lead to significant physics opportunities. The driving physics cases include the world's

[1] PhysRevLett.131.161802.
[2] PhysRevD.110.032009.
[3] 2024 URA Doctoral Thesis Award.
[4] UW Physics Dept. Thesis Award.

most precise test of lepton flavor universality violation (LFUV) and the uniquely clean determination of V_{ud} from a measure of pion beta decay. Both channels have implications to beyond the Standard Model physics models and are well aligned with the motivation in the 2023 Long Range Plan on Fundamental Symmetries. With development of an international collaboration, the PIONEER experiment has now been approved at the Paul Scherrer Institute with highest priority. The many articles below highlight some of our efforts that center on Simulations and Physics analyses, on the Active Target (ATAR) development, and on a LYSO crystal based calorimeter option.

Muon g-2

2.2 The Muon $g-2$ Experiment

D. W. Hertzog

The muon's anomalous magnetic moment, $a_\mu \equiv (g-2)/2$ can be measured and predicted to sub-ppm precision, enabling a sensitive test of the Standard Model (SM). As a flavor- and CP-conserving, chirality-flipping, and loop-induced quantity, a_μ is especially sensitive to new physics contributions[1]. The SM contributions from electromagnetic, strong, and weak interactions arise from virtual effects involving photons, leptons, hadrons, and the W, Z, and Higgs bosons. An international $g-2$ *Theory Initiative* (TI) was formed to evaluate these terms, producing a comprehensive recommendation in 2020[2]. The dominant uncertainty is the evaluation of the 1st-order hadronic vacuum polarization (HVP) contribution. The included input in 2020 was exclusively data-driven from e^+e^- hadronic cross sections; the emerging lattice efforts had not yet reached competitive precision.

Our 2023 $a_\mu^{\rm Exp}$ value is discrepant by 5 standard deviations with respect to the 2020 TI prediction. However, disruptive new information has been emerging that – if confirmed – will significantly bring closer the SM prediction, Fig. 2.2-1 right. A precise lattice evaluation[3] in 2024 by the BMW Collaboration suggests a much larger contribution, which would put the SM in agreement with our experiment. On the data-driven determination of HVP, the CMD-3 Collaboration reported their energy-scan-based $\pi\pi$ cross section[4], finding a much larger value compared to other experiments that employ the ISR technique from fixed-energy e^+e^- colliders. These updates are being scrutinized now by the TI and we expect that it will take a few years to sort out the discrepant inputs to draw a final conclusion. Our focus remains to ensure that the analyses of our large Run-4/5/6 data sets are completed with exceptional care and scrutiny. As always, our results are blinded until the final moment, which we expect to occur in spring 2025.

[1] Czarnecki, A. & Marciano, W. J.; Phys. Rev. D64, 013014 (2001); Stockinger, D.; J. Phys. G34 2007.

[2] Aoyama, T. et al; Phys. Rept. 887, 1–166 (2020).

[3] Boccaletti, A. et al; https://arxiv.org/abs/2407.10913.

[4] Ignatov, F. V. et al; Phys. Rev. Lett. 132, 231903 (2024); Ignatov, F. V. et al; Phys. Rev. D 109, 112002 (2024).

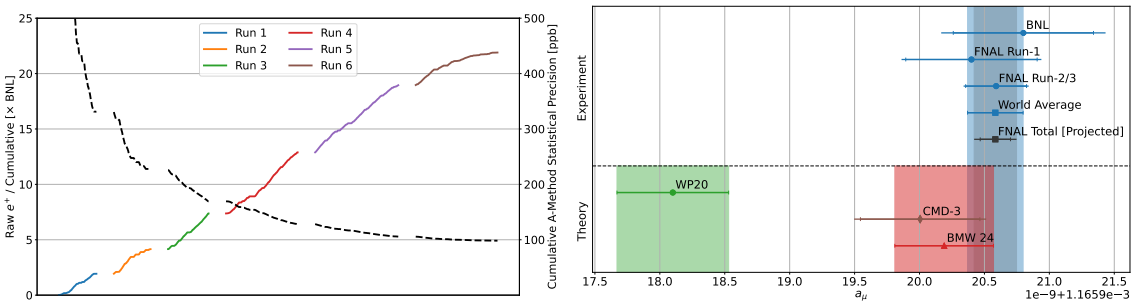

Figure 2.2-1. Left: Accumulated data for the six completed running periods in multiples of the full BNL-E821 data set. The accumulated precision realized and expected is also illustrated. Right: The experimental measurements and world average from BNL and FNAL. The SM prediction is sketched vaguely on purpose, with notable and incompatible TI(2020), Lattice(2024), and CMD-3 results drawn for illustration.

Experimental method and the UW roles

The muon anomaly is measured using a polarized muon beam injected into a highly uniform magnetic storage ring. The muons circulate with frequency $\vec{\omega}_c = -q\vec{B}/m\gamma$, and their spin precesses in the field with $\vec{\omega}_s = -(gq\vec{B}/2m) - [(1-\gamma)q\vec{B}/\gamma m]$. Under simple assumptions, the anomalous precession frequency can be expressed simply

$$\vec{\omega}_a \equiv \vec{\omega}_s - \vec{\omega}_c = -\left(\frac{g-2}{2}\right)\frac{q\vec{B}}{m} = -a_\mu \frac{q\vec{B}}{m}. \tag{1}$$

The average spin direction of the muon during a fill is encoded in the energy distribution of decay positrons. The UW system of electromagnetic calorimeters[1] is used to measure the decay positron times and energies, and from these data determine the anomalous spin precession frequency ω_a.

The magnetic field B is determined by our measurements of the proton's Larmor precession frequency ω_p in the same field. The pulsed-proton NMR system developed at UW is critical to this effort. It is further necessary to know the average muon spatial distribution moments in the storage ring for the muon population that contributes to the ω_a data. This distribution is folded with similarly determined azimuthally averaged magnetic field moments to give the effective magnetic field seen by the muons, $\tilde{\omega}_p$. One obtains a_μ through the relation

$$a_\mu^{\rm Exp} = R\frac{g_e}{2}\frac{m_\mu}{m_e}\frac{\mu_p}{\mu_e}, \quad \text{where} \quad R \equiv \omega_a/\tilde{\omega}_p \tag{2}$$

is measured by our collaboration[2].

[1] Fienberg, A. T. et al; Nucl. Instrum. Meth. A783, 12–21. arXiv: 1412.5525 (2015); Kaspar, J. et al. JINST 12, P01009 (2017); Khaw, K. S. et al; Nucl. Instrum. Meth. A945, 162558 (2019)

[2] The electron g_e factor, the muon-to-electron mass ratio, and the proton-to-electron magnetic moment ratio are known to sufficient precision.

The many details describing the storage ring and beam dynamics, the magnetic field equipment and analysis, and the extraction of the precession frequency were written in 3 long papers following the Run-1 release and another updated detailed paper following the 2023 results. We address here, samples of the specific work that is ongoing now by our UW group members.

UW roles in experimental operations and analysis

As shown in Fig. 2.2-1, we collected data in 6 running years, all using positive muons. Much of Run-6 was devoted to systematic uncertainty campaigns, many driven by members of the UW group to understand beam dynamics and acceptance systematics that have emerged as a block of the more subtle final uncertainties we must understand prior to final publications. In the articles that follow, members of our group describe some of the main current activities they have been leading related to the extraction of the muon spin precession frequency and an emerging systematic from correlations of the injected beam's momentum to the time within the bunch.

2.3 Analysis Challenges in the Run-4/5/6 ω_a Dataset

J. LaBounty and S. Braun

The Run-4/5/6 anomalous precession frequency (ω_a) analysis dataset (detailed in Table 1) consists of $\approx 7\dot{\text{P}}\text{B}$ of raw data files, $1.4\dot{\text{P}}\text{B}$ of analysis skim files, and yields a total statistical uncertainty of ≈ 110 parts per billion (ppb). This dataset represents $\approx 73\%$ of the total data taken in the Fermilab Muon $g-2$ Experiment, and more than $15\times$ what was achieved at the previous generation BNL experiment. This statistical power of this large dataset has allowed us to probe subtle effects with unprecedented detail. Two ongoing analysis challenges are detailed in the sections below: modeling of beam dynamics oscillations and subtle residual detector gain effects. At the time of this report, all results for these analyses remain blinded.

Dataset	**Running Period**	**Size of reconstructed files (PB)**	$\delta\omega_a$ **(ppb)**	**RF Status**
NoRF	Run-4 + DS-5A	0.525	181	Off
xRF	Run-5 (DS-5B – DS-5L)	0.303	235	Horizontal
xyRF-5	Run-5 (DS-5M – DS-5U)	0.324	244	Horizontal + Vertical
xyRF-6	Run-6	0.270	279	Horizontal + Vertical
Total	—	**1.422**	**112**	—

Table 2.3-1. Properties of the various datasets of the Run-4+ ω_a analysis.

2.3.1 Higher Order Beam Dynamics Envelopes

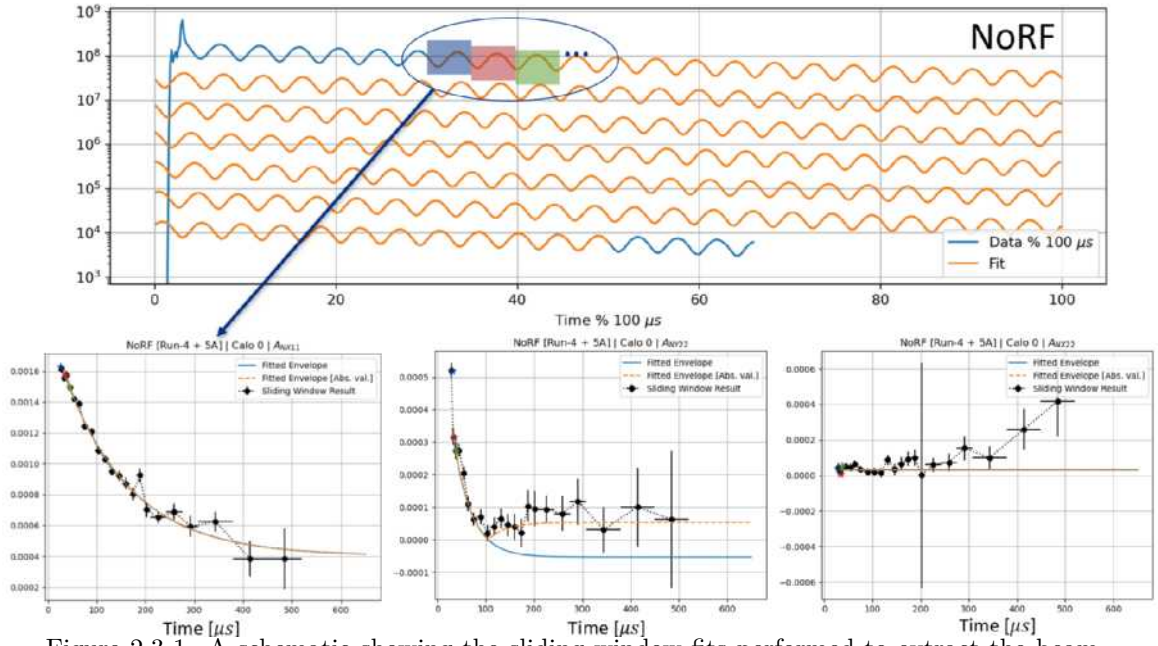

Figure 2.3-1. A schematic showing the sliding window fits performed to extract the beam dynamics envelopes. Each $4.7\mu s$ window indicated on the top fit corresponds to a single point in the diagrams below where the amplitude of a given beam dynamics oscillation is extracted.

The precession of the spin vector of the muons in the magnetic field of the $g-2$ storage ring results in a modulation of the observed positron energy spectrum (Fig. 2.3-1, top). A χ^2 minimization process is performed to fit the data and extract the precession frequency. To first order, the fit function used is:

$$N(t) = N_0 e^{-t/\tau_a} \left[1 + A_0 \cos\left(R\left(\omega_a\right) t - \phi_a\right)\right], \tag{1}$$

where $R(\omega_a)$ is the software blinded proxy for the spin precession frequency ω_a.

The motion of the beam in the storage ring couples to the positron energy spectrum (and thus the extraction of ω_a) through detector acceptance. In general, the fit function is modified to account for such affects through the modification of the following parameters:

$$N_0 \rightarrow N_0(1 + \mathcal{E}_{i,N}(t) * \cos\left(\omega_i t - \phi_i\right)...), \tag{2}$$

$$A_0 \rightarrow A_0(1 + \mathcal{E}_{i,A}(t) * \cos\left(\omega_i t - \phi_i\right)...), \tag{3}$$

$$\phi_a \rightarrow \phi_a + \mathcal{E}_{i,\phi}(t) * \cos\left(\omega_i t - \phi_i\right)... \tag{4}$$

The decoherence envelopes ($\mathcal{E}$) of the beam dynamics (BD) frequencies in the UW analysis are themselves modeled empirically using simple analytic functions, most commonly simple exponentials. The optimal form and the systematic associated with this modeling are determined empirically for each beam dynamics oscillation through a 'sliding window' procedure. For each dataset:

1. The full fit is performed and a reference χ^2 is established[1].
2. Using this fit as a baseline, a 'sliding window analysis' of the oscillation is performed.
   (a) The default envelope in the fit function is replaced with $\mathcal{E}_{\rm i}(t) = A_i * \cos(\omega_i * t - \phi_i)$ and the fit is restricted to the time window $(t_i, t_i + t_w]$[2].
   (b) The start time t_i is stepped forward until the entire fit range is probed. The amplitude of the oscillation is taken to be constant over each window and unrelated beam dynamics envelope parameters are held fixed.
   (c) Amplitudes from each window are combined into a single, empirical map of the decoherence.
3. A fit of the sliding window data to each of the envelope functions in Table 2.3-2 is performed (shown in Fig. 2.3-2). These parameters are used as the initial guess for this envelope in the full fit.
4. The envelope for the given oscillation is replaced in the full ω_a fit function with each of the potential envelopes and a new χ^2 minimum is obtained.
5. A given envelope is rejected if, either:
   - The adjusted χ^2 — defined as the χ^2 of the fit plus the number of additional free parameters from $\mathcal{E}_i$ — yields $\Delta\chi^2 + \Delta N_{\rm d.o.f.} \geq 3$.
   - The p-value of the envelope to the sliding window data, given the parameters obtained from the full fit, is below threshold (chosen empirically to be $p < 10^{-4}$).
6. For all envelopes which are accepted, the systematic associated with the choice of envelope is given by the largest $\Delta R(\omega_a)$ value between any individual envelope and the reference fit.

In the Run-2/3 analysis, a version of this procedure was applied to only the largest BD oscillation (the first order horizontal oscillation, or 'CBO') while all others were modeled simply as pure exponentials ($\mathcal{E}_i = A_i * e^{-t/\tau_i}$). With the higher statistics of Run-4+, this was found to be insufficient. This procedure was therefore extended for use in all BD terms, swapping out the appropriate term in the fit function as needed. Results for various $\mathcal{E}_{\rm CBO,N}$ in the NoRF dataset can be found in Table 2.3-3, and preliminary results for $\mathcal{E}_{\rm CBO,N}$ in all datasets are given in Table 2.3-4. Analysis of the higher order terms remains in progress, but initial results suggest a systematic effect of $<$ 10ppb. This analysis, combined with an overall reduction in the amplitude of the BD oscillations in Run-5/6, should decrease the systematic associated with these terms below the 21ṗpb level in the Run-2/3 analysis.

[1]The envelope chosen as the reference can be updated iteratively based on the results of this analysis, and is generally taken to be the one which produces the minimum χ^2. The default for most oscillations is 'Expo+C' $\rightarrow \mathcal{E}_{\rm i} = A_i\left(e^{-t/\tau_i} + C_i\right)$.

[2]Sliding windows are performed in two ways: with fixed windows of $t_w = 3 \times$ the oscillation period and with the window size dynamically adjusted over the fill to make up for decreases in statistics. The dynamic windows are used in the computation of the final results, with the static windows used as a cross check.

Name	**Form**	**Notes**
Exponential	$p_0 * e^{-t/p_1}$	
Expo+C	$p_0 * e^{-t/p_1} + p_2$	Three forms of this are employed: All parameters free, all parameters positive definite, and p_2 positive definite.
Double-Expo+C	$p_0 * e^{-t/p_1} + p_2 + p_3 * e^{-t/p_4}$	
Constant.	p_0	Only useful for higher order terms.
Removed	0	This removes the term from the fit entirely, which generally results in a poor χ^2 (as one might expect).
Expo + Linear	$p_0 * e^{-t/p_1} + p_2 + p_3 * t$	
Alpha + C	$p_0/(1 + p_1 * t^2) + p_2$	
Double-Alpha	$p_0/(1 + p_1 * t^2) + p_2/(1 + p_3 * t^2)$	
Sinc	$p_0 * (e^{(-t/p_1)} * (1 + p_3 * Sinc(t/p_4)) + p_5)$	Only used in per-calorimeter analyses in the RF datasets.
Fourier $[n = 1]$	$p_0 * cos(2\pi nt/p_2) + p_1 * cos(2\pi nt/p_2) + p_3$	Only used in per-calorimeter analyses in the RF datasets.
Generic	Sum of gaussians, documented elsewhere in GM2-DocDB:28208	Requires many parameters to be fixed from tracker analyses. Valid only in some per-calorimeter envelopes.

Table 2.3-2. BD decoherence envelope functions used in the Run-4/5/6 ω_a analysis.

	Name	χ^2	R [ppm]	$\Delta\chi^2 + \Delta N_{dof}$	ΔR [ppb]	acceptable?
1	Reference (expo+C)	4217.194	-63.528	0.000	0.000	True
2	unchanged	4217.194	-63.528	-0.000	-0.000	True
3	expo	4234.499	-63.549	17.306	-20.581	False
4	expo+c	4209.739	-63.529	-6.455	-1.097	True
5	expo+c [Abs.]	4209.739	-63.530	-6.455	-1.455	True
6	expo+c [Positive Definite]	4209.739	-63.530	-6.455	-1.512	True
7	double-expo+c	4209.531	-63.536	-4.663	-7.775	True
8	const	6187.885	-63.737	1969.691	-208.623	False
9	removed	43400.368	-63.640	39181.175	-111.797	False
10	exp_linear	4209.720	-63.529	-5.474	-0.681	True
11	alpha_const	4208.707	-63.547	-7.487	-19.088	True
12	alpha_alpha	4208.707	-63.547	-6.487	-18.435	True

Table 2.3-3. R values and $\Delta\chi^2$ for various envelope models in the NoRF A-Method dataset. In Row-2, 'unchanged' means that the nominal fit function is run through this analysis chain but with no perturbation to its envelopes. This serves as a closure test for the analysis.

Dataset	ΔR [ppb]
NoRF [Run-4 + 5A]	19.1
xRF	5.5
xyRF — Run-5 Only	3.3
xyRF — Run-6 Only	4.0

Table 2.3-4. Preliminary $\mathcal{E}_{\mathrm{cbo,N}}$ systematic results for all A-Method datasets. The reduction in CBO amplitude due to the RF system in Runs-5 and 6 is reflected in the smaller CBO systematic.

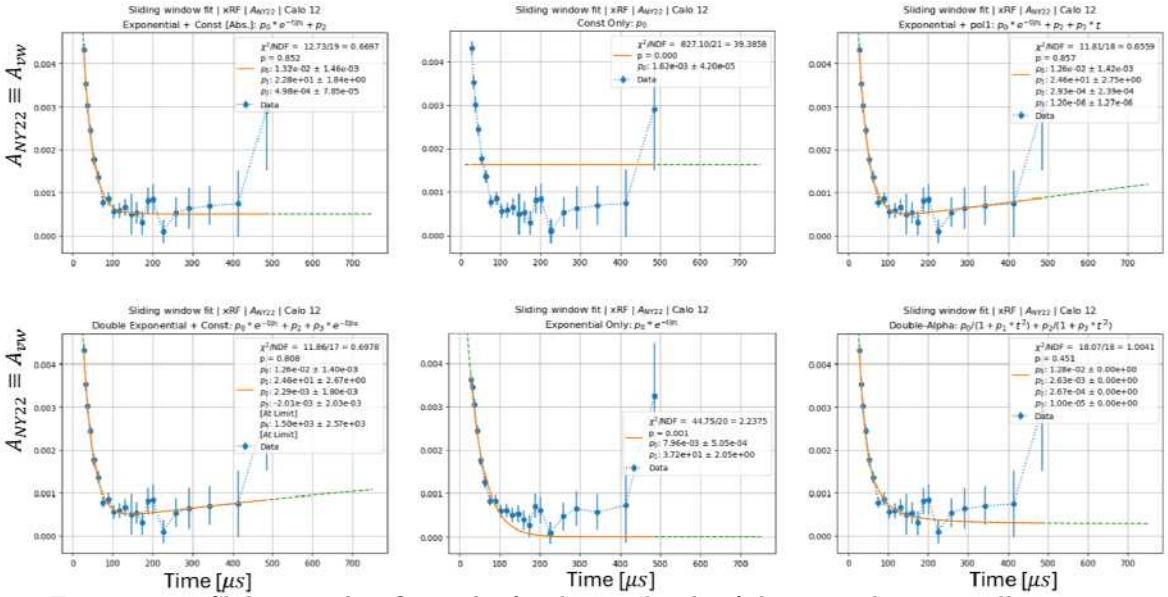

Figure 2.3-2. Sliding window fit results for the amplitude of the vertical waist oscillation to a selection of envelopes. A pure exponential (bottom middle), which was the model used in the Run-2/3 analysis, is not preferred in this case.

Corrections for a Slow, Gain-Like Effect

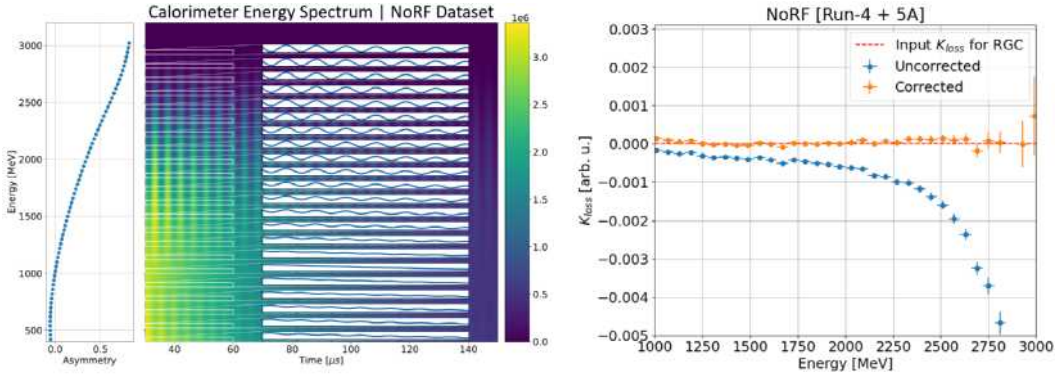

Figure 2.3-3. Left: A visual description of the energy-binned analysis. Many parameters (such as the $g-2$ asymmetry A) vary vs. positron energy, while others are constants. Right: the muon loss parameter K_{loss} should be constant over all energy bins. The variation seen in the blue curve is indicative of an uncontrolled slow gain-like effect. A correction for this is applied in the final ω_a analysis (orange).

Since Run-1, there has been evidence of a residual slow effect in the precession frequency data after all known gain corrections are applied. This slow effect couples to any slowly varying term in the main ω_a fit, such as the muon lifetime (τ_μ) or the muon loss function ($\propto K_{loss}$, Fig. 2.3-3, right), and creates a non-physical dependence of those terms versus the positron energy. In previous analyses, this was hypothesized to be a reconstruction-driven effect. This

led to the formulation of a correction:

$$G(t) = 1 + N_A e^{-t/\tau_\mu} \left[1 + A_A \cos\left(\omega_a t - \phi_a\right)\right], \tag{5}$$

in phase with ω_a where the values of N_A and A_A were determined through a χ^2 minimization process. This function was used to correct for the contents of the 2D (E, t) histogram bin to remove the gain effect before fitting. The difference in $R(\omega_a)$ from a set of histograms produced from $A_A, N_A \pm 2\sigma$ was used to parameterize the systematic uncertainty — 10 ppb in the Run-2/3 analysis.

Although the impact of this term on ω_a is relatively small, its unknown origin made it a topic of intense study. As part of this effort, a search was performed for any evidence of a hardware-level effect which could have gone unnoticed by the laser gain monitoring system. The system was generally used to examine two scales of effect: $\mathcal{O}(\mu s)$ timescale perturbations of global detector gain caused by the large particle 'flash' at beam injection and small $\mathcal{O}(ns)$ timescale perturbations of gain caused by the recovery of individual SiPM pixels. Both sets of gain effects were controlled at the $< 10^{-3}$ level, which met our design goal. Recently, it was hypothesized that an 'intermediate' correction — $\mathcal{O}(\mu s)$ timescale, but created by small perturbations of the detector gain due to single positron hits — could escape detection at the 10^{-4} level. Such a gain sag would then build up iteratively as more and more positrons impacted the calorimeters.

A search for this intermediate gain effect was first conducted using laser-positron coincidences in existing calibration data. For a subset of muon injections ($\approx 1/20$), the laser system was activated while the muons were present in the storage ring. Coincidences of positrons hitting the calorimeters occurring $1 - 100$ μs before the 'standard candle' of the laser pulse were identified (see Fig. 2.3-4). A histogram of the ratio of the perturbed laser energy to that of the synchronization pulse at the beginning of the fill vs. Δt_{L-e^+} was created and fit. In these data, a gain-like recovery effect with an amplitude of $\approx 5 \times 10^{-4}$ and a lifetime of $\tau \approx 1.41$ μs was observed. Although this amplitude was at the level required to explain the residual slow effect, the time constant was highly unusual. The engineers at CENPA were unable to identify any plausible mechanism for the creation of such a time constant in the calorimeter electronics chain. Given this fact, it was determined that an additional measurement would be required before this value could be incorporated into the main $g - 2$ analysis.

Two of the lasers and one calorimeter were shipped back to CENPA for reassembly into a local test stand. Images of this setup can be seen in Fig. 2.3-5. As of the writing of this report, measurements of the known gain effects have been repeated and the results have been found to be consistent with those measured during the running of the experiment. Searches for the intermediate gain effect are underway and are rapidly approaching the statistical precision necessary to probe this $\mathcal{O}\left(10^{-4}\right)$ correction.

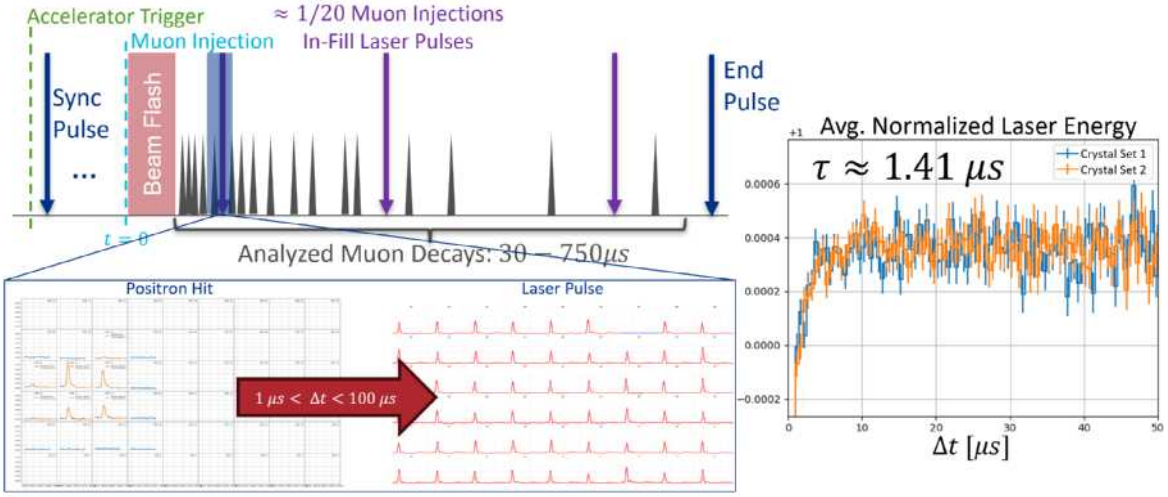

Figure 2.3-4. Schematic of the Laser-Positron coincidence analysis used to extract the amplitude and time constant of the intermediate laser-gain effect. The amplitude of this gain sag is of the required order of magnitude to explain the residual slow effect, but the $1.4\mu s$ time constant is not expected given the known detector electronics chain.

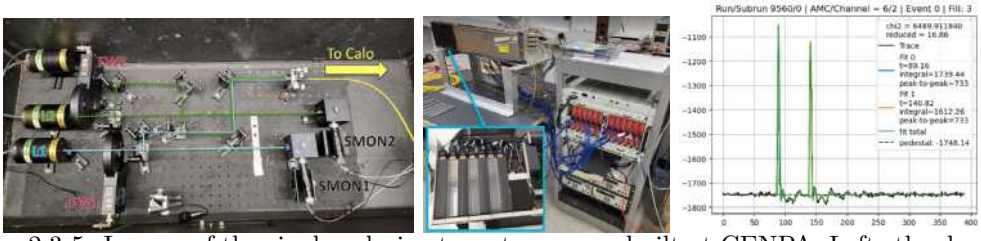

Figure 2.3-5. Images of the single-calorimeter setup now rebuilt at CENPA. Left: the dual-laser system. Middle: Calorimeter and digitizer crate. Right: Example dual-laser event from a single SiPM.

If the existence of this effect is confirmed through the CENPA hardware tests, the correction above will be extended to include an additional term out of phase with ω_a:

$$G(t) = 1 + N_A e^{-t/\tau_\mu} \left[1 + A_A \cos\left(\omega_a t - \phi_a\right)\right] + N_G e^{-t/\tau_\mu} \left[1 + A_G \cos\left(\omega_a t - \phi_G\right)\right], \quad (6)$$

where N_G, A_G, and ϕ_g are all fixed to a given value from the measured gain recovery curve. Because this additional term is out of phase with the main $g-2$ oscillation, it has the potential to introduce a change in the fitted value of ω_a at the level of a few 10's of ppb.

2.4 Direct beam measurements with the MiniSciFi detectors

C. Claessens, P. Kammel, and B. MacCoy

Beam dynamics corrections to ω_a rely on indirect measurements of the muon beam via decay positrons from the straw trackers and calorimeter detectors. In particular, the uncertainty

on the electric field correction was the largest source of systematic uncertainty on ω_a in the Run-2/3 result. This systematic was largely due to a distortion in the muon momentum reconstruction, which arises from an injection time dependence of the stored beam momentum caused by the varying strength of the injection kicker magnet.

We developed and implemented the Minimally Intrusive Scintillating Fiber (MiniSciFi) detectors with the goal to directly measure the stored beam with minimal disturbance, using 3 250 µm diameter scintillating fibers read out by Silicon photomultipliers. Simulations and data showed that the MiniSciFi causes an inward beam drift of less than 0.5 mm/µs and a lifetime reduction of the muon beam of less than 1.5%. A special measurement program in Run-6 used the MiniSciFi to characterize the *t*-*p* correlation and cross-check the indirect tracker and calorimeter beam measurements. Two detector configurations (Fig. 2.4-1) targeted distinct purposes: The horizontal fiber configuration sampled the circulating beam intensity, from which the momentum is reconstructed via a "fast rotation" frequency analysis. The vertical fiber configuration sampled the beam intensity via a radial scan to measure the horizontal beam profile over time in the muon fill, with an absolute position precision of 0.25 mm. MiniSciFi measurements have helped deepen our understanding of the beam dynamics in the $g-2$ storage ring in a variety of ways.

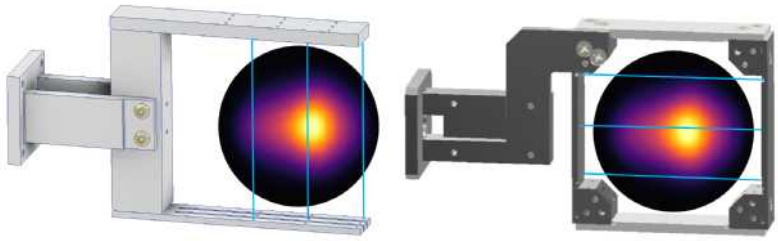

Figure 2.4-1. Vertical (left) and horizontal (right) MiniSciFi detector designs, overlaid with the transverse stored muon beam profile reconstructed by separate indirect tracking detectors.

Effects of the *t*-*p* correlation are better understood as a result of MiniSciFi measurements. The *t*-*p* distribution was directly mapped in time slices by scanning the kicker delay over a range of ±100 ns. At each delay the horizontal (H) MiniSciFi measured the stored beam momentum as a function of injection time relative to the kicker. To create sharper time slices, the injected muon bunches were shortened using an upstream proton abort kicker (Fig. 2.4-2). The finite-width short bunch shape then had to be unfolded from the measured distribution to recover the *t*-*p* storage efficiency (Fig. 2.4-3), from which the stored *t*-*p* distribution can be determined for any injected muon bunch. This method provides an independent distortion-free determination of the momentum distribution and corresponding electric field correction. Systematics for this method are being evaluated so that it can be meaningfully compared with existing methods. The short bunches also reduce the distortion in the Fourier fast rotation (FR) frequency analysis from the *t*-*p* correlation by selecting a narrower injection time width. With the reduced correlation effect, the short bunches improve the agreement between the Fourier FR reconstructed momentum and the independent "CERN extended" time-domain fit which is not distorted by the correlation, from a relative difference in the

mean momentum of 2e−4 with nominal bunches to 1e−4 with short bunches. Vertical (V) MiniSciFi measurements also resolved a long-standing discrepancy between the horizontal beam profile mean measured by the trackers and the beam equilibrium radius determined from FR analysis of calorimeter data. Comparing V-MiniSciFi measurements from nominal and short bunches showed that the discrepancy is caused by the t-p correlation and shrinks with short bunches (from 1.2(2) mm to 0.2(2) mm), confirming that both views of the beam are consistent when the correlation is eliminated.

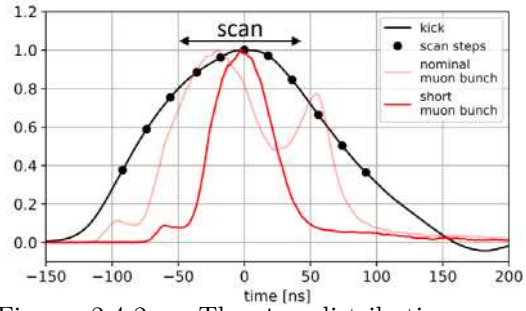

Figure 2.4-2. The t-p distribution was mapped with shortened injected muon bunches by scanning the kicker delay time relative to the muon injection time.

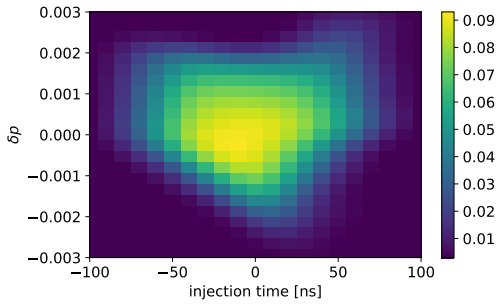

Figure 2.4-3. The reconstructed t-p storage efficiency encodes the correlation between the stored muons' injection time and momentum, from which the electric field correction can be determined.

H-MiniSciFi measurements also revealed the presence of a previously-unknown correlation between momentum and vertical (y) position in the stored beam aperture. The individual fibers at different y positions measure different momenta (Fig. 2.4-4). This p-y correlation was corroborated with both Fourier FR and CERN-ext momentum analyses of the H-MiniSciFi fibers and of y-sliced tracker data. Independent of any momentum reconstruction, the correlation is also seen in the y-dependence of the horizontal beam profile mean position, as the muons' momenta determine their equilibrium radii. Tracker data also showed that this correlation was present prior to Run-6. The Geant4-based $g-2$ ring simulation does not predict such a correlation. Initial studies suggest that the effect depends strongly on the vertical phase space of the injected beam. The simulation team is now using tracker data to check the vertical phase space input, which had not been fully validated before. The beam dynamics team is also investigating whether the p-y correlation will impact the ω_a corrections.

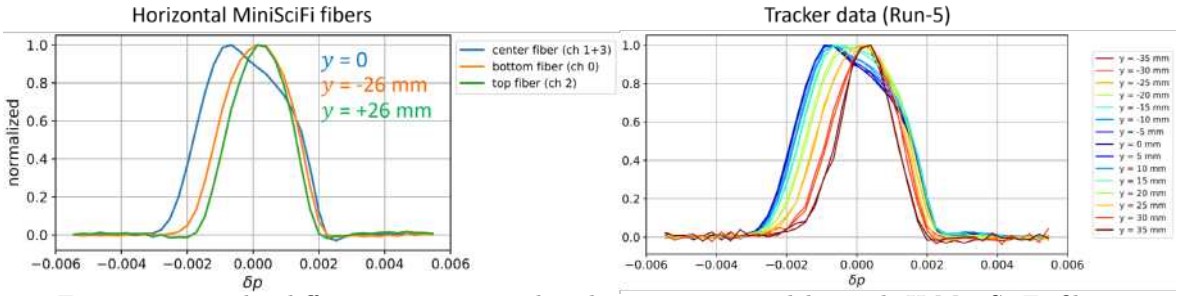

Figure 2.4-4. The different momentum distributions measured by each H-MiniSciFi fiber (left) indicates a correlation between y position and momentum, which is also seen in y-sliced tracker data (right). The momenta here were reconstructed using the Fourier FR method.

Unlike the trackers and calorimeters, the MiniSciFi detectors observe all charged particles present in the ring. The beamline selects nominal-momentum particles, so their velocities depend on their masses. Particles circulating in the ring can therefore be identified and separated by their cyclotron frequencies, which vary in proportion to their velocities. MiniSciFi frequency spectra (Fig. 2.4-5) show the presence of stored deuterons, which had previously been observed in the calorimeters only after the electric quadrupoles switched off after each muon fill. Because they are separated in the frequency domain, non-muon particles do not affect the Fourier FR muon momentum analysis of MiniSciFi data. Further, V-MiniSciFi measurements observed two beam populations with initial horizontal beam centroids which evolve independently. The stored deuterons become dominant as the muons decay; a fit to the beam centroid over time indicates that this transition occurs around 250 µs.

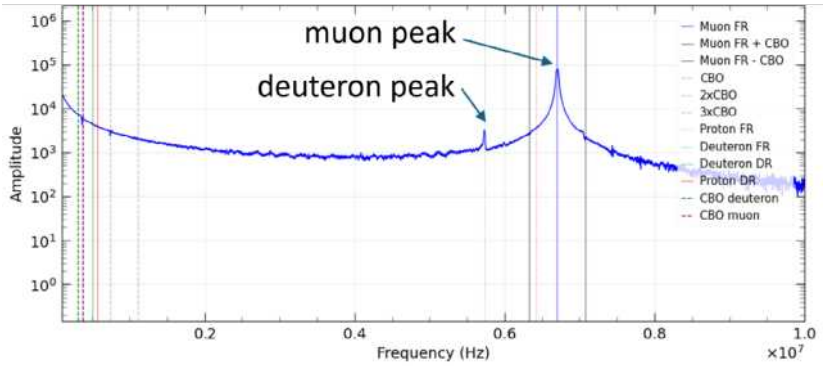

Figure 2.4-5. The FFT of summed signals from all fiber positions in a V-MiniSciFi scan has a dominant peak at the muon cyclotron frequency, and a relatively smaller peak at the deuteron cyclotron frequency indicating the proportional presence of deuterons in the circulating beam.

MiniSciFi direct beam measurements cross-checked and validated the indirect tracker and calorimeter beam measurements, independent of detector acceptance effects. Horizontal beam profiles measured with the V-MiniSciFi showed good agreement with the acceptance- and resolution-corrected tracker profiles (Fig. 2.4-6), and provide a basis to investigate subtle tracker acceptance effects and validate simulations. Time window fits of the beam profile

mean confirmed an unexpected nonlinear evolution of the horizontal beam oscillation observed by the trackers, which has to be modeled realistically in the ω_a fit function. Further, momentum distributions from Fourier FR and CERN-ext analyses of H-MiniSciFi data and calo data show good agreement (Fig. 2.4-7). The fibers measure y-dependent momentum distributions, but the sum of the fiber signals sufficiently represents the full beam population; this approach was cross-checked with y-sliced tracker data. Fourier FR analysis of summed V-MiniSciFi data from a full radial scan also agreed well with calo results, within 0.6 mm in the mean and width, although this was not among its original analysis goals.

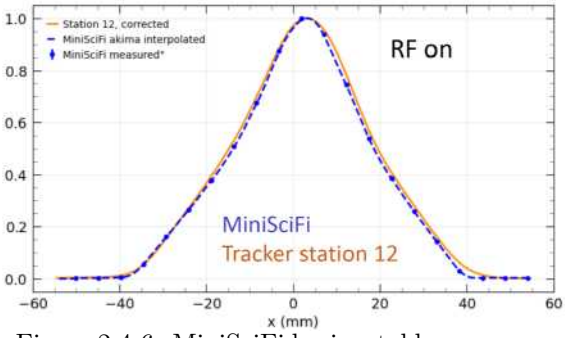

Figure 2.4-6. MiniSciFi horizontal beam profiles agree well with tracker profiles; the difference of 0.5(2) mm in the mean is within the tracker alignment uncertainty of 0.6 mm. The relatively small difference of 0.5(1) mm in the width may indicate an issue with the tracker corrections.

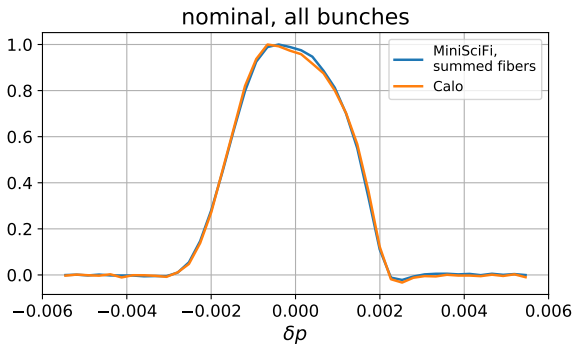

Figure 2.4-7. The momentum distribution reconstructed from H-MiniSciFi data agrees well with that from calorimeter data (here using the Fourier fast rotation method), within $\sim$ 5e−6 in the relative mean and width.

The MiniSciFi detectors made extensive special measurements which give a direct view of the stored muon beam, which was previously understood primarily via indirect measurements by the tracker and calorimeter detectors. As a result, the t-p correlation is better characterized, a previously-unseen p-y correlation was discovered, and beam measurements by the trackers and calorimeters were largely corroborated.

PIONEER

2.5 Rare pion decays: PIONEER

D. W. Hertzog and P. Schwendimann

In Phase I the rare pion decay experiment PIONEER aims to measure the charged pion branching ratio

$$R_{e/\mu} = \frac{\Gamma(\pi \to e\nu(\gamma))}{\Gamma(\pi \to \mu\nu(\gamma))} \tag{1}$$

to a precision of 1×10^{-4}, thus providing an experimental measurement that matches the precision of the Standard Model prediction $R_{e/\mu}$ (SM) $= (1.2352 \pm 0.0001) \times 10^{-4}$ by Cirigliano and Rosell[1]. This will mark an improvement of the current PDG experimental average $R_{e/\mu}$ (Exp) $= (1.2327 \pm 0.0023) \times 10^{-4}$ precision by a factor of 20 and is an excellent test of lepton flavour universality.

In Phase II and III the goal is to measure the pion beta decay branching ratio

$$R_{\pi\beta} = \frac{\Gamma(\pi^+ \to \pi^0 e^+ \nu)}{\Gamma(\text{all})} \tag{2}$$

with an ultimate improvement of the experimental precision by a factor 10. This measurement offers a theoretically pristine way to extract $|V_{ud}|$ and thus offers a handle on CKM unitarity. The current uncertainty of $|V_{ud}^{\pi}|$ is dominated by the branching ratio measurement.

An improvement of the branching ratio measurement by a factor 3 would put it competitive with the current PDG value obtained from neutron decays. With a factor of 6, the precision would match the best measurements from neutron decays that ignore tensions between different neutron measurements. The ultimate goal of a factor 10 puts the measurement on par with the value obtained from super-allowed beta decays.

Both measurements are well motivated and provide sensitive probes independently of the specific details of the new physics beyond the standard model. Through quantum-loop corrections, a sensitivity to very high mass scales is reached.

To drive the development of this next-generation experiment, our group took the lead on the overall simulation and analysis efforts (Buat, Schwendimann). On the pion-stopping target side, we heavily support the electronics design and use our Van-De-Graaff accelerator to explore first prototypes for the ATAR (Braun, Kammel, Yang). In addition, significant efforts were made to prove the LYSO calorimeter option feasible. Apart from detailed lab tests and dedicated simulation efforts, a two-week test beam was conducted at PSI where a small 10-crystal array was investigated (Beesley, Hertzog, LaBounty, Schwendimann, Swanson). Moreover, we contribute significantly to the development of the beamline design (Kammel). In all efforts, CENPA lead engineer Roehnelt plays a crucial role in designing and fabricating small test stand equipment for prototype experiments as well as in advising on the overall detector design for the entire experiment.

[1] Phys. Rev.Lett. 99, 231801.

The Basics of the $R_{e/\mu}$ Measurement

For a particle at rest, the pion lifetime is 26 ns and the muon lifetime is 2197 ns. If the pion decays to a positron immediately, it follows the exponential decay spectrum in time and the positrons are mono-energetic at half the pions mass ($E_e^{\pi\to e} = 69.8\,\text{MeV}$. If the pion decays to a muon, that muon comes to rest within a short time ($\mathcal{O}(10\,\text{ps})$) and subsequently decays to a positron $\mu \to e\nu\bar{\nu}$. The energy of this positron is limited by the Michel endpoint ($0\,\text{MeV} \leq E_e^{\mu\to e} \leq 52.8\,\text{MeV}$). Those positrons also follow a different time spectrum defined by pion and muon lifetime.

Thus, the mono-energetic positron signature of $\pi \to e\nu$ events are well above the Michel spectrum and feature a distinct time spectrum. However, counting both event to the require 10^{-4} precision requires a very detailed investigation of events that got moved out of their native region. These include $\pi \to e\nu$ events with significant energy loss (Tail events), muons that decay within the first few ps before coming to rest and boosting the decay positron above the Michel endpoint (MuDIF events, prev. annual report), pile-up events or radiative events ((Sec. 2.5)sec:raddec) where the photon does not get accounted for properly.

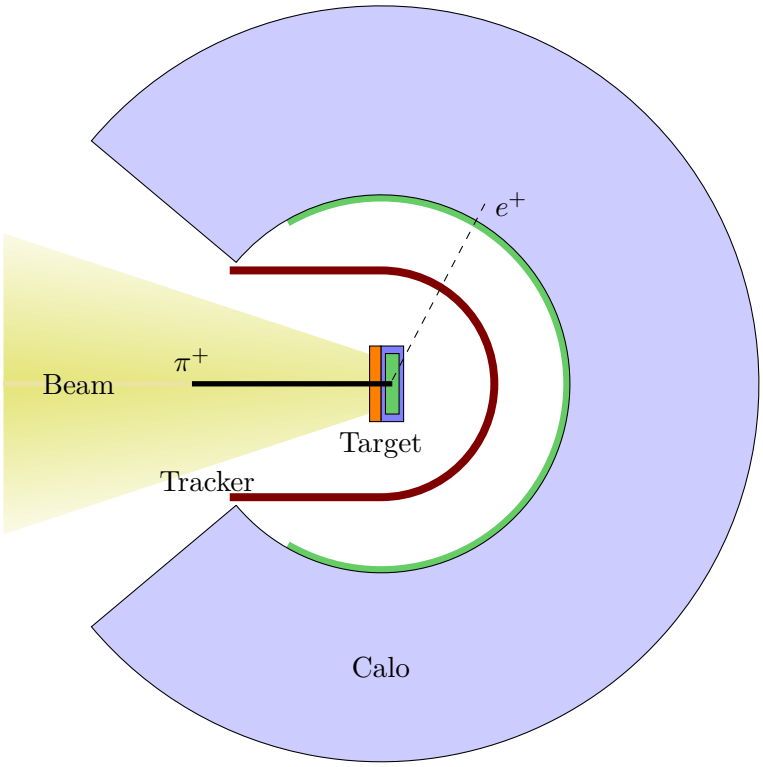

Figure 2.5-1. Sketch of the PIONEER Rare Pion Decay Spectrometer. Not to scale.

The mitigation strategies are as various as the characteristics of those perturbing events, most of which are rooted in the detector design sketched in Fig. 2.5-1. To reduce the impact

of tail events, a deep calorimeter is chosen to avoid leakage through the back. The depth was optimised based on extensive simulation studies by O. Beesley and reduced to 19 X_0. This balances depth leakage with albedo effects (front leakage) and scattering effects in target region materials. This keeps the fraction of tail events below 1 % of all $\pi \to e\nu$ events. To properly assess and correct for the tail events, the highly granular ATAR is used for a dedicated measurement. Similar strategies are deployed to deal with muon decay in flight. More details are presented in (Sec. 2.6).

Radiative decays and pile-up events both involve more than one particle entering the calorimeter. Thus, it is mandatory for the calorimeter to identify and resolve such topologies. The LYSO calorimeter presented in (Sec. 2.8) naturally satisfies this requirement because of its intrinsic segmentation. The details of extensive prototype testing are reported in (Sec. 2.10). Detailed mitigation strategies for radiative decays can be found in (Sec. 2.9).

2.6 PIONEER physics prospects

Q. Buat, J. Yang, P. Schwendimann, and B. Taylor

The prospects of the PIONEER experiment are described in Sec. 2.5. Progress was made on the LFU test, the piBeta measurement. In addition, the prospect of measuring radiative decays was investigated (Sec. 2.9).

Re/mu sensitivity analysis

Numerous improvements have been implemented in the simulation framework and the proto-reconstruction strategy as described in (Sec. 2.8).

These improvements enable a large-scale simulation exercise to generate samples with a size representative of the expectations from PIONEER Phase I. This exercise has been limited to an idealistic beam and was meant to understand the capability of the main PIONEER system to conduct the Phase I measurements.

Fig. 2.6-1 illustrates the reconstructed energy spectrum for events collected in a time window of 800 ns ($[-300, 500]$ ns around the time of arrival of the triggering pion). Events are classified into six categories:

	Sample name	Description
1	$\pi - e\nu$	Pion decay to positron and neutrinos
2	π [DAR] - μ [DAR] - e	Michel events where the pion and the muon decay at rest in the active target
3	π [DAR] - μ [DIF] - e	Michel events where the pion decays at rest in the active target while the muon decays in flight
4	π [DIF] - μ [DAR] - e	Michel events where the pion decays in flight in the active target while the muon decays at rest in the active target
5	pile-up	Events where the calorimeter records deposits from at least two positrons separated by less than 10 ns
6	rbm	'Recent' beam muons. Events where the pion decays before reaching the degrader and the muon is the incoming triggering particle of the event

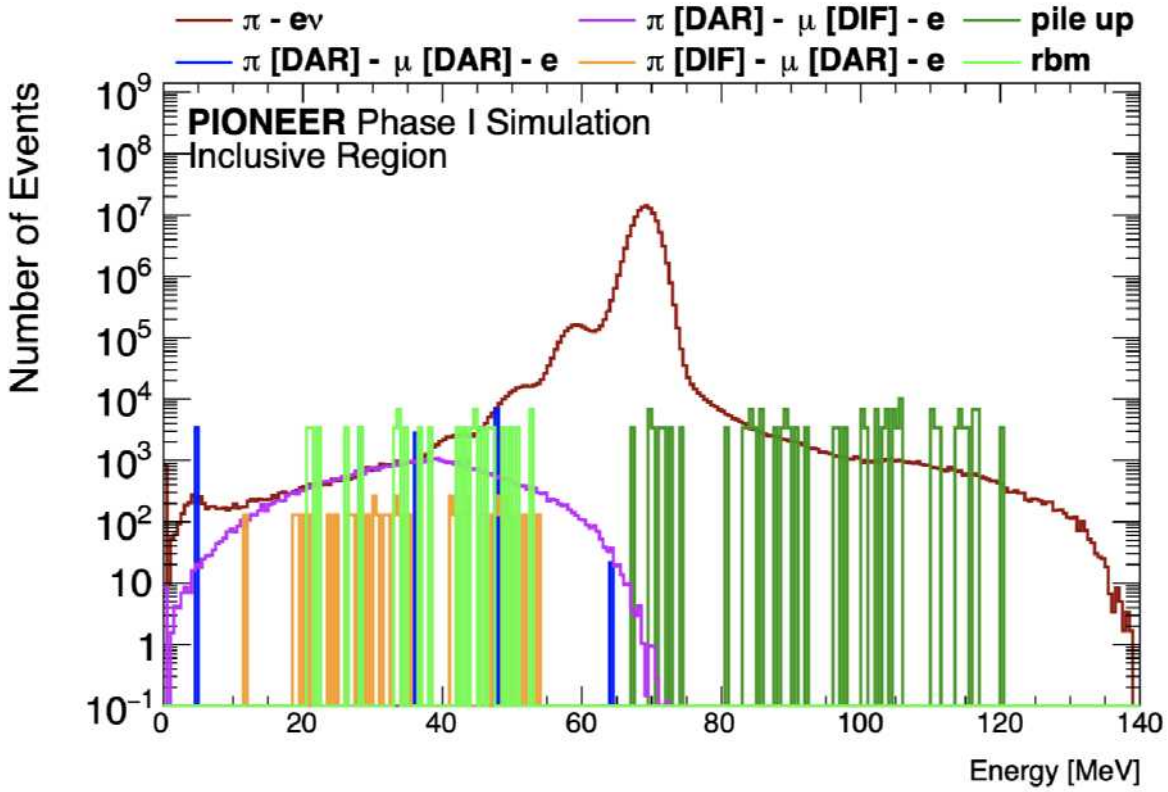

Figure 2.6-1. Energy spectrum of the events collected in a time window of 800 ns ($[-300, 500]$ ns around the time of arrival of the triggering pion).

The simulated samples were scaled to represent the Phase I expectations, the $\pi - e\nu$ sample was set to 2e8 and the other samples scaled accordingly. The size of the underlying simulations have been adjusted to make sure the samples are large enough to represent the statistical power we expect to achieve with the actual data.

Then, the analysis flow was performed on each sample. It consists on defining three regions: High Energy Bin, Low Energy Bin and TFA. They are defined in Table 2.6-1.

	Region name	Description
1	High Energy Bin	Events selected with minimum cuts with a energy measured above 57.5 MeV
2	Low Energy Bin	Events selected with minimum cuts with an energy measured below 57.5 MeV
3	TFA	Tail Fraction Analysis selection. Events selected with a series of cuts to reveal the low energy tail of the $\pi - e\nu$ sample

Table 2.6-1. Pioneer Phase I analysis regions.

The main challenge in defining the high-energy and low-energy bins is to be able to estimate the relative acceptance of the $pi - e\nu$ and $pi - mu - e$ events with a precision of 0.01 %. To achieve this, the fiducial volume must defined in the least biased way possible. The definition in the current analysis flow relies on the pion stopping position in the ATAR while the direction of the positron is still evaluated using the truth information of the Geant-4 record. Nevertheless, the stability of the acceptance was estimated to be 0.9991±0.0009 consistent with unity at ≈ 10^-3 precision-level. This indicates that the current definition is on the right track but the result needs to be confirmed with more statistics to reach 0.01 %. Additionally work will need to be carried to perform the most challenging part of this selection: the definition of the positron direction. Some preliminary studies using only a few hits near the pion stop in the ATAR showed promising results. The dominant biasing effect seems to be the anihilation in flight which is an energy-dependent process and introduce a bias as the positron from a $\pi - \mu - e$ event has a softer momentum than a positron from $\pi - e\nu$ event.

Defining the selection of the tail fraction analysis is also one of the main challenges of the PIONEER Phase I measurement, as the size of the tail fraction and its uncertainty were the main limitation of the PIENU experiment aside from the collected sample sizes. This challenge has been thoroughly investigated since the beginning of the PIONEER effort with major contributions from the UW group. The current analysis achieves a purity of the $\pi - e\nu$ component of 91 % in the low energy bin of the TFA. With a 9 % bacgkround contamination, the background components would be measured with a 15 % precision to reach the targeted sensitivity. However, the current analysis maintains a very high selection efficiency of 56 %, well above the O(1 %) needed to satisfy the statistical needs of the targeted sensitivity. This leaves ample room to better tune the selection criteria and reach the desired ≈ background-free definition of the TFA region. Additionally it is critical to monitor the bias of the event selection on the Tail Fraction itself. In the latest simulations, the tail fraction was measured from the TFA analysis to be (0.690±0.001) % while the true tail fraction from the unbiased selection of the low and high energy bins is (0.7061±0.0008) %. Therefore, the current analysis introduces a bias of ≈2 %. Ongoing studies are being carried out to understand the origins of these biases. The selection criteria are now applied inclusively, while a parameterization depending on the direction of the positron in the PIONEER detector would likely alleviated this discrepancy.

From the output of the simulation, templates of the time distributions are built for each of the sample in the high- and low-energy bins. These templates are shown in Fig. 2.6-2.

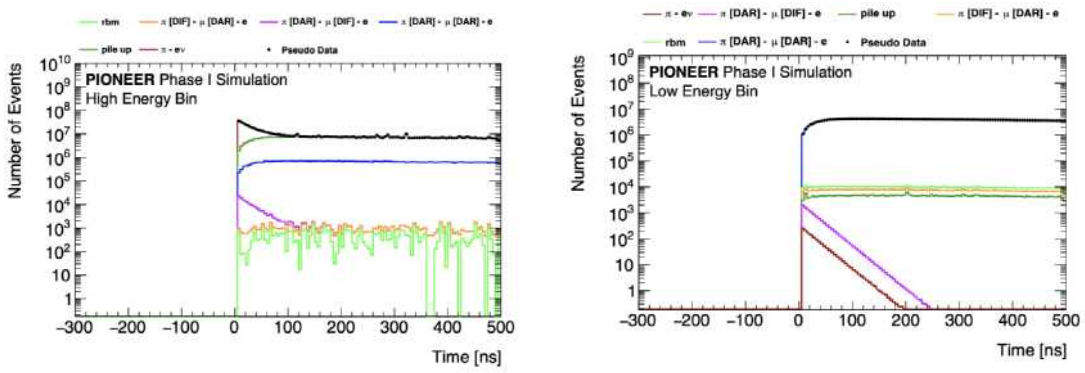

High Energy Bin Low Energy Bin

Figure 2.6-2. Time distribution in the low and high energy bin. The time is defined as the difference between the calorimeter timing of the positron and the time of the pion entrance in the degrader.

A binned likelihood was built using the **HistFactory** framework to perform a simultaneous fit in the High Energy Bin, the Low Energy Bin and the TFA region. In the High-Energy Bin and in the Low-Energy Bin, binned templates of the time distribution are used as input to the likelihood while in the TFA region is sub-divided in a low-energy and high-energy one and set up as a single-bin counting experiment.

A simultaneous fit is performed where the parameter of interest is defined as

$$R_{e/\mu} = \frac{N^{HE}_{\pi-e\nu}}{N^{LE}\pi - \mu - e}(1 + c_T) \tag{1}$$

with $c_T = N^{LE,TFA}_{\pi-e\nu}/N^{TFA}_{\pi-e\nu}$

The stack of simulated samples where the statistical uncertainty is replaced by the Poisson error on each bin count is used to define a pseudo-data dataset, the so-called 'Asimov' dataset. Fitting this data set provides an estimate of the sensitivity of the PIONEER experiment to $R_{e/\mu}$. The results are reported in Table 2.6-2.

Source	$R_{e\mu} \times 10^4$	$\Delta(R_{e\mu}) \times 10^4$	$\Delta(R_{e\mu})/R_{e\mu}(\%)$
PIONEER	1.23521	0.000203863	0.017
PIONEER (without c_T)	1.22656	0.000140104	0.011
PIENU Experiment	1.2327	0.0023	0.19
SM Expectations	1.23524	0.00015	0.012

c_T (%)	$\Delta(c_T)$ (%)	$\Delta(c_T)/c_T(\%)$
0.69	0.01	1.7

Table 2.6-2. Results of the binned likelihood fit on the Asimov dataset. The table also reports the results of the PIENU experiment and the current best theoretical estimate of $R_{e\mu}$.

The study demonstrates that PIONEER is on track to reach its target sensitivity of 0.01 % precision on $R_{e/\mu}$. We have developed the full analysis chain from event generation to the extraction of the parameter of interest using a simultaneous likelihood fit over all the regions of the analysis. The results rely on a simplistic digitization model and a proto-reconstruction still relying on the truth Geant4 record. One of the major next milestones of the effort is to evolve this digitization model to a more realistic one and employ a reconstruction flow where each step could run on real data.

Additionally, the work relies on an ideal beam and work is ongoing to design a realistic beam model along with the needed auxiliary entrance veto detectors to flag and suppress beam-related backgrounds.

Using the PIONEER experiment apparatus to measure pion beta decay: $\pi^+ \to \pi^0 e^+ \nu_e$

The goal of Phase II of PIONEER is to measure the pion beta decay ($\pi^+ \to \pi^0 e^+ \nu_e$) branching ratio, which can be used to determine $|V_{ud}|$. Currently, the first row of the CKM quark mixing matrix has a 3σ tension with unitarity. Although the extraction of $|V_{ud}|$ from pion beta decay is theoretically clean, the uncertainty on the pi-beta branching ratio dominates the overall uncertainty of $|V_{ud}^{\pi}|$ currently making it noncompetitive with extraction from superallowed beta decays and neutron decays.[1] The current state of these measurements and the predicted values from the improved pi-beta measurements are shown in Fig. 2.6-3.

[1] V. Cirigliano and M. Hoferichter, The case for a precision measurement of $\pi^+ \to \pi^0 e^+ \nu_e$ (2024).

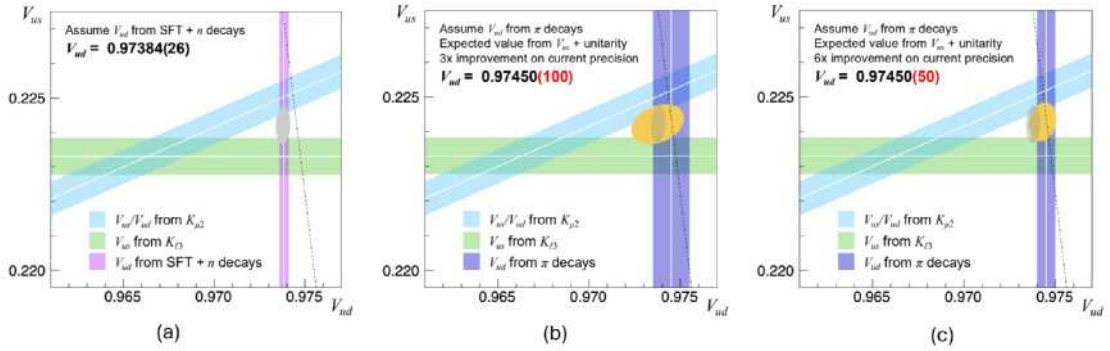

Figure 2.6-3. (a) Current State of 1st-Row CKM Measurements. $|V_{ud}|$ is determined from the best measurements of Superallowed Beta Decays and neutron decays. The dashed line shows unitarity and the grey oval denotes the fit with $|V_{us}|$ measurements.
(b) 1st-Row CKM with $|V_{ud}|$ determined by pi-beta with 3x improvement. $|V_{ud}^{\pi}|$ is assumed to agree with unitarity. The yellow oval shows the fit with $|V_{us}|$ measurements. The grey oval is left for comparison with (a).
(c) 1st-Row CKM with $|V_{ud}|$ determined by pi-beta with 6x improvement.[1]

PIONEER has an initial goal of 3 times improvement on the uncertainty of the pi-beta branching ratio, eventually aiming for a factor of 6 improvement. This would make the extraction of $|V_{ud}|$ from the pi-beta decay comparable to the extraction from neutron decay.[1]

To sufficiently decrease the statistical uncertainty for an overall factor of three improvement in uncertainty, 6.25×10^5 pion beta events are needed. To accomplish this, the PSI $\pi E5$ beamline will be run at 10^7 pions per second. This would necessitate a higher momentum than Phase I, about 85 MeV/c, and a larger momentum bite, about $\frac{\Delta p}{p} = 3\%$. The PIBETA experiment ran at 115 MeV/c.[1] To achieve greater precision, an even higher rate may be necessary. Dealing with pileup at high rates is the chief concern for a pion beta decay measurement.

To make this measurement, a segmented calorimeter with a small Molière radius is essential. Segmentation is necessary to distinguish the gammas and separate their signals from any coincident charged particle signals elsewhere in the calorimeter. A dense calorimeter is necessary to limit pileup events in which a charged particle deposits energy in the same region and at the same time as one of the pi-beta gammas. Given that 95% of the energy is contained in two Molière radii, we can calculate the percent of the surface area used by the calorimeter, as seen in Table 2.6-3. Since the probability of pileup is over six times higher in a liquid xenon calorimeter, identifying pion beta events would be much more difficult. Thus, a pion beta decay measurement is only being considered using the LYSO calorimeter option.

[1] Počanić, D. et al., Precise Measurement of the $\pi^+ \to \pi^0 e^+ \nu$ Branching Ratio, Phys. Rev. Lett. 93, 181803 (2004).

Calorimeter	Inner Radius	Molière Radius	Calo Surface Area*	pi-beta Area	Overlap Probability
PIBETA CsI	26 cm	3.5 cm	8495 cm^2	308 cm^2	3.6%
PIONEER LYSO	15 cm	2.07 cm	2827 cm^2	108 cm^2	3.8%
PIONEER LXe	15 cm	5.22 cm	2827 cm^2	685 cm^2	24.2%

Table 2.6-3. Comparison of calorimeters and their associated spatial pileup probabilities for pion beta decay. Note the similar probabilities of the PIBETA experiment's calorimeter and the PIONEER LYSO design.
* The Calo Surface Area includes the entire sphere, including regions without any calorimeter material.

Since the neutral pion resulting from the pion beta decay has an extremely short lifetime (8.5×10^{-17} s), a perfect calorimeter should see two, nearly back-to-back time coincident gammas, each with energy about 65 MeV. An example of this is shown in Fig. 2.6-4a.

The energy of the two gammas and the opening angles can be used to calculate the invariant mass of the neutral pion.

$$134.98 \text{ MeV/c}^2 = \sqrt{2E_1E_2(1-\cos\alpha)} \tag{2}$$

The PIONEER apparatus will also include a charged particle tracker. These can be used to identify gammas, and the invariant mass calculation can identify pion beta events with very high specificity. The PIONEER calorimeter has excellent timing resolution (Fig. 2.6-4b) but the current GEANT4 PIONEER simulation shows a large smearing in the calculated invariant mass (Fig. 2.6-4c). This is primarily due to the energy tail fraction and is not significantly dependent on the angular precision, so a correction could be made. The PIONEER tail fraction is smaller than the PIBETA tail fraction because the PIONEER calorimeter is deeper (19 radiation lengths) than the PIBETA CsI calorimeter (12 radiation lengths). Additional data from the ATAR could also increase the confidence in pi-beta identification, since the positron is usually observed.

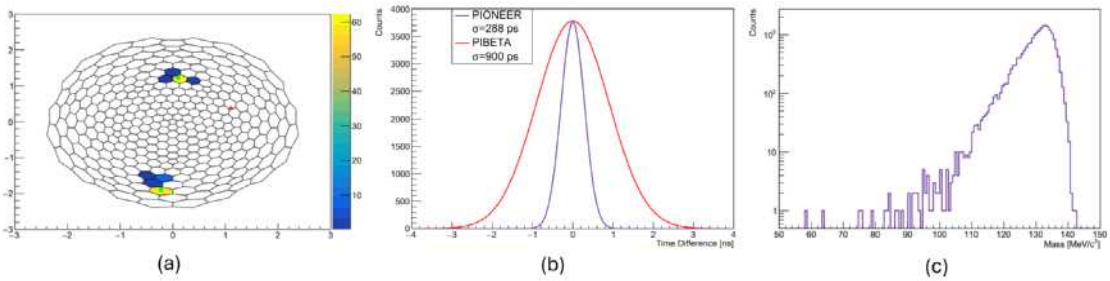

Figure 2.6-4. (a) An example of energy deposits of a pi-beta event in the PIONEER calorimeter. The dots denote the truth values of the momentum of the daughter particles; green denotes gammas and red denotes the positron, which does not deposit energy in the calorimeter.
(b) The distribution of time differences between the two pi-beta gamma energy clusters. The red line depicts the PIBETA time resolution (σ = 144 ps). The purple line depicts PIONEER time resolution (σ = 900 ps).
(c) The invariant mass spectrum of pi-beta events in the PIONEER calorimeter.

The only pion interaction that produces a similar signal is pion charge exchange $\pi^+ + n \rightarrow \pi^0 + p$. This interaction occurs over 1000 times more often than pion beta decay, but can only

occur when the pion has sufficient momentum to overcome the Coulomb barrier. However, these events occur within a nanosecond of the pion arrival (Fig. 2.6-5a) and thus can be removed by a time cut with minimal loss of pion beta decay events. This is one of the primary areas in which PIONEER will improve upon the previous PIBETA experiment. The PIBETA experiment made a hardware cut around 10 ns after the pion entrance. The uncertainty in the time of this cut resulted in a systematic uncertainty of 0. 26% in the fraction of pi-beta events in the observed window.[1] Due to the improved time resolutions of our calorimeter and triggers and increased technological capabilities, PIONEER will be able to remove charge-exchange events via a software cut at 2 ns (or possibly 1 ns). Since PIONEER will run at a much higher rate than PIBETA, it would also be necessary to cut ± 2 (or 1) ns around each RF with a pion arrival. (Since charge exchange occurs in flight, events must be cut whenever a pion arrives, regardless of DTAR or ATAR signals.) Depending on the size of the cuts necessary and the placement of the end of the window, 77% to 95% of pi-beta events can be observed when running at 10^7 Hz. Since pi-beta events can be easily distinguished from the Michel background (discussed below), it does not currently seem necessary to limit the collection time to the first 50 ns. If the full time window (to 250 ns) is considered, a ± 2 ns cut gives 90% of the events. Thus, PIONEER can collect a much larger percentage of pion beta events than PIBETA and determine the measured fraction to a very high degree of accuracy. The only sources of uncertainty in this timing acceptance are the pion lifetime and our timing resolutions, both of which are very small. This eliminates the largest experimental systematic uncertainty of the previous experiment. It may also be possible to measure the rate of charge exchange in our system and subtract those events from our pi-beta event count, as seen in Fig. 2.6-5b.

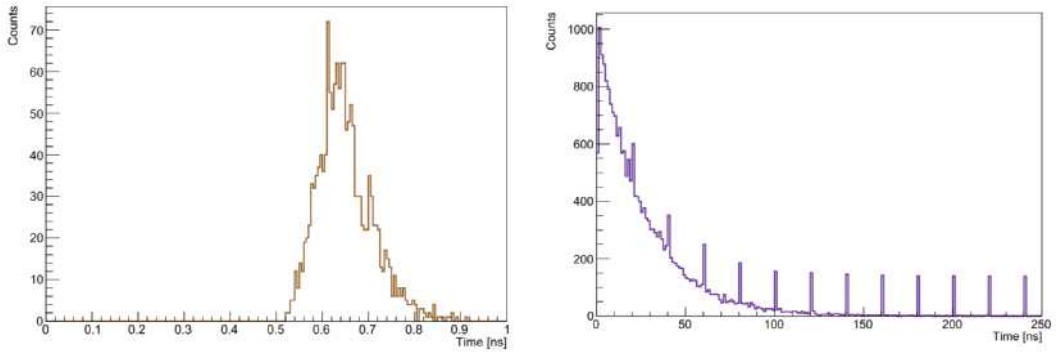

Figure 2.6-5. (a) Time of Pion Charge Exchange Energy Deposits. The actual time resolution of the LYSO calorimeter is slightly worse than the simulation, so the time cut may need to be made at 2 ns rather than 1 ns.
(b) Time spectrum of pi-beta decays with charge exchange overlay. The rate of charge exchange is not to scale - it would be much larger. The charge exchange probability is the same at each RF period. Thus, a measurement could be made and the number of charge exchange events could be subtracted from the pi-beta spectrum without removing any pi-beta events.

Pion beta decay can be easily distinguished from the Michel pileup using the charged particle tracker and the invariant mass. Using the current GEANT4 PIONEER simulation,

no Michel pileup events were identified as pion beta events when requiring an invariant mass greater than 90 MeV/c^2, an opening angle between the clusters greater than 130°, a time difference between clusters less than 0.8 ns and an event time less than 250 ns. Note that due to the limitations of the current simulation analysis, this analysis was performed at a rate of 10^6. This analysis did not include information from the tracker, which will improve the specificity, especially when the rate is increased. The same conditions identify 99.94% of pion beta events, where a few are lost due to the energy tail. The calculated invariant mass for charge exchange events, Michel pile-up events, and pi-beta events are shown in Fig. 2.6-6.

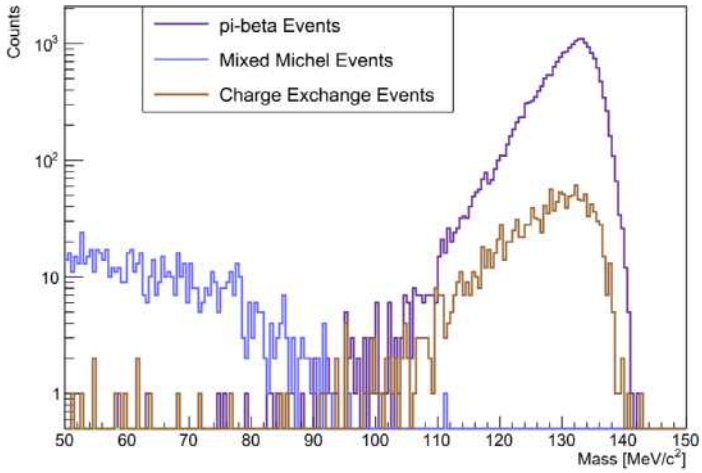

Figure 2.6-6. Calculated invariant mass of Michel pileup (blue), charge exchange (orange) and pi-beta (purple) events. The relative rates of Michel pileup and charge exchange to pi-beta are not to scale. Note the minimal overlap between the Michel pileup and pi-beta mass spectrums.

The presence of a Michel background usually does not hinder the identification of a pion beta decay event. Since the rate of two concurrent pi-beta events is infinitesimal, it is reasonable to look for the combination of clusters that gives an invariant mass closest to 134.98 MeV/c^2. This, coupled with a charged particle veto, makes the identification of pion beta decay simple, with one exception. When a charged particle enters the calorimeter in the same location and at the same time as a pi-beta gamma, the pion beta event will not be identified as such. This occurs in about 2.3% of the pion beta events at 10^7 Hz and increases with the beam rate. Although this pile-up prohibits the standard pi-beta identification, the resulting calorimeter pattern does not match other event types either. Such an event would have the signal of an approximately 65 MeV neutral particle and a >65 MeV charged particle (the pi-beta gamma energy plus the Michel energy) opposite from each other. Since the gamma has higher energy than typical radiative decays and the combined calorimeter cluster will have an unusually high energy (especially for high-energy Michels), these events (or a subset of them with high-energy Michels) could be identified and a correction could be made.

The resulting pion beta decay count must be normalized to obtain a branching ratio. The PIBETA experiment normalized to a count of $\pi^+ \to e^+\nu_e$ (pi-e-nu), which has a geometric

and timing acceptance similar to pi-beta. This is nominally the plan for PIONEER. Phase I will decrease the uncertainty of the pi-e-nu branch by a factor of 10, making it a subdominant contribution to the calculation of the PIBETA branch. Furthermore, the PIONEER ATAR will greatly improve the determination of the pi-e-nu tail, a systematic uncertainty of 0. 19% in the PIBETA experiment.[1] However, the feasibility of identifying pi-e-nu events at 10^7 Hz or higher has not yet been investigated. Alternatively, a normalization to the total pion count has been proposed.

The PIONEER apparatus has many advantages over the previous PIBETA experiment. Due to our high-precision ATAR, our pion-stopping distribution will be extremely well defined. This allows for a very small geometric acceptance uncertainty. Modern software and improved time resolution will result in hard time cuts, essentially removing the very large systematic uncertainty in the PIBETA experiment from the opening of the time window. The ATAR and the experience of Phase I will greatly improve the precision of the pi-e-nu tail fraction needed for normalization. Other necessary corrective factors, such as the pion lifetime and the Dalitz decay branching ratio, have been improved by other experiments since the last pi-beta measurement. Modern simulations will also improve the photonuclear correction uncertainty (0.1% in PIBETA[1]). Thus, 0.21% uncertainty (factor of 3 improvement) results from a measurement with less than about 0.09% systematic uncertainty in the pi-beta count, normalization, and photonuclear corrections. A factor of 6 improvement will require further reduction of these systematics to about 0.04% or less. Given the above discussion and the possibility of correcting for the pi-beta tail, a sufficiently low systematic uncertainty on pi-beta identification is reasonable.

With a geometric acceptance of about 50% resulting from the front opening of the calorimeter, a time acceptance of about 80% to eliminate charge exchange, 80% uptime and a beam rate of 10^7 Hz, 6.25×10^5 pion beta events can be collected in 7.1 months of running. This gives the necessary statistics for a factor of 3 improvement in the overall uncertainty. To achieve a factor of 6 improvement, 2.25×10^6 pion beta events can be collected in 25.6 months of running at 10^7 Hz. It does not appear that a higher rate significantly hinders the identification of pi-beta events. Thus, the feasibility of a higher rate is determined by the normalization method. If a high-rate normalization is possible, a factor of 6 improvement of the pi-beta branching ratio could be accomplished in under 3 years.

ALPs generator

In addition to the $R_{e/\mu}$ measurement in phase I and the $R_{\pi\beta}$ measurement in phase II and III of the PIONEER experiment, the data obtained can be used to look for the direct signature of light BSM physics. In order to investigate the PIONEER sensitivities to such models, they have to be included in the simulation, reconstruction and analysis. This has been done for ALPs in collaboration with theorists from UCSC. Based on the theorist's input, dedicated decay channels with differential decay rates were implemented where the ALP mass as well as its decay channels and lifetime are parameters that can be set at runtime. Currently, the

following channels are implemented

$$\pi \to ea\nu$$
$$\pi \to \mu a\nu$$

where the ALP a decays either to $\gamma\gamma$, ee or invisibly. While the generator has been implemented, the full simulation, reconstruction and analysis is a task to be taken care of in the future.

2.7 ATAR development and CENPA test run

S. Braun, Q. Buat, P. Kammel, and J. Yang

The active target (ATAR) is crucial to provide 4D tracking and energy measurements of the full event reconstruction from stopping pion to muon to positron decay chain. Low-gain avalanche detectors (LGADs) will be used as a technology choice, those are thin silicon detectors with an internal gain that are able to measure minimum ionizing particles (MIP) with a small time resolution (<20ps). For our experiment, we need a large dynamic range in order to detect energy deposits from positrons (MIP, 10s of keV) up to pions and muons up to 30MIPs (several MeV). LGAD gain suppression has been observed experimentally with large energy deposits and needs to be fully understood in order to be able to detect and separate these close-by hits. The gain suppression comes from the shielding of an electric field in the gain layer, which increases with the density of the deposited charge and a higher sensor gain (adjustable with applied bias voltage).

In July and August 2023 we had about 3 weeks of beam time using the Tandem accelerator at CENPA to study the LGAD response to MeV-range energy deposits from a proton beam. We used protons with 1.8 and 3 MeV energy and used a Rutherford-Backscattering (RBS) setup for acceptable particle rates ($\approx 1kHz$). The proton beam is scattered off a 110nm thick gold foil target, and the board is mounted on a rotating arm at 110-degree angle with respect to the incoming beam. The setup was optimized using SIMNRA simulations. The LGAD and PIN sensors are mounted on a fast analog single-channel electronic board (around 2 GHz bandwidth) and readout using an external amplifier and digitized with a 1 GHz bandwidth digital scope. The board is mounted on a rotation device to change the board angle with respect to the gold foil target, which can be controlled remotely. The whole setup is located in a vacuum chamber directly connected to the beamline. External power supplies provide low voltage to the amplifiers and high bias voltage to the sensor via feedthroughs.

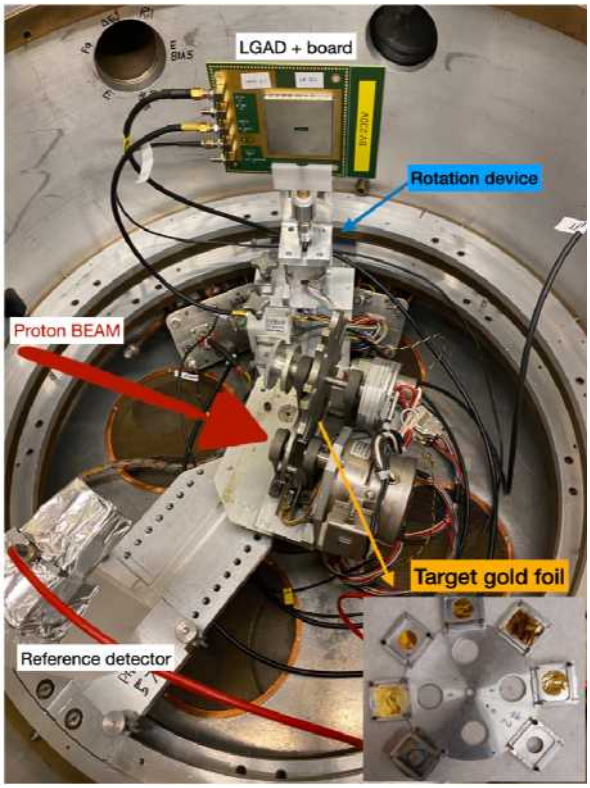

Figure 2.7-1. LGAD Testbeam setup in vacuum chamber at Tandem accelerator beamline.

Two single pad LGADs and a Hamamatsu Photonics (HPK) PIN with a thickness of $50\mu m$ and a geometry of 1.3x1.3 mm^2 were tested. The two LGADs have a different thickness of gain layer, the deeper gain layer has a larger gain. Those devices were tested as a function of bias voltage, incidence beam angle and proton energy. The simulated and measured charge deposit for the PIN device is shown in Fig. 2.7-2.
At 1.8 MeV, the proton always stops and deposits about 80fC of charge, whereas at 3MeV, the proton punches through at lower angles and stops at around 55 degrees, depositing 130fC. A MIP deposits around 0.5fC for the detector thickness therefore the protons correspond to 160MIP and 260 MIP at 1.8 MeV and at 3MeV respectively. For the two tested LGADs the results of the gain as a function of angle and bias voltage are shown in Fig. 2.7-3 left for 1.8MeV and right at 3 MeV. Here gain is defined as as the collected charge of the LGAD divided by the collected charge of the same-size PIN at the same run conditions. The gain increases for higher bias voltages and also with larger angle with respect to the incident beam angle up to 45-55 degrees, afterwards it decreases at higher angles. For zero degrees the charge density is the largest, therefore the gain suppression is largest thus the gain is lowest. The charge density is less for an angles track as the charged spread out over a larger area such the gain increases. For the largest angles the charge deposit is very close to the gain layer such that there is less lateral drift and the gain is suppressed. Both devices show a large gain suppression, which is higher for a larger bias voltage. The results of the testbeam were presented at conferences and also published in a paper (Sec. 2.12).

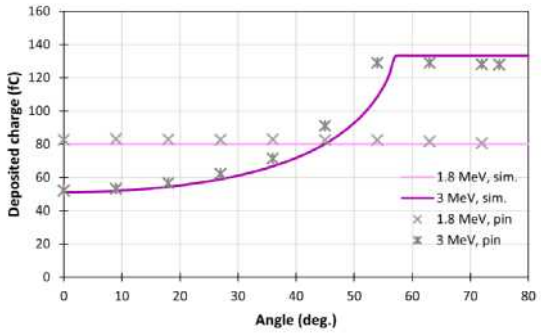

Figure 2.7-2. Simulated and measured charge deposit for PIN device as a function of incident angle for different proton energies.

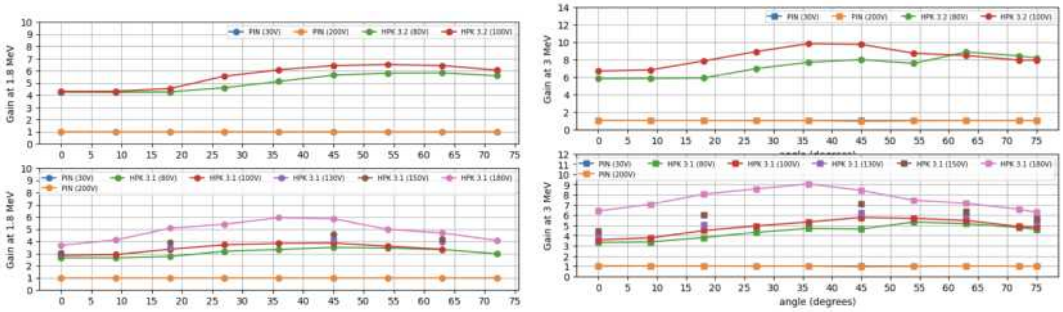

Figure 2.7-3. Gain as a function of angle for different bias voltages for proton energies of (a) 1.8 MeV and (b) 3 MeV, for HPK 3.2 (top) and 3.1 (bottom) LGADs.

In July 2024 we had another 3 weeks of beam time with a similar experimental setup, although much improved readout system, this time testing sensors from different producers FBK and BNL with a lower gain layer doping concentration and different thicknesses. Again those were tested at different energies and incident angles, which are summarized in Table 2.7-1. The idea is to investigate if the gain suppression can be reduced at a lower gain, in addition also thinned sensors were tested where the backside support wafer was partly removed which is closer to the planned LGAD prototype without any support wafer. We are currently analyzing the large amount of data and expect first results soon.

producer	LGAD/PIN	Wafer	thickness [μm]	energies [MeV]	HV [V]
FBK	LGAD	W1	50	1.8, 3	50,150, 250
FBK	PIN	W1	50	1.8, 3	50, 100, 400
FBK	LGAD	W8	100	6.5, 8	100, 200, 250, 300
FBK	thinned LGAD	W8	100	1.8, 3, 4.5	100, 200, 250, 350
FBK	PIN	W8	100	3, 4.5, 6.5	200, 300, 400
FBK	LGAD	W11	150	3.8, 5.5	200, 400, 600
FBK	PIN	W14	100	3.8, 5.5, 6.5	300, 500
BNL	LGAD		200	1.8, 3, 4.5, 5.5	200, 300, 400

Table 2.7-1. Summary of sensors tested in July 2024 test beam, FBK sensors are labeled by their wafer.

2.8 Simulation framework

P. Schwendimann, O. Beesley, Q. Buat, J. LaBounty, B. Taylor, and J. Yang

The simulation framework for PIONEER consists of four main building blocks.

- **Geometry Builder** A set of python scripts that define the geometrical shapes of the detector along with the corresponding material properties.
- **G4Pioneer** The Geant4 based event generation and tracking for PIONEER. It allows for a wide array of initial particle configuration and physics biasing to simulate dedicated rare events.
- **Detector Response** This part turns the Monte-Carlo truth into observable quantities expected after considering electronics response, digitisation windows, noise. It features a major bifurcation that allows waveform generation or produce directly reconstructed hits.
- **Reconstruction** The full collection of algorithms that turn waveforms into hits and clusters hits together to reconstructed and classified events.

Over a dozen of simulation developers and users from all over the world have been working on collecting the required input data, fine tune the internal parameters for algorithms and improve the output for easier analysing. As it is not possible, to cover all approximately 700 updates made, a selected collection is presented here as representation of the efforts ongoing.

Geometry Updates

The most notable geometry update was the implementation of an up-to-date LYSO geometry based on a GP(6,0) Goldberg Polyhedron. At an opening angle of 40°, it features 311 LYSO crystals with an inner radius of 15 cm and a crystal length of 21 cm.

Matching the new calo geometry, the tracker material budget was updated to reflect insights gained during technology development of the microRwell detector. It is designed in a way that it fits either a liquid Xenon or LYSO crystal calorimeter. Its support structure is implemented now as well.

While ATAR itself stayed roughly constant, cables and support structures were implemented based on first guesses. The exact design of the central region is however subject of an ongoing discussion between beamline, ATAR and calorimeter experts.

Directly affected by the outcome of this discussion is also the halo monitor whose purpose is to stop and identify halo muons, i.e. muons from pion decay close to the end of the beamline and would otherwise directly enter the calo.

The latest version of the geometry is shown in Fig. 2.8-1. An equivalent configuration with the same elements is also available for the liquid xenon configuration.

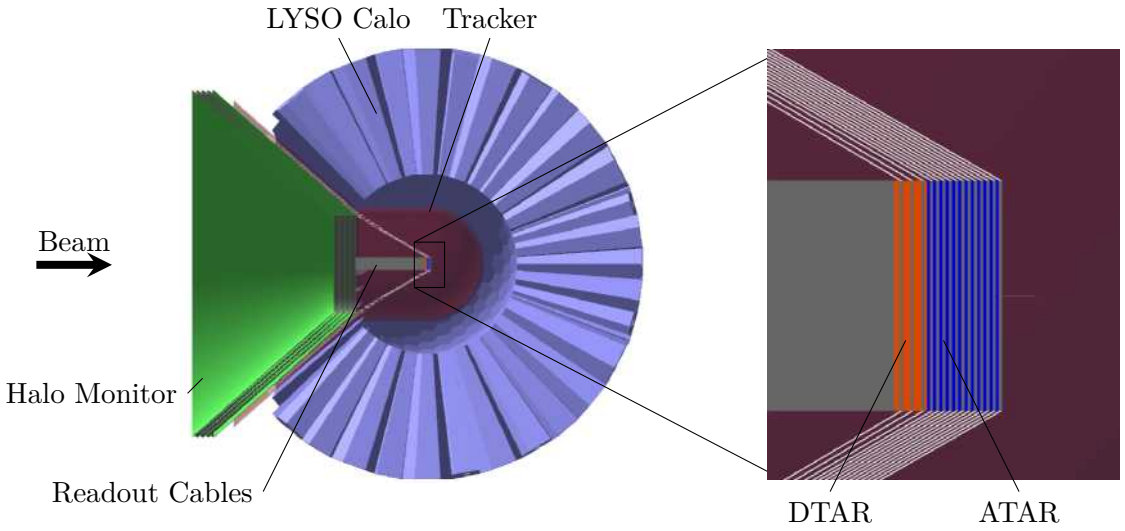

Figure 2.8-1. Current LYSO geometry in the simulation framework

Material Budget Estimates

As positrons leave the ATAR and head towards the calorimeter, they inevitably lose energy in various regions of dead material such as support structures and cables required for readout. Estimating this energy loss and systematically adding it back into each event's energy measurement can therefore serve to reduce the number of $\pi \to e\nu$ events that fall into the Michel region of the energy spectrum and improve our ability to differentiate between the two events.

Because the detector is largely spherically symmetric, the amount of dead material that a positron passes through can be parameterized by the polar angle of its momentum. The granularity of the ATAR will allow us to extract the direction of the positron and therefore get an estimate of the amount of dead material it will pass through before it reaches the calorimeter. Furthermore, it is known that the amount of energy deposited in that material will follow a Landau distribution. This was confirmed with Geant4 simulations that summed the amount of energy lost in dead material by a positron traveling towards the calorimeter at various polar angles. Thus, these simulations provided a mapping between the angle of travel of a positron and the distribution of its energy loss. The mean of these distributions could then be used as an estimate of the total energy lost by a positron as a function of the polar angle of its momentum. With this process, the estimates of energy lost in dead material can be recalculated each time the geometry of the framework is updated and then added to each event based on the momentum of the positrons.

Although adding this energy back into each measurement will improve the energy resolution of the detector compared to that would be the case if no estimates had been made, the

Landau distribution of the lost energy introduces an inherent uncertainty in each estimate. As the geometry in the simulation framework becomes increasingly realistic, the amount of dead material will undoubtedly increase, which will subsequently increase the uncertainty of any energy loss estimates. This study therefore not only improves the energy resolution of the detector, but also provides insight into the extent to which the dead material may adversely affect resolution for a given geometry compared to an ideal detector.

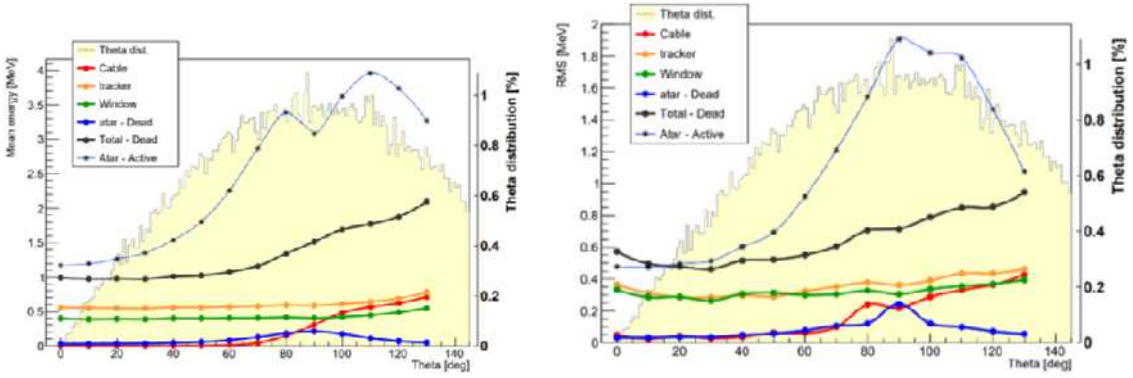

Figure 2.8-2. Inventory of energy deposited in dead material.

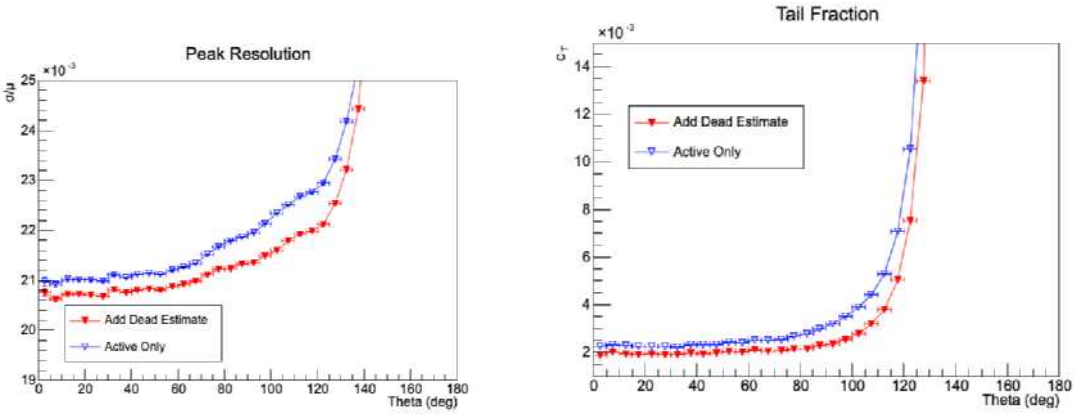

Figure 2.8-3. Effects of adding back energy loss estimates to each event.

G4Pioneer Updates

The largest physics update in the Geant4 part was the custom implementation of the radiative decay channels. This step was required because the implemented differential decay rates did not match the reported measurements well enough for our purposes.

For radiative pion decays, Richard Mischke was kind enough to share the Fortran codes used by NA62[1]. As radiative pion decays are three-body decays, it suffices to represent the

[1]D. Protopopescu, I. O. Skillicorn, D. Britton, CERN NA62-14-10.

differential decay rate as a function of the energies of the charged lepton and the photon. Thus, a look-up table is created for those decays that accelerate the sampling.

As the radiative muon decay $\mu \to e\nu\bar{\nu}\gamma$ is a four-body decay that is influenced by the muon spin, a five-dimensional space has to be sampled. As this exceeds the possibilities of a simple lookup table, a uniform sampling approach with weights according to theory prediction[1] was chosen as the fastest sampling strategy.

Additionally, biasing strategies for more physics processes were introduced. Notably, there is an enhancement strategy for pion decay in flight within ATAR which starts the decay time limiting as the pion crosses over from DTAR to ATAR and a similar strategy that forces pions to decay right before DTAR to study the effects of muons that are born from such decays. Recently, the cross section for the $\pi^+ n \to p\pi^0$ was made scalable as this charge-exchange reaction is a major background for the PiBeta search in Phase II of the experiment.

Further updates include user interfaces and additional data structures written in a file. Most notable is the newly added geometry header that catalogs the entire simulation geometry such that this information is made available in the reconstruction.

Detector Response Updates

This part was run on the basis of simple best-guess event mixing and hit merging strategies. These parts were updated on the basis of the November 2023 beam-time results for LYSO. This allows for more accurate calorimeter energy resolution estimates than before.

Additionally, a bifurcation was introduced in the execution sequence. This allows the user to select the strategy by which calorimeter hits should be processed. The first option is the fast response strategy currently used for all other detectors relying on hit merging if they are too close together in the same detector. The other option is a full-blown waveform simulation based on waveform data obtained from the LYSO prototype.

Reconstruction Updates

The reconstruction went from a few conceptual prototype scripts to a matured collection of intertwined algorithms that reconstruct events out of individual hits. In order to make fast progress across the board and provide rapid feedback to the detector design teams, truth-reliant reconstruction algorithms are deployed.

Especially on the ATAR side of the reconstruction, the hits obtained through the fast response are grouped together by truth information. The development of a truth-independent algorithm is in progress. Amongst other quantities, the energy to be added to the calo energy deposit as well as discriminating variables for event identification are computed by the ATAR reconstruction.

[1] A.B. Arbuzov, T.V. Kopylova, JHEP 2016 (2016) 109.

The calo reconstruction features a waveform fitter that can be used on calo waveforms from the detector response simulation. The fast response bypasses this step. A Calo cluster finder is available for segmented calorimeters that groups hits together based on time and spatial proximity.

The information from ATAR and Calo is matched based on time and potentially positional input to form full reconstruction summaries. For simplicity and computational throughput, there is the option of histogramging those summaries at the end of the reconstruction. This final histogramming step allows us to check those summaries against a complex set of cuts, some of which guarantee events in the fiducial region of the detector, others are used for special subanalyses. For most of the analysis work, those histograms are all that is required. More details on PIONEER analysis are presented in Section 2.6.

2.9 Radiative decays in PIONEER

P. Schwendimann

Introduction

In addition to the decays previously described in the context of PIONEER, $\pi \to \mu\nu$, $\pi \to e\nu$ and $\mu \to e\nu\nu$, a set of more subtle decay channels has to be considered to achieve the precision envisioned for the experiment. Those radiative decay channels are characterized by the emission of an additional, observable photon. Their existence and potential importance was acknowledged early on by aiming at measuring the inclusive branching ratio in Eqn. 2.5-1. For this reason, those rare decays have been studied in some more details.

In a somewhat simplified representation, such photons can be emitted either as internal bremsstrahlung (IB) by the initial- or final-state particles, or as a result of structure-dependent (SD) interactions. To compute cross sections, the interference terms between the two have to be considered as well. Although the fully differential theory predictions may feature a soft and a collinear singularity, the experiment will not be sensitive to these because of detection thresholds and finite angular calorimeter resolution.

In fact, the choice of a calorimeter to measure the positron energy was deliberately made to help with radiative events. Detecting a 70 MeV positron should result in an almost identical response to detecting a collinear 60 MeV positron and 10 MeV photon. Also, while collinear, 4-momentum conservation constrains the summed energy of the photon-positron pair to what would be possible for a single positron.

Also, very soft photons hardly influence our measurement as they will not perturb the positron momentum more than other material interactions, and the photon energy would not make it past the detection threshold. Thus, high-energy photons at large angles have been left for close investigation. In such cases, the total observed energy can exceed the expected energy of the positron. In fact, under given circumstances, the full π rest energy can be

observed through a back-to-back radiative pion decay as well as the full μ rest energy for a radiative muon decay.

$\pi \to \mu\nu\gamma$

The radiative decay of a pion to a muon has been calculated and measured 25 years ago[1]. They observed a branching ratio of 2×10^{-4} for a photon energy above 1 MeV. Their data agrees well with the IB predictions of the standard model down to the detection limit.

In the context of PIONEER, this specific decay channel can affect our analysis strategy in two ways. Option one is that a photon of higher energy gets emitted in time coincidence with a positron from old muon decay, such that the sum of photon and positron energy deposits mimic a $\pi \to e\nu$ event. Option two is that the energy carried away by photon smears out the 4 MeV signature deposit characteristic for a $\pi \to \mu\nu$ decay and thus fail to identify such events correctly.

On the other hand, this radiative decay has a very clear signature of a muon energy deposit below 4 MeV in ATAR as well as a time-coincidence photon in the calorimeter. As the muon will stay within ATAR, it might be possible to observe and characterize this decay channel early on with prototypes for the final PIONEER detector. Such a measurement would be an excellent proof of principle for detector technology, reconstruction methods, and analysis strategy.

$\pi \to e\nu\gamma$

This decay was measured by the PiBETA collaboration. The determined its branching ratio to be $7.386(54) \times 10^{-7}$ for the kinematic range of $E_\gamma > 10$ MeV and $\alpha_{e\gamma} > 40^\circ$ [2]. In addition to the branching ratio, a measurement of the pion weak form factor values F_A and F_V as well as a in $F_V(q^2) = (1 + aq^2)F_V(0)$ is presented. Their numbers were extracted based on 65×10^3 events in a limited kinematic region.

This decay can affect the phase I analysis strategy in two possible ways. On the one side, the photon can escape detection (e.g. through the beam entrance cone), while the positron of lower energy gets properly detected passing all cuts and ends in the tail region, and thus contributes to the tail fraction in a way that cannot be mitigated by a positron beam measurement. On the other side, both particles can get detected and thus pushing the combined energy well above what is expected for $\pi \to e\nu$ events. If we were unable to handle such events in the calorimeter, this forces an extension of the analysis to an energy region that is dominated by pile-up events.

$\mu \to e\nu\nu\gamma$

This decay has been investigated by multiple experiments over a wide range of kinematic limits, and those numbers are well described by theory [3]. One of the more recent measurements is by the MEG experiment $6.03(55) \times 10^{-8}$ close to the limit of the kinematic range

[1] G.Bressi et al. Nucl. Phys. B 513:3 (1998) 555.
[2] M. Bychkov et al. Phys. Rev. Lett. 103:5 (2009) 051802.
[3] G.M. Pruna, A. Signer Y. Ulrich Phys. Let. B 772 (2017) 452.

$E_e > 45\,\text{MeV}$ and $E_\gamma > 40\,\text{MeV}$ [1]. A larger value of $4.365(43) \times 10^{-3}$ are obtained by PiBeta for the kinematic region $E_\gamma > 10\,\text{MeV}$ and $\theta_{e\gamma} > 30\,\text{deg}$ [2]

This decay can impact the PIONEER analysis if the radiative energy deposit is not properly identified as such, and thus the sum of positron and gamma deposit exceeds the high bin threshold. This can promote Michel events far into the high bin and potentially even past the 70 MeV peak of $\pi \to e\nu$ events.

Simulation Results

The corrections in the resulting observed spectra are shown in Fig. 2.9-2. For the $\pi \to e\nu(\gamma)$ decay, one can on the one hand observe a large shoulder that extends well beyond the peak position at 70 MeV. To avoid losing more than 0.01 % of the events, it is required to integrate all the way to 115 MeV, which opens the gates to pile-up events in that region.

In addition, radiative pion decays where the photon escapes detection increase the tail fraction by about 10 %. This has to be considered carefully as this contribution of the tail fraction is inaccessible by any line-shaped measurement based on positron beams.

The Michel spectrum gains a high-energy tail as shown in Fig. 2.9-1b, which reaches far above the high bin threshold. However, those events follow a well-known time distribution and will be absorbed in a leakage term when fitting. However, one should pay close attention to the time spectra of other contributions that result in correlated fit parameters.

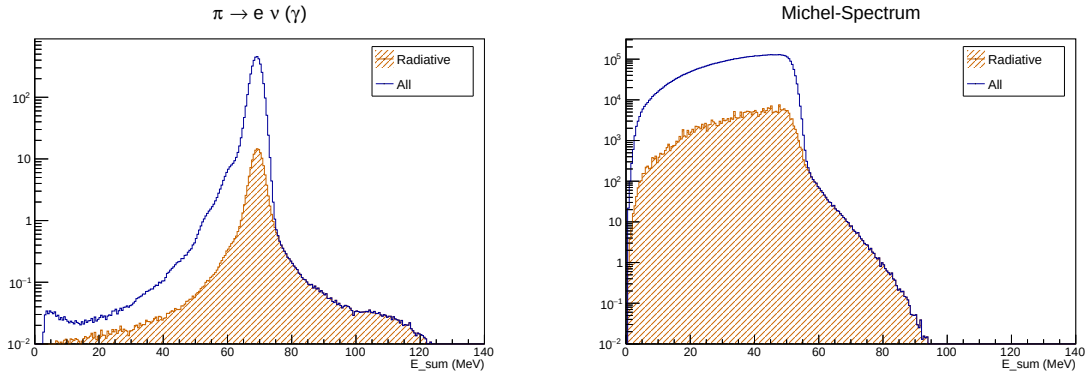

(a) $\pi \to e\nu(\gamma)$ (b) $\mu \to e\nu\bar{\nu}(\gamma)$

Figure 2.9-2. Distortion of the energy spectra due to radiative events.

By considering a calorimeter that not only measures the total energy deposited but also provides some directional measurement, and thus an estimate of the momentum, this additional information can be leveraged. Instead of computing the summed energy alone, the missing momentum can be computed in addition, and thus an estimate for the missing energy

[1] The MEG Collaboration, Eur. Phys. J. C. 76 (2016) 108.
[2] D. Pocanic et al. Int. J. Mod. Phys. Conf. Ser. 35 (2014) 1460437.

obtained. While this is especially powerful for $\pi \to e\nu\gamma$ events where the neutrino momentum can be estimated, it will also improve the situation for $\mu \to e\nu\bar{\nu}\gamma$ events by virtue of kinematics alone. To keep the energy scale at the same level the total energy (observed + missing) is divided by 2.

The results of this strategy are represented in Fig. 2.9-4 for a LYSO calorimeter. As can be seen, the high energy tail is handled for both radiative muon and pion decays and a major contamination in the high energy bin is significantly reduced.

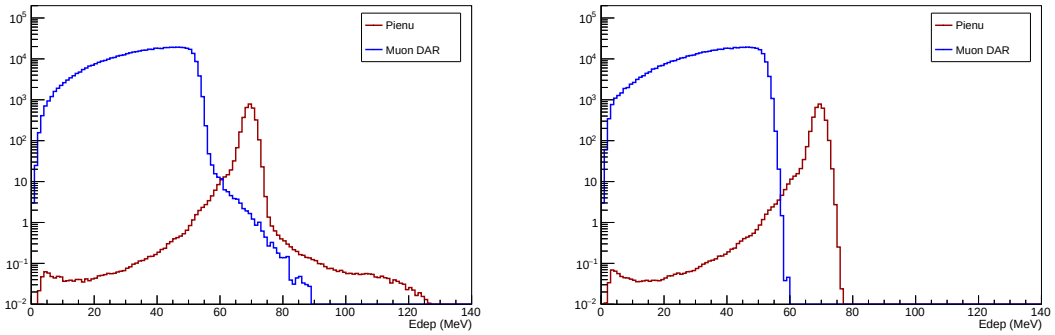

(a) Sum of Calo Edeps (b) Include Missing E

Figure 2.9-4. Energy Spectra for different energy definitions.

2.10 LYSO calorimeter development

O. Beesley, D. Hertzog, E. Swanson, and B. Taylor

The PIONEER experiment requires an electromagnetic calorimeter with high resolution (<2.5% at 70 MeV), high stopping power/depth for full positron shower containment (19 X_0), and relatively fast timing (less than 50 ns scintillator response time). LYSO crystals are an attractive calorimeter candidate with the following properties:

- High density ($\rho = 7.4$ g/cm^3)
- High stopping power ($X_0 = 1.14$ cm, $R_m = 2.07$ cm)
- High light yield (30,000 photons/MeV)
- Fast timing ($t_{decay} = 40$ ns)
- Visible wavelength light emission ($\lambda_{peak} = 420$ nm).

A truncated polyhedron calorimeter geometry composed of 300 large LYSO crystals would satisfy depth and speed requirements for a PIONEER calorimeter and would not need the complex cryogenics necessary for an alternative liquid xenon (LXe) design. A LYSO calorimeter would also posses intrinsic segmentation of its active calorimeter volume, a property useful

for pileup treatment in Phase I of the PIONEER experiment and necessary for signal identification in Phases II and III. Despite the aforementioned appealing properties, LYSO crystals have not previously been demonstrated to posses a sufficiently high resolution resolution at the PIONEER energy scale to be used in the PIONEER experiment.

An array of ten $2.5\times2.5\times18\,\mathrm{cm}^3$ LYSO crystals surrounded by four large NaI(Tl) detectors was constructed to test LYSO crystals at the PIONEER energy scale. The LYSO calorimeter array was tested in November 2023 at the πM1 beam line at the Paul Scherrer Institute (PSI) in Switzerland. Positrons ranging in energy from 30-100 MeV were aimed at the central region of the array to characterize its position, time, and energy resolution. At 66 MeV, the array was determined to have a position resolution of approximately 6 mm. Time resolution was determined using the largest energy deposit in the array as a clean reference time that other secondary hits in the array could be compared to; the dependence of the time resolution on the energy of the secondary hit is shown in Figure 1. Energy resolution was determined at each positron energy from a Crystal Ball fit of the summed energy deposits in the LYSO array; the NaI(Tl) detectors were used to veto events where lateral leakage from the array was likely present. The dependence of energy resolution on energy is shown in Fig. 2.10-2. Here, this dependence has been fit using the function: $\Delta E/E(\%) = b/E(\mathrm{MeV}) \oplus c$, where b and c are constants. The constant parameter c is attributed to miscalibration between the crystals, voltage instabilities, imperfect reconstruction of intrinsic LYSO radioactivity and lateral leakage from the LYSO array that was not captured in the NaI(Tl) detectors. We find $b = (99.7 \pm 1.5)\,\mathrm{MeV}$ and $c = 1.26 \pm 0.05$ which suggests a significant degradation of the energy resolution by noise, especially at lower energies.

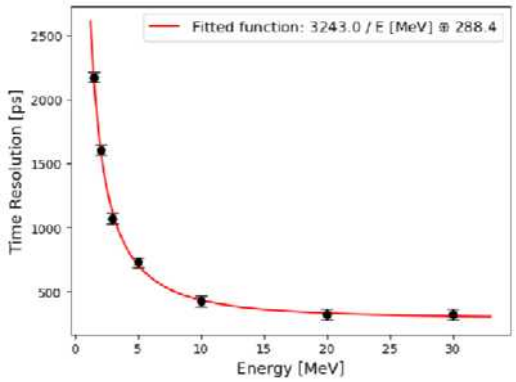

Figure 2.10-1. Dependence of time resolution of a LYSO crystal in the array on the energy deposition in the LYSO crystal for energy deposition between 1-30 MeV.

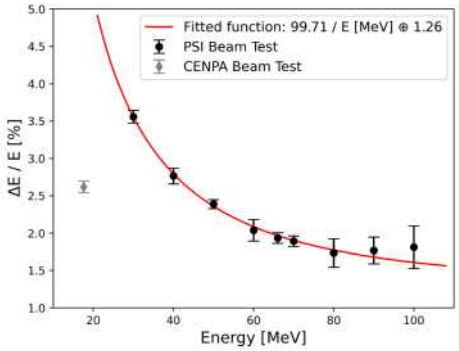

Figure 2.10-2. Dependence of energy resolution of the LYSO array on postitron energy for PSI runs and the 17.6 MeV γ run at CENPA detailed in the section by Swanson. PMTs were operated at 300 V higher voltages in the CENPA beam test, which is expected to have significantly improved data quality and energy resolution.

The large noise contribution is expected to be the result of operating PMTs at the low end of their operational voltages. This was done to minimize the effects of the non-linear

response from PMTs with linear voltage dividers,[1] but also increased PMT noise. An energy resolution measurement of the LYSO array using a proton-Lithium resonance was performed at CENPA after PSI tests; importantly, all PMTs had tapered voltage dividers[2] for this test and the PMTs were operated at an average of 300 V higher than at PSI. Representative 2 MeV pulses from the two different operating voltages normalized for the difference in gain are shown in Figure 3.

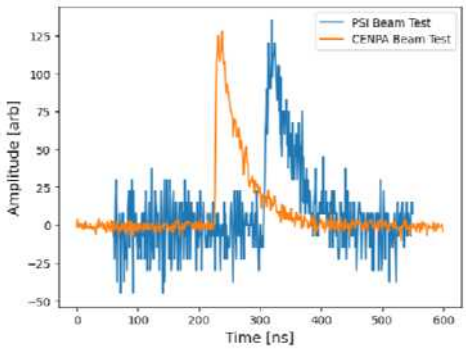

Figure 2.10-3. Two 2-MeV waveforms amplitude-normalized for differences in gain from the same LYSO crystal and PMT with different operating voltages. The PMT was operated at -1275 V during the CENPA test beam and -975 V at the PSI test beam, which resulted in significantly more noise in the data from the PSI test beam.

2.11 Proposed laser calibration system for the PIONEER LYSO calorimeter option

H. E. Swanson

The system proposed here monitors the relative light responses of individual crystals in the LYSO version of the calorimeter. Absolute calibration comes from known accelerator energies and accelerator produced gamma rays such as descried elsewhere in this report. The calorimeter has a spherical volume with over 300 individual LYSO crystals, each tapered to allow close packing within this volume.

The scintillation light produced in LYSO is from Cerium ions embedded in the crystal lattice. These ions are excited by photons with wavelengths in a band around 360 nanometers (nm) and de-excite by emmiting photons in the visible region of the spectrum. This process is monitored with our calibration scheme by using LYSO as a wavelength shifter and injecting 355 nm photons from a laser. Emmitted wavelength shifted photons are counted by photomultipliers.

Apart from using UV light, the laser calibration system is conceptually similiar to the system used in the muon g-2 experiment at Fermilab for 1296 crystals[3]. It is assembled

[1] The resistance at the last six dynodes is equal; this voltage divider is typically used to optimize phototube response for low light signals.

[2] The relative resistances at the last six dynodes were 0.425, 0.567, 0.683, 1.00, 1.00, 1.00; tapered voltage dividers are typically used to optimize PMT linearity over a large dynamic range.

[3] A. Anastasi et al JINST 14 P1125 .

on an optical breadboard as shown in figure Fig. 2.11-1. UV light (355 nm) is generated by Picoquant LDH-FA-355 lasers with 600 picosecond pulse widths and up to 450 milliwats average power. Amplitudes can be varied continuously by their controllers and in calibrated steps with selected ND filters in a filter wheel. Two lasers allow double pulsing with any pulse to pulse separation.

Laser light is split into 4 equal paths by 3 50/50 beam splitters. These are collimated by fiber launchers into 100 channel fiber bundles for distribution to individual crystals. The 4 light distribution fiber bundles include diffuser sections to uniformly spread out the gaussian input beam to all fibers in the bundle. For best efficiency the number of fibers in the bundle is the square of an integer. The custom fiber distribution bundles in the figure have a length of 4 meters with FC connectors for connecting to the crystals. They can be purchased from SQS Vláknová optika a.s.. The optical breadboard is contained in a light tight ventillated box mounted in the vacinity of the calorimeter.

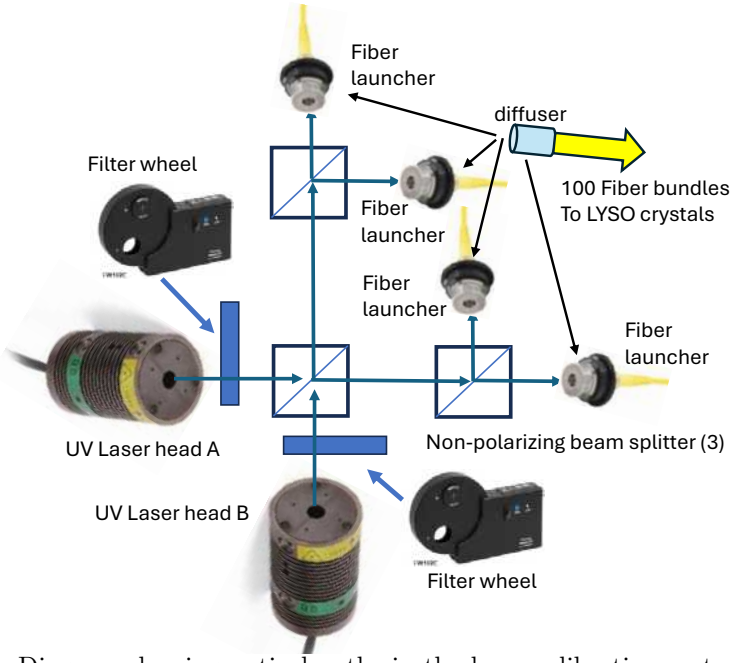

Figure 2.11-1. Diagram showing optical paths in the laser calibration system. Light from the lasers is split 4 ways with 3 50/50 beam splitters and collimated into the diffuser sides of 4 fiber bundles. Individual fibers from the bundles inject light into LYSO crystals adjacent to the photomultipliers that read them out. Lasers are triggered independently and their outputs are independently varied both continuously and in calibrated steps by neutral density filters.

2.12 Tandem accelerator 17.6 MeV gamma source

A. Garcia, N. Miedema, R. Roehnelt, and H. E. Swanson

Radioactive sources can only be used for testing and calibrating calorimeters up to a few MeV. With the tandem accelerator this can be extended to 17.6 MeV, a nice intermediate energy. This article describes the experimental setup on the L30 beam line in cave 1 for producing these gammas from the $^7Li(p,\gamma)$ reaction. The 440 keV resonance in the $^7Li + p$ system populates the 17.6 MeV level in ^8Be which decays to both the ground state and to a 3 MeV level with a 14.6 MeV gamma. Proton energies below an MeV are problematic for the tandem accelerator so we degrade higher energy protons that are in the range the tandem can produce efficiently.

The production target is shown in figure Fig. 2.12-1. It consists of a copper end cap, 0.0075 mmTantalum degrader foil and 1 mm thick LiF crystal. The LiF is a "thick target" given that the range of these protons in the crystal is 5 μm. This does not limit higher proton energies as the energy degrades while passing through the target. The constraint on higher tandem energies comes from proton energies exceeding 1 MeV as they populate the 18 MeV state in ^8Be which decays to the ground state as an unwanted background. As shown in the figure, two copper rings are used to form a sandwich and a wave spring presses the assembly against the end cap to maintain good thermal contact to dissipate heat generated by the proton beam. TRIM simulations were used to determine the degrader foil thickness and proton energy combination compatible with the tandem and resonances. The TRIM simulation showed 1.4 MeV protons transmitted through a 0.0075 mm Ta foil gave a mean energy distribution of 555 keV. It is well below the 1 MeV needed to excite the 18 MeV level and further degrades through the 440 keV resonance energy upon entering the crystal. At this energy we observe a proton beam rate of 1 to 2 μAmps on target. Figure Fig. 2.12-2 shows the low background 17.6 MeV gamma response in an array of LYSO crystals.

Stable Fluorine exists as a single isotope, ^{19}F. This proton energy also produces a 6.13 MeV gamma from the $^{19}F(p,\alpha\gamma)^{16}O$ reaction.

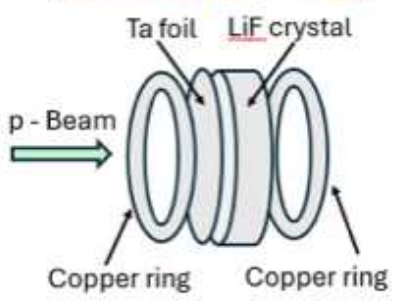

Figure 2.12-1. The LiF target is shown at the end of the L30 beam line in cave 1. Within the copper end cap is a sandwich consisting of two copper rings, a Ta degrader foil and a LiF crystal. The assembly is kept in good thermal contact with the end cap with a ring shaped wave spring. The end cap is isolated for reading the proton beam current.

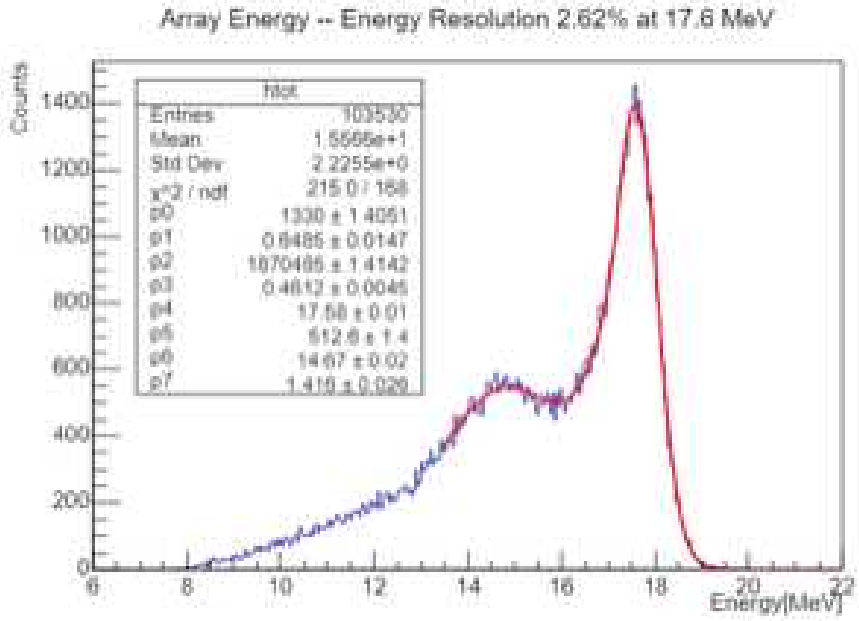

Figure 2.12-2. LYSO crystal array response to the 17.6 MeV gamma source.

2.13 Pulsed UVA light source for LYSO characterization

D. Hertzog, N. Miedema, D. Peterson, R. Roehnelt, H. E. Swanson and T. Van Wechel

A calorimeter using LYSO(Ce) scintillator crystals is a candidate for use in the PIONEER experiment. In addition to using gamma sourcesl to study LYSO(Ce)'s properties, light production in the crystals can be directly stimulated with ultraviolet (UV) radiation. We describe in this section a UV light source based on the Violumas VC1A1C45L6-365 light emitting diode (LED). It has a 365 nm wavelength, up to 775 milliwatts of radiant flux and a 35°beam opening angle (pictured on its heat sink in figure Fig. 2.13-2). An adjustable constant current supply (max 700 ma) sets the light output power. This is pulsed in the electronics by clamping the current to the LED when its off and unclamping for an adjustable 1 to 100 microsecond pulse width while its on. The stability of the light output flux while on is maintained by the current regulation of the power supply. Pulsing is triggered by an SRS DS 345 function generator typically at 1 kHz. We verified the crystal's emission spectrum from UV excitation with an Ocean Opttics spectrometer. Figure Fig. 2.13-1 shows the LYSO(Ce) crystal's response to UV light from the pulsed light source. The LED is positioned adjacent to the crystal on the lower left. The output power was sufficient to illuminate the crystal so it could be seen by the naked eye. The large amount of internal reflection is responsible for the uniform blue glow.

We used the same model LED in a calibration system for the LYSO(Ce) crystal array in the prototype calorimeter taken to the Paul Scherrer Institut (PSI) test beam. In this case the LED was coupled to a Thorlabs BF74HS01 1 to 7 fiber bundle fanout for transsmission

to the crystals. The LED heatsink was mounted to an aluminum disk placed in a Thorlabs KS05 kinematic mirror mount (shown in its light tight box in figure Fig. 2.13-2). The mount positions the LED in line with the FSMA connector for the fiber bundle on the side of the box . Precision adjustments of the mirror mount angle vary the LED beam output direction to equalize the light amoung the fibers. The LED was driven by an existing NIM module pulser from PSI. It has a 10 nsec pulse width and its output is adjustable to 70 Volts which was sufficient for the equivalent light output of a 70 MeV positron. Signal wafeforms were similiar to those from other radiation sources.

To monitor the stability of the system we used a plastic scintillator coupled to a photomultiplier(PM) with optical grease. A 3D printed cap on the PM held the scintillator with an FSMA optical fiber connector at its edge and thin reflective material (ESR) on top to both increase the light collected and seal out ambient light. An unused fiber from the bundle supplied light to the monitor. A radioactive source placed on the ESR would allow the monitor's own stability to be checked. Two complete calibration systems were used for the 10 crystals in the prototype calorimeter.

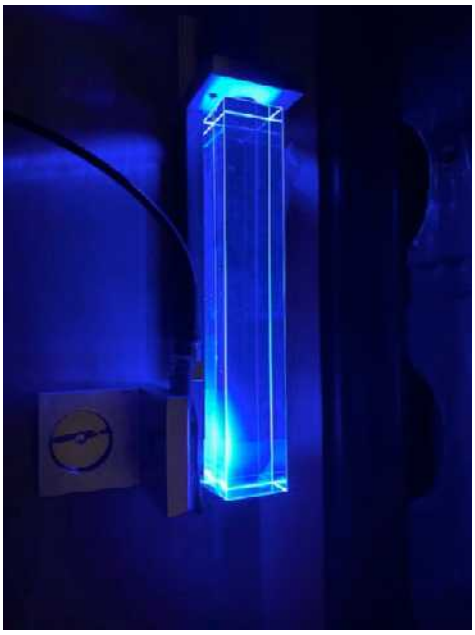

Figure 2.13-1. The figure shows a LYSO crystal illuminated by the 365 nm LED. The bright spot on the lower left side of the crystal shows the location of the LED light source. The large amount of internal reflection of the emitted light provides the uniform glow of the crystal.

Figure 2.13-2. Inside the light source box showing the UV LED and its heat sink on the kinematic mount. The FSMA connector for the fiber bundle is mounted in the wall on the left side of the box ajacent to the LED. The kinematic mount is adjusted to eqalize the light among the fibes in the bundle.

3 Physics with accelerator beams

^{6}He-CRES

3.1 He6-CRES Overview

W. A. Byron, N. Buzinsky, B. Dodson, A. García, A. Goodman, A. Gorman, H. Harrington, L. Hayen*, P.T. Kolbeck, B. Maxwell, L. Malavasi, D. McClain†, D. Melconian†, P. Mueller‡, N. Oaxaca, N. S. Oblath§, G. Savard‡, D. Stancil*, D. W. Storm, H. E. Swanson, R.J. Taylor*, J. Tedeschi§, B. A. VanDevender§, C. Wiseman, F. Wietfeldt¶, and A. R. Young*

He6-CRES is progressing toward high precision measurements of the ^{6}He and ^{19}Ne beta spectra. Our paper demonstrating the technique was published last year[1] and we recently published calculations of beta energy loss in waveguides [2].

The motivation is a high-sensitivity search for chirality-flipping interactions, which would signal physics beyond the Standard Model. Using an effective Lagrangian for the charged weak current with additional scalar and tensor interactions with couplings ϵ_S and ϵ_T[3]

$$\begin{aligned}\mathcal{L}_{\mathrm{CC}} = -\sqrt{2}G_{\mathrm{F}}^0 V_{\mathrm{ud}} \Big[& \bar{e}^L \gamma_\mu \nu_e^L \cdot \bar{u}\gamma^\mu(1-\gamma^5)d \\ & + \epsilon_S\, \bar{e}^R \nu_e^L \cdot \bar{u} d \\ & + \epsilon_T\, \bar{e}^R \sigma_{\mu\nu} \nu_e^L \cdot \bar{u}\sigma^{\mu\nu}(1-\gamma^5)d \Big] \end{aligned} \tag{1}$$

the beta spectra, $\frac{dN}{dE}$, are expected to present a distortion with respect to the Standard Model prescription, $\frac{dN_{SM}}{dE}$, proportional to m/E (the ratio of the mass to the total relativistic energy of the beta):

$$\frac{dN}{dE} \approx \frac{dN_{SM}}{dE} \left(1 + b\, \frac{m}{E}\right). \tag{2}$$

The so-called Fierz interference coefficient, b, is directly proportional to the couplings ϵ_S and ϵ_T. Significantly for us, the proportionality has opposite signs for β^- and β^+ decays. Thus, by taking *ratios* of measurements with ^{6}He and ^{19}Ne, we cancel systematic uncertainties while enhancing the signature of new physics.

*Department of Physics, North Carolina State University, Raleigh, NC.
†Texas A&M, College Station, TX.
‡Argonne National Laboratory, Lemont, IL.
§Pacific Northwest National Laboratory, WA.
¶Department of Physics, Tulane University, New Orleans, LA.

[1] Byron et al., Phys. Rev. Lett. **131**, 082502 (2023).
[2] N. Buzinsky et al., New J. Phys. **26**, 083021 (2024).
[3] Bhattacharya et al., Phys. Rev. D **85**, 054512 (2012).

Fig. 3.1-1(left) exemplifies the type of expected distortion, and Fig. 3.1-1(right) gives the sensitivity for $b < 10^{-3}$ measurements in comparison to other determinations[1]. Significantly, we are aiming for searches that are beyond the level of sensitivity of any previous experiment.

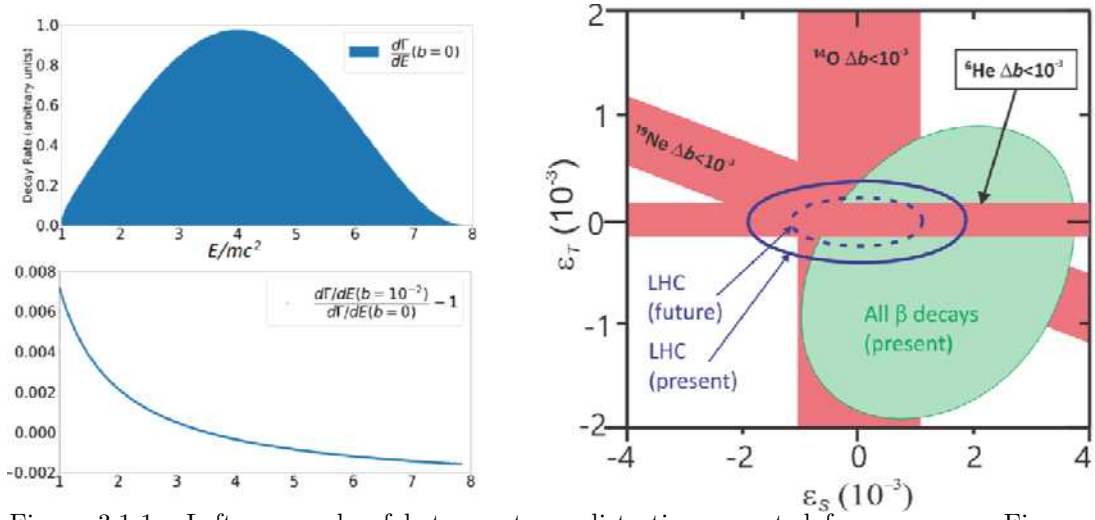

Figure 3.1-1. Left: example of beta-spectrum distortion expected from non-zero Fierz coefficient b. Right: sensitivites to scalar and tensor couplings from upper limits on b expected from the He6-CRES nuclei in red. In green, we show the result of a combination of all beta decay measurements up to date, including neutron decays. The blue lines indicate limits from the LHC.

We use the technique called Cyclotron Radiation Emission Spectroscopy (CRES), developed by the Project 8 collaboration for determining the neutrino mass using the tritium endpoint. The basic idea is to arrange for the beta decays to occur within a magnetic field. The betas undergo cyclotron motion with frequency

$$f = \frac{q\,c^2}{2\pi}\frac{B}{E}. \tag{3}$$

Letting the radioactive decays occur within an RF waveguide generates RF excitations with the cyclotron frequency. For $E \approx 1$ MeV in a $B \approx 1$ T field, the frequency is ≈ 20 GHz. Typically, we digitize RF waves in slices of ≈ 10 μs, calculate fast Fourier transforms (FFTs), and produce spectrograms, called 'waterfall' plots, which allow extraction of E at the point of decay, before any loss of energy. This feature, combined with low backgrounds, and a first-principles connection between the measured frequency and the energy, are very attractive for a method aimed at probing for new physics.

Our present RF-bandwidth covers 18-20.3 GHz, and the coverage of the beta spectrum is achieved by scanning the magnetic field, as shown in Fig. 3.1-2.

[1] M. Gonzlez-Alonso, O. Naviliat-Cuncic, and N. Severijns, Prog. Part. Nucl. Phys. **104**, 165 (2019).

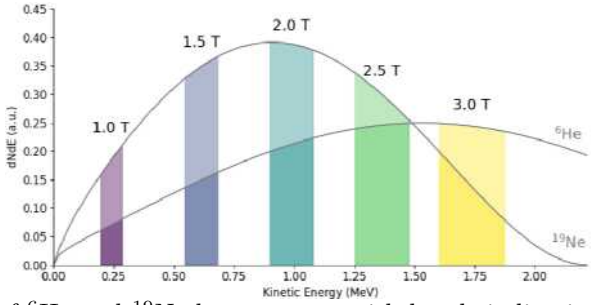

Figure 3.1-2. Sketch of ^{6}He and ^{19}Ne beta spectra with bands indicating the regions measured by a $18 - 20.3$ GHz RF-bandwidth system. For clarity, we only show bands corresponding to a few magnetic-field values. Typically 11 points are taken including overlaps.

Fig. 3.1-3 shows the main RF components. Careful attention was put into the distribution of heat in the design to allow for optimal temperatures at the RF amplifier, while keeping the decay cell warm enough to avoid freezing ^{83}Kr, which was used as a calibration source.

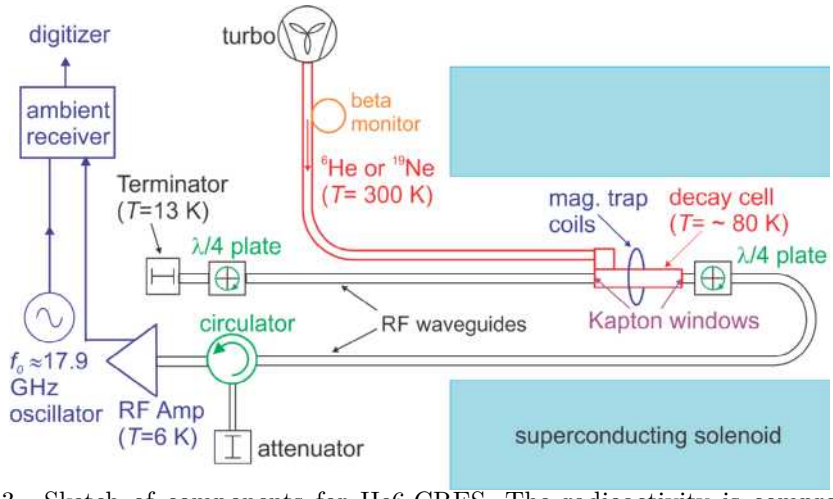

Figure 3.1-3. Sketch of components for He6-CRES. The radioactivity is compressed by a turbo pump into a decay cell, which is part of an RF waveguide. The waveguide was connected on one end to an RF amplifier (at $\approx$ 6 K) and on the other to a terminator at low temperature to optimize signal-to-noise ratio. The "beta monitor" measures beta rates and allows for normalizing spectra taken at different field values. Temperatures are approximate.

He6-CRES is organized into phases with milestones that are presented in Table 3.1-1.

Phase I: *proof of principle*
Observe ^{83}Kr lines
Understand RF issues and spectra
Study RF power distribution
Develop ^{19}Ne source
Show detection of cycl. radiation from ^{6}He
Phase II: *first measurement*
^{6}He and ^{19}Ne measurements at $b < 10^{-2}$
Develop next beta monitor
Analysis of uncertainties and improvements
^{6}He and ^{19}Ne measurements at $b < 10^{-3}$
Develop design of ion-trap systems
Develop ^{79}Kr and ^{14}O sources
Phase III: *ultimate measurement ($b < 10^{-3}$)*
Build ^{14}O source
^{14}O measurements
Use ion-trap for no limitation from geometric effect

Table 3.1-1. He6-CRES phases with proposed milestones.

We report here on progress between July 1, 2023 and Sept. 30, 2024. We have finished Phase I and are starting with Phase II. During last period we demonstrated detection of $\beta^{\pm}$ in the range between 5 keV and 2.3 MeV. Fig. 3.1-4 shows spectrograms and the corresponding ratios of counts.

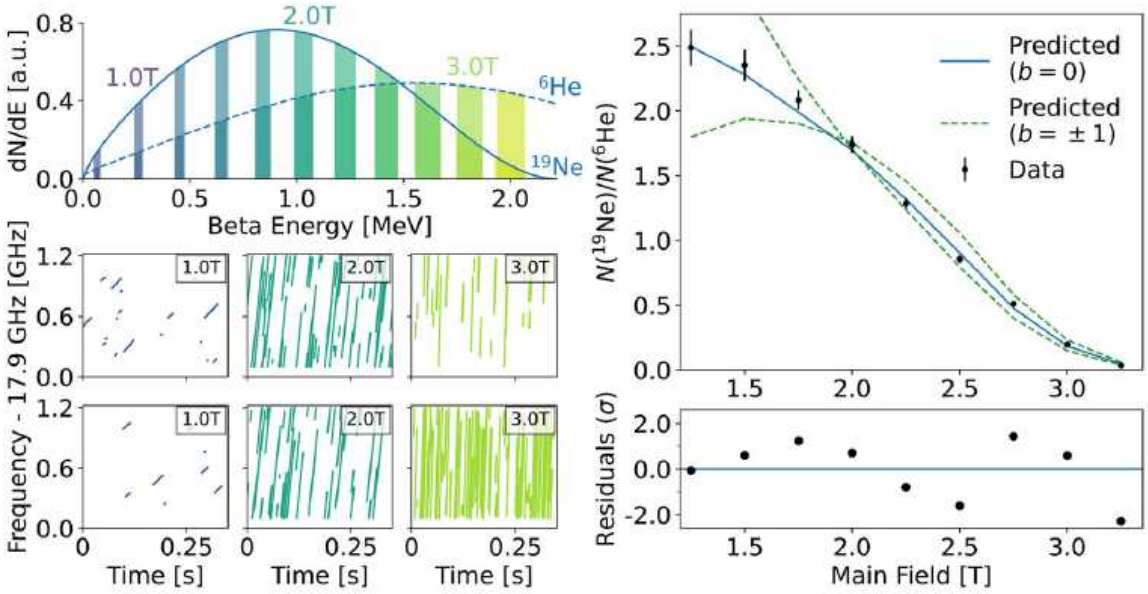

Figure 3.1-4. Left top: like Fig. 3.1-2 for former bandwidth. Left bottom: spectrograms at different fields; top row from ^{19}Ne and bottom row from ^{6}He. Right: plot of ratios of counts taken at the different fields indicating sensitivity to b with dashed lines. The whole data set corresponds to 90 minutes of data taking per isotope.

(Sec. 3.2) describes DAQ improvements. Over the last year, we have:

- doubled the RF bandwidth from 1200 MHz to 2400 MHz
- implemented online data compression, decreasing the size of our written data from ~ 1 Gigabyte/s to ~ 5 Megabyte/s,

both of which contribute to a much improved DAQ system, needed for our next steps.
(Sec. 3.3) describes hardware and vacuum improvements. Careful improvements in design led to implementation of a more reliable system and an improvement in vacuum from few $\times 10^{-7}$ Torr to few $\times 10^{-9}$ Torr. This is quite important in minimizing scattering, which can lead to systematic uncertainties.
(Sec. 3.4) describes CRES signal processing and the extraction of initial event frequencies. Much progress has occurred in understanding effects that could lead to systematic errors.
(Sec. 3.5) describes our beta monitor. This is used to normalize and connect data taken at different B field values so we can search for b. A new system, based on thin scintillators and SiPM readouts (to minimize sensitivity to B field) was implemented and is presently being tested.
(Sec. 3.6) describes improvements in the signal-to-noise ratio that were achieved by first analyzing possible sources for variations versus frequency, and careful hardware work that eventually led to valuable improvements.
(Sec. 3.7) describes work to understand the variation of frequency 'slopes', df/dt's, with beta energies, which depend on power loss in the guide, and lead to effects that contribute to

systematic errors.
(Sec. 3.8) describes an '$E \times B$ trap emptying system'. To minimize problems related to piling up of events, we empty the trap in a cycle that should ideally be of the order of milliseconds (roughly, the average time between events.) In the data published last year we turned off the trap coils during 15 ms and left them on for 40 ms. Shorter times were limited due to eddy currents. We designed and built a system for emptying the trap using electric fields. This will be an important tool for the upcoming data taking.
(Sec. 3.9) describes updates to the `he6-cres-spec-sims` Monte Carlo CRES simulation software, which include both broad performance upgrades and new features for a more physical treatment of scattering and the magnetic bottle trap.
(Sec. 3.10) describes developments toward a ^{79}Kr source. It produces conversion electrons of ≈ 11 keV, 31 keV, 130 keV, 604 keV, as well as a continuum β^+ spectrum with ≈ 604-keV endpoint, all of which will be useful for studying systematic uncertainties.
(Sec. 3.11) discusses the design of a new cryogenic vacuum pump for potential order of magnitude improvements in the event rate, without introducing non-radioactive contaminant gases.

3.2 Data Acquisitions Upgrades

N. Buzinsky, A. García, A. Goodman, and H. Harrington

The statistical sensitivity of the He6-CRES experiment to b_{Fierz} is inversely proportional to the square root of the number of observed events, following the heuristic:

$$\sigma_b \sim \frac{10}{\sqrt{N_{\text{events}}}}. \tag{1}$$

The number of observed events is a product of the efficiency ϵ, the event rate Γ, and the total run duration T:

$$N_{\text{events}} = \epsilon \Gamma T. \tag{2}$$

A series of modifications to the data acquisitions (DAQ) in He6-CRES was identified as being relatively high-impact, improving the eventual sensitivity of the experiment to b_{Fierz}. These changes were oriented at either directly increasing ϵ or the capacity for a larger T.

Firstly, the DAQ receiver code has been significantly revamped. Implemented in C++ , the program catches UDP (User Datagram Protocol) packets of spectrogram data output by the ROACH2 (our digitizer/FFT producing system), reading the data from the network interface controller (NIC) to memory, and then writing the data in memory to the hard drives. Data is output from the ROACH2 at ≈ 1200 Mb/s.

Previously, reading and writing was done sequentially and each second of data was run with an independent call of the C++ binary. The code is now multithreaded, using a double-buffer design pattern, in which the writing to disk of the previous second is done concurrently with the reading of the current second of data. A single call of the binary for N-seconds of data results in significantly less overhead in allocating and deallocating the memory buffers.

These changes together have resulted in improving the performance of the data collection from ≈ 5 real time seconds per second of data to ≈ 1.03 real time seconds per second of data.

CRES data is relatively sparse, as most Fourier bins in time-frequency space are occupied by relatively low-power thermal noise. To accommodate future potential week-long runs, spectrogram data can now be optionally compressed online, reducing the amount of data written to disk by $\approx \times 100$.

Finally, the He6-CRES RF bandwidth was extended from 1200 MHz to 2400 MHz (Fig. 3.2-1). The bandwidth limitation for the previous (1200 MHz) implementation was driven by the use of a standard code block for generating fast Fourier transforms (FFTs). While the pre-existing FFT code block offers flexibility to rapidly reconfigure the field programmable gate array (FPGA) software design, that comes at the cost of both timing closure (the ability of the software to process 1 s of data in ≤ 1 s real-time) at high sample rates and output FFT bit precision. Both these limitations were addressed by implementing a custom FFT design using the Xilinx core FFT with the appropriate "butterfly" calculations. The new integrated FPGA code design follows the same functional flow as its 1200 MHz predecessor: FFT results are generated and converted to power measurements, then (due to data transfer bandwidth limitations), the power values are truncated to 8 bits using a user-input scaling factor, and every other FFT 8-bit power result is transferred off the ROACH2 board.

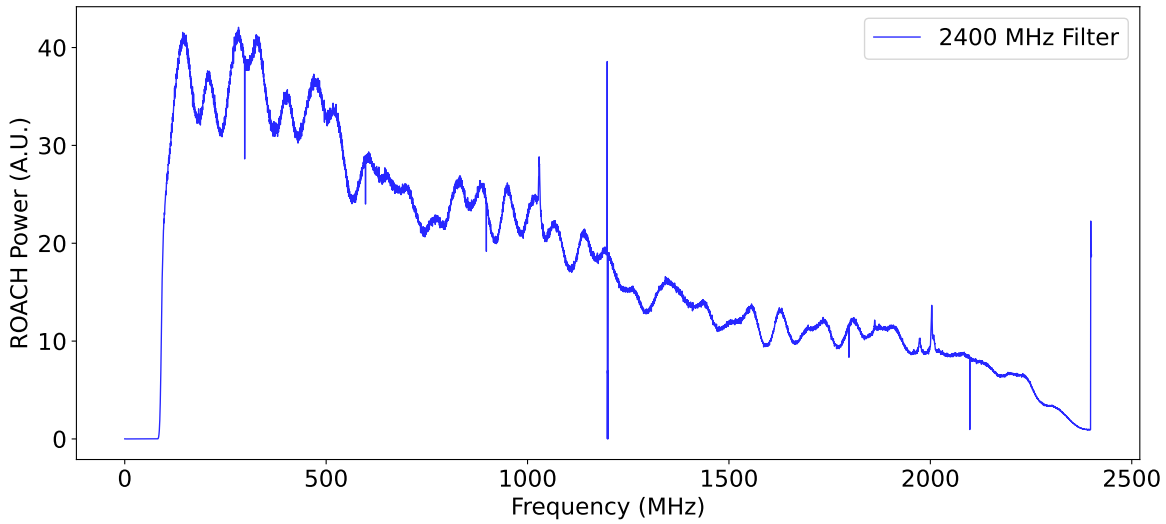

Figure 3.2-1. First noise data taken at 2400 MHz bandwidth (17.9 GHz – 20.3 GHz) taken with He6-CRES, with a 2400 MHz low-pass filter attached to the RF chain. Glitches at multiples of 300 MHz have been subsequently fixed.

In total, these upgrades to the DAQ have resulted in approximately an order of magnitude improvement in ϵ, and have opened the possibility of $\sim$ week-long runs without data bottlenecks.

3.3 Hardware improvements

A. García, H. Harrington, D. W. Storm, and H. E. Swanson

There are three goals of the transport and vacuum system.

1. Transport of the radioactive gas from the production targets to the CRES decay cell.
2. Maintaining a high vacuum in the CRES decay cell during running to minimize scattering of betas with residual gas.
3. Maintaining a stable vacuum in the CRES decay cell across time and between sources of the isotopes of study.

In addition to these, it would also be advantageous to be able to introduce controlled levels of background gases to do dedicated scattering studies, and see how the response function changes with the dominant partial pressures.

Before May 2024, the vacuum in the gas transport was very unstable and total and partial pressures were different between sources. This was a failure of points 2 and 3 above. We also had no further way to study the effect of scattering with the apparatus. In our 2021 and 2023 test datasets, we found that scattering at low energies (measured with fields < 1.25 T) caused statistically significant differences in CRES event topologies between the two gas sources. The result of this was that we had to exclude low field data from the analysis which is not desirable, as the superratio is most sensitive to non-zero b at low energies/fields.

In January 2024 we built a new gas handling system to regulate 3 (or more) partial pressures in out main vacuum by leaking in small amounts of gas. This could be used to force pressures to be the same between sources, or for precise scattering studies vs pressure. This system is now mostly built and not yet tested. Additionally we rebuilt a section of our main vacuum system with the goal of improving the overall vacuum to reduce scattering and extend the experiment into the lower energy region where our sensitivity is highest.

Previously, we had pressures of 2.5e-8 Torr without source running, unstable 1e-7 – 4e-7 Torr when running the ^{6}He source, 5e-8 Torr when running the ^{19}Ne source. This was dominated by Hydrogen or A=19 respectively. There was also suspected Fluorine contamination from Teflon in Cryo-II.

The design goal was to achieve $<$ 5e-9 Torr without a source running, and to be stable to 1e-9 Torr with a source. Main changes included removing old 500L/s of getters that were suspected of not working well anymore and replacing them with a new 1000 L/s getter, removing Teflon on cryo-II heater leads to attempt to remove source of Fluorine contamination, adding an ion gauge to calibrate the RGA and as a backup in case of failure, add the ability to isolate the getter from the RGA while regenerating, create better procedures for regenerating cryopumps so as to not load the getter, and do a rigorous vacuum conditioning.

With these improvements, we exceeded the design goals, achieving 2e-9 Torr without source, and 4e-9 Torr when running the ^{19}Ne source (^{6}He source not yet tested).

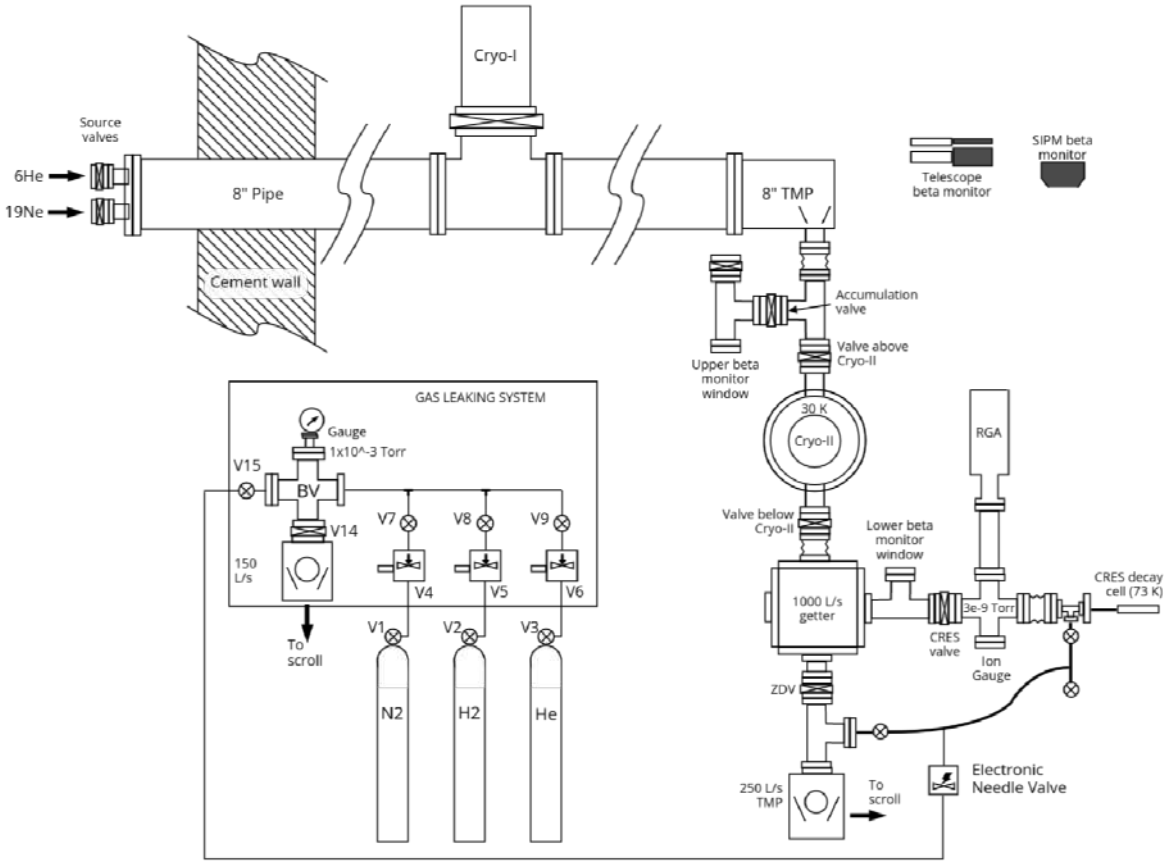

Figure 3.3-1. Upgraded vacuum system for He6-CRES, as well as gas handling system for pressure stabilization and pressure dependent studies.

3.4 CRES RF signal processing

W. A. Byron, N. Buzinsky, A. García, A. Gorman, H. Harrington, P.T. Kolbeck, and B. Maxwell

As described in (Sec. 3.7), the tracks in spectrograms created by radiating beta are actually highly non-linear. Over the range of energies measured in the experiment, the average slopes of these tracks range over three orders of magnitude as explained in (Sec. 3.7). At low energies, scattering will cause jumps in the tracks. Variation in pitch angle results in beta events producing mainbands and sidebands spaced by the axial frequency. Finally, SNR variations with frequency will cause single tracks to have variable detectability as they span the 2.4 GHz bandwidth.

All we truly care about is the start frequency of the event (all tracks resulting from the cyclotron radiation of a single beta). As long tracks make it more likely that the reconstruction will be thrown off by a resonance or SNR gap, we have pushed on the development of

the ExB decay cell for fast trap emptying and short accumulation periods. We use a signal generator to inject a tone into the spectrogram when the trap is being emptied for precise feature comparisons to Monte Carlo simulations. We have developed two main analysis directions to do event reconstruction and handle these features. First is an implementation of SequentialTrackFinder developed by Project 8 that assumes straight tracks. We use this to make many $\mathcal{O}(100s)$ small (3-5 time bin) track-segments which are then stitched together with a DBScan clustering algorithm into "events". This allows us to follow tracks across resonances and scatters quite well. We have also developed a new CRES track finding algorithm called LongTrackFinder which does not assume straight tracks. The key difference is that LongTrackFinder uses a recent running average slope to add new over-threshold points to the track, whereas SequentialTrackFinder uses the global slope of the track. Analysis can be done with either track finder. To deal with SNR oscillations, we have been pushing on hardware improvements, and also developed a secondary DBScan clustering that clustered candidate "events" on their intercept on an axis perpendicular to the average slope at that field. This has been shown to give much better resolution than time-intercept clustering. Finally, we have a tool to cluster mainbands and sidebands.

Using our developed toolkit for CRES signal processing, we have carried out a series or studies and small data campaigns. One of these was in May of 2023 and another in June 2024. The analysis for the 2023 data was performed in the timeframe of this annual report. From that dataset, we concluded that there were key systematic effects that we needed to study. These were:

- Scattering and changing vacuum conditions.
- Beta monitor instability.
- Analysis systematics that are density-dependent.
- Trap geometry differences
- RF Temp difference drift

In June 2024 we conducted a series of studies on these systematic effects. At the moment, uncontrolled variation in the magnetic trap geometry seems the most likely to have caused non-repeatable measurements in 2023.

3.5 Beta Monitor

A. García H. Harrington, B. Maxwell, D. McClain*, D. Melconian*, and C. Wiseman

The He6-CRES experiment seeks to demonstrate CRES using isotopes produced by the Van de Graaff accelerator. Since the total activity present in the decay cell is always changing from the fluctuations in the beam, it is necessary to work with a ratio of two rates. They are

*Texas A&M, College Station, TX.

the CRES event rate, binned by energy, and the event rate observed by a secondary detector placed before the injection point into the CRES cavity. Our group has been developing a SiPM scintillation detector toward that end. To discriminate against photon backgrounds, we have a pair of scintillators making a trigger in coincidence, as the chance that two thin scintillators will trigger on photons is very small. Our goal is to measure the activity rate to a precision of 10^{-4}.

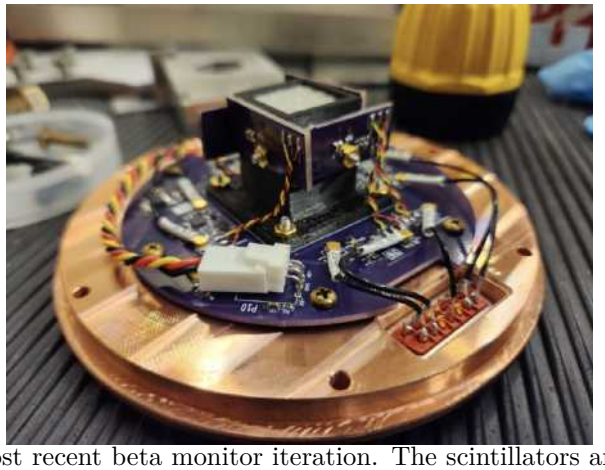

Figure 3.5-1. The most recent beta monitor iteration. The scintillators are placed close to a very thin Al window which views the vacuum chamber before injection into the CRES trap.

We spent time this year developing NIM hardware to identify coincidences between detectors, and output a rate (triggers per second) using a TTL logic signal. The rate is read by an Arduino, which sends the information over Ethernet for inclusion in the primary SQL database. The NIM logic requires amplitude thresholds be set for each of the SiPM's. To calibrate the system and avoid triggering on noise, energy thresholds are set with a Sr90 source mounted into a hole in the back plate of the beta monitor. The calibration rate from the Sr90 source is roughly 300 Hz, and during data taking it is expected to be as high as 50 kHz.

SiPMs, or Silicon photomultipliers, are arrays of many small pixels (or microcells) where each a series combination of an avalanche photodiode (APD) operated in Geiger mode, and a quenching resistor (RQ). These are connected in parallel and reverse biased. The gain of the photodiode increases strongly with voltage. The breakdown voltage is where the multiplication regions from many photo-electrons merge together to form a single avalanche. This is what puts it in "Geiger" mode where it can produce large avalanches from a single photon, and all pulses from any APD are the same amplitude. In a SiPM, the number of APD cells producing an avalanche is what is proportional to the number of incident scintillation photons, under the assumption that no more than one scintillation photon hits one APD. The APD and QR cells are connected in parallel, so that the current pulse is the sum of those from all triggered APDs. The overvoltage (operating voltage - breakdown voltage) determines the gain (size) of each APD pulse.

The gain, noise, and PDE (photon detection efficiency) all depend strongly on temperature and voltage. For example, temperature drift changes the breakdown voltage, which can change the optimal overvoltage. A set of 4 Hamamatsu SiPM power supplies were purchased with automatic temperature compensation, programmable by an Arduino.

A NIM logic chain implements the coincidence calculation between scintillators, producing a logic pulse which is fed to a second Arduino count unit and posted to the primary database. This allows for real-time beta monitor rate readout. For offline analysis, we are developing a CAEN digitizer readout, which saves the energy, channel, and timestamp, of each pulse, with minimal deadtime at the 50 kHz maximum rate. We are currently considering additional design improvements to the beta monitor system, including a fiber-optic laser pulser system (to actively monitor dead time).

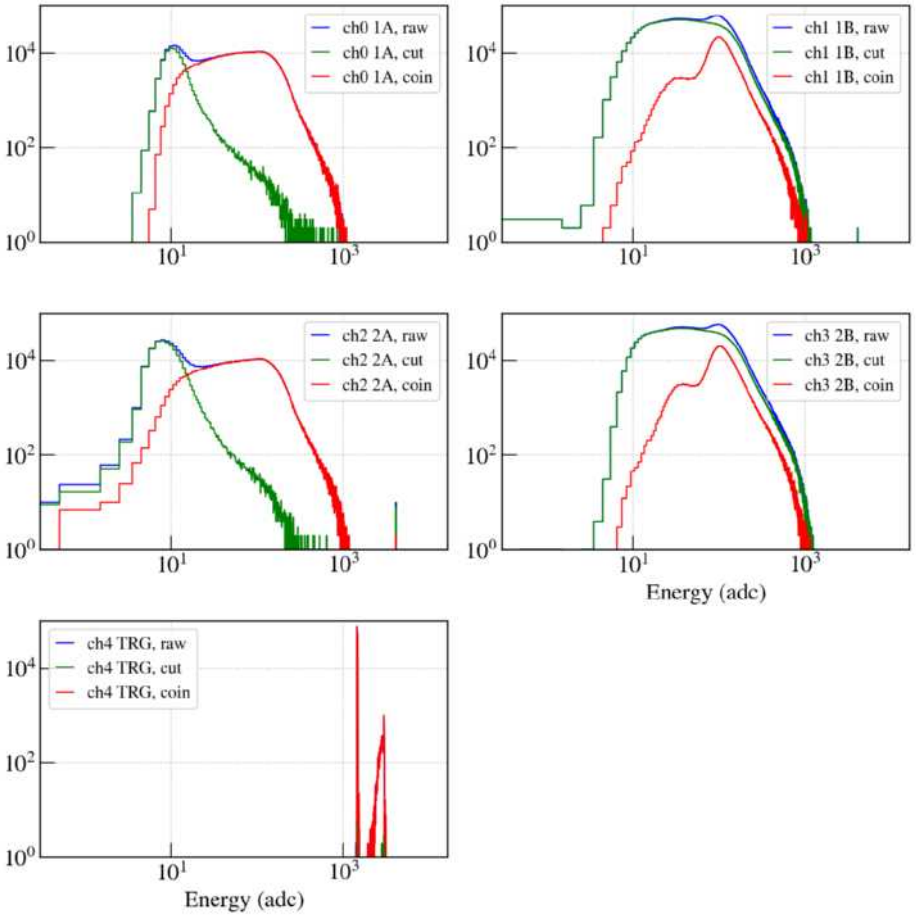

Figure 3.5-2. Offline coincidence calculation and energy spectrum from the 4 SiPMs on the beta monitor during a 90Sr calibration run.

3.6 Minimizing Signal-to-Noise Ratio Variations due to RF Reflections

N. Buzinsky, A. García, H. Harrington, and R.J. Taylor*

Signal-to-noise ratio (SNR) variations as a function of frequency can have a pernicious effect on event reconstruction. In particular, if SNR increases as a function of frequency, CRES events can go from invisible to visible, resulting in a misreconstruction (overestimate) of the true start frequency of the event.

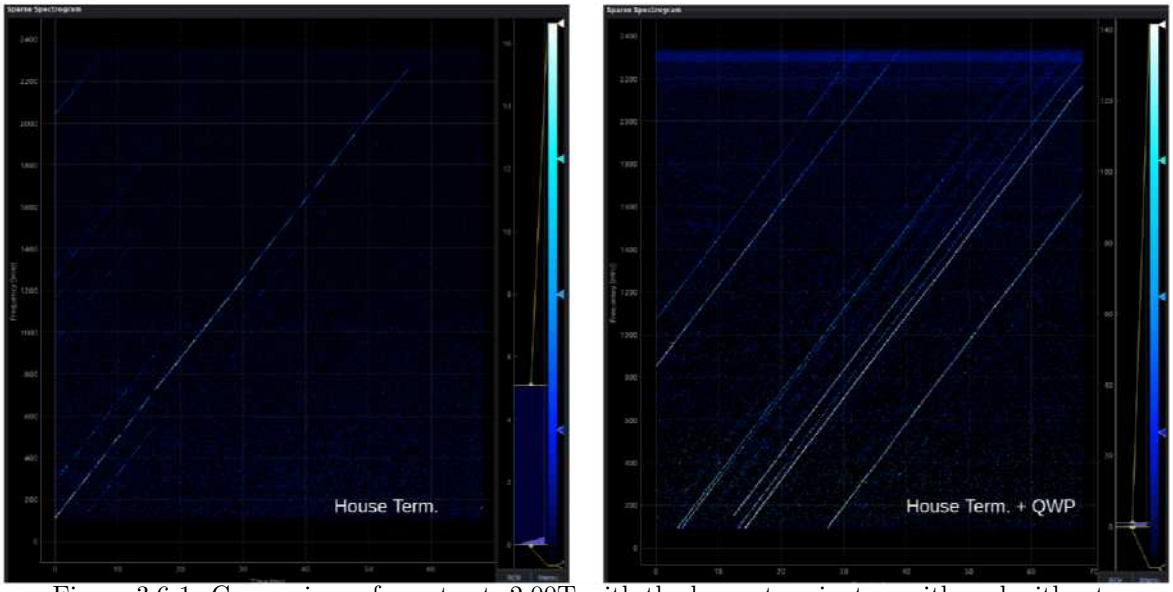

Figure 3.6-1. Comparison of events at -2.00T with the house terminator, with and without the QWP.

Sample ^{19}Ne events corresponding to the RF configuration of the science run of May 2023 (Figure Fig. 3.6-1: left) shows the effect of SNR variations on observed spectrogram data. Figure Fig. 3.6-2 (upper left: purple) shows the mean $\pm 1\sigma$ SNR as a function of frequency, over an ensemble of detected betas, in this RF configuration. The dominant SNR variation has $\approx$ 100 MHz spacing between peaks, and peak-to-trough SNR variations are $\approx$ 60% of the average SNR. These SNR variations are attributed to reflections off of the "house" graphite-epoxy terminator, located 97 cm away from the trap center in the direction opposite of the LNA. Cyclotron radiation reflected off the terminator interferes with radiation emitted directly from the beta towards the LNA, resulting in constructive/destructive interference at different frequencies.

*Department of Physics, North Carolina State University, Raleigh, NC.

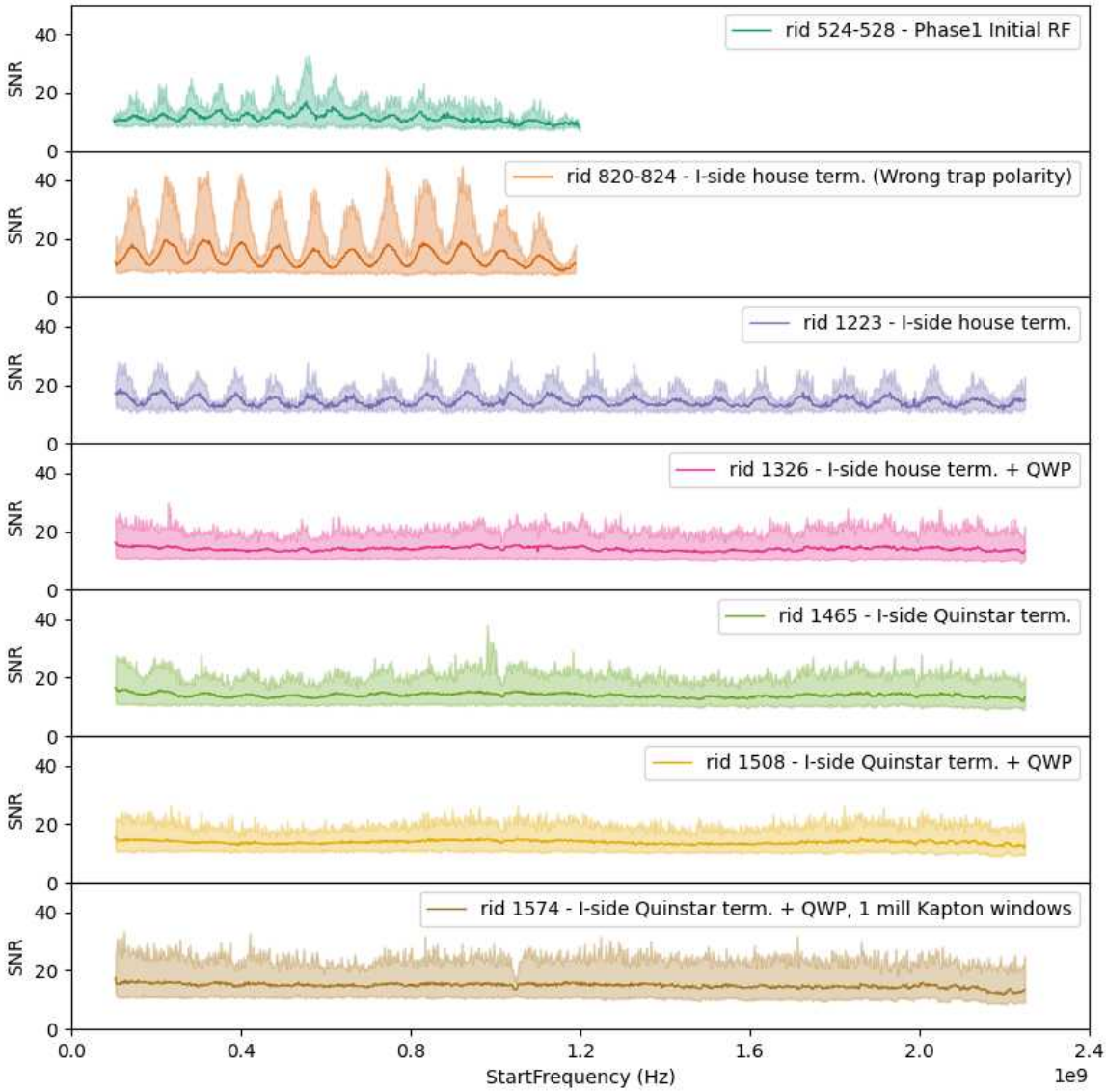

Figure 3.6-2. Grid of CRES signal-to-noise ratios as a function of frequency, for varying RF configurations. A 1σ band surrounds the mean SNR at each frequency for an ensemble of reconstructed Ne19 events at -2.0 T.

To minimize the SNR variations in the He6-CRES apparatus, we:

1. Replaced the I-side house terminator with a purchased Quinstar terminator
2. Added a quarter-wave plate (QWP) to the I-side between the decay cell and the terminator
3. Replaced the 5 mil-thick kapton windows surrounding the decay cell with 1 mil-thick kapton windows

In comparison to the house terminator, the Quinstar terminator (Figure Fig. 3.6-2: center left, green) exhibits approximately an order of magnitude reduction in these 100 MHz SNR oscillations attributed to reflections off the terminator. A similar reduction in SNR oscillations is attained by adding a QWP (Figure Fig. 3.6-2: top right, pink) between the decay cell and the I-side terminator.

Decisively, using both the Quinstar terminator and the I-side QWP results in a better configuration than either change individually (Figure Fig. 3.6-2: center right, yellow). The $\sim$ 1 GHz SNR oscillation is attributed to reflections off of the 5 mil-thick kapton windows surrounding the decay cell used to confine the radioactive gas, due to an impedance mismatch with respect to the vacuum. Item 3 has resulted in SNR vs. frequency given by Figure Fig. 3.6-2 (bottom left, brown). Remaining SNR variations are believed to be currently dominated by limited data-taking bit depth, which is believed to be readily addressable by tweaking DAQ parameters. Given the marked improvement in reducing the SNR variations as a function of frequency, increasingly precise analysis tools are required for evaluating the variations present in the current RF configuration.

Together with the ExB trap emptying, He6-CRES event reconstruction has entered a new regime, with new challenges. Long-duration events with significant amplitude modulation are replaced with short-duration, near-constant SNR events. As He6-CRES nears a percent-level b_{Fierz} measurement, clustering high-power Fourier bins into events will be less error-prone, and event detection will become more sensitive.

3.7 Modeling CRES Event Slopes

N. Buzinsky, A. García, H. Harrington, R.J. Taylor*, and A. R. Young*

In addition to its primary scientific purpose as a probe of BSM Fierz interference in beta decays of ^{6}He and ^{19}Ne, He6-CRES offers a unique experimental window into the radiation of charged particles in a waveguide via the track slope, df_c/dt. Events slopes are positively-sloped in time-frequency space as the cyclotron radiation decreases the total energy E of the underlying charged particle:

$$\frac{df_{\mathrm{c}}}{dt} = -\frac{f_{\mathrm{c}}}{E}\frac{dE}{dt}. \tag{1}$$

For a 90° beta with mainband frequency within the He6-CRES RF bandwidth (17.9 GHz – 20.3 GHz), a considerable fraction of the total radiation emitted by the beta will be outside the RF bandwidth and not contribute to the event SNR, only to be observed (indirectly) via the event slope.

Experimental CRES slopes in a circular waveguide are observed to be broadly consistent with the expectation for the free-space result, from the Larmor formula, scaling with the Lorentz factor of the underlying beta as γ^4.

*Department of Physics, North Carolina State University, Raleigh, NC.

Track SNR and slope data are modified by reflective surfaces within the He6-CRES RF system. Fig. 3.7-1 shows the SNR and slope of an e^+ event observed at 1 T from a decay of ^{19}Ne, as a function of frequency (black). A naive model of a superconducting, infinitely long waveguide (blue), correctly derives (to $\sim$ percent-level), the scale of the slope of the resultant event, though none of the frequency-dependent features.

SNR oscillations are attributed to reflections off the conical graphite-epoxy termination, which was constructed to absorb radiation emitted by the beta in the direction opposite of the low-noise amplifier (LNA). Cyclotron radiation which reflects off the termination then interferes with the radiation emitted by the beta in the direction of the LNA, interfering constructively and destructively at different frequencies. This interference manifests as SNR oscillations, which can result in misreconstructions. The consequence of SNR oscillations due to interference, slope oscillations at the same frequency, are likewise observed. A more detailed model of the RF, including a reflective termination and finite conductivity for the waveguide is shown in red.

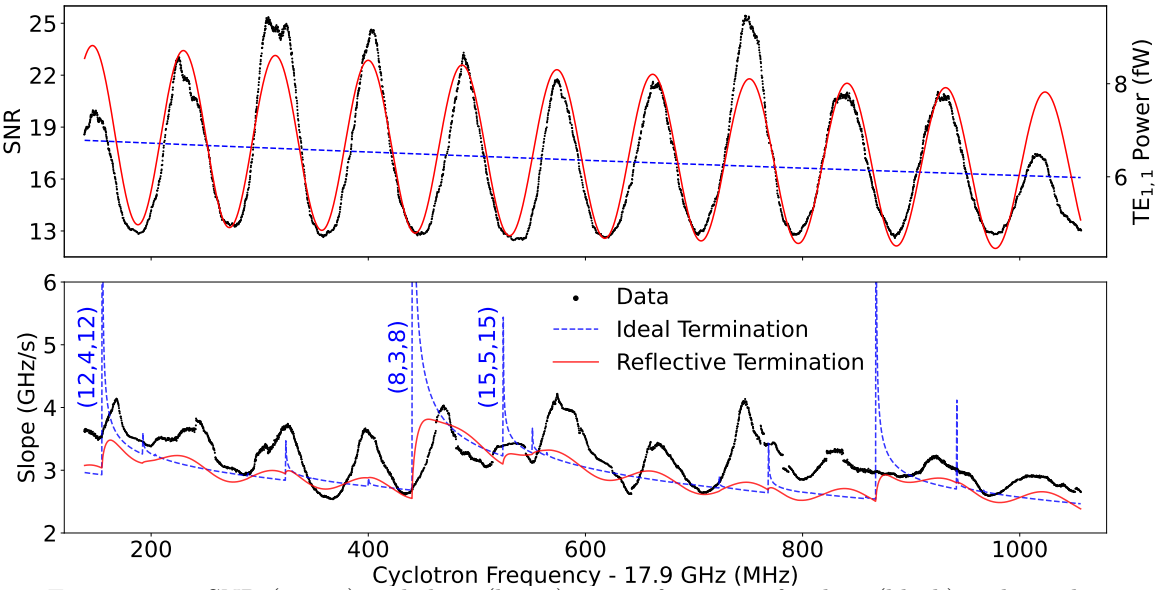

Figure 3.7-1. SNR (upper) and slope (lower) versus frequency for data (black) and simulations with (red) and without (dashed blue) accounting for termination reflections and finite waveguide conductivity. SNRs observed in data (upper, left axis) are compared to simulated $TE_{1,1}$ powers (upper, right axis). In the ideal termination model, simulated slopes diverge at TE cutoff frequencies, several of which are labeled with their respective n, m, and ℓ.

In principle, a detailed understanding of the track slope, and therefore the instantaneous cyclotron frequency $f_c(t)$, could be used to infer the underlying parameters of the radiating beta (e.g. pitch angle, radius), allowing better experimental energy resolution.

3.8 $E \times B$ system for trap emptying

N. Buzinsky, A. García, H. Harrington, H. E. Swanson, R.J. Taylor*, and A. R. Young*

In CRES experiments high-energy betas outside of the detection bandwidth will lose energy as they radiate and appear at the lowest frequency measured. Not only can these events be misidentified as having been created at the energy associated with the low energy cutoff, but given enough time the spectrogram will be completely filled by tracks from such events. This makes event construction difficult, so the magnetic trap must be emptied regularly. Thus far, this has been done by intermittently turning the magnetic trap coils on and off. This method requires leaving the trap off for ~ 15 ms, resulting in approximately a quarter of the data collection time spent emptying the trap.

The magnetic trap can be emptied much faster by using an electric field. Applying an electric field perpendicular to the magnetic field results in $\mathbf{E} \times \mathbf{B}$ drift, where the guiding center velocity of the betas gains an additional term

$$\boldsymbol{\nu}_d = \frac{\mathbf{E} \times \mathbf{B}}{B^2}. \tag{1}$$

For simple linear fields, we can estimate that for $|E| = 1000$ V/m and $B = 2$ T, the drift velocity is 500 m/s, and therefore it would take $\sim 20\mu$s to empty our trap. The chosen field magnitude could be accomplished by applying a 10V potential across the decay cell. Using an electric field would therefore be significantly faster and would avoid other possible issues with constantly changing the magnetic trap field (reproducibility, inducing currents in main magnet coils).

This past year, we have constructed 3 versions of the $\mathbf{E} \times \mathbf{B}$ decay cell: the original prototype with short electrodes, and refined short and long electrode versions. The original prototype exposed some design and construction issues that were fixed in the refined versions. We also designed and constructed a full-bridge high-voltage switch that allows each electrode to be powered independently with an external power supply and controlled by an external TTL pulse. The switch can power the electrodes up to 600 V and has an increase time of 50 ns. Fig. 3.8-1 shows pictures of the short and long decay cells in their testing assembly (no trapping coils, simplified flanges).

*Department of Physics, North Carolina State University, Raleigh, NC.

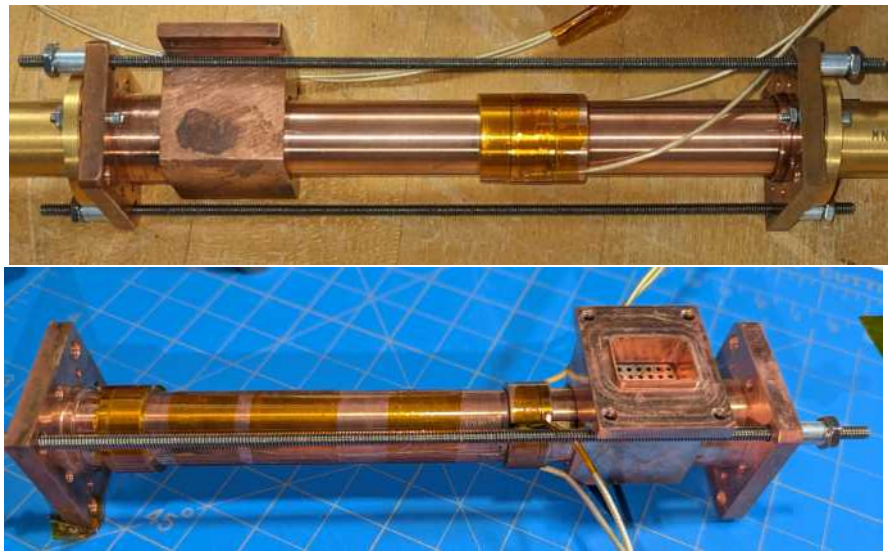

Figure 3.8-1. Pictures of short (top) and long (bottom) electrodes in a testing assembly.

We installed the short electrode $\mathbf{E} \times \mathbf{B}$ decay cell and tested its trap emptying efficiency to 3.25 T with ^{19}Ne. A detailed analysis of these data is forthcoming, but a preliminary inspection of the spectrograms indicates that the $\mathbf{E}\times\mathbf{B}$ decay cell is removing all trapped betas when pulsing each electrode once at voltages greater than 200 V. An example spectrogram is presented in Figure Fig. 3.8-2, where $B = 2$ T and $V = 600$ V. The total pulse time is 168 μs which is about 100 times faster than the trap emptying by turning off the trap coils. This improvement will increase our CRES event detection rate and allow us to decrease the time between trap emptying, which reduces events radiating into our bandwidth and decreases track lengths. Shorter track lengths will simplify event reconstruction by avoiding problems with changing power and slopes versus frequency that are discussed in Section 3.7.

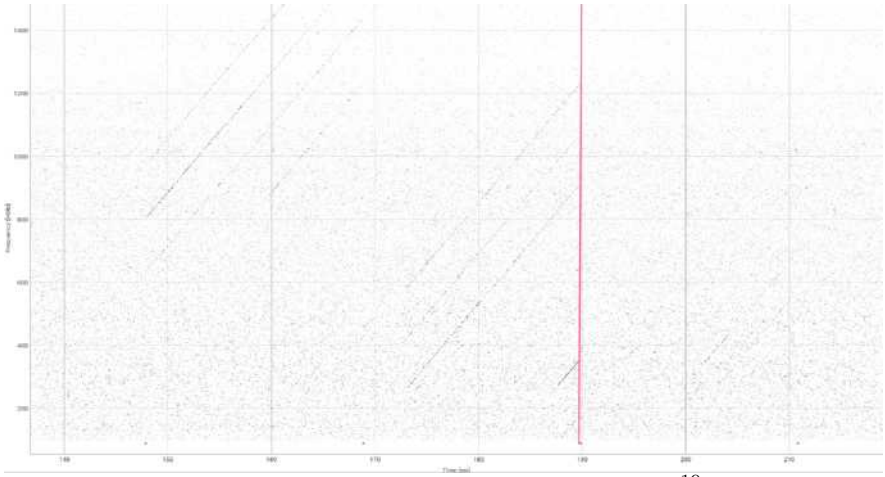

Figure 3.8-2. A spectrogram of a $\mathbf{E} \times \mathbf{B}$ emptying test. Taken with ^{19}Ne decays at 2 T and 600 V $\mathbf{E} \times \mathbf{B}$ pulses. $\mathbf{E} \times \mathbf{B}$ pulses are indicated by the 100 MHz high power signals. A red line is drawn to show that at the start of a pulse all tracks end.

3.9 Upgrades to `spec-sims` Monte Carlo tool

W. A. Byron, N. Buzinsky, A. García, L. Malavasi, and R.J. Taylor*

He6-CRES is developing `he6-cres-spec-sims`[1], a Monte Carlo simulation of CRES signals. To visualize the need to go outside of typical tools, such as GEANT or typical charged-particle trackers, it is useful to consider the large dynamic range needed. For example, we are interested in cyclotron frequencies of the order of 20 GHz and betas that can persist for seconds within a magnetic trap. So tracking of a single beta without appropriate approximations can take $\sim 10^{10}$ steps and we need to simulate millions of events under many different conditions. This all is before considering how the RF waves are generated, what possible effects there can be due to imperfect transmission of RF signals, echoes, etc.

The code base is undergoing an upgrade and refactoring campaign with the goal of optimizing computational performance and including simulations of a wide range of systematics that are present in the physical system. Given a configuration file setting both physical and simulation parameters, `spec-sims` executes a series of "simulation blocks": 1) generating distributions of beta energy, position, and direction, 2) from these distributions, generating "events" or individual betas trapped in a circular orbit without colliding with the waveguide wall, 3) generating a list of scattered track segments comprising an event and simulated physics information for each, and 4) for each segment, generating side-band frequencies and powers, recording track start and end times and frequencies, and downmixing track frequencies to DAQ bandwidth. The simulation relies on a number of computational functions to perform CRES dynamics calculations and to define the trap geometry and field profile. Prior to the refactor, these simulation blocks were combined in a single Python file, which has now been split up.

Many computational functions were rewritten to leverage the performance benefits of vectorized operations over a large number of events and segments, for example, improving the time for interpolating magnetic field strength by $10\times$. Additional new features include an improved technique for generating physical scattering angles, and a function for calculating the ∇B guiding center position drift frequency. The refactor also generally cleaned up the code base by removing a number of unused branches, functions, and additional scripts.

Previously, one of the largest performance bottlenecks was the numerical evaluation of axial integrals for axial frequency and mean magnetic field, and ∇B drift over an axial period. These integrals are of the form

$$4\int_0^{z_{max}} \frac{f(z)}{\sqrt{1-\frac{B(\rho,z)}{B(\rho,z_{max})}}}dz \tag{1}$$

The integral is over a quarter period, from the trap center at $z = 0$ to the turning point z_{max}, and multiplied by 4 for the full period. The simulation previously used Gaussian

*Department of Physics, North Carolina State University, Raleigh, NC.

[1]https://github.com/Helium6CRES/he6-cres-spec-sims.

quadrature to accurately but slowly integrate up to the singularity at z_{max}. Applying the following change of variables to an arbitrary integrand $f(x)$,

$$\int_a^b f(x)dx = \int_0^{\sqrt{b-a}} 2tf(b-t^2)dt = (b-a)\int_0^1 2uf(b(1-u^2)+au^2)du, \tag{2}$$

a singularity in the integrand at $z = b$ would transform into a discontinuity with finite limit at $t = 0$, and the integral can be evaluated with a faster numerical quadrature such as the Semi-open Simpson's rule skipping evaluation at $t = 0$. The second change of variables casts every integral over the same domain $u \in (0, 1]$ for fast vectorization. The integral optimization alone reduced total non-DAQ simulation time by a factor of almost 10, with the bottleneck still set by these integrals.

The code that defines the magnetic trap field profile and calculates trapped beta dynamics assumed a symmetric trap centered at $z = 0$. This was generalized to asymmetric traps at arbitrary trap centers. The motivation of this upgrade was to study the effect on CRES signals of an inverted trap current polarity or unwanted quadrupole and sextupole magnetic moments from current induced on the magnetic shim coils of the main magnet. Since the trap field is no longer symmetric about the trap center, integrals over a period of axial motion must be performed over a half period rather than a quarter period. Using the turning points z_{min} and z_{max} on either side of the trap center position z_c, the integrals are now of the form

$$2\int_{z_{min}}^{z_{max}} \frac{f(z)}{\sqrt{1-\frac{B(\rho,z)}{B(\rho,z_{max})}}}dz = -2\int_{z_c}^{z_{min}} \frac{f(z)}{\sqrt{1-\frac{B(\rho,z)}{B(\rho,z_{max})}}}dz + 2\int_{z_c}^{z_{max}} \frac{f(z)}{\sqrt{1-\frac{B(\rho,z)}{B(\rho,z_{max})}}}dz. \tag{3}$$

Note that the field at the two turning points is identical $B(\rho, z_{max}) = B(\rho, z_{min})$. In this form, the same method for fast numerical integration over the discontinuities at z_{max} and z_{min} as described for the symmetric trap is applied. In addition to the generalized integrals, the trap field class and simulation blocks were updated with the necessary properties and functions to find the trap center through minimization (Nelder-Mead) and both turning points by root-finding (Brent's method). Furthermore, considering a general asymmetric trap has prompted consideration of new ways a randomly generated beta may be found to be untrapped, for example a beta that is trapped in one direction along z but not in the other.

3.10 Toward a ^{79}Kr source

A. García, N. Oaxaca, D. W. Storm, and H. E. Swanson

Toward the goal of characterizing the CRES detection system over a broad range of energies, we are working on the production, purity, and transport of a ^{79}Kr calibration source. It produces conversion electrons of $\approx$ 11 keV, 31 keV, 130 keV, 604 keV, as well as a continuum

β^+ spectrum with $\approx$ 604-keV endpoint. We are using the ^{79}Br$(p,n)^{79}$Kr reaction by firing a proton beam from the tandem accelerator at 13 MeV at a potassium bromide target through a 2 mil Al window.

For this study, we built a simple Faraday cup, our target, and a copper tube connection from our target in the 24 inch scattering chamber in Cave 2. The copper tube was connected to a turbo pump which was used to compress the gaseous activity. At the back of the turbo pump we placed a cell with valves on both sides so it could be isolated and a copper window for gamma-ray observation.

A 5-min bombardment with $\approx$ 0.9 μA yielded a decay rate of 4×10^9 decays/s in rough agreement with expectations, based on the known cross section. A Ge-detector spectrum is shown in Fig. 3.10-1.

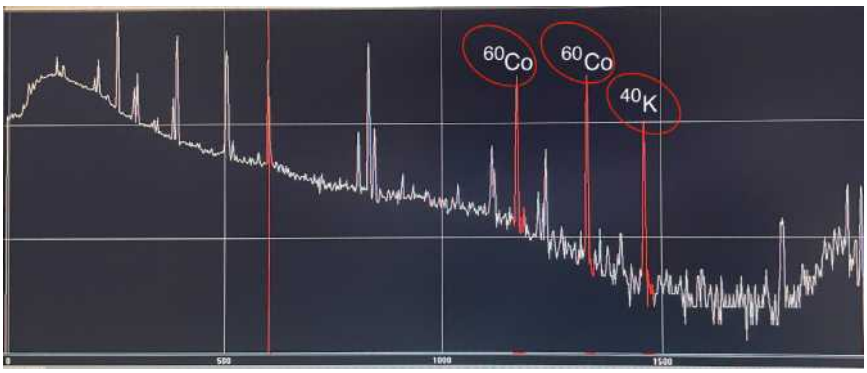

Figure 3.10-1. Gamma-ray spectrum from a Ge detector placed near the cell containing the ^{79}Kr produced at CENPA.

Compressing the activity into a cell with pressure monitors indicated $\approx$ 0.3 Torr. The pressure due to only the ^{79}Kr, according to the measured rate is $< 10^{-9}$ Torr, so most of the pressure is due to contaminants. No indication of a radioactive contaminant was found using the gamma-ray spectrum. The reaction used can also produce ^{37}Ar and ^{39}Ar on the potassium in the target, but they should be produced at a much lower rate according to our calculations. Their effects for CRES signals is easily distinguishable from those of ^{79}Kr.

The next step is to reduce the contaminants using a combination of zeolites and a getter pump with the goal of achieving ^{79}Kr of high purity, which would allow observation of CRES signals.

3.11 Redesigning the cryo-II vacuum pump

A. García, H. Harrington, and P.T. Kolbeck

The Cryo-II vacuum pump (C2) is an important step in cleaning the vacuum of contaminant gases, mainly CF_4 and SF_6, and secondarily common contaminants such as nitrogen and water. The pump is based on a modified CTI-Cryogenics Cryo-Torr 8F pump (8F), where a custom-built smaller chamber (adsorption volume) connected to the CRES decay cell, is thermally connected to the 8F cold head so as to get cooled down to temperatures below 40K, but has its vacuum isolated from the 8F volume. The contaminant gasses should condense on the walls of the adsorption volume while the neon and helium, which have lower condensation temperatures, pass through onto the detector.

Two main effects are at play at these low temperatures: cryosorption, by which the gases adsorb in less than a monolayer onto a particular surface, such as charcoal, and cryocondensation, by which gases freeze out in more than one layer. Cryosorption temperatures tend to be higher than cryocondensation temperatures because of surface effects. Condensation saturation curves are easily available. Adsorption isotherms are dependent on the adsorbant/adsorbate and rely on specific experimental data. At a vapor pressure of 10^{-5} Pa, the cryocondensation temperatures for Ne and He are, respectively, $\sim$6.5 K and $\sim$0.5 K, while the contaminant gases are between 20 and 120 K at [1].

[1] C. Day, Basics and applications of cryopumps, 2007, https://cds.cern.ch/record/1047069.

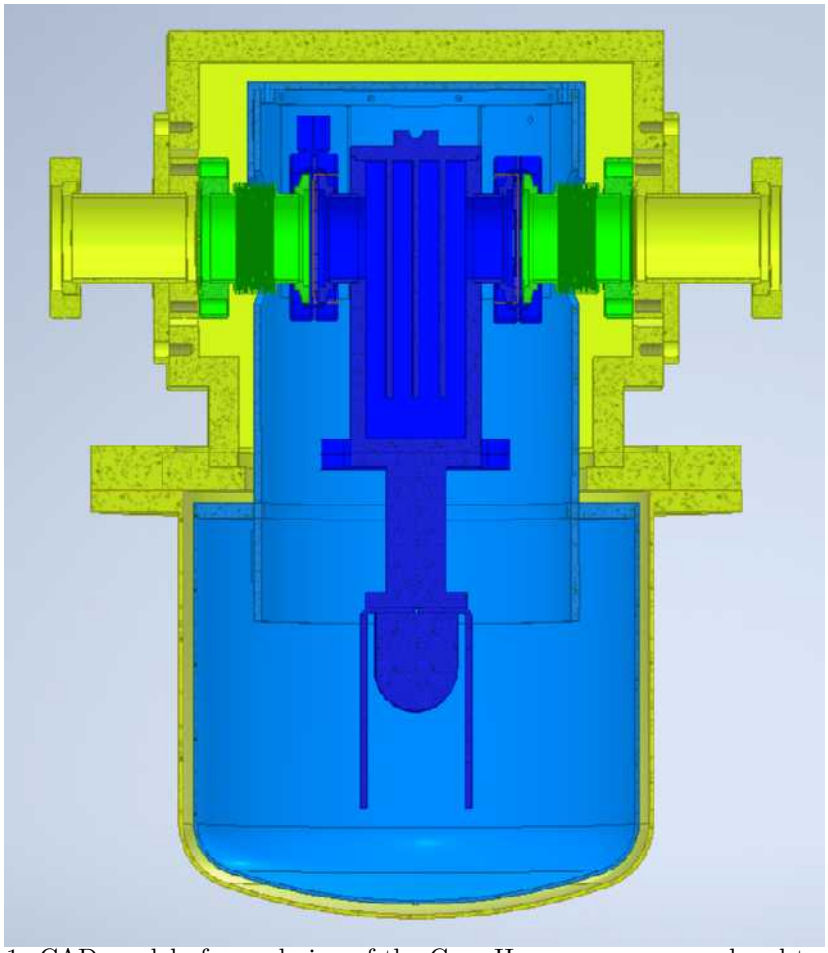

Figure 3.11-1. CAD model of new design of the Cryo-II vacuum pump, colored to indicate different temperature regions of the design. The outer hull (yellow) is at room temperature. The radiation shield (light blue) is at ∼70 K. The adsorbtion volume and cold head (dark blue) are at ∼15 K. There is a thermal gradient between room temperature and 15 K across the flex bellows (green).

The existing C2 has a leak connecting the adsorption volume and the 8F volume, exposing the active gas to the charcoal adsorbers and the cold head of the 8F pump. With current C2, the CRES rate decreases rapidly when the cold head drops below ∼12.5 K, at which temperature the pumping speed of charcoal in Ne rapidly increases[1], indicating that neon is adsorbing onto charcoal adsorbers in the 8F volume. Operating with a cold head above 12.5 K does not adsorb neon, however, the large, cold 8F volume sequesters it. Only ∼10% of the neon passes through C2, with the other 90% stuck in the 8F volume.

To resolve this issue, C2 is being redesigned with UHV seals, shown in Fig. 3.11-1. The new design will similarly have an adsorption volume thermally connected to the 8F cold head. The stress of thermal contraction, as well as the insulation between 300 K and ∼15 K, will be handled by a flex bellows, connected by standard KF and CF seals. The heat transfer through

[1]Matthieu Scannapiego and Christian Day 2017 IOP Conf. Ser.: Mater. Sci. Eng. 278 012160.

the flex bellows is conservatively expected to be $< .7$ W. Aluminum gaskets are used for the KF seals to prevent failure due to thermal cycling. The cryocondensation curves indicate that to condensate contaminant gases, temperatures below 20 K are required. Cryosorption temperatures are higher than cryocondensation temperatures, due to surface effects, which makes the capability to reach 20 K more than sufficient. Given specifications for the 8F refrigerator and the flex bellows, along with conservative estimates, the new C2 sorb vol is expected to be able to reach a temperature of 12 K, with heating loads of $\sim$ 9 W in the first stage and $\sim$.7 W in the second stage of the 350C cryodyne refrigerator. The expected cooldown time to 20 K (a valid operating temperature) is expected to be $\sim$3 hours, and another $\sim$1 hour to 12 K. There is a heater clamped to the outside of the adsorption volume together with a thermometer to provide control of the adsorption volume temperature. The final steps include optimization of the thermal / gas conductance and volume by adjusting the connection to the cold head and the size and interior of the box.

The adsorption volume consists of a copper box with stainless steel KF flanges soldered to either side of the box. The box has a lid which is sealed with indium and will hold fins that stick into the adsorption volume. These fins will hold charcoal adsorbers to provide additional pumping capacity. The lid is easy to remove and reinstall, allowing multiple adsorber designs to be tested to optimize conductance and pumping capacity at later times. The feedthroughs for gas and electronics can also be removed and switched for new designs without issue, allowing for easy future modification. All vacuum seals are ultra high vacuum, ensuring that there are no leaks between the adsorption/CRES volume and the 8F volume, which should increase the amount of neon in the decay cell by a factor of 10.

4 Dark matter searches

ADMX (Axion Dark Matter eXperiment)[1]

4.1 Searching for QCD axions between 800 MHz and 2 GHz

T. Braine*, K. Enzian, M. Guzzetti, C. Goodman, C. Hanretty, L. J. Rosenberg, G. Rybka, J. Sinnis, and D. Zhang

The Axion Dark Matter eXperiment (ADMX) is an axion haloscope[2] housed at the University of Washington's Center for Experimental Nuclear Physics and Astrophysics. It consists of a 136-liter cylindrical, copper-plated, resonant microwave cavity with a copper tuning rod that is immersed in a 7.6 Tesla superconducting solenoid. The magnetic field stimulates the decay of axions into microwave photons producing a signal which, when on resonance with the cavity frequency, becomes amplified making something once thought to be undetectable, detectable.

Axions were first proposed as a solution to a long-standing mystery related to the quantum chromodynamics (QCD) Lagrangian, known as the strong CP problem, by Peccei & Quinn in 1977[3]. Not long after the axion was introduced, physicists realized that its properties such as electric neutrality, feeble interactions with standard model particles, and abundant production in the early universe make it a compelling dark matter candidate as well.

There are two benchmark models that describe the QCD axion: the Kim-Shifman-Vainshtein-Zakharov (KSVZ) [4,5] model and the Dine-Fischler-Srednicki-Zhitnitsky (DFSZ)[6,7] model. Many find the more weakly coupled of the two, DFSZ, to be more compelling due to its compatibility with Grand Unified Theories. However, reaching this level of sensitivity is nontrivial. ADMX was the first group to reach DFSZ[8], and to date remains one of only two groups[9] that have reached it at all.

So far, ADMX has excluded both KSVZ and DFSZ axions between 645-800 MHz (2.66-3.3 μeV) over the course of two data taking runs[10,11] Additionally, ADMX excluded KSVZ

*Presently at Pacific Northwest National Laboratory

[1]ADMX is supported by the DOE Office of High-Energy Physics and makes use of CENPA resources by recharge to the cost center.

[2]P. Sikivie, Phys. Rev. Lett. **51**, 1415 (1983).
[3]R.D. Peccei and H. Quinn, Phys. Rev. Lett. **38**, 1440 (1977).
[4]J.E. Kim, Phys. Rev. Lett. **43**, 103 (1979).
[5]M.A. Shifman, A.I. Vainstein, and V.I. Zakharov, Nucl. Phys. **B166**, 493 (1980).
[6]M. Dine, W. Fischler, and M. Srednicki, Phys. Lett. **B104**, 199 (1981).
[7]A.R. Zhitnitsky, Sov. J. Nucl. Phys. **31**, 260 (1980).
[8]N. Du et al. (ADMX Collaboration), Phys. Rev. Lett. **120**, 151301 (2018).
[9]Andrew K. Yi et al. (ADMX Collaboration), Phys. Rev. Lett. **130**, 071002 (2023).
[10]N. Du et al., Phys. Rev. Lett. **120** 151301 (2018).
[11]T. Braine et al., Phys. Rev. Lett. **124** 101303 (2020).

and DFSZ axions between 800-1015 MHz (3.3-4.2 μeV) and 943-991 MHz (3.9-4.1 μeV) respectively during its third data taking run[1]. Beginning in December 2023, a fourth data taking run has searched for axions between 1 and 1.4 GHz. Preliminary analysis of this data, with sufficient sensitivity to exclude or detect axions consistent with KSVZ models, even at subdominant contribution to dark matter.

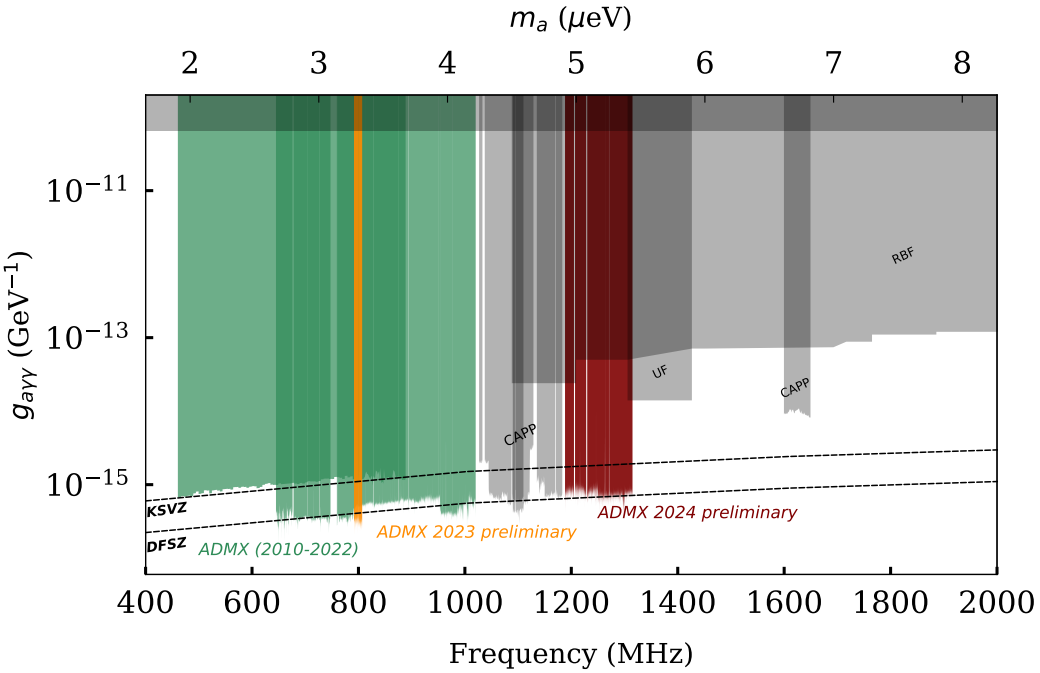

Figure 4.1-1. Axion-photon coupling constant sensitivity plot. The vertical axis is the axion-photon coupling constant, $g_{a\gamma\gamma}$, with smaller values indicating higher sensitivity. The two horizontal axes are axion mass and frequency respectively. Exclusion limits previously set by ADMX are shown in green, while those set by other experiments are shown in gray. Sensitivity for ADMX's most recent data taking run are shown in orange and red.

[1] C. Bartram et al. (ADMX Collaboration), Phys. Rev. Lett. **127**, 261803 (2021).

4.2 Preparing for a high frequency axion search with ADMX Orpheus

G. Rybka and J. Sinnis

Orpheus is a pathfinder axion haloscope project which uses a novel cavity design to search for axions in mass ranges generally above the values that traditional tunable haloscopes are sensitive to. Orpheus searches for axions with the 18th order TEM mode of a Fabry-Perot interferometer. The frequency of this mode is tuned from about 15.8-16.8 GHz, which corresponds to axion masses of roughly 65-70 μeV. Generally, the use of the higher order modes of a resonator in an axion search is not feasible, because the axion signal power scales with the effective volume V_{eff}, which follows this proportionality relation:

$$V_{eff} \propto \int \vec{E} \cdot \vec{B} d^3x \tag{1}$$

where $\vec{E}$ is the electric field of the mode used to search for the axion and $\vec{B}$ is an externally applied magnetic field. The direction of $\vec{B}$ is fixed, so using a higher order mode for $\vec{E}$ introduces oscillations into the integral which cancel out. To avoid this cancellation of the effective volume, dielectric plates are placed along the length of the resonator with even spacing, such that select oscillations of $\vec{E}$ have diminished amplitudes. This reduces the cancellation due to the oscillations in the integral.

The experimental hardware has been completed and is undergoing testing. The final major piece of the experiment is the dipole magnet, which was constructed over the last three years. In the last year, the wire-guide structures for connecting the two sides of the magnet and the vapor-cooled leads were designed and built and the magnet has been assembled and installed, with various necessary modifications and fixes. The magnet's power supply and its control software have been installed and programmed, and a fixture with multiple hall-effect sensors to map the field has been built and installed.

A significant improvement in the cryogenic system is nearly completed: connecting Orpheus to the ADMX helium recovery plant. The duration last data-taking run was limited by the boil-off of liquid helium used to cool the experiment. In order to run longer during data-taking and while testing our superconducting magnet, we have installed stainless steel pipes along the north wall of the accelerator hall, leading down into the pit beneath the tandem, to channel our helium boil-off into the ADMX helium recovery system. This will allow us to run for longer within our limited budget.

Another point of progress for the experiment in the last year was the simplification of the DAQ software. The experiment used to be orchestrated by a host of computer programs that were relatively difficult to use and unnecessarily complicated for a small experiment with only one operator. Furthermore, the old system relied on Kubernetes and Dripline (a controls software developed for use in Project 8), and we have lost all on-site personnel with relevant expertise. Because of this, it was decided to remove the DAQ orchestration software and rely on python scripts. The magnet testing will be a soft test-run of the new DAQ. We expect to turn on and test the magnet within the next two months.

Figure 4.1-1. The Orpheus insert with the hand-made dipole magnet installed. The wire-guide and the bottom of the vapor-cooled leads are partially visible as well.

DAMIC

4.3 DAMIC-M detector

A. E. Chavarria, C. M. Hastings, M. Heuhn, R. Roehnelt, and outside collaborators*

Following an extensive development, the design of the DAMIC-M detector was finalized and components are currently being procured for its installation in the Modane Underground Lab (LSM) in France. A cross sectional view of the detector is shown in Fig. 4.3-1.

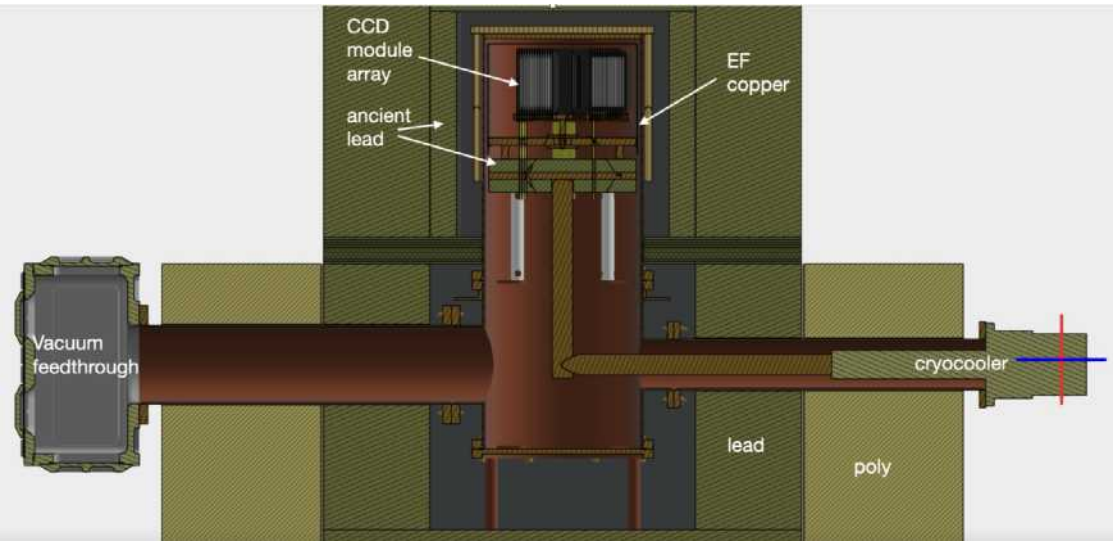

Figure 4.3-1. Cross sectional view of the DAMIC-M detector inside its shield with its main components labeled.

The design of the 208-CCD array that lies at the heart of the experiment was prototyped and validated at CENPA[1], with the construction and testing of the first 28 modules ongoing (Sec. 4.4). A first deployment of 26 modules (104 CCDs, half of the array) will happen by mid-2025, and the detector will be commissioned in the latter half of the year.

The CCD array is supported by an ultra-high radiopurity copper structure that is currently being machined at the Sanford Underground Research Facility (SURF) in South Dakota. The array is surrounded by a copper infrared (IR) shield and housed inside a copper cryostat. Both the IR shield and the top vacuum can of the cryostat are made from ultra-high radiopurity copper. The copper was gifted by the MAJORANA Collaboration thanks to CENPA. Other copper parts will be machined from oxygen-free high-conductivity (OFHC) copper that is currently being procured from Luvata. Extensive precautions are being taken to minimize the cosmogenic activation of radioactive cobalt in the copper. Smaller copper

*DAMIC-M Collaboration.

[1]CENPA Annual Report, University of Washington (2023) p. 92.

parts are machined underground, while, for larger parts, we are coordinating with the machine shops to minimize their time on the surface. The copper parts machined at SURF will be transported to LSM in a shielded container.

The CCD array will be shielded in all directions by 20 cm of lead, with the inner 5 cm of ancient origin with ^{210}Pb activity < 50 mBq/kg. We await quotes from LEMER Foundry in France and MTH Metall-Technik in Germany for the casting of the ancient lead. The outer 15 cm of lead will be made from high-radiopurity bricks. A fraction of the bricks will come from the lead that CENPA contributed to the MAJORANA Demonstrator. We are currently investigating whether the "clean SS" lead available in NPL could be used to complete the shield.

The DAMIC-M electronics were developed by collaborators and validated at CENPA during the procedural testing of DAMIC-M CCDs (Sec. 4.4). The electronics components for the 26 CCD modules are being fabricated in Europe.

A calibration source to generate charge in the CCDs and confirm their response in-situ was developed and tested at CENPA. It consists of a thin high-radiopurity copper wire that loops around the base of the array and is connected to an external DC power supply. By running a current, the wire heats up and emits thermal radiation inside the IR shield, which is absorbed and ionizes the CCD silicon target.

Once completed in 2025, DAMIC-M will acquire kg-year exposures with a radiogenic background $< 1\,(\text{keV kg day})^{-1}$ and an energy threshold of a few electron volts. This will provide unprecedented sensitivity to the interactions of sub-GeV dark-matter particles with electrons, which will allow us to probe several benchmark models of hidden-sector theories.

4.4 Packaging and Testing of DAMIC-M CCD Modules at UW

K. Aggarwal, A. E. Chavarria, M. Conde, C. M. Hastings, M. Huehn, H. Lin, R. Roehnelt, and M. Traina.

The DAMIC-M Collaboration is currently fabricating its first 28 CCD (Charge-Coupled Device) modules at the University of Washington (UW). The modules will be installed in the DAMIC-M experiment at the Modane Underground Laboratory (LSM) in France. The DAMIC-M team at CENPA developed and validated the CCD module design and leads the fabrication effort.

DAMIC-M has strict radiopurity requirements to achieve an overall background rate less than 1 (keV kg day)$^{-1}$. A few critical sources of contamination must be mitigated to this end: ubiquitous U/Th in dust and material residues, environmental radon and cosmogenic activation. U/Th mitigation involves chemical cleaning with various solvents and clean-room/laminar-flow hood operations. Radon plate-out is mitigated by handling detector parts in nitrogen flushed environments and/or using radon abatement systems. Cosmogenic mitigation requires at least several meters water-equivalent of shielding. At UW, we have put in place procedures to suppress contamination from these sources and meet DAMIC-M

radiopurity requirements.

The DAMIC-M CCD module consists of three main elements: 4 CCDs, 1 silicon pitch adapter and 1 low-background flex cable. Pitch adapters and CCDs are both produced starting with n-doped, high-resistivity silicon wafers from an ingot grown by Topsil for the Collaboration. DAMIC-M CCDs were fabricated at Teledyne-DALSA in Quebec, Canada. Precautions were taken from ingot growth to storage of the diced CCD wafers to mitigate radiocontamination, including the use of an 18-ton steel shield in a container for transport across the North Atlantic and North America to Seattle. The pitch adapter consists of aluminum traces patterned on a silicon frame, on which four CCDs are glued, and acts as an interposer between the flex cable and the CCDs. The pitch adapters are fabricated in the Washington Nanofabrication Facility (WNF) on UW campus. The flex cables are fabricated by Q-Flex in collaboration with Pacific Northwest National Laboratory (PNNL) to ensure low radioactive contamination[1]. Fig. 4.4-1 shows a DAMIC-M CCD module with the main components labeled.

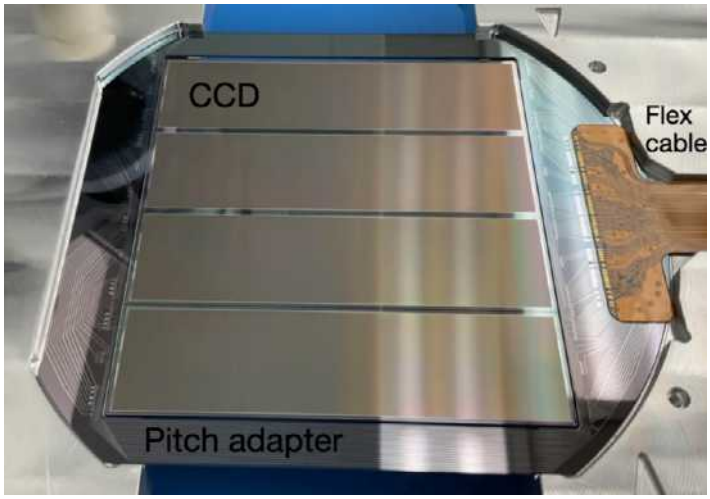

Figure 4.4-1. Close-up of a DAMIC-M CCD module with its salient components: CCD, pitch adapter and flex cable.

To optimize DAMIC-M performance, individual CCD dice must be evaluated first, with the best selected for modules. The basic requirements for the selected CCDs are: low electronic noise of $\sim 4e^-$ in a single pixel measurement, single-electron resolution when performing $\sim$100 non-destructive charge measurements of the same pixel, low defect density in the CCD active silicon and high charge-transfer efficiency. Modules are then packaged with the best CCDs and tested to confirm their good performance. The process flow of DAMIC-M packaging and testing activities at UW is:

- Storage in the Gravity Garage in the North Physics Laboratory (NPL);
- CCD die packaging in the Physics and Astronomy Building (PAB);

[1]I. Arnquist *et al.*, EPJ Tech. Instrum. **10**, 17 (2023).

- CCD die testing in PAB;
- Storage in Gravity Garage in NPL;
- Module packaging in PAB;
- Module testing in PAB.

Storage with cosmogenic-neutron and radon mitigation

To mitigate cosmogenic activation, we use the Gravity Garage in NPL for long-term storage, which offers between 4.3 m and 6.1 m of soil overburden. Cosmogenic tritium production in silicon is dominated by fast neutrons with kinetic energies >16 MeV. From a measurement of the rate of neutron signals >10 MeV_{ee} on the surface and in the Gravity Garage with a BC501-A scintillator detector, we found a suppression of a factor ∼50 in the fast-neutron flux. The rate was also measured in the PAB basement lab, and we confirmed a fast-neutron suppression of ∼5.

The CCDs arrived to UW in two wafer cassettes, each containing 24 diced silicon wafers, with 4 CCDs per wafer. To minimize exposure of component surfaces to radon in the air, we set up nitrogen-flushed storage bins using boil-off from a liquid nitrogen dewar. The nitrogen concentration is monitored by an oxygen sensor, which is connected to an Arduino that controls solenoid valves to keep the nitrogen (oxygen) concentration above (below) a set point. A similar system is set up in the PAB clean room where packaging and testing operations are conducted. Either one or two wafers are transferred every day from NPL to PAB, using electrostatic discharge-safe (ESD-safe) equipment and a laminar-flow hood. We double bag wafer shippers and flush the inner bag with boil-off nitrogen for transport.

Die Packaging and Testing

Our PAB clean room features a packaging workstation equipped with a K&S wire-bonder, ESD-safe tools: mats, straps, tools, humidity and radon sensors. In addition, we assembled and commissioned two CCD test chambers contributed by the DAMIC-M group at Johns Hopkins. The PAB clean room was cleaned thoroughly to remove dust and oil before starting activities, and cleaned daily thereafter. The packaging consists of installing and connecting the CCD in a die-test box, from which it can later be retrieved. After packaging, three die-test boxes are installed in each test chamber to characterize their performance. The operations were conducted seven days a week with packaging and testing shifts split between UW and UChicago collaborators, respectively. A full cycle, encompassing die packaging, testing, and retrieval, is optimized to be completed in 24 hours, for a total of six CCDs tested daily. In October 2024, we completed the testing of 188 dice in 35 days, with 58% of the devices deemed good for modules, sufficient for the packaging of 28 modules for DAMIC-M (Sec. 4.4). The radon concentration during die packaging was measured to be 4 ± 2.5 Bq/m^3 and we exposed the dice to clean-room air for 1.5 ± 0.5 hours.

Fig. 4.4-2 shows the main components of the die-test box. The box itself consists of three parts: a bottom layer that supports the CCD die, a mid layer where a flex cable is affixed, and a top lid. Once the CCD is installed in the box, aluminum wires are bonded to connect 74 pairs of pads from the CCD to the flex cable. During wire bonding, a presser plate with rubber cups is used to hold the CCD in place. The presser is subsequently removed when the box is installed in the test chamber to prevent introducing additional stress on the die.

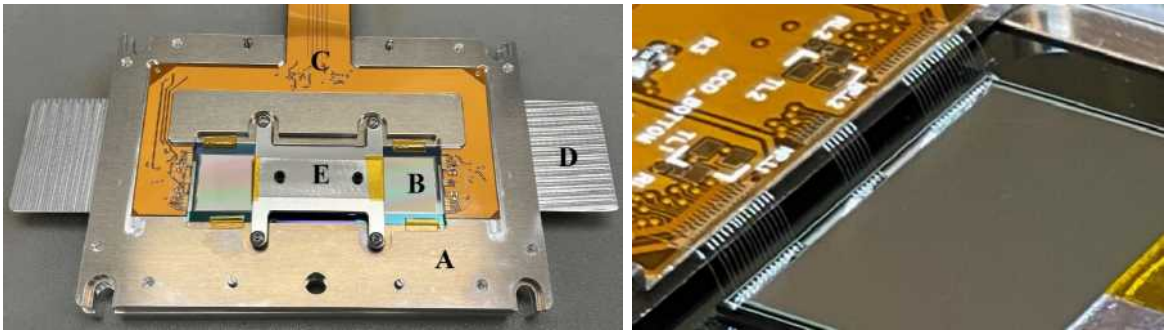

Figure 4.4-2. Left: Components of the die-test box: (A) the middle layer. (B) the CCD mounted on the bottom layer. (C) the flex cable. (D) the lever plate used to disassemble the box. (E) the presser plate, which is installed only during the wire bonding and CCD retrieval. Right: The wires bonded from the CCD pads to the flex cable pads.

Fig. 4.4-3 shows the test chambers and three die-test boxes installed inside. The test chamber consists of a 12-inch cubic cryostat, a vacuum pump, a cryocooler, temperature sensors and controllers, and the DAMIC-M custom electronics chain. The die-test boxes are mounted vertically on a 10 inch-long copper cold finger that is attached to the cold tip of the cryocooler. This configuration ensures the cooling (warming) process can be completed in less than 6 (3) hours. The die test is conducted at a target temperature of 180 K, where the lattice defects can be identified effectively as hot spots in the CCD images from leakage current. We look for CCDs that produce "clean" images, with a uniform background from leakage current and sharp tracks from environmental ionizing radiation. Images are also taken specifically to measure the noise and charge-transfer efficiency of the CCDs.

Figure 4.4-3. Left: Main components of the test chamber. Right: Three die-test boxes installed vertically inside the test chamber. The Teflon table below below the boxes provides support during the installation to minimize the torque on the cryocooler cold tip.

When the test is finished, the die-test boxes are uninstalled and the wire bonds are broken to retrieve the CCD. The middle layer of the box is lifted with the assistance of two lever plates inserted from the sides. Due to the geometry of the wire loops (Fig. 4.4-2), >99% of wires detach from the CCD side and are left on the flex pads. The retrieved CCDs are stored in Gel-Pak membrane boxes and moved to the Gravity Garage in NPL.

Module Packaging and Testing

As of November 2024, we are preparing to package the 28 CCD modules for DAMIC-M. The modules will be ready by the end of 2024 and will be shipped to LSM in France in the shielded container. We already received the first batch of 20 flex cables, while the pitch adapters are being fabricated in WNF.

The radiopure flex cables for DAMIC-M are 1.5 m long to traverse the detector shield and reach the feedthrough box (Sec. 4.3). QFlex and PNNL identified radiopure material alternatives and implemented cleaner production processes to minimize radiocontamination. For the DAMIC-M flexes specifically, they achieved a reduction factor of 26 in ^{238}U contamination compared to commercial flex cables.

Pitch-adapter fabrication at WNF starts with oxidation of a 1.6 μm thick silicon dioxide layer on the wafer surface. Traces are deposited on the wafer oxide through a bi-layer lift-off process. The wafer is first coated with photoresist layers and a Heidelberg-DWL66plus mask writer is used to inscribe the trace patterns on the photoresist using a 405 nm laser. The trace patterns are then etched by performing acetone wet etching followed by reactive-ion etching. Metal of 1 μm (20 nm Ti + 980 nm Al) in thickness is then deposited by evaporation or sputtering on the wafer. After the remaining photoresist layers are "lifted off" to leave only the traces, a central square window is cut from the wafer. The corners of the window are rounded with a radius of 1 mm to mitigate the risk of cracks in the corners. The corners

are cut with the 355 nm laser in NPL, while the remaining cuts are performed with the dicing saw at WNF. All fabrication steps, except the laser cutting, happen in the ISO class-5 clean room at WNF. For the laser cutting, a protective photoresist layer is applied, which is later removed when the wafer returns to WNF for dicing.

The modules are packaged in our PAB clean room. Four CCDs and a flex cable are glued to the pitch adapter with Epotek 301-2 epoxy. Three stackable jigs, each capable of holding one module, accurately position all components in place when gluing. Fig. 4.4-4 shows one module resting on the jig with epoxy applied between components. The jigs are heated up to 80 °C to speed up the glue curing, and they are kept in a semi-hermetic container flushed with nitrogen to mitigate radon exposure. Once glued, wires are bonded between the CCDs, the pitch adapter, and the flex cable. Three modules can be fabricated per day.

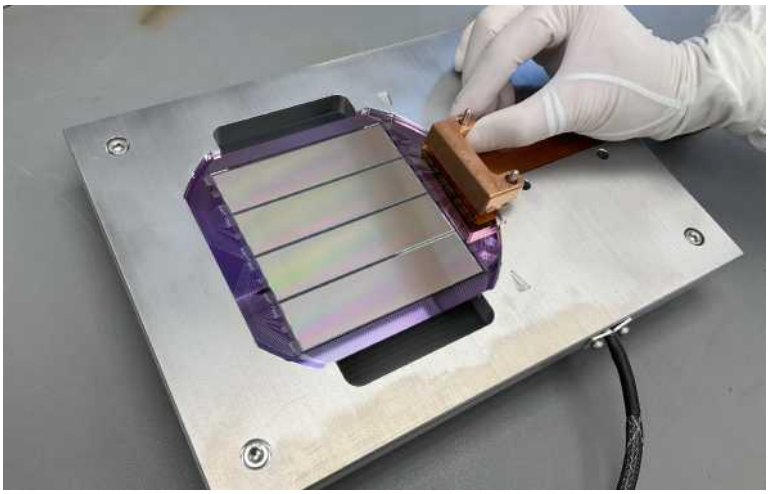

Figure 4.4-4. The jig for DAMIC-M module packaging. The jig aligns the components and keeps them in place when gluing. A copper weight is loaded on the flex cable to flatten the contact surface.

Following module packaging, testing will be conducted similarly to the die testing procedure, with three modules at a time in each of the two test chambers. The modules will be tested at 180 K, where the defects can be mapped, and at 135 K for characterization at the operating temperature of DAMIC-M. Additionally, each module-test box will include two 25 μm-thick activated iron foils affixed to the top and bottom lids, respectively, for calibration. The foils were activated at the nuclear reactor in the University of Maryland and their ^{55}Fe and ^{59}Fe activities were measured in our CCD test system in NPL. As planned, by now most of the high-energy radiation from ^{59}Fe has decayed, leaving only low-energy ^{55}Fe X rays with the desired intensity for calibration.

4.5 Recent results and progress with prototypes underground

A. E. Chavarria, M. Traina, and outside collaborators*

The DAMIC-M Collaboration deployed prototypes in two test systems underground to inform the design and operation of the upcoming DAMIC-M detector (Sec. 4.3): the Low Background Chamber in Modane Underground Lab (LSM) and the DAMIC detector at SNOLAB. All prototypes were packaged at CENPA and deployed by CENPA personnel.

In October 2021, two large-format 24 megapixel skipper CCDs were installed in the LBC, with first dark-matter search results previously reported[1]. A fraction of the data was re-analyzed to search for a daily modulation in the rate of single-electron events. Dark-matter particles with MeV masses and relatively large, yet unexplored, interaction cross sections ($\bar{\sigma}_e > 10^{-34}\,\mathrm{cm}^2$) can scatter in the Earth, which leads to a daily modulation in the dark-matter flux through the detector as the Earth rotates about its axis, as depicted in Fig. 4.5-1. Such dark-matter particles have only a few electron volts of kinetic energy and can only ionize single electrons in silicon. The absence of a modulation on top of the decaying rate of single-electron events from dark current over 63 days allowed us to place world-leading constraints on the scattering of dark-matter particles of ∼1 MeV mass with electrons[2].

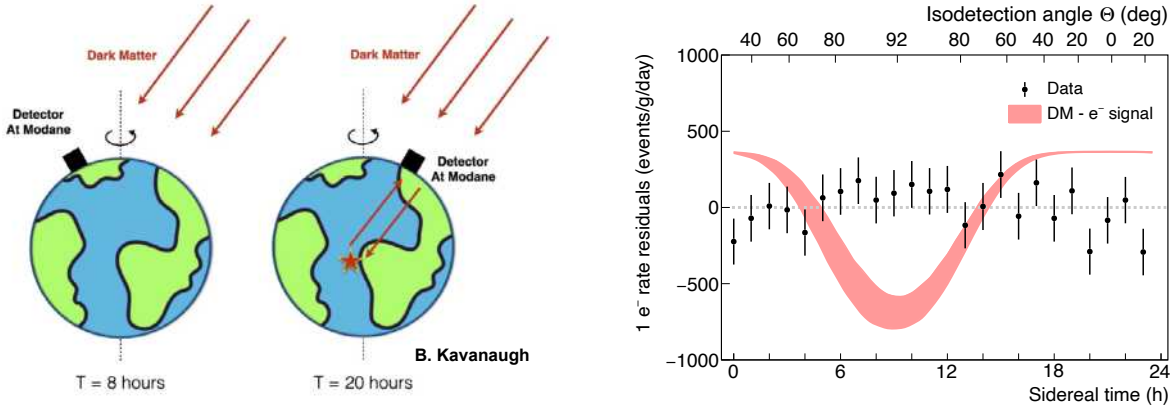

Figure 4.5-1. Left: At large enough interaction cross sections, the Earth acts as a reflector, leading to a daily modulation of the dark-matter flux through the detector. Right: Single-electron rate above backgrounds as a function of sidereal time (or isodetection angle). The red band shows the expected signal from dark-matter particles with a mass of 1 MeV and an interaction cross section $\bar{\sigma}_e = 10^{-32}$ via an ultralight mediator.

In February 2023, the LBC was upgraded with two prototype DAMIC-M four-CCD modules[3]. Several data runs were acquired to understand the background sources and the performance of the modules. The use of high-radiopurity copper lids for the CCD box, which were electroformed at the Canfranc Underground Laboratory (LSC), resulted in a decrease

*DAMIC and DAMIC-M Collaborations.

[1] CENPA Annual Report, University of Washington (2023) p. 97.
[2] DAMIC-M Collaboration, Phys. Rev. Lett. **132**, 101006 (2024).
[3] CENPA Annual Report, University of Washington (2023) p. 93.

in the overall background rate to half of its previous value[1]. The differential background rate of $6.7 \pm 1.1\,\mathrm{keV}^{-1}\,\mathrm{kg}^{-1}\,\mathrm{day}^{-1}$ is the lowest ever achieved in a CCD detector. The modules were also upgraded with DAMIC-M electronics and its operating parameters optimized to mitigate sources of dark current. In addition, efforts were made to minimize light leaks into the copper box. This resulted in a total single-electron rate $< 0.5\,e^-\,\mathrm{mm}^{-2}\,\mathrm{day}^{-1}$, a factor of 50 lower than the previous installation. A science run is ongoing with these significant improvements in backgrounds. We aim to acquire $>1\,\mathrm{kg\,day}$ of exposure by the end of 2024 to improve by several orders of magnitude our sensitivity to dark-matter interactions.

In July 2023, we upgraded the DAMIC at SNOLAB detector with two large-format 24 megapixel skipper CCDs that were "back thinned" to remove the few micrometer-thick region of partial charge collection on the back of the CCDs. Only a fraction of the ionization signal from background events in this region is recorded by the CCDs, which results in a population of low-energy events that falls in the dark matter-search energy window[2]. The detector exhibited an increase in the total background rate, consistent with higher sensitivity to events from the surfaces (in particular, ^{210}Pb and daughters in copper) that face the back of the CCDs. The dark current is consistent with the previous detector installation[3], which demonstrates that the back-thinning process does not introduce additional sources of dark current at the level of $\sim 10\,e^-\,\mathrm{mm}^{-2}\,\mathrm{day}^{-1}$. Studies are ongoing to determine whether back thinning should be performed for the second deployment of CCDs in DAMIC-M.

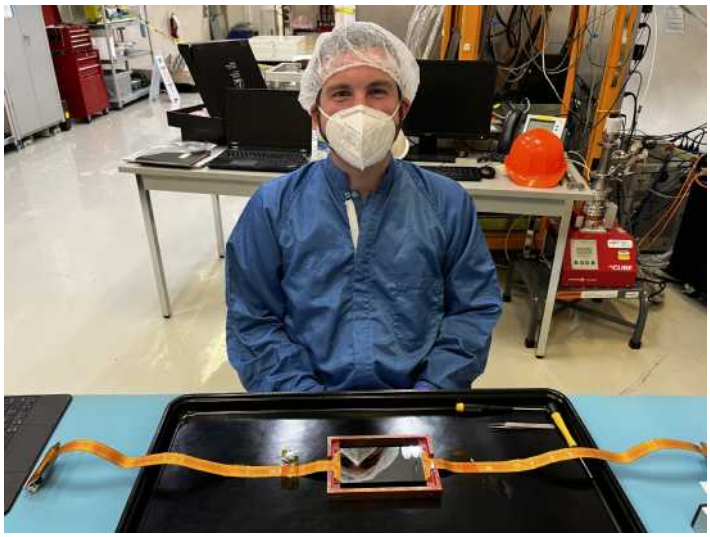

Figure 4.5-2. Postdoc Michelangelo Traina during the CCD installation at SNOLAB. The mirror finish of the back of the CCD is a result of the back-thinning process.

Dedicated runs have also been performed in DAMIC at SNOLAB under different read-out configurations, in order to develop new strategies to identify and discriminate between different sources of single- and few-electron events.

[1]DAMIC-M Collaboration, arXiv:2407.17872 (2024).
[2]CENPA Annual Report, University of Washington (2023) p. 98.
[3]CENPA Annual Report, University of Washington (2023) p. 95.

4.6 Single-electron rate from surface backgrounds

J. Busch, A. E. Chavarria and K. J. McGuire

Skipper-CCD detectors search for low-energy ionization signals from the interactions of sub-GeV dark matter particles with silicon atoms. Different background sources contribute to the region of interest (ROI) from 1 to 7 e^-, with primary ionization from electronic and nuclear recoils dominating above 3 e^-, while the single-electron rate dominates the 1 and 2 e^- bins. The main contributors to the single-electron rate are device leakage current and photoelectric absorption of optical and near-infrared light. Motivated by the large radioactive backgrounds in the SENSEI detector[1], Du *et al.* have considered secondary processes where electronic recoils in the detector may produce light[2]. These processes include: Cherenkov radiation and transition radiation in detector materials, and radiative recombination in the CCD silicon. We use data previously acquired to study the response of CCDs to surface events from a ^{14}C source[3] to demonstrate that the contribution to the single-electron rate from fast electrons entering the CCD is negligible at the background level achieved by DAMIC-M.

The experiment was performed by irradiating the front and back surfaces of CCDs with β electrons from ^{14}C in our CCD calibration system in PAB. Two large-format 24 megapixel CCDs, UW6420D and PNNL01, were used in the experiment. UW6420D is a "standard" DAMIC-M CCD as received from the foundry, while PNNL01 underwent the "back thinning" post-process to remove the few-μm dead and partial charge collection regions on the back. Fig. 4.6-1 shows a schematic of the layer structure of the two CCDs. A comparison between the results from backside irradiation of UW6420D and PNNL01 provides insight into the effect of radiative recombination, since the process is expected to be much more efficient in the thick in-situ doped polysilicon (ISDP) layer of UW6420D.

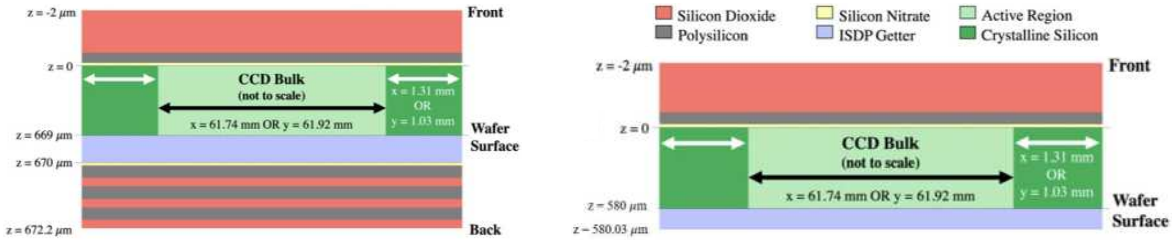

Figure 4.6-1. Layer structure of the two CCDs used in this experiment. Left: UW6420D with the residual ISDP and other layers deposited during the fabrication of the front-side gate structure. Right: PNNL01 with the backside layers removed and, instead, only a 30 nm ISDP backside contact to apply the depletion bias.

We acquired images of a small 250 × 250 pixels region of the CCD with single-electron resolution. The source shutter was opened for only one to three minutes during exposure, followed by readout. Fig. 4.6-2 shows a sample image. Clusters of contiguous pixels with high charge are the primary tracks from the β electrons and other environmental radiation.

[1] SENSEI Collaboration, Phys. Rev. Lett. **125**, 171802 (2020).
[2] Du *et al.*, Phys. Rev. X **12**, 011009 (2022); JHEP **2024**, 164 (2024).
[3] CENPA Annual Report, University of Washington (2023) p. 98.

In the analysis, we first mask all clusters from primaries and a two-pixel "halo" around them, and then measure the single-electron rate in the image background. By taking the difference between the single-electron rate with and without the source, and dividing by the number of ^{14}C events from the source, we obtain the increase in single-electron rate normalized by irradiation intensity.

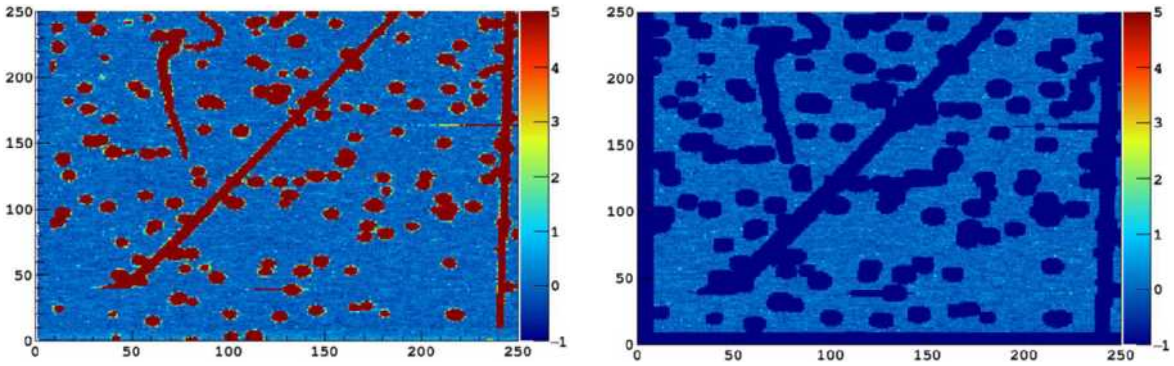

Figure 4.6-2. Left: Sample 250 × 250 pixels image with the source irradiating the back of the CCD. The color axis is in units of ionized charges (e^-). Red pixels collect $\geq 5\,e^-$ and belong to the primary ionization tracks. The circular pixel clusters are ^{14}C β particles, while the long straight tracks are cosmic muons. Right: Image after masking, where all blue pixels are masked. We measure the single-electron rate in the remaining image background.

Results from the irradiation of the front and back of UW6420D, and the back of PNNL01 show an increase in the single-electron rate of 3 to 6 $\times\, 10^{-6}$ e^-/pixel per ^{14}C event/cm^2. The largest value was obtained for the back of PNNL01, which suggests that there is no dramatic increase from radiative recombination in the thick ISDP layer. This could be because radiative recombination is not as efficient as predicted, or because any increase from radiative recombination is compensated by light absorption in the thick ISDP layer. Regardless, the DAMIC-M CCDs installed underground (Sec. 4.5) have surface-event rates of $\sim 8 \times 10^{-2}$ events/cm^2/day. Assuming they are comparable to ^{14}C surface events, their contribution to the single-electron rate would be at most $\sim 4 \times 10^{-7}$ e^-/pixel/day, which is negligible compared to the lowest rate achieved so far of $\sim 10^{-4}$ e^-/pixel/day.

4.7 Discrimination between nuclear and electronic recoils in CCDs

A. Alvarez, A.E. Chavarria, J. Jung, S. Lee*, K.J. McGuire, and outside collaborators†[1]

CCDs are a competitive technology for use in low-energy rare event searches because of their eV-scale energy threshold and micron-scale spatial resolution. The sensitivity of future experiments using CCDs could be further enhanced by distinguishing between signals arising from electron scatters in the CCD and those arising from interactions with the silicon nuclei. Here at UW we recently demonstrated a technique for uniquely identifying nuclear recoils in the bulk silicon of a DAMIC CCD, down to an ionization energy of 0.2 keV_{ee}, via thermal stimulation of defects generated in the CCD silicon by the recoiling nucleus.

At sufficiently high ionization energies ($\sim$ 85keV), nuclear and electronic recoil events can be easily distinguished in a CCD image by cluster topology alone, since only the latter generate ionization tracks that extend beyond the width of a physical pixel (15μm). At lower energies, where both types of interactions produce point-like, diffusion-limited clusters, this distinction breaks down and a different method of discrimination is necessary, Fig. 4.7-1. At low energies, nuclear recoils can still be identified by the defect in the silicon lattice left behind by the recoiling nucleus. Such defects are not generated by recoiling electrons, making this a reliable signature for nuclear recoils down to energies of $\sim$ 1keV_{nr}.

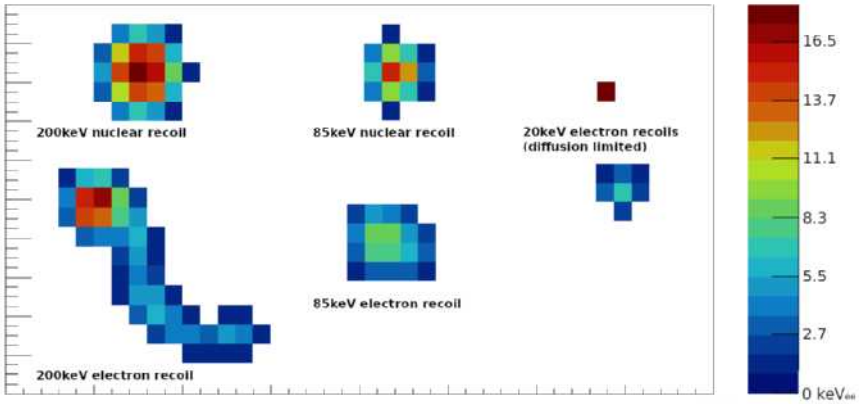

Figure 4.7-1. At high ionization energies, nuclear and electronic recoils are identifiable by cluster topology. This distinction dissappears at lower energies, where pointlike interactions produce diffusion-limited clusters.

Using an $^{241}\text{Am}^{9}\text{Be}$ neutron source to generate nuclear recoils in a DAMIC skipper CCD, we searched for defects that arose during the neutron irradiation and spatially correlated these with ionization clusters in the irradiated images. Defects will appear in CCD images as

*University of Zurich, Zurich, Switzerland.
†DAMIC-M Collaboration.

[1]Editor's Note: this article was originally drafted for the 2023 CENPA Annual Report. This work is now published in K.J. McGuire *et al.*, Phys. Rev. **D** 110, 043008 (2024).

localized clusters of excess, thermally stimulated leakage charge. To search for these defects, we ran a clustering algorithm on a "median-difference" image, which we generated by taking the difference between a median of images taken at "high" temperature (220K) before and after irradiation. This method filters out any pre-existing defects as well as all ionization clusters, so only newly generated defects appear in the median-difference image. We then performed a simple coincidence search by requiring that the center of a defect cluster be within one pixel width of the center of an ionization cluster, where cluster centers are calculated from a charge-weighted mean of pixels in the cluster. After accounting for accidental coincidences, we generated a spectrum of ionization events coincident with defects. We repeated the entire process with a ^{24}Na γ-ray source and with no source and observed no significant correlation between defects and ionization events in those data sets, as shown in Fig. 4.7-2.

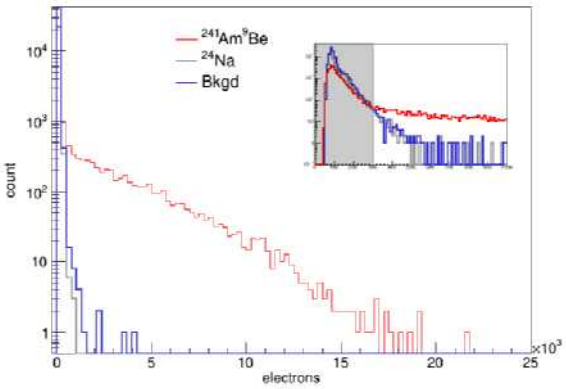

ID	Defects	Coincidences	Accidentals
bkgd	234	4	2
^{241}Am^{9}Be	5726	4272	140
^{24}Na	178	4	4

Figure 4.7-2. *Left*: Defects identified from the difference between median images taken at 220K before and after irradation, showing the excess clusters from leakage charge generated by defects. The inset shows the same spectra up to 1000 electrons. Defects with total charge below 300 electrons (shaded region) correspond to noise clusters and are omitted from the analysis. *Right*: Defects found in the three data sets, including number of coincidences and accidentals. Around 11% of coincidences are lost to pileup in the ^{241}Am^{9}Be data.

To estimate the fraction of nuclear recoils that generate visible defects, we extracted the nuclear recoil spectrum by subtracting from the total ^{241}Am^{9}Be ionization spectrum the spectral components from environmental backgrounds and from electron recoils produced by γ rays from the source. As a first approximation, we used the ^{24}Na data, whose ionization spectrum in the CCD is qualitatively identical to the ^{241}Am^{9}Be 4.44 MeV γ-ray spectrum below 140keV$_{ee}$, which we verified by `Geant4` simulations (Fig. 4.7-3). The defect-generation efficiency is taken to be the ratio of events coincident with defects, minus accidentals, and nuclear recoils (Fig. 4.7-4). Our preliminary results show that most nuclear recoils above a few keV$_{ee}$ (corresponding to $\sim$10 keV$_{nr}$) generate a visible defect, opening the possibility to use this strategy to effectively discriminate between nuclear and electron recoils in a CCD.

We are currently working on improving our ^{241}Am^{9}Be simulations, including simulating the nuclear recoil spectrum directly. We plan to release a paper in summer 2023.

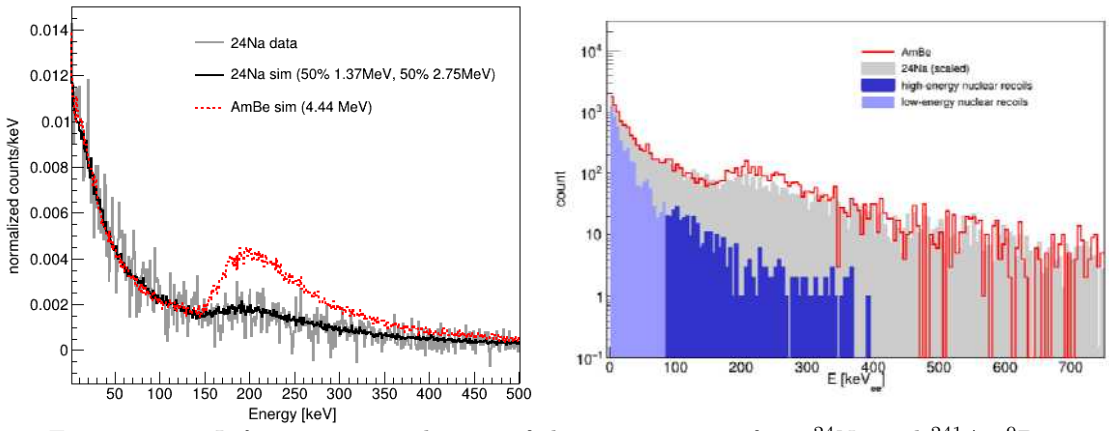

Figure 4.7-3. *Left*: `Geant4` simulations of the γ-ray spectra from ^{24}Na and ^{241}Am^{9}Be in a DAMIC-M CCD. Below 140keV the two spectra are identical. Also showing the normalized spectrum, minus background, of the ^{24}Na irradiation. *Right*: The nuclear recoil spectrum (blue histograms) determined by cluster topology (dark blue) and by subtracting ^{24}Na from ^{241}Am^{9}Be spectra below 85keV$_{ee}$ (light blue).

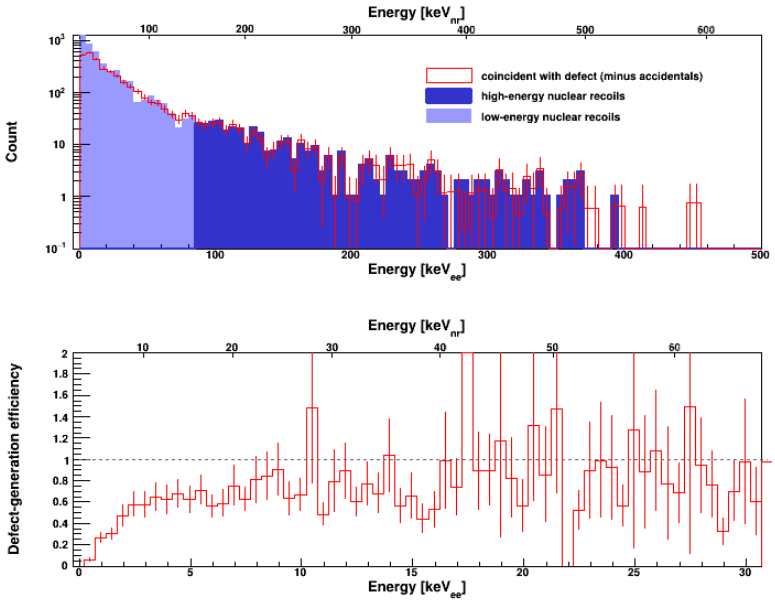

Figure 4.7-4. *Upper*: The extracted nuclear recoil spectrum from ^{241}Am^{9}Be irradiation compared with the number of defects coincident with ionization events, minus accidentals. *Lower*: The efficiency of low-energy nuclear recoils generating defects above noise. Above approximately 30 keV$_{ee}$ the efficiency is 100%.

5 Gravity and fundamental symmetries

5.1 Tests of the Equivalence Principle

S. K. Apple, C. Gettings, J. H. Gundlach, and M. P. Ross

The Equivalence Principle (EP) is foundational to our current geometric theory of gravity (i.e. General Relativity). EP-violations are typically parameterized by the Eötvös parameter:

$$\eta = \frac{2(a_1 - a_2)}{a_1 + a_2} \tag{1}$$

where $a_{1,2}$ are the gravitational accelerations of two test bodies. The EP states that η is exactly zero for all choices of test bodies. This implies that all test bodies follow geodesic paths in a given curved space-time. We are currently operating two seperate EP-test: a test of the EP for superconductors and an upgraded version of our traditional rotating test of the EP.

EP for Superconductors - We tested the EP for superconductors using a cryogenic torsion balance whose pendulum was comprised of four niobium test bodies and four copper test bodies in a dipole arrangement. When the torsion balance was cooled to ∼5 K, the niobium became superconducting which form a superconductor-normal dipole. We then searched for proposed violations of the EP for the Cooper pairs within the niobium using the sun as a natural source mass.

The experiment finished data taking in April 2024. We are able to set limits on the Eötvos parameter for superconducting niobium of $\eta_{\text{Nb*-Cu}} \leq 2.0 \times 10^{-9}$. Additionally, a limit for the EP-violation of Cooper pairs versus unpaired electrons can be extracted from these results yielding $\eta_{\text{CP-ee}} \leq 9.2 \times 10^{-4}$. A publication detailing these results was recently submitted to Physical Review D.

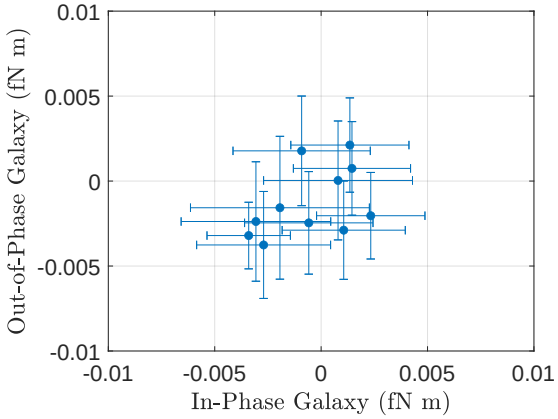

Figure 5.1-1. Fit amplitudes for day-long cuts of the torque measured by our rotating EP apparatus. In-phase indicates torques towards the center of the galaxy while out-of-phase is along the orthogonally oriented vector. An EP violation would appear as a non-zero in-phase component.

Rotating EP Test - We have completed the upgrade to our long standing test of the EP utilizing a rotating torsion balance. This balance consists a pendulum with a beryllium-aluminum composition dipole suspended from a $\sim$ 1-m long fused-silica fiber. The suspension point, vacuum chamber, and angular readout are attached to a air bearing which rotates the entire experiment at $\sim$ 0.5 mHz. This apparatus allows us to test the EP utilizing a variety of natural source masses.

We are in the midst of a science campaign to test the EP towards the dark matter over-density at the center of the galaxy. Unfortunately, the demolition of Haggett Hall has removed our ability to collect data during weekdays which decreases our duty cycle by 70%. Despite this, our preliminary data, shown in Fig. 5.1-1, already shows improvement over previously published results. We plan to continue data collection until at least the end of the year.

5.2 A Test of the Gravitational Inverse Square Law at Sub-50μm Scales

S. K. Apple, C. Gettings, J. H. Gundlach, and M. P. Ross

Probing gravity at small scales is important as it tests theories that that solve many unanswered questions in modern physics. Most prominent amongst these is String Theory's proposed solution to the gauge-hierarchy and cosmological constant problems that implies the existence of extra spatial dimensions at $\sim$μm scales. The implication of this posit is that Newton's Inverse Square Law (ISL) would be violated at mass separations below this scale length [1]. A violation of the ISL is often represented by an additional Yukawa interaction

$$V(r) = V_N(r)[1 + \alpha e^{-r/\lambda}], \tag{1}$$

where $V_N(r)$ is the usual Newtonian potential, r is the separation between test masses and α and λ are respectively the strength and scaling parameters corresponding to the extra spatial dimensions. This implies that measuring the ISL at mass separations, r, close to the proposed extra-dimensional scale, λ, would be an effective test of this theory.

Building on the success of the group's previous test of the ISL at mass separations down to 52-μm [2], a novel new design has been proposed which should allow tests down to mass separations of the order of 30-μm. The new experimental setup involves switching from a horizontal test-source mass design to a vertical one as shown in Fig. 5.2-1. The principle advantage of this new design is that any potential Yukawa signal is of a similar magnitude as the Newtonian signal when $r \approx \lambda$ as described in Equation 1; whereas in the previous experiment the Newtonian signal was at least a factor of 10 larger, which resulted in much more stringent demands on sensitivity and systematic error mitigation for any science results to be accepted. The modelled signals for the new design are shown in Fig. 5.2-2.

[1] N. Arkani-Hamed, S. Dimopoulis, and G. R. Dvali, Phys. Lett. **436**, 257 (1998).

[2] J. G. Lee, E. G. Adelberger, T. S. Cook, S. M. Fleischer, and B. R. Heckel, Phys. Rev. Lett. **124**, 101101 (2020).

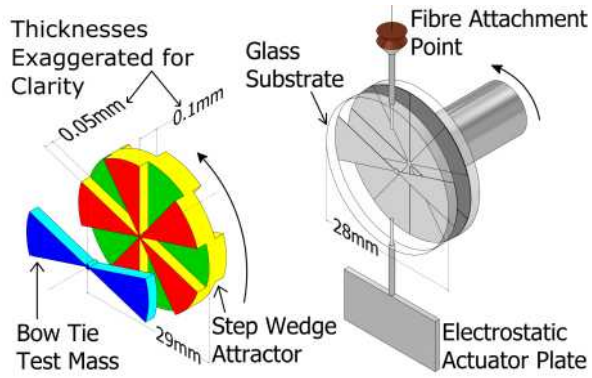

Figure 5.2-1. A schematic diagram of the new test (bow tie) and source (attractor) mass design. A realistic rendering is shown on the right, whereas the left has the dimensions blown up and colour highlights to emphasize the step design of the attractor.

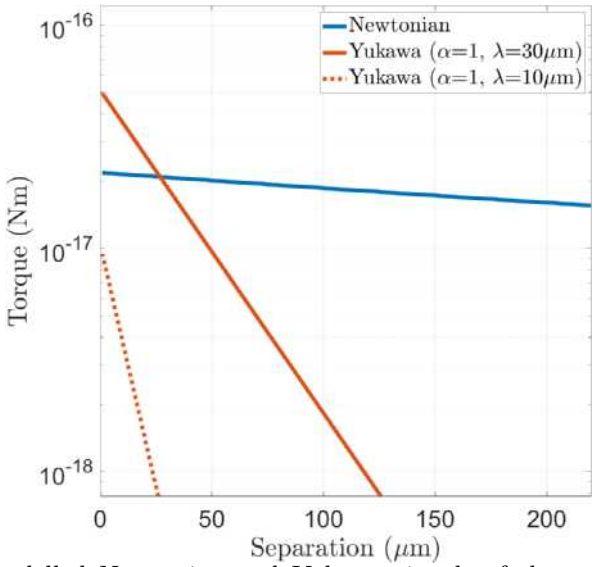

Figure 5.2-2. The modelled Newtonian and Yukawa signals of the experimental design shown in Fig. 5.2-1. The Yukawa signals for the cases of λ =30µm and λ =10µm are shown for comparison.

In order for this vertical setup to work, a servo-control loop must be in place to keep the test mass at a constant distance from the source mass (attractor). Work has begun on building and characterising the performance of such a control scheme through the use of voltage-controlled electrostatic plates acting on the test mass pendulum as shown in Fig. 5.2-1. In addition to this, preliminary studies have been performed on the assembly of the foils used on the test mass and attractor and the required tolerances on their geometry. Future work will include the implementation of a clean-room for the experiment, as well as the use of active-seismic feedback to allow as small mass separations as possible in the ISL measurements.

5.3 Rotation Sensing for Gravitational Wave Detectors (LIGO)

S. K. Apple, C. Gettings, J. H. Gundlach, and M. P. Ross

The Laser Interferometer Gravitational-Wave Observatory (LIGO) uses both passive and active seismic isolation systems in order to combat seismic noise. Currently the platform from which the mirrors (test masses) are suspended from are limited in rotational isolation due to the sensitivity of the pairs of seimometers used to detect the platform's tilt.

In order to improve the rotational sensitivity, and thus reduce low frequency noise in LIGO, we have continued development on the Cylindrical Rotation Sensor (CRS), an on-board rotation sensor described in more detail in M. P. Ross *et al*[1]. The CRS is constructed of two primary components, a cylindrical proof mass, and an aluminum support system connected to the platform. The proof mass is suspended from the support system using two 15-μm Be-Cu flexures, allowing the proof mass to remain inertially isolated from the platform. The rotation of the platform is recorded using two quadrature homodyme interferometers [2] on either side of the support system and a target mirror attached to the proof mass as shown in Fig. 5.3-1 and Fig. 5.3-2.

We have reached a sensitivity level on the order of pico-radians in the 1 Hz range with the CRS located at CENPA[1]. In addition to the CRS at CENPA, we have built two CRSs at the LIGO Lab at the California Institute of Technology for further testing in preparation for installation at the LIGO Hanford observatory before the start of LIGO's fifth observing run in 2025.

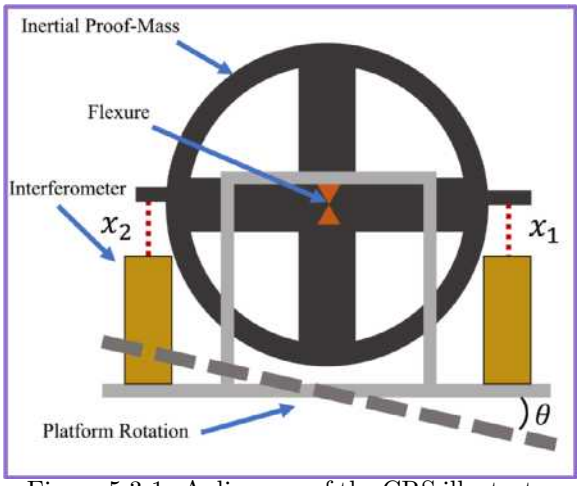

Figure 5.3-1. A diagram of the CRS illustrating how the readout works. The interferometers attached to the platform rotate while the proof mass stays stationary.

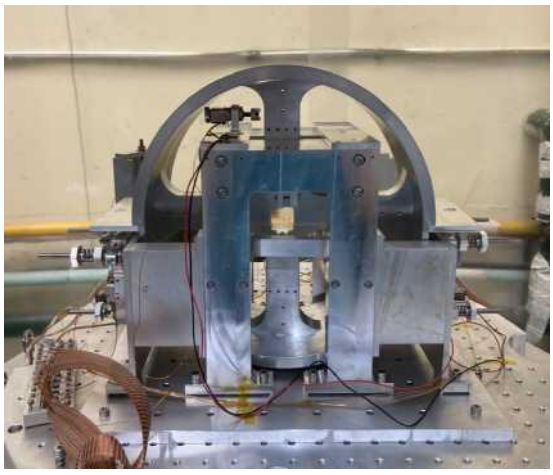

Figure 5.3-2. A photo of the CRS.

Additionally we are in the process of designing a prototype, Fig. 5.3-3, of a new ground

[1] M. P. Ross et al., Review of Scientific Instruments 94, 094503 (2023).
[2] S. J. Cooper et al,. Class. Quantum Grav. 35, 095007 (2018).

based rotation sensor for the LIGO collaboration intended to detect Newtonian Noise. Newtonian Noise is caused by fluctuating gravitational fields exerting a force on the LIGO mirrors. The primary expected source of Newtonian noise for above ground detectors, like LIGO, is Rayleigh Waves passing through the ground below the mirrors.

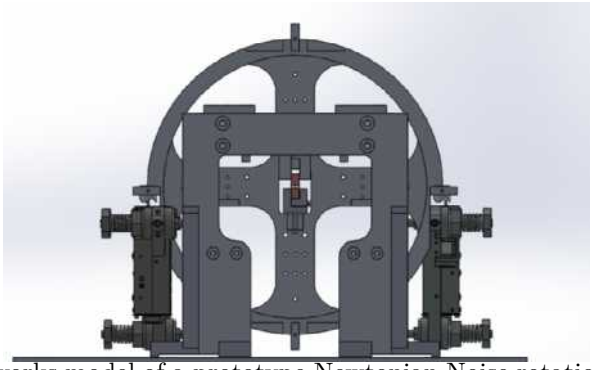

Figure 5.3-3. A Solidworks model of a prototype Newtonian Noise rotation sensor using the same optics as the CRS.

While it is impossible to cancel out the effect of Newtonian Noise in real time, by detecting the tilt of the ground caused by a passing Rayleigh wave, given by $\tau_x = ikcos(\phi)\xi_z e^{i(\vec{k}\cdot\vec{r_0}-\omega t)}$, where $\vec{r_0}$ is the position of the LIGO test mass, ξ_z is the vertical motion of the ground, k and ω are the wave number and frequency of the wave, and ϕ is the angle between $\vec{k}$ and the direction normal to the test mass face, the signal can be corrected by subtracting the Newtonian Noise.

6 Accelerator and Ion Sources

6.1 Tandem Van de Graaff overview

B. Dodson, A. Chu, A. Morgan, D. Short, N. Ramien, and C. Wiseman

The Tandem Van de Graaff accelerator (VdG) at CENPA celebrated its 60th year in the lab in 2024. The VdG remains an important resource for many, including the flagship He6CRES beta decay program, and users such as PIONEER and LEGEND. New engineers face the challenge of recovering institutional knowledge about machine maintenance and opportunities for new design work. We have pursued a collaborative environment between CENPA staff and experimental groups, performed preventive maintenance on single-point failure hardware, and begun working on significant upgrades to decades-old control systems. 2024 saw a significant increase in machine uptime from previous years, providing 43 days (working hours 10a - 7p) of beam for He6CRES, 19 days of beam for PIONEER and 1 day of beam for LEGEND, yielding a 35% uptime. In the period July 2023 - September 2024, the Pelletron chains of the VDG operated for 587 hours, and the DEIS operated for 939 hours. This 35% uptime is significantly higher than in previous years. The isotopes produced included 19Ne and 79Kr (for the He6CRES group), 7Li for PIONEER, and 56Co for LEGEND.

Figure 6.1-1. Left: Operating the Van de Graaff. Right: Work on refurbishing SPIS ion source.

The staff is pursuing a variety of projects aimed at preserving historical knowledge and extending the useful runtime of the machine into the next decade. We are developing a new control system to replace some 40- and 60-year-old control system components, many of which were last upgraded when the LINAC booster accelerator was built in the mid-1980s. The new system will consist of modern PLCs interfaced with the VdG relay logic and networked together with control software using software tools from Project 8, LEGEND and KATRIN. We have also embarked on a project to consolidate, scan, and archive the most relevant large-

format print drawings of electrical and mechanical systems still in use today and combine them with our digital CAD files into a single large reference database.

Finally, we are working with students from LEGEND to refurbish the "Model 860" Sputter Ion Source, which is capable of producing a large number of heavy-ion beams for the accelerator and last ran in the mid-2010s. Through these efforts to upgrade the control system, digitally archive our historical and institutional knowledge, perform long-overdue preventative maintenance, and develop new ion sources, we expect the CENPA VdG to continue to see increased uptime for a variety of users in the coming years.

6.2 Accelerator Maintenance

B. Dodson and C. Wiseman

This year, the accelerator has seen significant efforts in long-overdue preventive maintenance. Most critically, we have begun replacing a set of high-pressure nitrogen gas cooling coils (the "intercooler") on our 1960s-era Ingersoll-Rand tank gas compressor, which had rusted significantly over the last decade and were declared unsafe for use. Major maintenance on the Ingersoll has been thankfully rare, including remachining of a copper valve sealing ring in 2002, and the first replacement of the intercooler coils in 1983. Based on historical documents, CENPA staff designed replacements for these large steel coils, and as of September 2024 we are preparing to install the newly fabricated coils. We note that the cost of a new gas compressor system is significantly higher than the cost of replacement coils.

We also performed work on numerous aging vacuum systems that support the accelerator. A new compressor for the switching magnet cryopump was purchased, as well as a new mechanical pump for the high-energy side of the tandem. Since new pumps are often cost prohibitive and integrate poorly with our current control system, we located a company in Maryland, AdVaCo, which was able to refurbish a cryopump compressor and two sets of mechanical pumps, cryopumps, turbopumps, and turbo controller boxes. With these additional spares in hand, we protect against failures and resulting downtime and also gain unused hardware with which to test new software control methods.

In addition to vacuum and gas handling maintenance efforts, the accelerator team rediscovered the lost art of floating carbon foils. In November 2023 during an experimental run, the last of the old set of 198 stripper foils broke. Located in the center of the accelerating column inside the accelerator tank, these foils strip injected negative ions of their electrons, creating high-energy positive ions. To no avail, the operating team spent several days scanning through all foils in an attempt to find one that would deliver microamps of positive current to the high energy faraday cup. It was also the case that the inventory of foils from which we had long been pulling had finally depleted. Facing a recent loss of lead engineering institutional knowledge, the team embarked on entering the accelerator tank, venting the beam tube, fabricating and installing new stripper foils, closing and filling the tank with insulating gas.

It had been more than 10 years since the last batch of foils was created. Past engineers

left some procedural documentation that allowed a novice foil floater to successfully stage the necessary equipment and create a set of mounted foils. The foil material is a thin 2 ug/cm^2 carbon deposited on a microscope slide, scored with a razor to the appropriate size. The slides are dipped in a 10% collodion 90% amyl acetate mixture that aids in frame adhesion. The slide is slowly inserted at a 45 degree angle via a mechanical arm into a bath of warm deionized water, gently floating the carbon foil on the surface. By hand, an aluminum frame captures the carbon foil so that there is enough surface area to adhere to the frame. The surface area of the carbon foil to the frame acts as an important heat sink as the ion beam passes through the center of the foil. The frames are then mounted on a small pump manifold with eight hand valves, carefully opened to slacken sets of foils to increase mechanical strength during transport and foil wheel rotation. The process requires practice and a steady hand, but yields a couple hundred foils in about a week. Part of the process is shown in Figure Fig. 6.2-1.

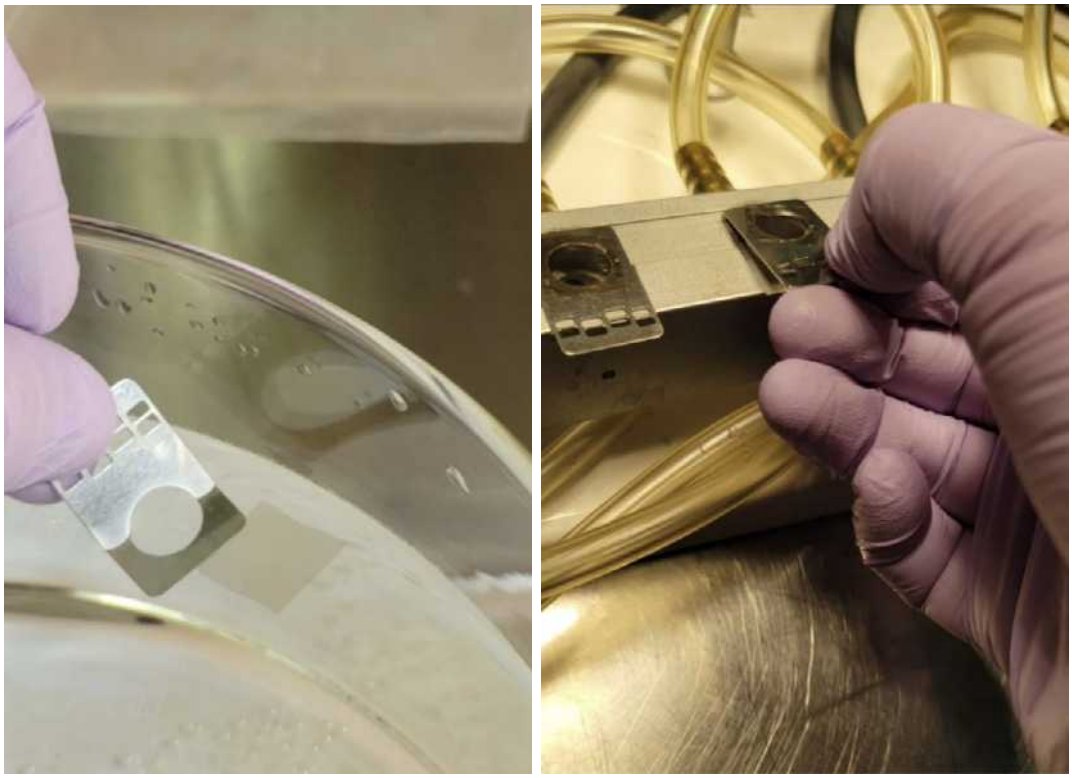

Figure 6.2-1. Snapshots of the foil floating procedure.

The new foils were installed in the foil wheel, taking careful notes on the communication between the Low Energy Gordo and Terminal Computer, and foil wheel indexing mechanism. The tank was closed following proper closeout procedures, filled with insulating gas, and produced ∼5 uA of positive beam on the high energy cup upon first test beam in February 2024. In early March, the accelerator returned to delivering beams for experimental use.

6.3 Control system upgrade

C. Wiseman and S. Enomoto

Motivated by a desire to remove single points of failure on the accelerator, we have renewed efforts to upgrade the control system of the Van de Graaff at CENPA. Much of the system is driven by relay logic, including the vacuum system and the radiation safety interlocks. While the relays themselves usually continue to be robust, the old control computers are always in danger of permanent failure. They are: a VAXStation 3200, two LSI-11+, the in-house-built knob boxes, and several ANAC units. This year, our efforts focused on understanding the layout of the current control system, finding relevant historical documentation and code backups, and developing a vacuum system test stand in the High Bay area with a software-driven programmable logic controller, using software developed by S. Enomoto at CENPA, also intended for use with Project 8, LEGEND, and KamLAND2. By leveraging these new software tools, we remove much of the need for programming graphical user interfaces, and can focus effort on communicating with hardware.

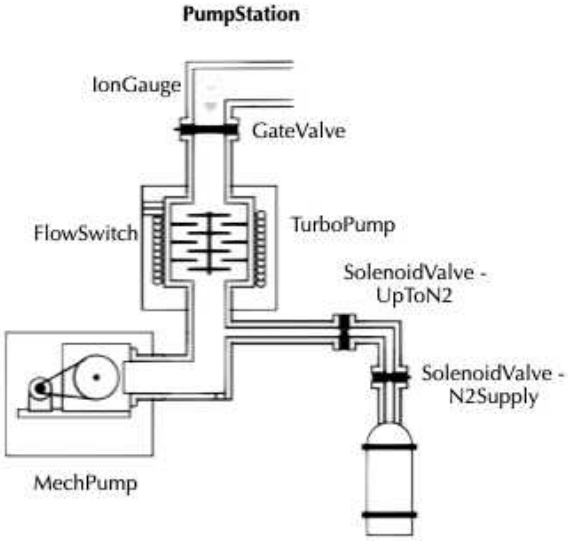

Figure 6.3-1. An illustration of a pumping unit. The VDG currently maintains eight of these stations. The vacuum test stand under development will control two pump stations, and test control logic for events such as power failures, etc.

The control system of the accelerator can be grouped by its various functions - vacuum systems, ion sources, beam optics and steering, beam measurement, pelletron charging system, analyzing and switching magnets. In the LINAC era (circa 1985 - 2005), the vacuum system past the high-energy (HE) side turbopump was operated by the Vacuum Satellite, a late 1970s-era LSI-11+ computer programmed in MicroPower Pascal. Another LSI-11+ computer, the Deck Satellite, is the interface to several other ANAC computers near the ion source deck and offdeck beam optics. In addition, a set of Texas Instruments programmable logic units used in the 1980s were replaced by a C++ PC control program in the early 1990s. These “Gordo” computers control the vacuum system of the VDG tank (LE and HE

ends), the Group3 Terminal Computer, the low-energy Faraday cup, and many other pieces of hardware, using banks of optically-isolated relays. These satellites are controlled by CSX, a C program written at UW in the 1980s running on our last operating VAXStation 3200. Many systems are not part of this control and are operated either manually from the main control room console, or in the case of the radiation protection system, hard-wired to various indicator dials and safety interlock switches.

Developing a new control system for a machine of this size and complexity is a carefully approached project, especially if we wish to minimize downtime for the users of the beam. To that end, we are first exploring the replacement of the Vacuum Satellite computer, as being the lowest-hanging fruit on the control system. A test stand is being built in the high bay consisting of two copies of the pump station shown in Figure Fig. 6.3-1, controlled by opto-isolator relay boards. Typically, software such as LabView is chosen to control systems, or in an industrial setting, other programmable logic control (PLC) software is employed. We are currently developing a proposal for a PLC scheme of control, starting from the test stand, which is expandable to hundreds of digital I/O channels, and dozens of analog-to-digital (ADC) channels, across the entire VDG area.

For high-level interaction with the future PLC system, we are evaluating the use of "Slow-Dash", a web-based software control system developed for Project 8, LEGEND, and Kam-LAND2 by Sanshiro Enomoto. Much of the control code is written in Python, making it easy for new users to read and understand. A central SQL database server will be hosted on a private network in the control room, logging many observables such as pressure, voltages, temperatures, knob settings, etc. Updating the communication between devices from RS232 to Ethernet and common protocols like Modbus and SCPI affords a great deal of flexibility in attaching new hardware; we are also exploring options to replace control room oscilloscopes and Faraday cup picoammeters with new units supporting signal readout over Ethernet. his upgrade will not only remove aging hardware, but significantly improve our ability to tune a particular ion beam and consulting previous historical values. Using our in-house software development capability will provide us with a high degree of flexibility, as well as a degree of robustness and memory safety from utilizing software already developed to run large physics experiments.

7 Facilities

CENPA Engineering

7.1 Engineering

M. Huehn, M. Kallander, N. Miedema, and R. Roehnelt

To go from theory to experiment, a project needs hardware. Although the physics faculty, postdocs, graduate students, and undergraduates are at least above average at hardware - it is not their primary focus. To assist them in creating viable hardware, they often turn to the CENPA engineering team for assistance. The engineering team most often helps with mechanical design, procurement, fabrication, and assembly, but also has the tools necessary to perform various analyses. Most often, mechanical or thermal analysis is performed using finite element analysis with Ansys or COMSOL. Sometimes, the analysis may be more specialized and could be magnetic or RF using Ansys High-Frequency Simulation Software (HFSS) or COMSOL.

Routine Design Tasks

Among the simplest tasks are "Can you 3D print this for me?" Frequently, the answer is that we can, as long as the item to be printed is small enough to fit in our 3D printer volume. Some examples are a protective cover for an electrical feedthrough (Fig. 7.1-1), or an optics holding mechanism for Selena(Fig. 7.1-2).

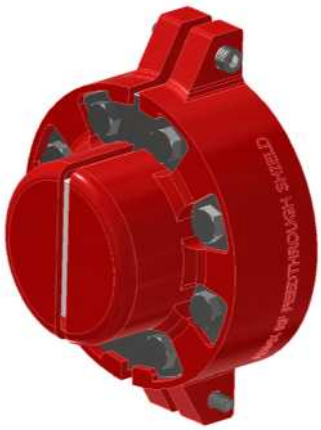

Figure 7.1-1. ADMX Electrical Feedthrough Cover (Design: R. Roehnelt).

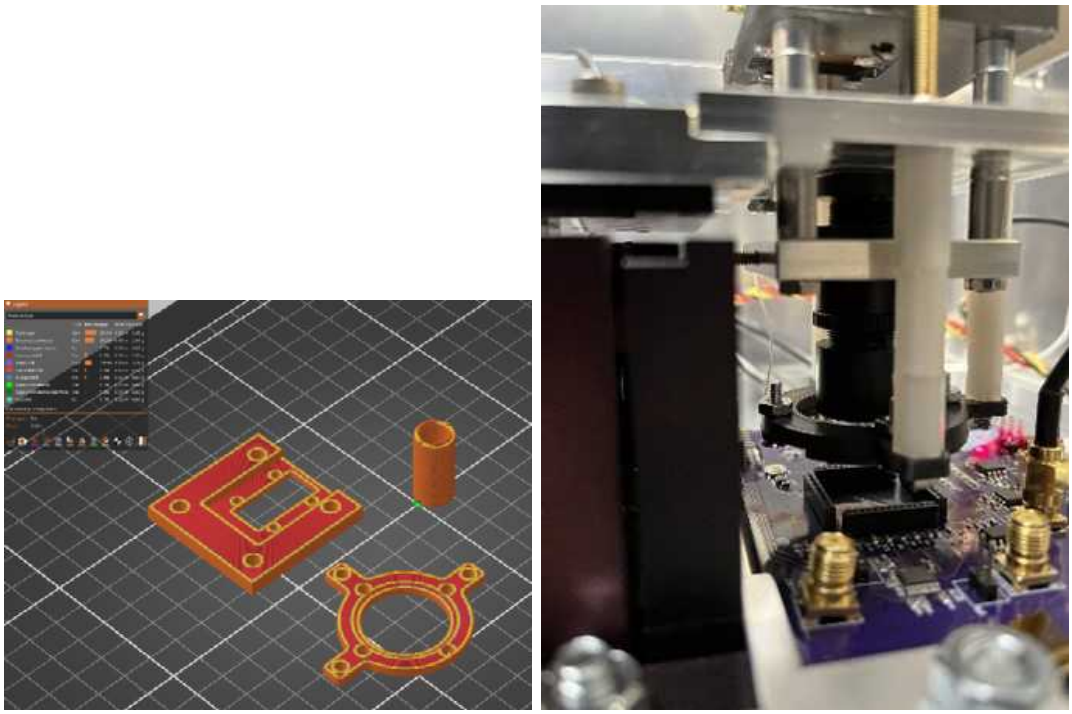

Figure 7.1-2. Optic Holder Components for Selena (Designed: H. Lin). Left: Prusa software slicer image. Right: installed parts.

Or getting more complicated - "Can you take this basic design of a Cu plate we are using to cool our CCD box, remove half the mass, but make it so that we don't have to change anything else?" We accomplished by pocketing the backside for the mass removal but left the connection points full thickness, and installed Heli-Coils for thread robustness (Fig. 7.1-3).

Figure 7.1-3. Light weight Cu plate for cooling DAMIC CCDs (Design: R. Roehnelt, Machining: N. Miedema).

Increasing Complexity

As we assist physicists with hardware, many times the requirements are not what you would find in a standard shop. Some of the mid-complexity customer requirements from this reporting period are:

- A vacuum-tight accelerator target to hold an Au foil and a Lithium Fluoride window, but with a very thin vacuum barrier. However, it must also be electrically floating so we can connect to it and read off the deposited beam current (Fig. 7.1-4).

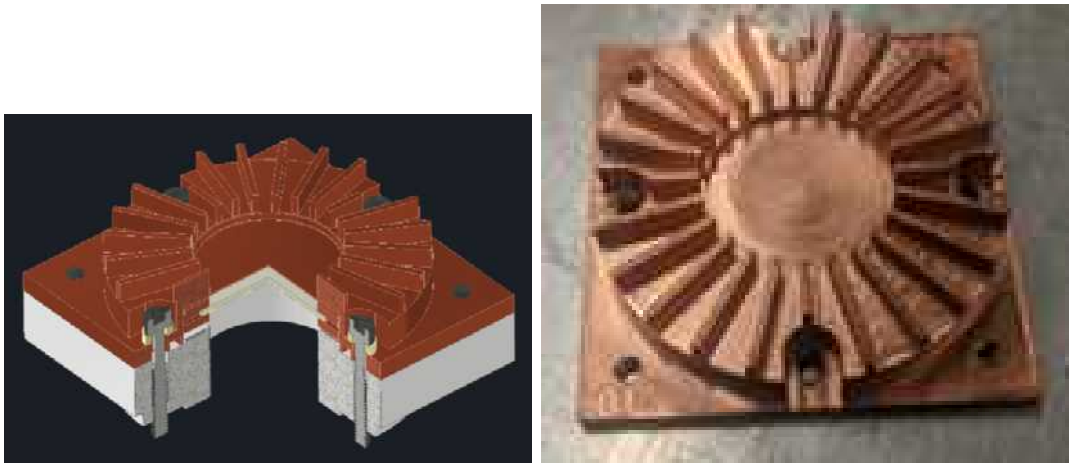

Figure 7.1-4. CAD model (left) and fabricated Cu target window (right).

- A beta radiation monitor, using scintillators, SiPMs, a vacuum window, light tight, that sits in a space about this big (waves hands). This beta monitor took a few iterations and was a combined work of engineering and the CENPA electronics shop. The outer housing is 3D printed ESD safe material with a 0.5 inch thick Cu backplane for low SiPM readout noise (Fig. 7.1-5).

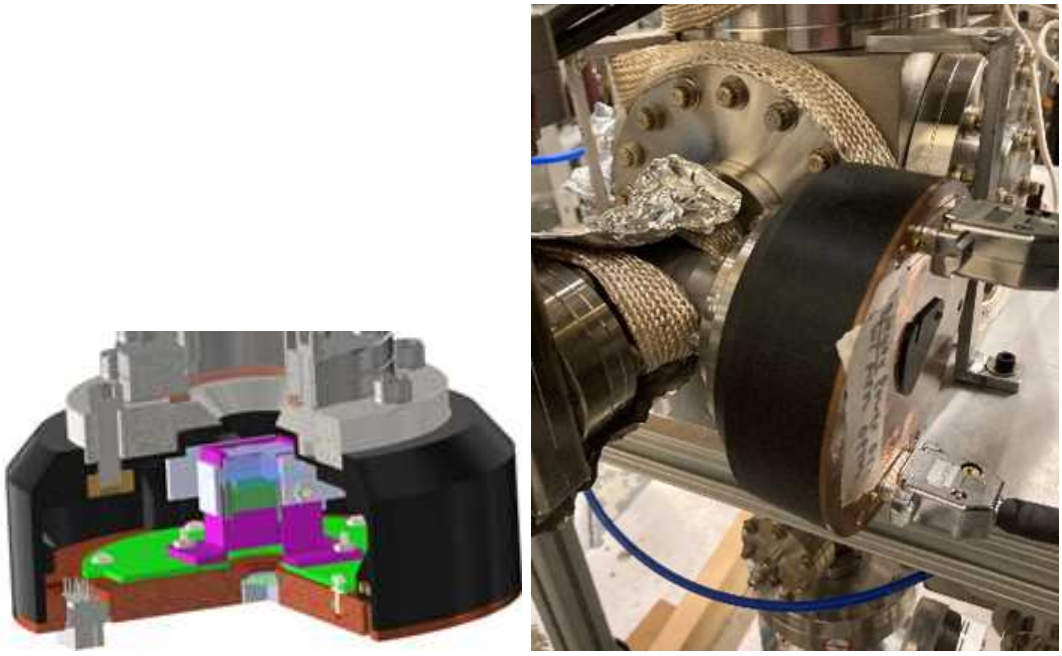

Figure 7.1-5. Beta monitor CAD (left) and fabricated and installed (right).

- Design a holder for 10 LYSO crystals (Fig. 7.1-6).
  - Light tight
  - Photomultiplier mounting
  - Optical fiber access for individual crystal calibration
  - Mounting for NaI crystals around the LYSO array for tail catchers
  - Has to interface with existing XY gantry at PSI for positioning in the beam

Figure 7.1-6. LYSO crystal holder CAD Assembly (left) Assembly installed at PSI (right)

Large and Complex

In this reporting period, the projects with the greatest complexity for the CENPA engineering staff were Legend-1000, Pioneer, and Project-8. These projects are all long-term and require significant design and analysis work. All three of these projects are international collaborations that require the coordination of multiple institutions, funding agencies, time zones, and software.

LEGEND-1000

The CENPA contribution to the project is the design of the lock system for moving Germanium detectors into and out of the liquid Argon cryostat. This design is a crane portable airlock that has to stay very clean inside from chemicals, radiological, and general dirt (Fig. 7.1-7). Any Radon introduced into the cryostat would lead to increased experimental background. Any chemical or particulate contamination would result in degradation of the liquid Argon. Making sure that all requirements are understood and satisfied is a large undertaking.

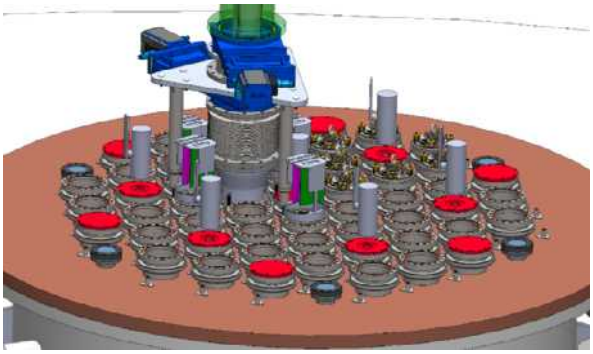

Figure 7.1-7. Top of Legend 1000 cryostat with Lock table, as of Dec 2023. Multi-institution CAD model (Duke, University of Washington).

PIONEER

The CENPA portion of this collaboration is focused on a possible LYSO calorimeter design and developing compact analog electronics to read the fast- and low-amplitude signals from the active target. The goal is to build and test pieces of the experiment in collaborating institutions, assemble the entire experiment at PSI, and run it on the PiE5 beamline. The concept with the most detail is shown in Fig. 7.1-8. In this concept, the calorimeter is on a mobile stage that can move along the Z-axis of the beam and rotate. This enables calibration with a Cockroft-Walton beam at the other end of the tracks.

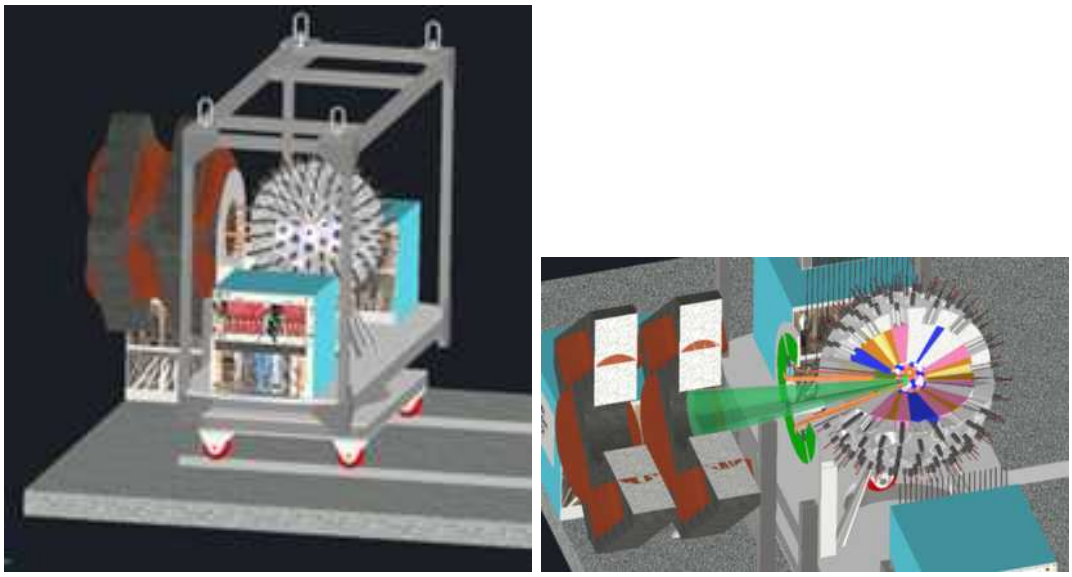

Figure 7.1-8. Left: PIONEER calorimeter (CAD). Right: closeup of the calorimeter.

Project8

This project has an incredible number of moving pieces, many of which require the development of vastly improved versions of existing technology. Atomic disassociator with 100x more throughput than what is on the market, a UW designed and built electron gun, beam chopper, beam evaporative cooling, and a finely tuned cryogenic RF resonant cavity that happens to be inside an MRI. This project has a lot of advanced technology packed into a very small space. Structural, thermal, RF, and magnetic analysis (see, e.g. Fig. 7.1-9 and Fig. 7.1-10) is done to ensure that all components will work together to provide the required experimental results.

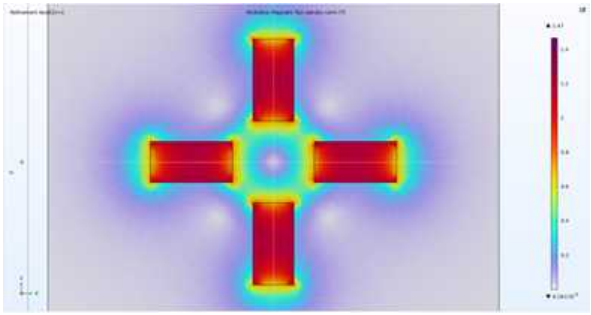

Figure 7.1-9. COMSOL - Magnetic Quadrapole analysis

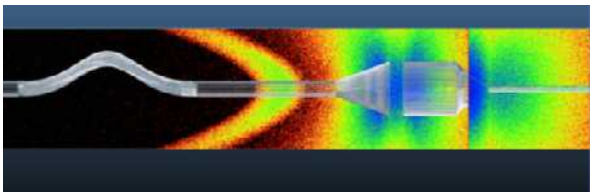

Figure 7.1-10. MolFlow - Atomic Source Accommodator analysis

CENPA electronics shop

7.2 CENPA electronic shop

D. A. Peterson and T. D. Van Wechel

The electronics shop is responsible for the design and construction of new laboratory electronic equipment as well as the maintenance and repair of existing CENPA electronics. Projects undertaken by the electronics shop in the past year include the following:

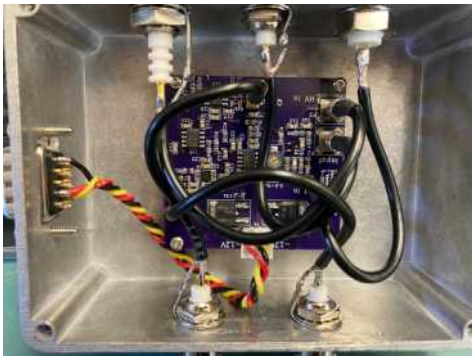

Figure 7.2-1. Designed and built Q and I sensitive preamplifier for LEGEND.

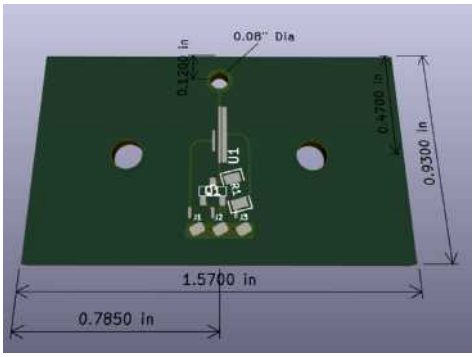

Figure 7.2-2. Continued supporting LEGEND with new form factor charge amplifiers.

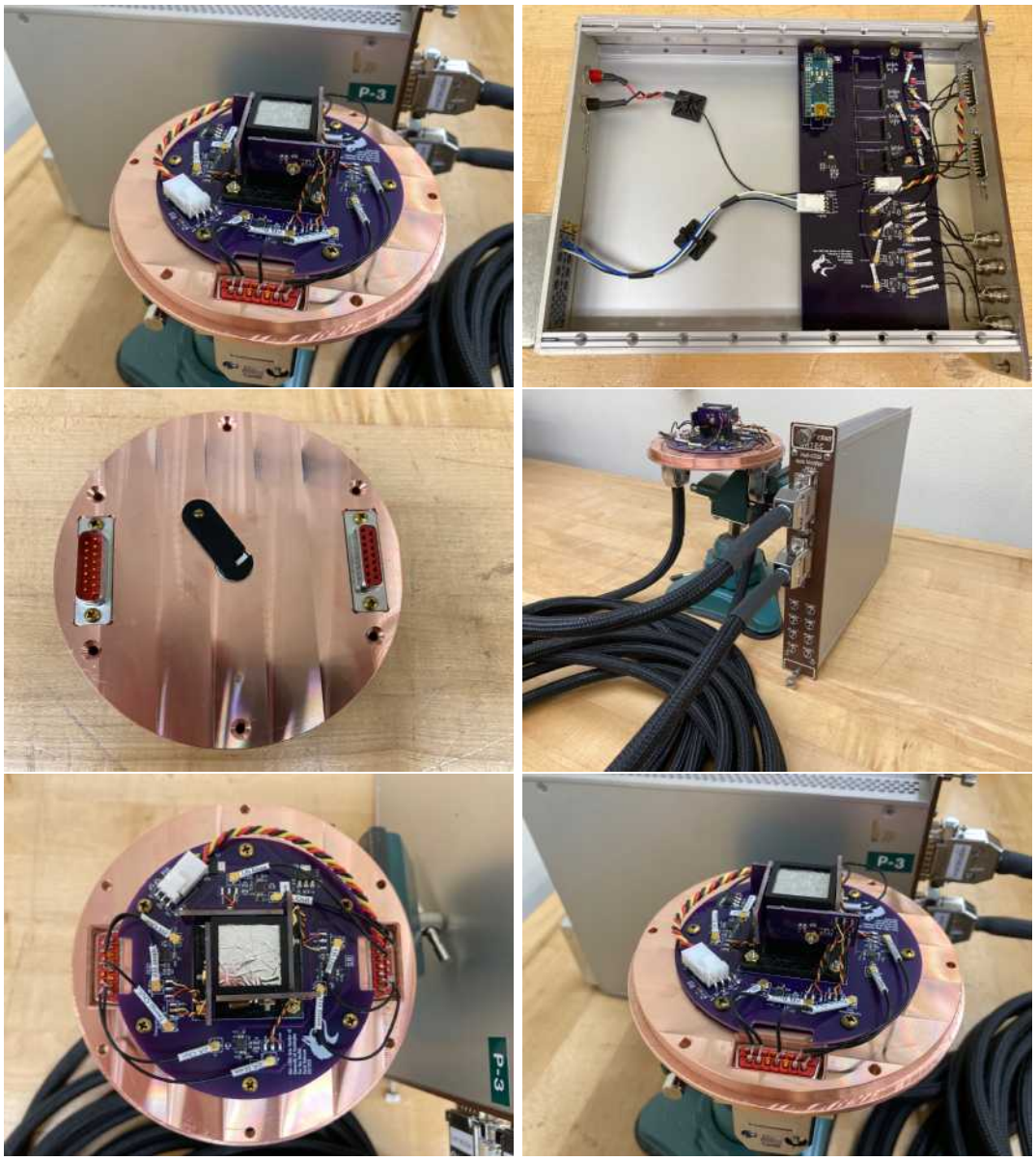

Figure 7.2-3. Designed and built a new version of the He6-CRES beta monitor.

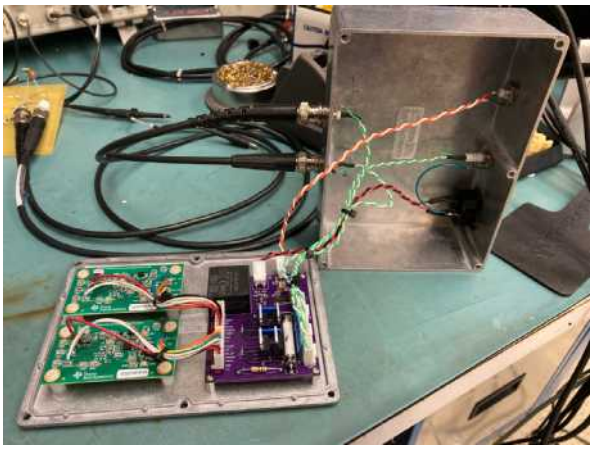

Figure 7.2-4. Designed and built 600VDC electrostatic plate driver for He6-CRES.

Figure 7.2-5. Built the Project 8 E-Gun telemetry system.

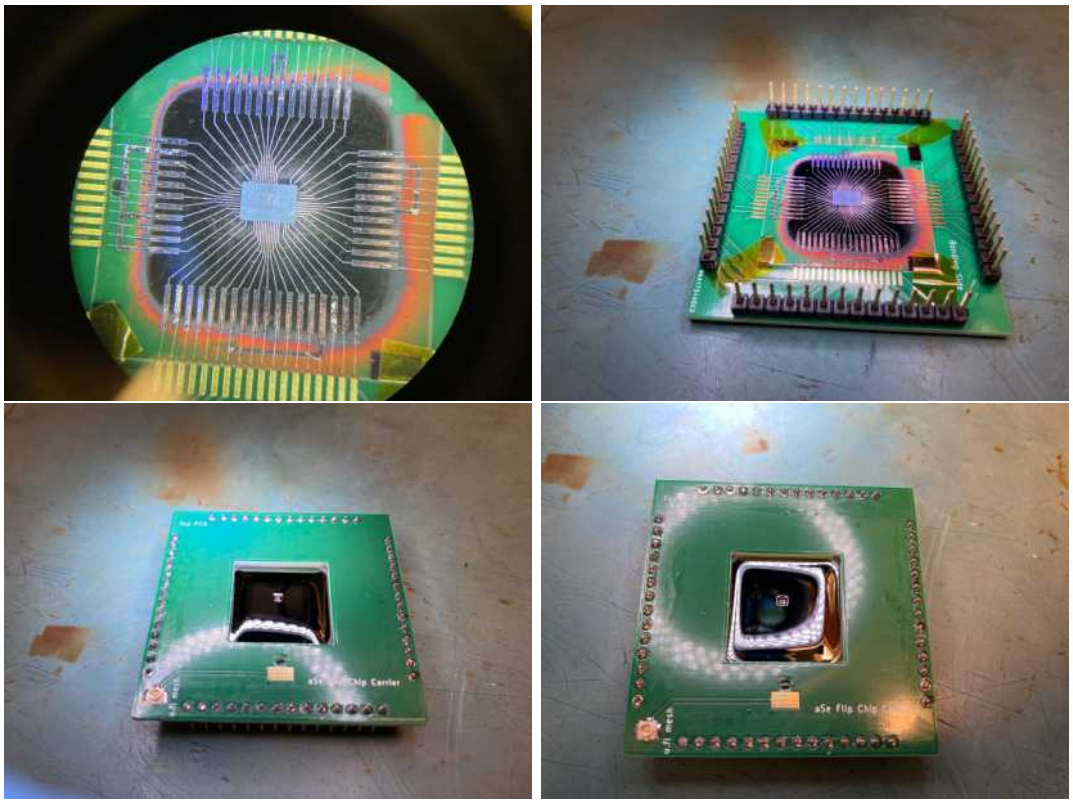

Figure 7.2-6. PCB manufacture of various carrier boards for the SELENA detector.

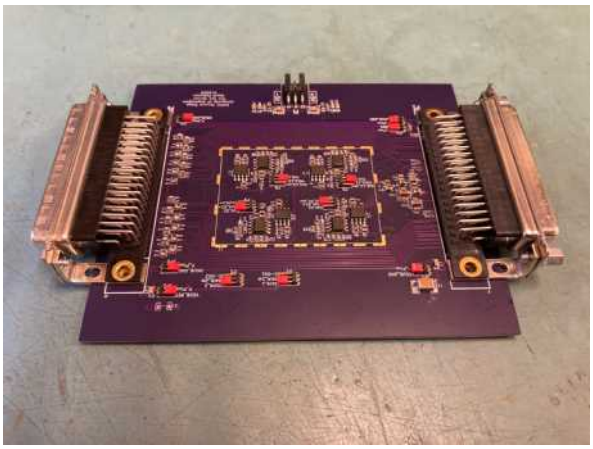

Figure 7.2-7. Continuing Support for DAMIC with PCB assembly.

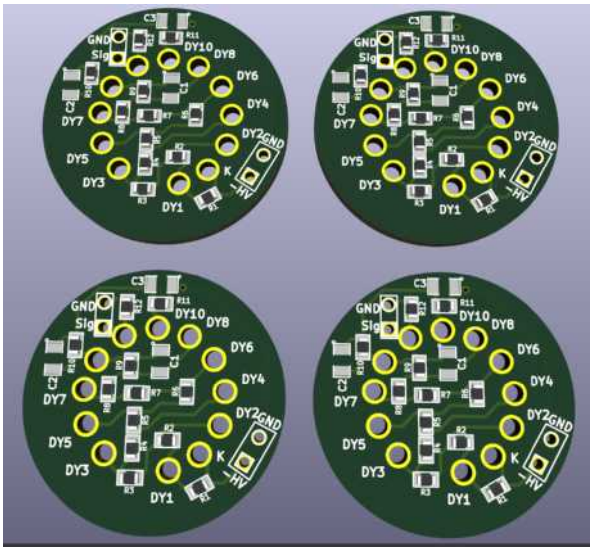

Figure 7.2-8. Made new PMT bases for the PIONEER project.

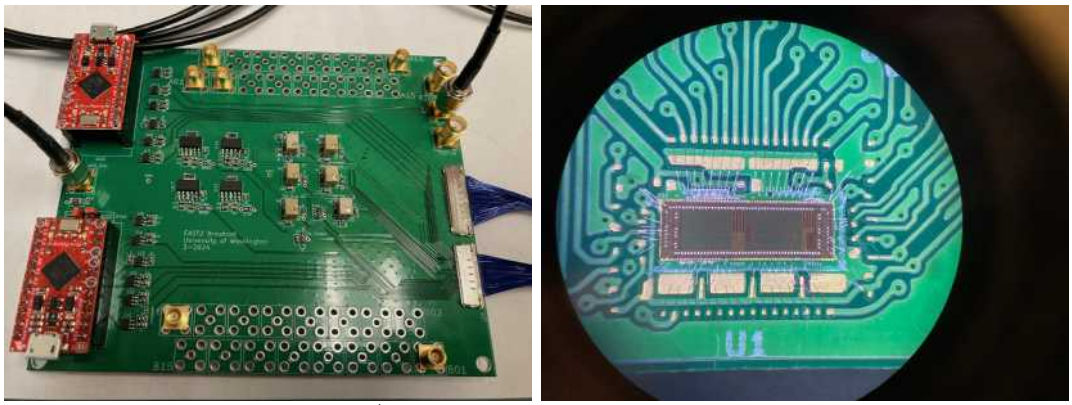

Figure 7.2-9. Made new FAST2/3 amplifier interface and readout boards for the PIONEER project.

CENPA IT & compute cluster

7.3 Operation IT infrastucture and cenpa-rocks computer cluster

G. Holman and C. Wiseman

CENPA is a mixed shop of Windows 7 (some legacy), 10, Mac OS X, and various Linux distributions. Windows 11 is installed on new workstations, FreeDOS 1.2 on accelerator controllers, and an embedded Win 98 for a mechanical shop mill. As with every year, the IT focus was directed toward server consolidation, network security, process documentation, and removal of redundant processes. We continue to utilize Xen virtualization for Autodesk Vault versions, ELOGs, wikis, collaboration calendars, and document servers. The CENPA

website and the research group web pages run on a Drupal 7 web framework. The NPL mail server still provides NPL presence, but all email is relayed to UW e-mail hardware. The workstations are connected to the UW Delegated Organization Unit (OU), which mainly eliminates the need to run a dedicated domain or LDAP server.

Two Dell 510 20-TB servers (Lisa and Marie) continue to offer user storage and a server backup set. Linux, Windows, and Mac workstations are backed up to the 20-TB Marie raid, which is backed up off-site using the UW Trivoli backup service. Lisa ran the Crash Plan Pro backup application (now retired), which supported all operating systems and provides differential and encrypted backups. We now use the updated UW Crash Plan Pro suite license. Whereas workstations rely on Crash Plan Pro for backups, all servers utilize rsnapshot. Marie provides 20 TB for research, user, and shared group data.

The CENPA network has undergone a major restructuring. The 12-year-old Shorewall, DNSMasq, Strongswan gateway and firewall appliance is now retired mostly. The new appliance is a Dell PE620 with eight 10G network interfaces running PFsense gateway/firewall on FreeBSD. Many DLink switches are still in place; however, some have been replaced with updated Aruba 48P switches. We have isolated workstations and labs through VLANs. Although we are still on a 1G-ethernet backplane, our uplink is now two 10G-connections with traffic shaping.

We continue to operate the cenpa-rocks Linux cluster as a computing resource for CENPA. This is a heterogeneous cluster that consists of roughly 130 nodes. These compute nodes are DELL Power Edge R410 blades of three types: one with 12 cores and 48 GB of memory per node, one with eight cores and 24 GB of memory per node, and one with eight cores and 16 GB of memory per node. The cluster is managed with rocks cluster software[1]. Users connect to a login node and interact with the compute nodes using Sun Grid Engine (SGE). In addition to the compute nodes, we have significant data storage in three large raid systems that offer a total of 175 TB of storage. The raid systems are connected to DELL Power Connect 6248 switches with paired 10 Gb/s fiber connections, and the switches are connected to the compute nodes via 1 Gb/s ethernet. There are also hard drives distributed throughout the compute nodes managed as a single 40 TB filesystem using XRootD.

We have been able to operate the cluster inexpensively by relying on the infrastructure (and some of the compute nodes) left from the previous Athena cluster, which was installed in 2009. This infrastructure includes the power and power distribution, the cooling and the racks, and physical setup. Two years ago, we reported on the increase in our compute nodes with NERSC surplus nodes[2]. These nodes and our original Athena nodes are all more than ten years old, and over the past year a number of them have gone offline. We acquired 150 Dell R620 servers from the generous donation by Bryce Livingston at The Institute for Health Metrics and Evaluation (IHME). These were acquired through an inventory transfer UW form 1024. Lastly, some of the Power Connect switches show signs of age. We plan to replace these with refurbished units for less than $200 each or upgrade the backplane to 10GBE.

[1] https://www.rocksclusters.org/

[2] CENPA Annual Report, University of Washington (2019) p. 161.

At over 1000 cores and significant data storage, cenpa-rocks offers a powerful computing platform at very low cost. As much of the infrastructure is quite old, there are a number of possible failure points. Among these are the switches, power strips and cooling fans. These can be replaced at low cost. We expect to be able to maintain and, with new nodes obtained from surplus, enhance the cenpa-rocks cluster as a computing resource for CENPA over the next year and hopefully beyond.

8 CENPA Personnel

8.1 Faculty

Eric G. Adelberger[1]	Professor Emeritus
Quentin Buat[1]	Assistant Emeritus
Alvaro Chavarria	Assistant Professor
Jason Detwiler	Professor
Sanshiro Enomoto	Research Professor
Alejandro García	Professor
Jens H. Gundlach[1]	Professor
David W. Hertzog	Professor; Director
Peter Kammel	Research Professor
Elise Novitski	Assistant Professor
R. G. Hamish Robertson	Professor Emeritus
Leslie J. Rosenberg[1]	Professor Emeritus
Gray Rybka	Associate Professor
Claudio Savarese	Research Assistant Professor
Derek W. Storm[1]	Research Professor Emeritus

[1]Not supported by DOE CENPA grant.

8.2 Postdoctoral Research Associates

Svende Braun[1]	Muon $g-2$ / PIONEER
Nicholas Buzinsky	He-6 CRES
Christine Claessens[2]	Project 8 / Muon $g-2$
Conner Gettings[3]	Gravity
Joshua Labounty[4]	Muon $g-2$ / PIONEER
Heng Lin	DAMIC-M / Selena
Brynn MacCoy[2]	Muon $g-2$ / PIONEER
Michael Ross[3]	Gravity
Patrick Schwendimann	Muon $g-2$ / PIONEER
Ya-Hao Sun[5]	Project 8
Michaelangelo Traina	DAMIC / Selena
Louis Varriano	LEGEND
Dan Zhang[1]	ADMX

[1]Departed December, 2024.
[2]Departed September, 2024.
[3]Not supported by DOE CENPA grant.
[4]Graduated April 2024; Started Postdoc Appt. April 20, 2024.
[5]Arrived October, 2024.

8.3 Predoctoral Research Associates

Kush Aggarwal	DAMIC / Selena
Shoshana Apple[1]	Gravity
Omar Beesley	Pioneer
Sam Borden	LEGEND
Jackson Busch[1,2]	DAMIC
Thomas Braine[2]	ADMX
Madison Durand	COHERENT[3]
Kieran Enzian[1]	ADMX
Michaela Guzzetti[1]	ADMX
Heather Harrington	He-6 CRES
Paul Kolbeck	He-6 CRES / Project 8
Yuan Ru Lin	LEGEND
Christian Nave	LEGEND
Xiaochen (Harry) Ni[1]	Selena
Ian Paulson[1,4]	Gravity
Akira Pfeffer[1]	Gravity
James Sinnis[1]	ADMX
Grace Song	LEGEND
Meg Wynne	Project 8
Jessie Yang[5]	Pioneer

[1]Not supported by DOE CENPA grant.
[2]Graduated May, 2024.
[3]Departed March, 2024.
[4]Arrived September, 2024.
[4]Arrived January, 2024.

8.4 Undergraduates

Leo Ahlburg	He6-CRES - Garcia
Moritz Blum	He6-CRES - Garcia
Charli Chambers	Gravity - Gundlach
Kit Hastings	DAMIC - Chavarria
Senna Keesing	ADMX - Rybka
Skylar Kemper	ADMX - Rybka
Isaac Kunen	LEGEND - Detwiler
Qi Li	KATRIN - Enomoto
Eliz Locke	Gravity - Gundlach
Gabrielle Loop	ADMX - Rybka
Marcos Marroquin	ADMX - Rybka
Nicolas Oaxaca	He6-CRES - Garcia
Bradley Taylor	Pioneer - Hertzog
Forest Tschirhart	LEGEND - Detwiler
Ian Wang	LEGEND - Detwiler
Leo Weimer	ADMX - Rybka

8.5 Professional staff

The professional staff are listed with a description of their recent major efforts.

Marcel Conde	RS/E2	DAMIC fabrication & Jr. Engineer
Brittney Dodson	RS/E3	Accelerator Engineer
Cyrus Goodman[1]	RS/E2	ADMX liquification operator
Charles Hanretty	RS/E3	ADMX engineer project manager
Gary T. Holman	Associate Director	Computer systems
Michael Huehn	RS/E2	Jr. Engineer, Project 8, DAMIC
Matthew Kallander	RS/E1	Jr. Engineer, Project 8
Mason Newman	RS/E2	Jr. Accelerator Engineer
Ryan Roehnelt	RS/E3	Sr. Mechanical Engineer
H. Erik Swanson	RS/E4 Sr	Precision experimental equipment
Timothy Van Wechel	RS/E4	Analog and digital electronics design
Clint Wiseman	RS/E3	Accelerator, He6-CRES, computer systems

8.6 Technical staff

Nate Miedema	Instrument Maker
David A. Peterson	Electronics Technician

8.7 Administrative staff

Angela Lawson	Program Operations Specialist
Kyle Fitzsimmons	Fiscal Specialist 2

8.8 Hourly staff

Yasin Chowdhury	Undergrad RA
Arif Chu	Undergrad RA
Gail Guisinger	Student Assistant
Luciano Malavasi	Research Aide 2
Anthony McKeirnan	Undergrad RA
Armina Moghadasi	Student Assistant
Alex Morgan	Undergrad RA
Ethan Muldoon	Research Aide 2
Peter Park	Research Aide 2
Natalia Ramien	Laboratory Assistant
Devin Short	Laboratory Assistant
Brooke Yommarath	Student Assistant
Adam Yusopov	Student Assistant

9 Publications

Published papers

1. Boutan, C. *et al.* Axion Dark Matter eXperiment: Run 1A analysis details. *Phys. Rev. D* **109,** 012009. https://link.aps.org/doi/10.1103/PhysRevD.109.012009 (1 Jan. 2024). DOE Supported.
2. Rybka, G. *et al.* Axions beyond Gen 2. *International Journal of Modern Physics A* **38,** 2330012. eprint: https://doi.org/10.1142/S0217751X23300120. https://doi.org/10.1142/S0217751X23300120 (2023). DOE Supported.
3. Rybka, G. Axion dark matter searches above 1 μeV. *Nuclear Physics B* **1003.** Special Issue of Nobel Symposium 182 on Dark Matter, 116481. ISSN: 0550-3213. https://www.sciencedirect.com/science/article/pii/S0550321324000476 (2024). DOE Supported.
4. Chakrabarty, S. *et al.* Low frequency, 100–600 MHz, searches with axion cavity haloscopes. *Phys. Rev. D* **109,** 042004. https://link.aps.org/doi/10.1103/PhysRevD.109.042004 (4 Feb. 2024). DOE Supported.
5. Nitta, T. *et al.* Search for a Dark-Matter-Induced Cosmic Axion Background with ADMX. *Phys. Rev. Lett.* **131,** 101002. https://link.aps.org/doi/10.1103/PhysRevLett.131.101002 (10 Sept. 2023). DOE Supported.
6. Bartram, C. *et al.* Nonvirialized axion search sensitive to Doppler effects in the Milky Way halo. *Phys. Rev. D* **109,** 083014. https://link.aps.org/doi/10.1103/PhysRevD.109.083014 (8 Apr. 2024). DOE Supported.
7. Arnquist, I. *et al.* Search for Daily Modulation of MeV Dark Matter Signals with DAMIC-M. *Phys. Rev. Lett.* **132,** 101006. arXiv: 2307.07251 [hep-ex] (2024).
8. Aguilar-Arevalo, A. *et al.* Confirmation of the spectral excess in DAMIC at SNOLAB with skipper CCDs. *Phys. Rev. D* **109,** 062007. arXiv: 2306.01717 [astro-ph.CO] (2024).
9. McGuire, K. J. *et al.* Nuclear recoil identification in a scientific charge-coupled device. *Phys. Rev. D* **110,** 043008. arXiv: 2309.07869 [physics.ins-det] (2024).
10. Ross, M. *et al.* A vacuum-compatible cylindrical inertial rotation sensor with picoradian sensitivity. *Review of Scientific Instruments* **94** (2023).
11. Aker, M. *et al.* Search for keV-scale sterile neutrinos with the first KATRIN data. *The European Physical Journal C* **83.** ISSN: 1434-6052 (Aug. 2023). DOE Supported.
12. Wydra, J. *et al.* ViMA—The Spinning Rotor Gauge to Measure the Viscosity of Tritium Between 77 and 300 K. *Fusion Science and Technology* **80,** 616–622. ISSN: 1943-7641 (Sept. 2023).

13. Abe, S. *et al.* Combined Pre-supernova Alert System with KamLAND and Super-Kamiokande. *Astrophys. J.* **973,** 140. arXiv: 2404.09920 [hep-ex] (2024).

14. Abe, S. *et al.* Search for charged excited states of dark matter with KamLAND-Zen. *Phys. Lett. B* **855,** 138846. arXiv: 2311.09676 [hep-ex] (2024).

15. Arnquist, I. J. *et al.* Search for charge non-conservation and Pauli exclusion principle violation with the Majorana Demonstrator. *Nature Phys.* **20,** 1078–1083. arXiv: 2203.02033 [nucl-ex] (2024). DOE Supported.

16. Arnquist, I. J. *et al.* Exotic Dark Matter Search with the Majorana Demonstrator. *Phys. Rev. Lett.* **132,** 041001. arXiv: 2206.10638 [hep-ex] (2024). DOE Supported.

17. Barbeau, P. S. *et al.* Accessing new physics with an undoped, cryogenic CsI CEvNS detector for COHERENT at the SNS. *Phys. Rev. D* **109,** 092005. arXiv: 2311.13032 [hep-ex] (2024). DOE Supported.

18. An, P. *et al.* Measurement of Electron-Neutrino Charged-Current Cross Sections on I127 with the COHERENT NaIνE Detector. *Phys. Rev. Lett.* **131,** 221801. arXiv: 2305.19594 [nucl-ex] (2023). DOE Supported.

19. Arnquist, I. J. *et al.* Constraints on the Decay of Ta180m. *Phys. Rev. Lett.* **131,** 152501. arXiv: 2306.01965 [nucl-ex] (2023). DOE Supported.

20. An, P. *et al.* Measurement of Pbnat(νe,Xn) production with a stopped-pion neutrino source. *Phys. Rev. D* **108,** 072001. arXiv: 2212.11295 [hep-ex] (2023). DOE Supported.

21. Arnquist, I. J. *et al.* Energy calibration of germanium detectors for the Majorana Demonstrator. *JINST* **18,** P09023. arXiv: 2306.08661 [physics.ins-det] (2023). DOE Supported.

22. Abbott, R. *et al.* GWTC-2.1: Deep extended catalog of compact binary coalescences observed by LIGO and Virgo during the first half of the third observing run. *Physical Review D* **109,** 022001 (2024).

23. Abbott, R. *et al.* GWTC-3: Compact binary coalescences observed by LIGO and Virgo during the second part of the third observing run. *Physical Review X* **13,** 041039 (2023).

24. Abbott, R *et al.* Constraints on the cosmic expansion history from GWTC-3. *Astrophysical Journal* **949,** 1–37 (2023).

25. Abbott, R *et al.* Search for gravitational waves associated with fast radio bursts detected by CHIME/FRB during the LIGO–Virgo observing run O3a. *The Astrophysical Journal* **955,** 155 (2023).

26. Ross, M. *et al.* A vacuum-compatible cylindrical inertial rotation sensor with picoradian sensitivity. *Review of Scientific Instruments* **94** (2023).

27. Ganapathy, D *et al.* Broadband quantum enhancement of the LIGO detectors with frequency-dependent squeezing. *Physical Review X* **13,** 041021 (2023).

28. Abac, A. *et al.* Ultralight vector dark matter search using data from the KAGRA O3GK run. *arXiv preprint arXiv:2403.03004* (2024).

29. Fletcher, C. *et al.* A joint Fermi-GBM and Swift-BAT analysis of gravitational-wave candidates from the third gravitational-wave observing run. *The astrophysical journal.-Chicago, Ill., 1895, currens* **964,** 1–35 (2024).

30. Abbott, R *et al.* Search for gravitational-wave transients associated with magnetar bursts in Advanced LIGO and Advanced Virgo data from the third observing run. *The Astrophysical Journal* **966,** 1–32 (2024).

31. Jia, W. *et al.* Squeezing the quantum noise of a gravitational-wave detector below the standard quantum limit. *Science* **385,** 1318–1321 (2024).

32. Aguillard, D. P. *et al.* Detailed report on the measurement of the positive muon anomalous magnetic moment to 0.20 ppm. *Phys. Rev. D* **110,** 032009. `https://link.aps.org/doi/10.1103/PhysRevD.110.032009` (3 Aug. 2024). DOE Supported.

33. Aguillard, D. P. *et al.* Measurement of the Positive Muon Anomalous Magnetic Moment to 0.20 ppm. *Phys. Rev. Lett.* **131,** 161802. `https://link.aps.org/doi/10.1103/PhysRevLett.131.161802` (16 Oct. 2023). DOE Supported.

34. Braun, S, Buat, Q, *et al.* Gain suppression study on LGADs at the CENPA tandem accelerator. *Nucl. Instrum. Meth. A* **1064,** 169395. arXiv: `2405.02550 [physics.ins-det]` (2024). DOE Supported.

35. Fotev, V. *et al.* Search for Muon Catalyzed 3Hed Fusion. English. *Physics of Particles and Nuclei* **55.** Publisher Copyright: © Pleiades Publishing, Ltd. 2024. ISSN 1063-7796, Physics of Particles and Nuclei, 2024, Vol. 55, No. 3, pp. 672–684. Pleiades Publishing, Ltd., 2024., 672–684. ISSN: 1063-7796 (June 2024). DOE Supported.

36. Edmonds, A *et al.* Measurement of proton, deuteron, triton, and α particle emission after nuclear muon capture on Al, Si, and Ti with the AlCap experiment. *Phys. Rev. C* **105,** 035501. `https://link.aps.org/doi/10.1103/PhysRevC.105.035501` (3 Mar. 2022). DOE Supported.

37. Buzinsky, N. *et al.* Larmor power limit for cyclotron radiation of relativistic particles in a waveguide. *New Journal of Physics* **26,** 083021. arXiv: `2405.06847 [nucl-ex]` (Aug. 2024). DOE Supported.

Papers submitted or to be published

38. ADMX Collaboration *et al. Axion Dark Matter eXperiment around 3.3 μeV with Dine-Fischler-Srednicki-Zhitnitsky Discovery Ability* Sept. 2024. DOE Supported.

39. Chavarria, A. E. *et al.* The DAMIC excess from WIMP-nucleus elastic scattering. arXiv: `2308.12176 [astro-ph.CO]` (2023).

40. Arnquist, I. *et al.* The DAMIC-M Low Background Chamber. arXiv: `2407.17872 [physics.ins-det]` (2024).

41. Ross, M. *et al.* Test of the Equivalence Principle for Superconductors. *arXiv preprint arXiv:2407.21232* (2024).

42. Aker, M. *et al. Direct neutrino-mass measurement based on 259 days of KATRIN data* 2024. DOE Supported.
43. Aker, M. *et al. Measurement of the electric potential and the magnetic field in the shifted analysing plane of the KATRIN experiment* 2024. DOE Supported.
44. Arnquist, I. J. *et al.* Final Results of the Majorana Demonstrator's Search for Double-Beta Decay of 76Ge to Excited States of 76Se. arXiv: 2410.03995 [nucl-ex] (Oct. 2024). DOE Supported.
45. Araki, T. *et al.* Limits on the Low-Energy Electron Antineutrino Flux from the Brightest GRB of All Time. arXiv: 2410.01996 [astro-ph.HE] (Oct. 2024).
46. Arnquist, I. J. *et al.* An assay-based background projection for the Majorana Demonstrator using Monte Carlo Uncertainty Propagation. arXiv: 2408.06786 [nucl-ex] (Aug. 2024). DOE Supported.
47. Adamski, S. *et al.* First detection of coherent elastic neutrino-nucleus scattering on germanium. arXiv: 2406.13806 [hep-ex] (June 2024). DOE Supported.
48. Abe, S. *et al.* Search for Majorana Neutrinos with the Complete KamLAND-Zen Dataset. arXiv: 2406.11438 [hep-ex] (June 2024).
49. Borden, S., Detwiler, J. A., Pettus, W. & Ruof, N. W. Characterization of Silicon Photomultiplier Photon Detection Efficiency at Liquid Nitrogen Temperature. arXiv: 2405.01529 [physics.ins-det] (May 2024). DOE Supported.
50. Abac, A. *et al.* Search for eccentric black hole coalescences during the third observing run of LIGO and virgo. *arXiv preprint arXiv:2308.03822* (2023).
51. Abac, A. *et al. arXiv: Search for Eccentric Black Hole Coalescences during the Third Observing Run of LIGO and Virgo* tech. rep. (2023).
52. Jia, W. *et al.* LIGO operates with quantum noise below the Standard Quantum Limit. *arXiv preprint arXiv:2404.14569* (2024).
53. Raman, G. *et al.* Swift-BAT GUANO follow-up of gravitational-wave triggers in the third LIGO-Virgo-KAGRA observing run. *arXiv preprint arXiv:2407.12867* (2024).
54. Ross, M. *et al.* Test of the Equivalence Principle for Superconductors. *arXiv preprint arXiv:2407.21232* (2024).
55. Abac, A. *et al.* Observation of Gravitational Waves from the Coalescence of a 2.5-4.5 M Compact Object and a Neutron Star (2024).
56. Soni, S *et al.* LIGO Detector Characterization in the first half of the fourth Observing run. *arXiv preprint arXiv:2409.02831* (2024).
57. Beesley, O *et al.* Measurements of a LYSO crystal array from threshold to 100 MeV. arXiv: 2409.14691 [physics.ins-det] (Sept. 2024). DOE Supported.
58. Acharya, B. *et al.* Solar fusion III: New data and theory for hydrogen-burning stars. *arXiv e-prints,* arXiv:2405.06470. arXiv: 2405.06470 [astro-ph.SR] (May 2024). DOE Supported.

Invited talks

59. Rybka, G. *Nonstandard Uses for Axion Haloscopes* 19th Patras Workshop on Axions, WIMPs and WISPs, Patras, Greece. Sept. 2024. DOE Supported.
60. Guzzetti, M. *Latest Results and Current Progress of ADMX G2* 19th Patras Workshop on Axions, WIMPs and WISPs, Patras, Greece. Sept. 2024. DOE Supported.
61. Rybka, G. *ADMX G2 Run1D Overview* ADMX Collaboration Meeting, Batavia, IL. Apr. 2024. DOE Supported.
62. Zhang, D. *Operational status of ADMX-G2 Run1D* APS April Meeting, Sacramento, CA. Apr. 2024. DOE Supported.
63. Braine, T. *The Axion Dark Matter Experiment* Lake Louise Winter Institute. Feb. 2024. DOE Supported.
64. Garcia, A. *Beta spectroscopy with microwaves* Seminar, Universite de Caen Normandie, ENSICAEN, Caen, France. Nov. 2023. DOE Supported.
65. Garcia, A. *Cyclotron radiation for nuclear spectroscopy* Radioactive Molecules Workshop, Oak Ridge, TN, Sept. 2024. DOE Supported.
66. Garcia, A. *Novel techniques for searching for new physics in nuclear beta decays* Plenary talk, Department of Atomic Energy Symposium on Nuclear Physics, Roorke, India. Dec. 2024. DOE Supported.
67. Garcia, A. *Searching for new physics using an FN tandem accelerator* Seminar, Inter Universities Accelerator Center (IUAC), Dehli, India. Dec. 2024. DOE Supported.
68. Marsteller, A. *KATRIN* Invited talk, 58th Rencontres de Moriond, Electroweak Interactions & Unified Theories Session, La Thuile, Italy. Mar. 2024. DOE Supported.
69. Detwiler, J. A. *Searching for the Creation of Matter without Antimatter* INTURN Summer Lecture, Institute of Nuclear Theory, Seattle, WA, USA. Aug. 2024. DOE Supported.
70. Detwiler, J. A. *Searching for the Creation of Matter (Without Antimatter) in* Majorana *and LEGEND, Physics Seminars* T. D. Lee Institute and Shanghai Jiao-Tong University, Shanghai, China. Sept. 2023. DOE Supported.
71. Detwiler, J. A. *Searching for Neutrinoless Double-Beta Decay with KamLAND-Zen and LEGEND, Invited Talk* MAYORANA Workshop, Modica, Italy. July 2023. DOE Supported.
72. Novitski, E. *Cryogenic 3He NMR for the Project 8 Neutrino Mass Experiment* Invited talk, 3He Magnetometry Workshop, Ann Arbor, MI. Oct. 2024. DOE Supported.
73. Novitski, E. *Project 8: precisely probing neutrino mass with Cyclotron Radiation Emission Spectroscopy* Invited talk, Precision Measurements and BSM Physics Workshop, APS-DNP meeting, Boston, MA. Oct. 2024. DOE Supported.
74. Novitski, E. *Investigating neutrinos and the weak interaction with Cyclotron Radiation Emission Spectroscopy* Invited Freedman Prize talk, APS-DNP meeting, Waikoloa, HI. Nov. 2023. DOE Supported.

75. Novitski, E. *A new approach to measuring neutrino mass* Physics Division Colloquium, Argonne National Lab, Lemont, IL. Jan. 2024. DOE Supported.
76. Novitski, E. *A new approach to measuring neutrino mass* Physics Department Colloquium, University of Texas Arlington, Arlington, TX. Oct. 2023. DOE Supported.
77. Claessens, C. *Precision Tests of the Standard Model: The Project 8 and Muon g-2 Experiments* CENPA Seminar, Seattle, WA. Apr. 2024. DOE Supported.
78. Claessens, C. *The Project 8 neutrino mass experiment: First results and future prospects* LEPP Experimental Seminar, Cornell University, Ithaca, NY. Dec. 2023. DOE Supported.
79. Robertson, R. G. H. *Direct probes of neutrino mass* APS April Meeting, Sacramento CA. Apr. 2024. DOE Supported.

Abstracts and contributed talks

80. Lin, H. *Latest Progress of the DAMIC-M Experiment* Contributed talk, American Physical Society (APS) April Meeting 2024, Sacramento, CA. Apr. 2024.
81. Traina, M. *Confirmation of the excess of ionization events in DAMIC at SNOLAB with skipper CCDs* Contributed talk, TAUP2023: XVIII International Conference on Topics in Astroparticle and Underground Physics 2023, Vienna, Austria. Aug. 2023.
82. Taylor, R. *6He-CRES: Apparatus Upgrades* Contributed talk, APS-DNP meeting, Hawaii. Oct. 2023.
83. Harrington, H. *Techniques for Improving Event Reconstruction in He6-CRES* Contributed talk, APS-DNP meeting, Hawaii. Oct. 2023. DOE Supported.
84. Buzinsky, N. *He6-CRES: Cyclotron Radiation of Relativistic Particles in a Waveguide* Contributed talk, APS-DNP meeting, Hawaii. Oct. 2023. DOE Supported.
85. Cole, A. & Sanshiro Enomoto: Hamish Robertson: Alexander Marsteller: Matt Kallander Team. *Characterization of a Candidate Electron Detector for the KATRIN Neutrino Experiment* Contributed talk, APS-DNP meeting, Waikoloa Village, HI. Nov. 2023. DOE Supported.
86. Marsteller, A. *et al. Velocity slip coefficient measurements at cryogenic temperatures using a Spinning Rotor Gauge* Contributed talk, EVC17, Harrogate, UK. June 2024.
87. Novitski, E. *Project 8: results and prospects* Contributed poster, The XXXI Intl. Conf. on Neutrino Physics and Astrophysics, Milan, Italy. July 2024. DOE Supported.
88. Novitski, E. *Cyclotron Radiation Emission Spectroscopy and the Project 8 neutrino mass experiment* Contributed talk, APS-DNP meeting, Waikoloa, HI. Dec. 2023. DOE Supported.
89. Claessens, C. *Sensitivity analysis for the neutrino mass experiment Project 8* Contributed poster, The XXXI Intl. Conf. on Neutrino Physics and Astrophysics, Milan, Italy. July 2024. DOE Supported.

90. Claessens, C. *Neutrino mass limit and final analysis of the first tritium spectrum recorded with CRES* Contributed talk, APS-DNP meeting, Waikoloa, HI. Dec. 2023. DOE Supported.
91. Ni, X. *Development of a hybrid amorphous Selenium/CMOS detector for the Selena Neutrino Experiment* Contributed talk, 2023 IEEE NSS MIC RTSD: 2023 IEEE Nuclear Science Symposium and Medical Imaging Conference, together with the International Symposium on Room-Temperature Semiconductor X-Ray and Gamma-Ray Detectors, Vancouver, Canada. Nov. 2023. DOE Supported.
92. Chavarria, A. E. *R&D status of the Selena Neutrino Experiment* Contributed talk, TAUP2023: XVIII International Conference on Topics in Astroparticle and Underground Physics 2023, Vienna, Austria. Aug. 2023. DOE Supported.

Book publications

Ph.D. degrees granted

93. Braine, T. & Rybka, G. *Superconducting Resonator Development for the Axion Dark Matter eXperiment* PhD thesis (Washington U., Seattle, Aug. 2024). arXiv: `2408.03444 [hep-ex]`. DOE Supported.
94. Shaw, E. *Equivalence Principle Tests and Direct Searches for Ultra-Light Dark Matter with Fused-Silica Torsion Fibers* PhD thesis (Washington U., Seattle, Aug. 2023).
95. Byron, W. *Developments in the application of Cyclotron Radiation Emission Spectroscopy (CRES) towards the precise determination of MeV-scale beta-energy spectra* PhD thesis (Washington U., Seattle, Dec. 2023). DOE Supported.
96. Hostiuc, A. *Search for Neutrinoless Double Beta Decay Using the Full MAJORANA DEMONSTRATOR Dataset* PhD thesis (Washington U., Seattle, Aug. 2023). DOE Supported.
97. Muldoon, E. *MuSun: A Complete Analysis of the Precision Measurement of Nuclear Muon Capture in Deuterium* PhD thesis (Washington U., Seattle, 2023). DOE Supported.
98. LaBounty, J. *Analysis of the Anomalous Spin Precession of the Muon for the Fermilab Muon g-2 Experiment* PhD thesis (Washington U., Seattle, Mar. 2024). DOE Supported.

9 Publications

Published papers

3. Abe, S. *et al.* Combined Pre-supernova Alert System with KamLAND and Super-Kamiokande. *Astrophys. J.* **973,** 140. arXiv: 2404.09920 [hep-ex] (2024).
5. Abe, S. *et al.* Search for charged excited states of dark matter with KamLAND-Zen. *Phys. Lett. B* **855,** 138846. arXiv: 2311.09676 [hep-ex] (2024).
9. Arnquist, I. J. *et al.* Search for charge non-conservation and Pauli exclusion principle violation with the Majorana Demonstrator. *Nature Phys.* **20,** 1078–1083. arXiv: 2203.02033 [nucl-ex] (2024). DOE Supported.
10. Arnquist, I. J. *et al.* Exotic Dark Matter Search with the Majorana Demonstrator. *Phys. Rev. Lett.* **132,** 041001. arXiv: 2206.10638 [hep-ex] (2024). DOE Supported.
11. Barbeau, P. S. *et al.* Accessing new physics with an undoped, cryogenic CsI CEvNS detector for COHERENT at the SNS. *Phys. Rev. D* **109,** 092005. arXiv: 2311.13032 [hep-ex] (2024). DOE Supported.
12. An, P. *et al.* Measurement of Electron-Neutrino Charged-Current Cross Sections on I127 with the COHERENT NaIνE Detector. *Phys. Rev. Lett.* **131,** 221801. arXiv: 2305.19594 [nucl-ex] (2023). DOE Supported.
13. Arnquist, I. J. *et al.* Constraints on the Decay of Ta180m. *Phys. Rev. Lett.* **131,** 152501. arXiv: 2306.01965 [nucl-ex] (2023). DOE Supported.
14. An, P. *et al.* Measurement of Pbnat(νe,Xn) production with a stopped-pion neutrino source. *Phys. Rev. D* **108,** 072001. arXiv: 2212.11295 [hep-ex] (2023). DOE Supported.
15. Arnquist, I. J. *et al.* Energy calibration of germanium detectors for the Majorana Demonstrator. *JINST* **18,** P09023. arXiv: 2306.08661 [physics.ins-det] (2023). DOE Supported.
37. Buzinsky, N. *et al.* Larmor power limit for cyclotron radiation of relativistic particles in a waveguide. *New Journal of Physics* **26,** 083021. arXiv: 2405.06847 [nucl-ex] (Aug. 2024). DOE Supported.
40. Aker, M. *et al.* Search for keV-scale sterile neutrinos with the first KATRIN data. *The European Physical Journal C* **83.** ISSN: 1434-6052 (Aug. 2023). DOE Supported.
41. Wydra, J. *et al.* ViMA—The Spinning Rotor Gauge to Measure the Viscosity of Tritium Between 77 and 300 K. *Fusion Science and Technology* **80,** 616–622. ISSN: 1943-7641 (Sept. 2023).
50. Aguillard, D. P. *et al.* Detailed report on the measurement of the positive muon anomalous magnetic moment to 0.20 ppm. *Phys. Rev. D* **110,** 032009. https://link.aps.org/doi/10.1103/PhysRevD.110.032009 (3 Aug. 2024). DOE Supported.

52. Aguillard, D. P. *et al.* Measurement of the Positive Muon Anomalous Magnetic Moment to 0.20 ppm. *Phys. Rev. Lett.* **131,** 161802. https://link.aps.org/doi/10.1103/PhysRevLett.131.161802 (16 Oct. 2023). DOE Supported.

53. S. Braun Q. Buat, J. D.-P. K. S. M. F. M.-M. A. M. C. L. J. O. A. S. B. S. & Zhao, Y. Gain suppression study on LGADs at the CENPA tandem accelerator. *Nucl. Instrum. Meth. A* **1064,** 169395. arXiv: 2405.02550 [physics.ins-det] (2024). DOE Supported.

54. Fotev, V. *et al.* Search for Muon Catalyzed 3Hed Fusion. English. *Physics of Particles and Nuclei* **55.** Publisher Copyright: © Pleiades Publishing, Ltd. 2024. ISSN 1063-7796, Physics of Particles and Nuclei, 2024, Vol. 55, No. 3, pp. 672–684. Pleiades Publishing, Ltd., 2024., 672–684. ISSN: 1063-7796 (June 2024). DOE Supported.

55. Edmonds, A. *et al.* Measurement of proton, deuteron, triton, and α particle emission after nuclear muon capture on Al, Si, and Ti with the AlCap experiment. *Phys. Rev. C* **105,** 035501. https://link.aps.org/doi/10.1103/PhysRevC.105.035501 (3 Mar. 2022). DOE Supported.

65. Boutan, C. *et al.* Axion Dark Matter eXperiment: Run 1A analysis details. *Phys. Rev. D* **109,** 012009. https://link.aps.org/doi/10.1103/PhysRevD.109.012009 (1 2024). DOE Supported.

66. Rybka, G. *et al.* Axions beyond Gen 2. *International Journal of Modern Physics A* **38,** 2330012. eprint: https://doi.org/10.1142/S0217751X23300120. https://doi.org/10.1142/S0217751X23300120 (2023). DOE Supported.

67. Rybka, G. Axion dark matter searches above 1 μeV. *Nuclear Physics B* **1003.** Special Issue of Nobel Symposium 182 on Dark Matter, 116481. ISSN: 0550-3213. https://www.sciencedirect.com/science/article/pii/S0550321324000476 (2024). DOE Supported.

68. Chakrabarty, S. *et al.* Low frequency, 100–600 MHz, searches with axion cavity haloscopes. *Phys. Rev. D* **109,** 042004. https://link.aps.org/doi/10.1103/PhysRevD.109.042004 (4 2024). DOE Supported.

69. Nitta, T. *et al.* Search for a Dark-Matter-Induced Cosmic Axion Background with ADMX. *Phys. Rev. Lett.* **131,** 101002. https://link.aps.org/doi/10.1103/PhysRevLett.131.101002 (10 2023). DOE Supported.

70. Bartram, C. *et al.* Nonvirialized axion search sensitive to Doppler effects in the Milky Way halo. *Phys. Rev. D* **109,** 083014. https://link.aps.org/doi/10.1103/PhysRevD.109.083014 (8 2024). DOE Supported.

82. Arnquist, I. *et al.* Search for Daily Modulation of MeV Dark Matter Signals with DAMIC-M. *Phys. Rev. Lett.* **132,** 101006. arXiv: 2307.07251 [hep-ex] (2024).

83. Aguilar-Arevalo, A. *et al.* Confirmation of the spectral excess in DAMIC at SNOLAB with skipper CCDs. *Phys. Rev. D* **109,** 062007. arXiv: 2306.01717 [astro-ph.CO] (2024).

84. McGuire, K. J. *et al.* Nuclear recoil identification in a scientific charge-coupled device. *Phys. Rev. D* **110,** 043008. arXiv: 2309.07869 [physics.ins-det] (2024).

85. Ross, M. *et al.* A vacuum-compatible cylindrical inertial rotation sensor with picoradian sensitivity. *Review of Scientific Instruments* **94** (2023).

87. Abbott, R. *et al.* GWTC-2.1: Deep extended catalog of compact binary coalescences observed by LIGO and Virgo during the first half of the third observing run. *Physical Review D* **109,** 022001 (2024).

88. Abbott, R. *et al.* GWTC-3: Compact binary coalescences observed by LIGO and Virgo during the second part of the third observing run. *Physical Review X* **13,** 041039 (2023).

89. Abbott, R *et al.* Constraints on the cosmic expansion history from GWTC-3. *Astrophysical Journal* **949,** 1–37 (2023).

90. Abbott, R *et al.* Search for gravitational waves associated with fast radio bursts detected by CHIME/FRB during the LIGO–Virgo observing run O3a. *The Astrophysical Journal* **955,** 155 (2023).

93. Ganapathy, D *et al.* Broadband quantum enhancement of the LIGO detectors with frequency-dependent squeezing. *Physical Review X* **13,** 041021 (2023).

94. Abac, A. *et al.* Ultralight vector dark matter search using data from the KAGRA O3GK run. *arXiv preprint arXiv:2403.03004* (2024).

96. Fletcher, C. *et al.* A joint Fermi-GBM and Swift-BAT analysis of gravitational-wave candidates from the third gravitational-wave observing run. *The astrophysical journal.-Chicago, Ill., 1895, currens* **964,** 1–35 (2024).

97. Abbott, R *et al.* Search for gravitational-wave transients associated with magnetar bursts in Advanced LIGO and Advanced Virgo data from the third observing run. *The Astrophysical Journal* **966,** 1–32 (2024).

101. Jia, W. *et al.* Squeezing the quantum noise of a gravitational-wave detector below the standard quantum limit. *Science* **385,** 1318–1321 (2024).

Papers submitted or to be published

1. Arnquist, I. J. *et al.* Final Results of the Majorana Demonstrator's Search for Double-Beta Decay of ^{76}Ge to Excited States of ^{76}Se. arXiv: 2410.03995 [nucl-ex] (Oct. 2024). DOE Supported.

2. Araki, T. *et al.* Limits on the Low-Energy Electron Antineutrino Flux from the Brightest GRB of All Time. arXiv: 2410.01996 [astro-ph.HE] (Oct. 2024).

4. Arnquist, I. J. *et al.* An assay-based background projection for the Majorana Demonstrator using Monte Carlo Uncertainty Propagation. arXiv: 2408.06786 [nucl-ex] (Aug. 2024). DOE Supported.

6. Adamski, S. *et al.* First detection of coherent elastic neutrino-nucleus scattering on germanium. arXiv: 2406.13806 [hep-ex] (June 2024). DOE Supported.

7. Abe, S. *et al.* Search for Majorana Neutrinos with the Complete KamLAND-Zen Dataset. arXiv: 2406.11438 [hep-ex] (June 2024).

8. Borden, S., Detwiler, J. A., Pettus, W. & Ruof, N. W. Characterization of Silicon Photomultiplier Photon Detection Efficiency at Liquid Nitrogen Temperature. arXiv: 2405.01529 [physics.ins-det] (May 2024). DOE Supported.

38. Acharya, B. *et al.* Solar fusion III: New data and theory for hydrogen-burning stars. *arXiv e-prints,* arXiv:2405.06470. arXiv: 2405.06470 [astro-ph.SR] (May 2024). DOE Supported.

42. Aker, M. *et al. Direct neutrino-mass measurement based on 259 days of KATRIN data* 2024. DOE Supported.

43. Aker, M. *et al. Measurement of the electric potential and the magnetic field in the shifted analysing plane of the KATRIN experiment* 2024. DOE Supported.

49. O. Beesley J. Carlton, B. D.-P. D. D. S. F. K. F. L. G. T. G. D. H. S. H. J. H. P. K. J. L. J. L. h. R. R. P. S. A. S. E. S. B. T. Measurements of a LYSO crystal array from threshold to 100 MeV. arXiv: 2409.14691 [physics.ins-det] (Sept. 2024). DOE Supported.

76. ADMX Collaboration *et al. Axion Dark Matter eXperiment around 3.3 μeV with Dine-Fischler-Srednicki-Zhitnitsky Discovery Ability* Sept. 2024. DOE Supported.

80. Chavarria, A. E. *et al.* The DAMIC excess from WIMP-nucleus elastic scattering. arXiv: 2308.12176 [astro-ph.CO] (2023).

81. Arnquist, I. *et al.* The DAMIC-M Low Background Chamber. arXiv: 2407.17872 [physics.ins-det] (2024).

86. Ross, M. *et al.* Test of the Equivalence Principle for Superconductors. *arXiv preprint arXiv:2407.21232* (2024).

91. Abac, A. *et al.* Search for eccentric black hole coalescences during the third observing run of LIGO and virgo. *arXiv preprint arXiv:2308.03822* (2023).

92. Abac, A. *et al. arXiv: Search for Eccentric Black Hole Coalescences during the Third Observing Run of LIGO and Virgo* tech. rep. (2023).

95. Jia, W. *et al.* LIGO operates with quantum noise below the Standard Quantum Limit. *arXiv preprint arXiv:2404.14569* (2024).

98. Raman, G. *et al.* Swift-BAT GUANO follow-up of gravitational-wave triggers in the third LIGO-Virgo-KAGRA observing run. *arXiv preprint arXiv:2407.12867* (2024).

99. Abac, A. *et al.* Observation of Gravitational Waves from the Coalescence of a $2.5 - 4.5\bar{M}_{\odot}$ $CompactObjectandaNeutronStar$ (2024).

100. Soni, S *et al.* LIGO Detector Characterization in the first half of the fourth Observing run. *arXiv preprint arXiv:2409.02831* (2024).

Invited talks

18. Detwiler, J. A. *Searching for the Creation of Matter without Antimatter* INTURN Summer Lecture, Institute of Nuclear Theory, Seattle, WA, USA. 2024. DOE Supported.
19. Detwiler, J. A. *Searching for the Creation of Matter (Without Antimatter) in* MAJORANA *and LEGEND, Physics Seminars* T. D. Lee Institute and Shanghai Jiao-Tong University, Shanghai, China. 2023. DOE Supported.
20. Detwiler, J. A. *Searching for Neutrinoless Double-Beta Decay with KamLAND-Zen and LEGEND, Invited Talk* MAYORANA Workshop, Modica, Italy. 2023. DOE Supported.
25. Novitski, E. *Cryogenic ^{3}He NMR for the Project 8 Neutrino Mass Experiment* Invited talk, ^{3}He Magnetometry Workshop, Ann Arbor, MI. 2024. DOE Supported.
26. Novitski, E. *Project 8: precisely probing neutrino mass with Cyclotron Radiation Emission Spectroscopy* Invited talk, Precision Measurements and BSM Physics Workshop, APS-DNP meeting, Boston, MA. 2024. DOE Supported.
27. Novitski, E. *Investigating neutrinos and the weak interaction with Cyclotron Radiation Emission Spectroscopy* Invited Freedman Prize talk, APS-DNP meeting, Waikoloa, HI. 2023. DOE Supported.
30. Novitski, E. *A new approach to measuring neutrino mass* Physics Division Colloquium, Argonne National Lab, Lemont, IL. 2024. DOE Supported.
31. Novitski, E. *A new approach to measuring neutrino mass* Physics Department Colloquium, University of Texas Arlington, Arlington, TX. 2023. DOE Supported.
32. Claessens, C. *Precision Tests of the Standard Model: The Project 8 and Muon g-2 Experiments* CENPA Seminar, Seattle, WA. 2024. DOE Supported.
33. Claessens, C. *The Project 8 neutrino mass experiment: First results and future prospects* LEPP Experimental Seminar, Cornell University, Ithaca, NY. 2023. DOE Supported.
36. Robertson, R. G. H. *Direct probes of neutrino mass* APS April Meeting, Sacramento CA. 2024. DOE Supported.
44. Marsteller, A. *KATRIN* Invited talk, 58th Rencontres de Moriond, Electroweak Interactions & Unified Theories Session, La Thuile, Italy. 2024. DOE Supported.
58. Garcia, A. *Beta spectroscopy with microwaves* Seminar, Universite de Caen Normandie, ENSICAEN, Caen, France. 2023. DOE Supported.
59. Garcia, A. *Cyclotron radiation for nuclear spectroscopy* Radioactive Molecules Workshop, Oak Ridge, TN, 2024. DOE Supported.
60. Garcia, A. *Novel techniques for searching for new physics in nuclear beta decays* Plenary talk, Department of Atomic Energy Symposium on Nuclear Physics, Roorke, India. 2024. DOE Supported.
61. Garcia, A. *Searching for new physics using an FN tandem accelerator* Seminar, Inter Universities Accelerator Center (IUAC), Dehli, India. 2024. DOE Supported.

71. Rybka, G. *Nonstandard Uses for Axion Haloscopes* 19th Patras Workshop on Axions, WIMPs and WISPs, Patras, Greece. 2024. DOE Supported.
72. Guzzetti, M. *Latest Results and Current Progress of ADMX G2* 19th Patras Workshop on Axions, WIMPs and WISPs, Patras, Greece. 2024. DOE Supported.
73. Rybka, G. *ADMX G2 Run1D Overview* ADMX Collaboration Meeting, Batavia, IL. 2024. DOE Supported.
74. Zhang, D. *Operational status of ADMX-G2 Run1D* APS April Meeting, Sacramento, CA. 2024. DOE Supported.
75. Braine, T. *The Axion Dark Matter Experiment* Lake Louise Winter Institute. 2024. DOE Supported.

Abstracts and contributed talks

28. Novitski, E. *Project 8: results and prospects* Contributed poster, The XXXI Intl. Conf. on Neutrino Physics and Astrophysics, Milan, Italy. 2024. DOE Supported.
29. Novitski, E. *Cyclotron Radiation Emission Spectroscopy and the Project 8 neutrino mass experiment* Contributed talk, APS-DNP meeting, Waikoloa, HI. 2023. DOE Supported.
34. Claessens, C. *Sensitivity analysis for the neutrino mass experiment Project 8* Contributed poster, The XXXI Intl. Conf. on Neutrino Physics and Astrophysics, Milan, Italy. 2024. DOE Supported.
35. Claessens, C. *Neutrino mass limit and final analysis of the first tritium spectrum recorded with CRES* Contributed talk, APS-DNP meeting, Waikoloa, HI. 2023. DOE Supported.
39. Cole, A. & Sanshiro Enomoto: Hamish Robertson: Alexander Marsteller: Matt Kallander Team. *Characterization of a Candidate Electron Detector for the KATRIN Neutrino Experiment* Contributed talk, APS-DNP meeting, Waikoloa Village, HI. 2023. DOE Supported.
45. Marsteller, A. *et al. Velocity slip coefficient measurements at cryogenic temperatures using a Spinning Rotor Gauge* Contributed talk, EVC17, Harrogate, UK. 2024.
46. Ni, X. *Development of a hybrid amorphous Selenium/CMOS detector for the Selena Neutrino Experiment* Contributed talk, 2023 IEEE NSS MIC RTSD: 2023 IEEE Nuclear Science Symposium and Medical Imaging Conference, together with the International Symposium on Room-Temperature Semiconductor X-Ray and Gamma-Ray Detectors, Vancouver, Canada. 2023. DOE Supported.
48. Chavarria, A. E. *R&D status of the Selena Neutrino Experiment* Contributed talk, TAUP2023: XVIII International Conference on Topics in Astroparticle and Underground Physics 2023, Vienna, Austria. 2023. DOE Supported.
62. Taylor, R. *6He-CRES: Apparatus Upgrades* Contributed talk, APS-DNP meeting, Hawaii. 2023.

63. Harrington, H. *Techniques for Improving Event Reconstruction in He6-CRES* Contributed talk, APS-DNP meeting, Hawaii. 2023. DOE Supported.

64. Buzinsky, N. *He6-CRES: Cyclotron Radiation of Relativistic Particles in a Waveguide* Contributed talk, APS-DNP meeting, Hawaii. 2023. DOE Supported.

78. Lin, H. *Latest Progress of the DAMIC-M Experiment* Contributed talk, American Physical Society (APS) April Meeting 2024, Sacramento, CA. 2024.

79. Traina, M. *Confirmation of the excess of ionization events in DAMIC at SNOLAB with skipper CCDs* Contributed talk, TAUP2023: XVIII International Conference on Topics in Astroparticle and Underground Physics 2023, Vienna, Austria. 2023.

Book publications

Ph.D. degrees granted

77. Braine, T. & Rybka, G. *Superconducting Resonator Development for the Axion Dark Matter eXperiment* PhD thesis (Washington U., Seattle, Aug. 2024). arXiv: `2408.03444 [hep-ex]`. DOE Supported.